Load Calculations in Wind Turbine Power Trains – Design, Maintenance & Reliability

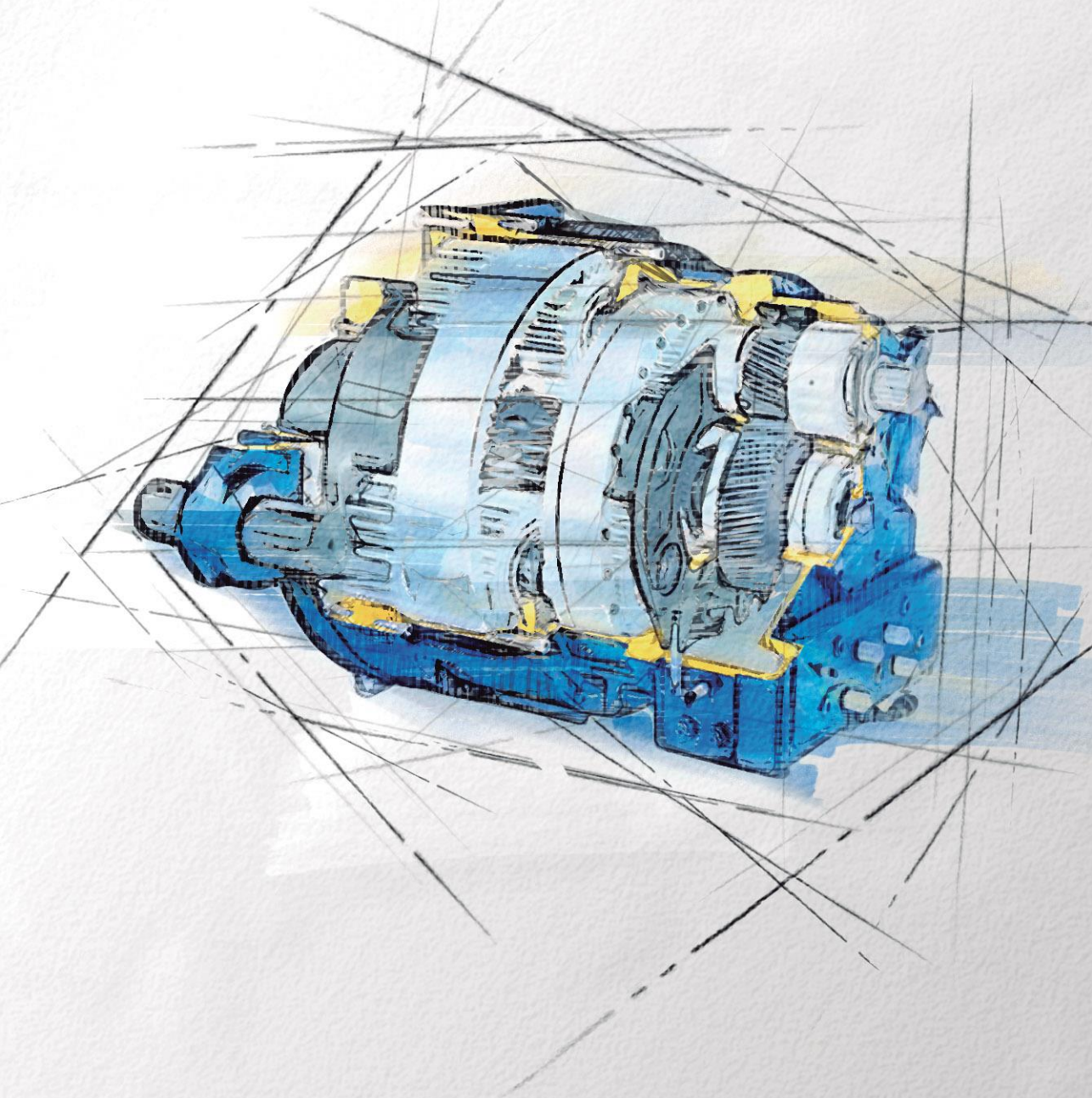

D. P. Rommel

LOAD CALCULATIONS IN WIND TURBINE POWER TRAINS – DESIGN, MAINTENANCE & RELIABILITY

Damian P. Rommel

Graduation Committee:

Chairman:

prof. dr. ir. H. F. J. M. Koopman	University of Twente

Supervisor:

prof. dr. ir. T. Tinga	University of Twente

Co-supervisor:

dr. D. Di Maio	University of Twente

Committee Members:

prof. dr. ir. D. J. Schipper	University of Twente
prof. dr. J. A. Ferreira	University of Twente
prof. dr. S. J. Watson	Delft University of Technology
prof. dr. D. G. Infield	University of Strathclyde (Glasgow)

PhD thesis, University of Twente, Enschede, The Netherlands
July 2020

To cite this dissertation, please use: Rommel, D.P. (2020). Load Calculations in Wind Turbine Power Trains – Design, Maintenance & Reliability. PhD Thesis, University of Twente, Enschede, The Netherlands
ISBN: 978-90-365-5008-6
https://doi.org/10.3990/1.9789036550086

This research has been funded and supported by TKI Wind op Zee, IX Wind and Joulz Energy Solutions as part of the Wind turbine Maintenance and Operation decisions Support (WiMOS) project.

Printed by Gildeprint – Enschede
The cover illustration is made by Jorge Méndez Palacios

LOAD CALCULATIONS IN WIND TURBINE POWER TRAINS – DESIGN, MAINTENANCE & RELIABILITY

DISSERTATION

to obtain
the degree of doctor at the University of Twente,
on the authority of the rector magnificus,
prof. dr. T.T.M. Palstra
on account of the decision of the graduation committee
to be publicly defended on
Friday the 3rd of July 2020 at 16:45 p.m.

by
Damian Peter Rommel

born on the 25 of June 1986
Lindenberg im Allgäu, Germany

This dissertation has been approved by:

Supervisor:
prof. dr. ir. T. Tinga

Co-supervisor:
dr. D. Di Maio

ISBN: 978-90-365-5008-6
DOI: 10.3990/1.9789036550086
Online available at: https://doi.org/10.3990/1.9789036550086

Table of Contents

Summary

Due to high failure rates and long downtimes, extensive research has been done on wind turbines during the last decades. A particular focus has been given to power train components like gearboxes and generators. However, significant reductions of the failure rates could not be achieved despite of the enhancements in gearbox designs and the development of direct driven wind turbines. As a consequence of this, the wind industry has started to focus on failure prediction in order to reduce and optimize cost and thus, has initiated research to develop methods for effective failure and maintenance prediction.

Failures of wind turbine systems are commonly predicted by data-driven and statistics-based approaches. However, statistics-based methods have the drawback to be less precise than model-based ones, especially when large variations in design, loads or operating conditions occur, as is typical for wind turbines. As these variations cannot be adequately incorporated in statistics-based methods, large uncertainties in life predictions and associated conservative maintenance intervals are found. On the other hand, model-based approaches using physical equations and calculations aim to incorporate these variations and consequently, to improve the life time prediction.

Therefore, in this thesis, global loads will be the input for the load-based predictions as they can be of different sources and can be aggregation of various external loads. The term global loads is used here because different sources of global loads (root causes) can lead to various external loads, i.e. forces and moments. These external loads generate internal loads (e.g. stresses), which govern the degradation and failure of components. For example, global loads are: the reaction loads associated to the power transmission (torque and speed), component motions or misalignments.

The usage of (global) load-based prediction approaches provides the advantage that the failure or remaining useful life can already be predicted when the system is still “healthy”, i.e. at a stage where the real system still runs at or close to normal conditions and system degradations cannot be measured yet. Further, the proposed load-based prediction policy can be combined with measurements determining the actual system loads. This has the potential that the system life time can be evaluated more accurately than during the system design procedure. During the system design (global) loads are often assumed. Estimating the system loads based on measurements allows a more detailed specification of the load profiles during operation. This means that the load-based prediction approaches also provide feedback for improving the system design.

However, to apply load-based prediction, physics-based models used for global load calculations must be developed. As the global loads depend on the system design, operation and environment, these models should be i) usable for design purposes and ii) able to handle measurements of operational and environmental responses (conditions). Further, the physics-based models should allow detailed analyses of system loads and behavior to evaluate the most dominant influences of system design, operation and environment on the system life time. To comply with these requirements, the load-based prediction approaches are, in addition to physics-based, also analytical-based in this thesis because finite element based methods are very time consuming.

It is demonstrated that (global) load-based prediction approaches cannot only be used for system design and maintenance but also for system reliability. Application of these

approaches in practice yields three major challenges, namely: i) the lack of information of component dimensions and materials, ii) the measurement of operational conditions and iii) the conversion of calculated loads into life time. By using design standards the third problem can be solved. However, design standards require design details from the Original Equipment Manufacturer (OEM) and thus, lead to the first problem, lack of information. As a system operator can probably realize the measurements of operational (and environmental) conditions, the remaining challenge is the lack of information, which can be reduced by either the cooperation with the system OEM or by engineering expertise.

In this thesis, analytical models are developed for a number of power train components. Chapter 2 provides a method to calculate the loads (e.g. exerted on bearings) caused by the wind turbine rotor. It also shows how these loads are influenced by different effects of asymmetric wind flow. Chapter 3 develops a method to calculate the reaction loads of flexible connecting couplings with metal disc packs. The load calculations considers both joint kinematics and disc pack deformations due to misalignment between gearbox and generator. Further, a load sensitivity analysis is executed to clarify the effect of misalignment on gearbox and generator bearings. Chapter 4 proposes methods to evaluate i) transformer core and winding losses based on rms input and output currents and voltages and ii) the hot spot temperature in transformer windings and cores based on a virtual twin derived from transformer rating information. An accurate detection of the transformer hot spot temperature is important for the transformer life prediction.

This thesis also shows that the maintenance intensity and reliability of any system (here wind turbine power trains) are directly related to their design. This means that the observation of high maintenance activities and low system reliability indicates that system loads and system design are created from different assumptions. Further, the design of any system should be chosen such that the mechanical and electrical subsystem as well as the different components are decoupled from each other so that the effects of transient behaviors and dynamic loads of subsystems and components are not transmitted, i.e. they are minimized or even avoided. This will provide the lowest maintenance costs and the highest system reliability.

This concept is again demonstrated for several components. Chapter 5 considers the drive train reliability from a physics-based design perspective. Methods are developed to improve the drive train reliability during early concept and design stages. Principles of system load reduction are applied to achieve a higher reliability, i.e.: minimization of load magnitude, prevention of load superposition, specification of system excitation and evaluation of transfer functions. Chapter 6 discusses the system transfer behavior for reliability improvements. The transfer functions are derived for shaft-inertia and gear-gear assemblies. To calculate the transfer function based on fundamental dimensions a simple gear mesh stiffness approximation is provided. Furthermore, the transfer behavior of a direct drive and geared wind turbine are compared. Chapter 7 derives requirements for the stability of renewable energy grids. It is discussed whether a grid connected generator or electrical power converter fulfills these requirements. Based on the discussion of the results an alternative power train concept is presented which seeks to stabilize energy grids based on renewable sources.

Finally, the (global) load-based prediction methods provided in this thesis are not only applicable to wind turbine, industrial or automotive (e.g. electrical car) power trains, the renewable energy grid or any other energy system. Rather, as global loads are a generic concept and any system is determined and exposed to them, global load-based prediction methods (for system design, maintenance and reliability) can be developed for and applied to any mechanical and electrical system. In this sense the methods and calculations presented

in this thesis are just a sample of the potential and possibilities which provide global load-based prediction approaches.

Samenvatting

Vanwege de hoge uitvalpercentages en lange stilstandtijden is de afgelopen decennia uitgebreid onderzoek gedaan aan windturbines. Er is in het bijzonder aandacht besteed aan componenten in de aandrijflijn zoals versnellingsbakken en generatoren. Ondanks de verbeteringen in het ontwerp van tandwielkasten en de ontwikkeling van direct aangedreven (*direct drive*) windturbines konden er echter geen significante verbeteringen in de uitvalpercentages worden bereikt. Daarom is de windindustrie zich gaan concentreren op het voorspellen van storingen om de kosten te verlagen, en is onderzoek gestart naar methoden voor effectieve voorspelling van storingen en onderhoud.

Traditioneel wordt het falen van windturbinesystemen voorspeld met methoden die data gedreven zijn, en gebaseerd op statistieken. Statistische methoden hebben echter als nadeel dat ze minder nauwkeurig zijn dan methoden gebaseerd op modellen, vooral wanneer er grote variaties in ontwerp, belastingen of bedrijfsomstandigheden optreden, zoals bij windturbines. Omdat deze variaties niet goed kunnen worden verwerkt in statistische methoden, levert dat grote onzekerheden in levensduurvoorspellingen op, en daardoor conservatieve onderhoudsintervallen. Modelgebaseerde methoden met fysische vergelijkingen en berekeningen zijn daarentegen juist bedoeld om deze variaties mee te nemen in de berekening, en resulteren daardoor in een nauwkeurigere bepaling van de levensduurverwachting.

Daarom worden in dit proefschrift voorspellingsmethoden gepresenteerd die gebaseerd zijn op de daadwerkelijke globale belastingen. De term globale belastingen wordt hier gebruikt omdat verschillende bronnen van globale belastingen (hoofdoorzaken) tot verschillende externe belastingen (op specifieke onderdelen) kunnen leiden. Deze externe belastingen genereren op hun beurt interne belastingen (bijvoorbeeld spanningen), die maatgevend zijn voor de degradatie en het falen van componenten. De reactiekrachten ten gevolge van de krachtoverbrenging van rotor naar generator (koppel en snelheid) zijn bijvoorbeeld globale belastingen die externe belastingen (krachten en momenten) genereren. Maar ook secundaire bewegingen van componenten en verkeerde uitlijning zijn (globale) belastingen.

Het gebruik van op (globale) belasting gebaseerde voorspellingsmethoden biedt het voordeel dat het falen of de resterende levensduur al kan worden voorspeld wanneer het systeem nog "gezond" is, dat wil zeggen in een stadium waarin het systeem nog steeds opereert onder normale omstandigheden, en systeemdegradaties nog niet kunnen worden gemeten. Verder kan de hier gepresenteerde aanpak op basis van belasting worden gecombineerd met metingen die de werkelijke systeembelastingen bepalen. Dit heeft de potentie om de levensduur van het systeem nauwkeuriger te bepalen dan tijdens de reguliere systeemontwerpprocedure. Bij het systeemontwerp wordt vaak uitgegaan van (globale) belastingen. Door de systeembelasting te schatten op basis van metingen, kan een meer gedetailleerde specificatie van de operationele belastingsprofielen worden verkregen. Dit betekent dat de voorgestelde voorspellingsmethoden ook feedback geven om het systeemontwerp te verbeteren.

Om echter deze voorspellingsmethoden toe te kunnen passen, moeten eerst op fysica gebaseerde modellen worden ontwikkeld voor globale belastingberekeningen. Aangezien de globale belastingen afhankelijk zijn van het ontwerp, de werking en de omgeving van het systeem, moeten deze modellen *i)* bruikbaar zijn voor ontwerpdoeleinden en *ii)* metingen van operationele en omgevingscondities aankunnen. Verder moeten de fysische modellen

gedetailleerde analyses van systeembelastingen en -gedrag mogelijk maken om de meest dominante invloeden van systeemontwerp, werking en omgeving op de levensduur van het systeem te bepalen. Om aan deze vereisten te voldoen, zijn de in dit proefschrift gepresenteerde methoden niet allen gebaseerd op de fysica, maar ook analytisch van aard.

Verder wordt aangetoond dat voorspellingsmethoden op basis van globale belastingen niet alleen kunnen worden gebruikt voor systeemontwerp en onderhoud, maar ook voor het bepalen van systeembetrouwbaarheid. Toepassing van deze benadering in de praktijk levert drie grote uitdagingen op, namelijk: *i)* het gebrek aan informatie over afmetingen en materialen van componenten, *ii)* het meten van de precieze bedrijfsomstandigheden en *iii)* het omzetten van berekende belastingen in levensduur. Door gebruik te maken van ontwerpstandaarden kan het derde probleem worden opgelost. Ontwerpnormen vereisen echter ontwerpdetails van de fabrikant (Original Equipment Manufacturer - OEM) en leiden dus tot het eerste probleem, gebrek aan informatie. Aangezien een gebruiker / beheerder van een systeem waarschijnlijk zelf metingen van operationele (en omgevings-) omstandigheden kan realiseren, is de enige resterende uitdaging het gebrek aan informatie. Dit dat kan worden opgelost door samenwerking met de fabrikant, of door technische expertise.

In dit proefschrift worden modellen ontwikkeld voor een aantal aandrijflijncomponenten. In Hoofdstuk 2 wordt een methode gepresenteerd om de belastingen (bijv. op lagers) veroorzaakt door de windturbinerotor te berekenen. Het laat ook zien hoe deze belastingen worden beïnvloed door verschillende effecten van asymmetrische windstroming. In Hoofdstuk 3 wordt een methode ontwikkeld om de reactiekrachten veroorzaakt door flexibele koppelingen (tussen versnellingsbak en generator) op basis van metalen schijven te berekenen. Bij de belastingberekeningen wordt rekening gehouden met zowel de kinematica als de vervormingen van het schijfpakket als gevolg van een verkeerde uitlijning tussen de versnellingsbak en de generator. Verder wordt een gevoeligheidsanalyse uitgevoerd om inzicht te krijgen in het effect van verkeerde uitlijning op tandwielkast- en generatorlagers. In Hoofdstuk 4 worden methoden gepresenteerd voor het berekenen van *i)* transformator kern- en windingsverliezen op basis van ingangs- en uitgangsstromen en spanningen, en *ii)* de hotspot-temperatuur in transformatorwindingen en -kernen op basis van een *virtual twin* die is afgeleid van basis transformatorinformatie. Een nauwkeurige bepaling van de hotspot-temperatuur van de transformator is belangrijk voor de levensduurvoorspelling van de transformator.

Dit proefschrift laat ook zien dat de onderhoudsintensiteit en betrouwbaarheid van een willekeurig systeem (hier windturbine-aandrijflijnen) rechtstreeks verband houden met het ontwerp. Dit betekent dat de constatering van veel onderhoudsactiviteiten en lage systeembetrouwbaarheid aangeeft dat systeembelastingen, en dus ook het systeemontwerp, niet goed zijn doordacht. Verder moet het ontwerp van elk systeem zo worden gekozen dat zowel het mechanische en elektrische subsysteem als de verschillende componenten van elkaar worden ontkoppeld, zodat de effecten van niet-stationair gedrag en dynamische belastingen van subsystemen en componenten niet worden overgedragen aan andere componenten. Dit zorgt voor de laagste onderhoudskosten en de hoogste systeembetrouwbaarheid.

Ook dit concept wordt gedemonstreerd voor verschillende componenten. Hoofdstuk 5 beschouwt de betrouwbaarheid van de aandrijflijn vanuit een op fysica gebaseerd ontwerpperspectief. Er zijn methoden ontwikkeld om de betrouwbaarheid van de aandrijflijn te verbeteren tijdens vroegtijdige concept- en ontwerpfasen. Het principe van het verminderen van de systeembelasting wordt toegepast om een hogere betrouwbaarheid te bereiken, d.w.z.: minimalisatie van de grootte van de belasting, voorkomen van superpositie

van belastingen, specificatie van (potentiele) systeemexcitaties en berekening van overdrachtsfuncties. Hoofdstuk 6 gaat specifiek in op dat laatste aspect, de systeemoverdracht, voor verbetering van de betrouwbaarheid. De overdrachtsfuncties zijn afgeleid voor as-traagheid en tandwieloverbrengingen. Om de overdrachtsfunctie te berekenen op basis van fundamentele afmetingen wordt een eenvoudige stijfheidsbenadering voor de vertandingen afgeleid. Verder wordt het overdrachtsgedrag van een *direct drive* en *geared* windturbine vergeleken.

Hoofdstuk 7 leidt vereisten af voor de stabiliteit van electriciteitsnetwerken voor hernieuwbare energie. Er wordt besproken of een direct op het net aangesloten generator of een elektrische omvormer aan deze eisen voldoet. Op basis van de discussieresultaten wordt een alternatief aandrijflijnconcept gepresenteerd dat gericht is op het stabiliseren van hernieuwbare energienetten.

Ten slotte zijn de op belasting gebaseerde voorspellingsmethoden in dit proefschrift niet alleen van toepassing op aandrijflijnen voor windturbines, industriële installaties, in de automotive sector (bijv. elektrische auto's), het hernieuwbare energienetwerk of enig ander energiesysteem. Aangezien globale belastingen een generiek concept zijn en elk systeem er aan wordt blootgesteld, kunnen op globale belasting gebaseerde voorspellingsmethoden (voor systeemontwerp, onderhoud en betrouwbaarheid) worden ontwikkeld voor en toegepast op elk willekeurig systeem. In feite zijn de methoden en berekeningen die in dit proefschrift worden gepresenteerd dus slechts een voorbeeld van de mogelijkheden die belasting gebaseerde voorspellingsbenaderingen bieden.

CHAPTER 1

Introduction

1.1 Background

During the last decades extensive research has been done on wind turbines. Due to high failure rates and long downtimes [1]–[6], a particular focus in this research has been given to power train components like gearbox [7] and generators [8]. As a consequence of this, not only geared but also direct driven wind turbines have been developed. However, the direct drive wind turbines have not significantly reduced the failure rates and thus, have not solved the problems. They have rather shown higher failure rates in the electrical components like power converters than geared wind turbines [9][10]. So the direct drive wind turbines have just shifted the problems and high failure rates of the mechanical to the electrical power train components, i.e. from the gearbox and generator to the electrical power converter.

As neither the direct drive wind turbines nor enhancements of the geared wind turbines achieved, for example, by more sophisticated simulations and calculations [11][12] have led to significant improvements of the failure rates, the wind industry has started to accept higher failure rates and downtimes. At the same time, more focus has been given to failure prediction in order to reduce the costs of repairs and downtimes [13][14]. Especially, the offshore wind industry is interested in reducing these costs because they are significantly higher due to the limited accessibility of wind turbines. Therefore, a novel research has been focused on the development of methods for effective failure and maintenance predictions.

1.2 Failure prediction methods: state of the art

Failures of wind turbine systems are often predicted based on failure statistics [2]. Other approaches follow data-driven or model-based methods for failure prediction. Data driven methods or big data frameworks [15] directly use condition monitoring or SCADA data [16] in combination with prognostics methods like Bayesian probability theory [17] [18], Wiener process [19] or artificial neural networks [20] [21] to evaluate the remaining useful life (RUL). Model-based methods utilize, for example, physics of failure [22] [23] to predict failures and calculate the life time of components. Some model-based methods are inspired by physical principles, but are statistics-based in reality. This means that a lot of approaches for life time prediction proposed in literature are statistics-based. However, statistics-based maintenance is less precise than model-based maintenance [24], especially when large variations in design, loads or operating conditions occur, as it is typical for wind turbines. As these variations cannot be adequately incorporated in statistics-based methods, this leads to large uncertainties in life predictions and conservative maintenance intervals [23]. Consequently, the accuracy of life time predictions can be increased by a model-based approach which uses purely physical equations and calculations. Djeziri et al. [25] propose a hybrid method for the prediction of the RUL in order to not apply statistics-based methods, i.e. a finite element based model of the wind turbine are combined with measurements at a real wind turbine. The model simulates the system behavior under normal and faulty condition, e.g. bearing failure. The RUL is evaluated by comparing the measured and simulated, normal and faulty conditions. This also means that Djeziri et al. [25] follow the approach of condition based maintenance where maintenance decisions are based on measurements of system performance or degradation. The closer the measured condition is to the faulty condition, the shorter is the RUL.

In this thesis a (global) load-based maintenance approach is proposed to utilize the model-based methods based on purely physical equations. Load- and usage-based maintenance policies have already been proposed and applied by Tinga [23]. For usage-based maintenance, he proposed to translate the system usage (on the global level) to the local (internal) loads like stress, strain or temperature. But, in mechanical systems these internal loads can also be retrieved from the forces and moments (external loads) acting on or inside the mechanical system. Consequently, load-based maintenance can be executed by evaluating the global loads of the mechanical system. Note the term global loads is used here because different root causes can lead to certain external loads. For example, the reaction loads (in bearings or a structure) due to transmitting power (torque and speed) are equal to the external loads (forces and moments). However, component motions or misalignments are also (global) loads. They all are root causes and result in external loads which are the consequence. So the term global loads (on a system) refers to all sources that results in external loads in or on that system.

1.3 Benefits and challenges of load-based prediction

Using load-based maintenance provides the advantage that the RUL can already be simulated when the system is still “healthy”, i.e. at a stage where the real system still runs at or close to normal condition and degradation cannot be measured yet. Further, load profiles, i.e. the range of loads a specific components is subjected to, rather depend on operational and

environmental conditions than on time. If the system has, at least once, run through the range of operational and environmental conditions, the load profile is known. Then, the life time can be predicted from a combination of these conditions over time. Moreover, it is important to note that the proposed load-based maintenance policy uses actual loads and load profiles which can differ from the loads and load profiles assumed during system design. This means that load-based maintenance has the potential to predict the system life time more accurately than as it is evaluated during the system design procedure.

However, to apply the concept of load-based maintenance, the physical models used for the global load evaluations must be specified. Firstly, it is important to note that global loads like forces, moments and misalignments in mechanical systems, are dependent on the design, operation and environment of the considered system. Hence, the physical model used for global load calculations must, on the one hand, be based on a design model and, on the other hand, consider the actual operational and environmental conditions. This means that the algorithms behind the physical design model must be able to read inputs from quasi real-time measurements. Secondly, load-based maintenance requires a detailed analysis of loads and system behavior to select the most dominant influences of design, operation and environment on the system load profiles. These dominant effects must, at least, be incorporated in the (life time) prediction. Therefore, the physical models used for the global load calculation must describe the system design, operate in real time and be able to easily represent the system behavior. To comply with these requirements, Gokhale and Trivedi [26] recommend the usage of analytical-based models.

In addition, physics-based models describing system design and behavior are not only applicable to load-based maintenance but also to reliability considerations. The system reliability is already largely determined at early concept stages while designing the system [27], i.e. wind turbine power train. Addressing and identifying reliability concerns during design and development processes by the approach of physics of failure demonstrates a better accuracy than the classical approach because it is based on identifying the critical failure modes and on estimating the impact of contributing environmental factors [28]. The classical approach relies on the availability of extensive component libraries providing reliability measures for similar parts. Failure rate prediction using this approach often results in inaccurate reliability prediction and assessment [28]. Further, system reliability is determined by the system stresses and strengths [29]. The actual system stresses are governed by the actual load profiles evaluated for load-based maintenance. Consequently, analytical-based load calculation methods and algorithms cannot only be applied to and used for system design and (load-based) maintenance but also for system reliability analyses where, for example, a (computationally) expensive FEM model is not available, yet.

1.4 Research objectives

In this thesis, load-based prediction methods are developed for wind turbine systems and subsystems. The driving questions are: when, how and why do wind turbine components fail?

The answer to the question “when do components fail” requires the combination of actual load calculations with life time prediction methods. The latter are specified in the design standards like ISO 281, ISO 6336 or IEEE Std. C57.91 and hence, are already available. Therefore, this thesis focuses on the development of load-based calculation and prediction methods. Nevertheless, the question “when do components fail” is exemplary considered for

bearings because the ISO 281 provides a simple method to convert bearing loads into bearing life time.

The question “why do components fail” is answered assuming that a system or subsystem overload leads to a failure. This means that a deviation between assumed (during design) and actual loads could lead to an early failure due to overload. The load deviation can occur, if some of the system loads are not considered or not properly specified during system design. To detect such a (potential) load deviation, load sensitivity analyses are executed in this thesis.

Similarly, the question “how do components fail” can be answered. It is assumed that an overload of a component shows the weak point in the (sub)system. By applying the overload to the different failure mechanism described in the design standards, it can be clarified how the critical power train part will fail. This, however, goes beyond the scope of this thesis and thus, is not demonstrated. So the answer to the question “how do components fail” is only partly given by identifying overload conditions with sensitivity analyses.

Now, with the focus on actual system load calculations, the following objectives are set for this thesis:

1. Development of analytical-based load calculation methods for wind turbine components considering physical system and component behavior as well as operational conditions
2. Identification of deviations between design and actual (sub)system loads as well as overload conditions and quantifying their effects on life time (sensitivity analyses)
3. Gain insights in design, maintenance and reliability considerations of wind turbine components.

The objectives can be achieved by answering the following research questions:

1. How can the loads of wind turbine components be evaluated using analytical load calculations?
   a. What is the physics behind the wind turbine components?
   b. How can the physical behavior be described by analytical equations?
   c. How can the component loads be expressed based on these equations?
   d. Which input parameters and variables of these equations are representative for and deducible from measurable operational conditions?

2. How sensitive are the load calculations to the input parameters and variables (of the analytical equations)?
   a. What are the dominant parameters and variables in the load calculations?
   b. How do these parameters and variables affect the load increase of critical component parts and thus, the life time?

3. How are design, maintenance and reliability of wind turbine components related to load calculations?
   a. What aspects can be learnt by describing the fundamental and essential physics?
   b. What aspects can be derived from the load sensitivity analyses?
   c. What effect do the learnt and derived aspects have on design, maintenance and reliability considerations?

1.5 Approach

Physics-based, i.e. analytical-based, methods are chosen here. They are beneficial for i) considering the system loads, usage, local part loads, the physics of failures and accumulated damage in the remaining life calculation [30] (cp. Figure 1.1) and ii) providing insights in system design, maintenance and reliability as it is demonstrated in this thesis

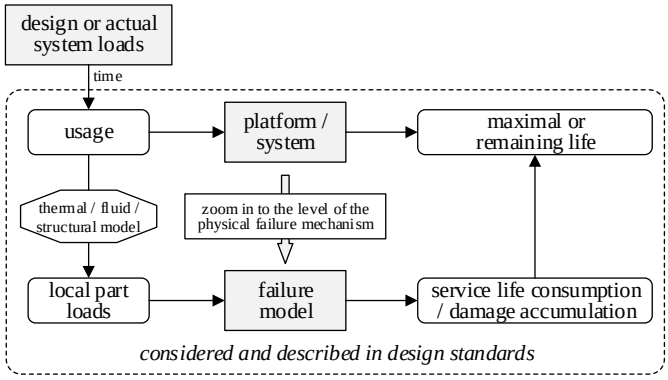

Figure 1.1 Relation between system loads and system life

Further, physics-based prediction methods can be found in design standards. They can be used to calculate the expected time to failure, i.e. maximal life, for particular loads and failure mechanisms (physics of failures). Evaluating the maximal life includes implicitly that usage and damage accumulation are considered. The prediction methods provided in the standards are often developed empirically and verified for specific conditions, i.e. for selected system loads and time periods from which the usage is derived (cp. Figure 1.1). On the one hand, this means that these methods can be considered as reliable and that further research in prediction methods is not necessary unless it provides essential improvements of the already existing methods. On the other hand, the design or actual system loads can be identified as crucial input parameters of these methods having a significant influence on the predicted (maximal) life. This means that the system load description is fundamental for the (physics-based) life time prediction.

Moreover, any system is subjected to static and dynamic loads. Here, loads are considered as forces and moments in mechanical (sub)systems and current and voltages in electrical (sub)systems. The static loads are needed to transmit the system input to the system output. Dynamic load variations, however, interfere in this transmission and thus are not desired. The (load) interferences can lead to critical system conditions and can cause early system failures. This means that the dynamic load description is important for the life time prediction.

Another important aspect is the selection of the critical (sub)system for which the load-based prediction methods should be developed and to which they should be applied. To do so, failure rates and downtimes available in literature are analyzed for wind turbine subsystems (components). However, by comparing the failure rate and downtime statistics the following two findings can be observed: i) a common way of categorizing wind turbines in their subsystems does not exist in literature and ii) different sources in literature highlight

different subsystems (components) as the most critical. Hence, failure rates and downtime statistics provided in literature do not allow a consistent evaluation of the most critical subsystem in wind turbines. Figure 1.2 demonstrates the average number of failures and downtime calculated based on statistics provided by [1]–[4][6][31][32]. It is visible that several subsystems have significant number of failures and downtimes. Therefore, it is unclear which subsystems are the most critical.

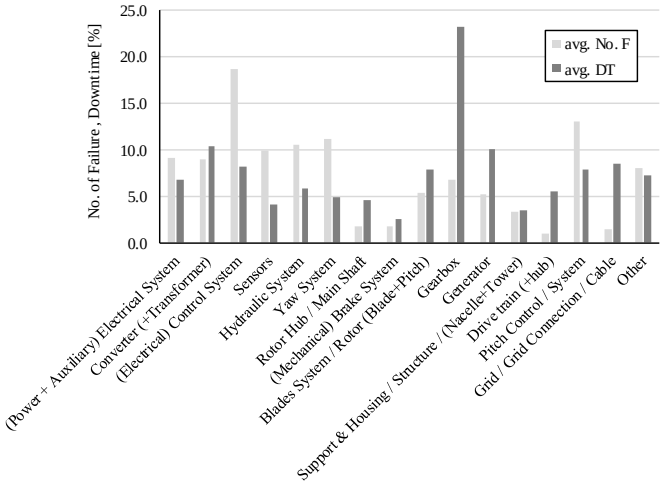

Figure 1.2 Averaged Number of Failures (per year) and Downtimes in wind turbine components

Furthermore, to efficiently apply the load prediction methods, a modular concept is desirable. This means that prediction methods are developed for certain types of components which might be installed several times in the wind turbine and just differ in size (dimensions) and loads (power range). It also means that one method can be used in different wind turbine subsystems. However, to implement such a modular concept the wind turbine must be categorized in consistent systems and subsystems. In this thesis, the concept of "power transmission" is utilized to define the system. A system contains the complete power transmission chain which is, in the case of the wind turbine aerodynamic-, mechanical and electrical power transmission. The reason of using this system concept is the interconnection between the different power transmitting components and elements. For example, unsteady dynamic behavior in the aerodynamic power transmission is detectable in the mechanical power transmission and thus, possibly in the electrical power transmission, too. So based on this reasoning the wind turbine can be divided in four systems, i.e.:

- Main power train system: includes all components (subsystems) which transport power from the rotor (aerodynamic power) to the grid (electrical power). It consists of wind turbine rotor, main shaft with bearings, gearbox, generator, electrical power converter and transformer. As the power flows from the wind turbine rotor (application) to the electrical grid, the main power train system is in generator operation and thus is a power supply.
- Pitch power train system: includes all components which are needed to convert electrical power into a blade motion. A possible system configuration is: transformer,

electrical power converter, electrical motor, gearbox and blades with gear rings (application). As electrical power is consumed to move the blades, the pitch power train system works in motor operation and thus is a power demand.

- Yaw power train system: includes all components which are needed to convert electrical power into a nacelle motion. A possible system configuration is: transformer, electrical power converter, electrical motor, gearbox and nacelle with gear ring (application). As electrical power is consumed to move the nacelle, the yaw power train system works in motor operation and thus is a power demand.
- Wind turbine structure system: in addition to the three power train system (main, pitch and yaw), the wind turbine structure can be considered as a fourth system, The structure includes the tower and its base frame. It is not a power transmission system after the above described criteria. However, it must carry the reaction load of the three power train systems and hence, is directly affected by them.

By comparing the main, pitch and yaw power train system it can be seen that these systems consist of the same components (cp. Figure 1.3). The essential differences between them are only their size (dimensions) and power range (loads).

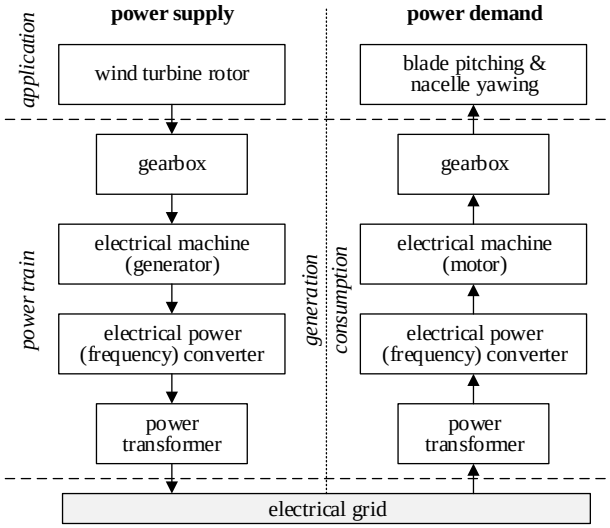

Figure 1.3 Power transmission chain of main, pitch and yaw system

Moreover, the power transmission concept can also be applied to the different power train components (subsystems). The parts which participate in the power transmission can be evaluated for every power train component, i.e.:

- *Gearbox*: mechanical power transmission via shaft-bearing assemblies, mechanical power conversion via gear stage (gear-gear assembly), conversion ratio k specified by gear diameters

- *Mechanical power converter*: mechanical power transmission via shaft-bearing assembly, hydrodynamic power conversion via pump turbine stator assembly for speed variability
- *Electrical machine*: mechanical power transmission via shaft-bearing assembly, electro-mechanical power conversion via rotor stator assembly, electrical power transmission via cables
- *Electrical power converter*: electrical power transmission via cables, AC-DC-AC power conversion for frequency variability
- *Transformer*: electrical power transmission via cables, mechanical power conversion via stator-stator assemblies (including common core), conversion ratio *k* specified by number of windings

Note that the mechanical power converter is added here, although it is not part of current wind turbine power trains. It is mentioned for completeness and will be discussed in more details later in the thesis.

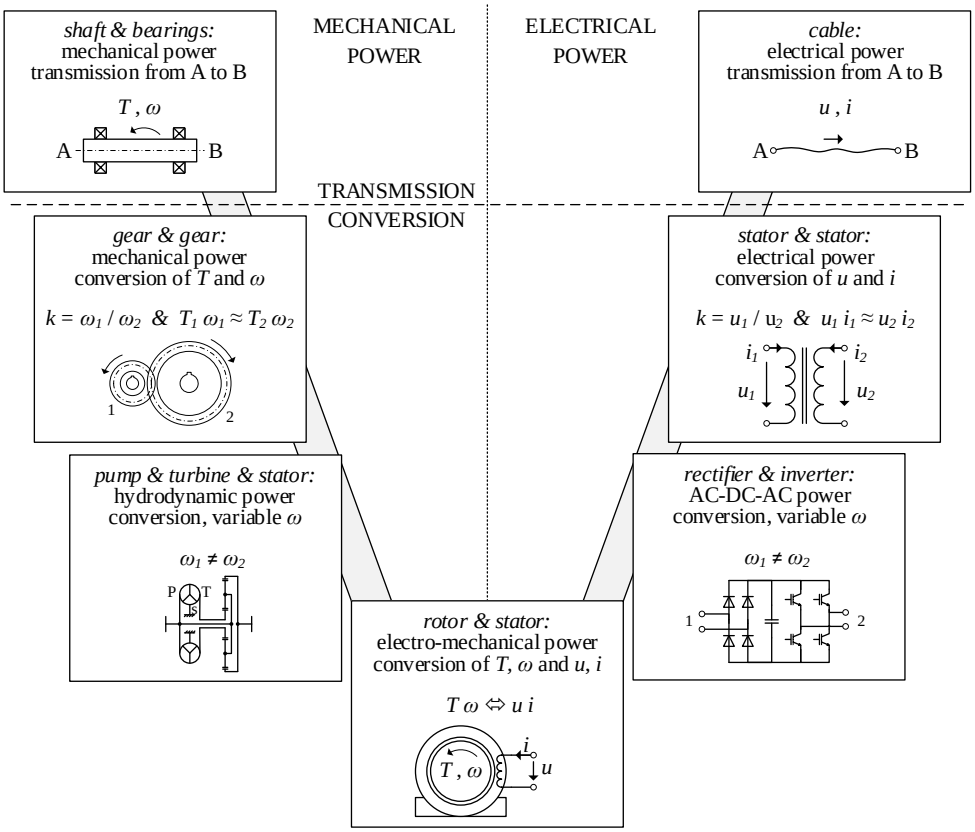

Figure 1.4 Critical parts required for power transmission and conversion

An overview of the different power transmitting and converting parts is demonstrated in Figure 1.4. In this thesis these parts are considered as the most critical. It is also apparent that

Figure 1.4 is applicable for any power train in any power range in power generation and consumption. So developing physics, load and analytical-based calculation methods for these critical components is highly beneficial because the methods have an extensive range of applications. For example, in power plants (gas, steam, hydro power turbines), steel production plants (rolling mill), pump stations (for gas or water), mines (conveyors, mills, crusher) and so on.

1.6 Thesis outline

The thesis consists in total of nine chapters including the introduction. In the chapters two, three and four the wind turbine rotor, flexible connecting coupling between gearbox and generator shaft and power transformer are considered. Then, the view is broadened and the complete drive train (mechanical power train subsystem) is analyzed in chapter five and six, while the electrical grid stability is discussed in chapter seven. After a discussion chapter, the thesis closes with the chapters conclusions and recommendations.

- Chapter 2: provides a method to calculate the loads caused by the wind turbine rotor. It also shows how these loads are influenced by different effects of asymmetric wind flow.
- Chapter 3: develops a method to calculate the reaction loads of flexible connecting couplings with metal disc packs. The load calculations considers both joint kinematics and disc pack deformations due to misalignment between gearbox and generator. Further, a load sensitivity analysis is executed to clarify the effect of misalignment on gearbox and generator bearings.
- Chapter 4: proposes methods to evaluate i) transformer core and winding losses based on rms input and output currents and voltages and ii) the hot spot temperature in transformer windings and cores based on a virtual twin derived from transformer rating information. An accurate detection of the transformer hot spot temperature is important for the transformer life prediction.
- Chapter 5: considers the drive train reliability from a physics-based design perspective. Methods are developed to improve the drive train reliability during early concept and design stages. Principles of system load reduction are applied to achieve a higher reliability, i.e.: minimization of load magnitude, prevention of load superposition, specification of system excitation and evaluation of transfer functions.
- Chapter 6: considers system transfer behavior for reliability improvements, as an extension and complement to Chapter 5. The transfer functions are derived for shaft-inertia and gear-gear assemblies. To calculate the transfer function based on fundamental dimensions a simple gear mesh stiffness approximation is provided. Furthermore, the transfer behavior of a direct drive and geared wind turbine are compared.
- Chapter 7: derives requirements for the stability of renewable energy grids. It discusses whether a grid connected generator or electrical power converter fulfill these requirements. Based on the discussion results an alternative power train concept is presented which seeks to stabilize renewable energy grids.

- Chapter 8: provides a higher-level discussion on different aspects of wind turbine design, maintenance and reliability, this integrating and connecting the foregoing chapters. It is not only shown that design, maintenance and reliability are interrelated but it is also discussed how current wind turbines could be improved.
- Chapter 9: outlines the conclusions and recommendations of this thesis.

1.7 List of publications

Rommel, D. P., Di Maio, D., Tinga, T. (2020). Calculating Wind Turbine Component Loads for Improved Life Prediction. *Renewable energy*, *146*, 223-241.

Rommel, D. P., Di Maio, D., Tinga, T. (2020). Calculating Loads and Life Reduction of Wind Turbine Gearbox and Generator Bearings due to Shaft Misalignment. *Wind Engineering*.

Rommel, D. P., Di Maio, D., Tinga, T. (n.d.). Transformer Hot Spot Temperature Prediction based on basic Operator Information. revision submitted

Rommel, D. P., Di Maio, D., Tinga, T. (n.d). Wind Turbine Power Train Reliability from a Physics Based Design Perspective. submitted.

Rommel, D. P., Di Maio, D., Tinga, T. (n.d). Dynamic Load Absorption in Drive Trains for an Improved Wind Turbine Reliability. submitted.

Rommel, D. P., Di Maio, D., Tinga, T. (n.d). Stabilization of the Renewable Energy Grid by Wind Turbine Generators. submitted.

References

[1] J. Ribrant, “Reliability performance and maintenance - A survey of failures in wind power systems,” 2006.

[2] J. Ribrant and L. M. Bertling, “Survey of Failures in Wind Power Systems With Focus on Swedish Wind Power Plants During 1997-2005,” *IEEE Trans. Energy Convers.*, vol. 22, no. 1, pp. 167–173, 2007.

[3] Noordzee Wind CV, “Operations Report 2008,” 2009.

[4] Noordzee Wind CV, “Operations Report 2009,” 2010.

[5] M. Wilkinson *et al.*, “Methodology and results of the reliawind reliability field study,” 2010.

[6] Tavner, *Offshore Wind Turbines: Reliability, availability and maintenance*. 2013.

[7] D. Infield, N. Barltrop, J. Coultate, K. Scott, and A. Shahaj, “Effects of Extreme and Transient Loads on Wind Turbine Drive Trains,” pp. 1–24, 2014.

[8] K. Alewine and W. Chen, “A review of electrical winding failures in wind turbine generators,” *IEEE Electr. Insul. Mag.*, vol. 28, no. 4, pp. 8–13, 2012.

[9] F. Spinato, P. J. Tavner, G. J. W. van Bussel, and E. Koutoulakos, “Reliability of wind turbine subassemblies,” *IET Renew. Power Gener.*, vol. 3, no. 4, p. 387, 2009.

[10] J. Carroll, A. Mcdonald, and D. Mcmillan, “Reliability comparison of wind turbines with DFIG and PMG drive trains,” *Energy Conversion, IEEE Trans.*, vol. 30, pp. 663–670, 2015.

[11] J. Peeters, D. Vandepitte, and P. Sas, “Flexible multibody model of a three-stage planetary gearbox in a wind turbine,” *Isma*, pp. 3923–3942, 2004.

[12] J. Peeters, “Simulation of dynamic drive train loads in a wind turbine,” 2006.

[13] B. Maples, G. Saur, M. Hand, R. van Pietermen, and T. Obdam, “Installation, Operation, and Maintenance Strategies to Reduce the Cost of Offshore Wind Energy,” *Tech. Rep. Nrel/Tp-5000-57403*, no. July, pp. 1–106, 2013.

[14] M. Asgarpour and J. D. Sørensen, “State of the art in Operation and Maintenance planning of offshore wind farms,” in *Safety and Reliability: Methodology and Applications - Proceedings of the European Safety and Reliability Conference, ESREL 2014*, 2015.

[15] M. Canizo, E. Onieva, A. Conde, S. Charramendieta, and S. Trujillo, “Real-time predictive maintenance for wind turbines using Big Data frameworks,” *2017 IEEE Int. Conf. Progn. Heal. Manag. ICPHM 2017*, pp. 70–77, 2017.

[16] Y. Zhao, D. Li, A. Dong, D. Kang, Q. Lv, and L. Shang, “Fault prediction and diagnosis of wind turbine generators using SCADA data,” *Energies*, vol. 10, no. 8, pp. 1–17, 2017.

[17] J. Herp, M. H. Ramezani, M. Bach-Andersen, N. L. Pedersen, and E. S. Nadimi, “Bayesian state prediction of wind turbine bearing failure,” *Renew. Energy*, vol. 116, pp. 164–172, 2018.

[18] M. Asgarpour and J. Sørensen, “Bayesian Based Diagnostic Model for Condition Based Maintenance of Offshore Wind Farms,” *Energies*, vol. 11, no. 2, p. 300, 2018.

[19] Y. Hu *et al.*, “A prediction method for the real-time remaining useful life of wind turbine bearings based on the Wiener process,” *Renew. Energy*, vol. 127, pp. 452–460, 2018.

[20] Z. Tian, T. Jin, B. Wu, and F. Ding, “Condition based maintenance optimization for wind power generation systems under continuous monitoring,” *Renew. Energy*, vol.

36, no. 5, pp. 1502–1509, 2011.
[21] L. Vera-Tudela and M. Kühn, “Analysing wind turbine fatigue load prediction: The impact of wind farm flow conditions,” *Renew. Energy*, vol. 107, pp. 352–360, 2017.
[22] C. S. Gray and S. J. Watson, “Physics of failure approach to wind turbine condition based maintenance,” *Wind Energy*, 2010.
[23] T. Tinga, “Application of physical failure models to enable usage and load based maintenance,” *Reliab. Eng. Syst. Saf.*, vol. 95, no. 10, pp. 1061–1075, 2010.
[24] M. Engeler, D. Treyer, D. Zogg, K. Wegener, and A. Kunz, “Condition-based Maintenance: Model vs. Statistics a Performance Comparison,” *Procedia CIRP*, vol. 57, pp. 253–258, 2016.
[25] M. A. Djeziri, S. Benmoussa, and R. Sanchez, “Hybrid method for remaining useful life prediction in wind turbine systems,” *Renew. Energy*, vol. 116, pp. 173–187, 2018.
[26] S. S. Gokhale and K. S. Trivedi, “Analytical Modeling,” *Encycl. Distrib. Syst.*, 1998.
[27] M. Silverman and A. Kleyner, “What is design for reliability and what is not?,” *Proc. - Annu. Reliab. Maintainab. Symp.*, no. November, 2012.
[28] Z. Matić and V. Sruk, “The Physics-of-Failure approach in reliability engineering,” *Proc. Int. Conf. Inf. Technol. Interfaces, ITI*, no. May, pp. 745–750, 2008.
[29] M. Rausand and A. Høyland, *System Reliability Theory: Models, Statistical Methods, and Applications*. Wiley, 2003.
[30] T. Tinga, *Principles of loads and failure mechanisms. Applications in maintenance, reliability and design*. London: Springer, 2013.
[31] C. Kaidis, “Wind Turbine Reliability Prediction a Scada Data Processing & Reliability Estimation Tool,” no. September, pp. 1–72, 2013.
[32] R. Bi, K. Qian, C. Zhou, D. M. Hepburn, and J. Rong, “A survey of failures in wind turbine generator systems with focus on a wind farm in China,” *Int. J. Smart Grid Clean Energy*, pp. 366–373, 2014..

CHAPTER 2

Calculating Wind Turbine Component Loads for Improved Life Prediction

ABSTRACT

A wind turbine's life time is commonly predicted based on statistical methods. However, the success of statistics-based maintenance depends on the amount of variation in the system design, usage and load. Life time prediction based on physical models seeks to overcome this drawback by considering the actual design and evaluating the specific usage, load and operating condition of the considered systems. In this chapter, a load-based maintenance approach is proposed to predict the life time of a wind turbine. Physical models are used to evaluate load profiles at wind turbine blade root, rotor hub center and tower head. The effects of surface roughness, side winds, yaw misalignment, rotor tilt and blade cone angle, individual blade pitching and wind turbulences are considered and quantified. It is shown that centrifugal, gravity, Euler and Coriolis accelerations dominate the blade root loads. Tilt and cone angle, as well as individual blade pitching, affect the rotor hub and dynamic tower head loads. Further, the actual wind speed distribution is considered which is also proven to be a critical life time prediction parameter. Finally, a set of parameters is proposed that need to be monitored in a specific wind turbine to enable the practical implementation of a predictive maintenance policy.

This chapter is reproduced from: Rommel, D. P., Di Maio, D., Tinga, T. (2020). Calculating Wind Turbine Component Loads for Improved Life Prediction. *Renewable energy*, *146*, 223-241.

Nomenclature

Symbol	Unit	Quantity
A	[m^2]	area
A	-	Amplitude
a	-	axial induction factor
a	[m/s^2]	acceleration
a'	-	tangential induction factor
a,b,c,d,e	-	polynomial constants
B	-	number of blades, bearing
b	-	bending
bl	-	blade
c	[m]	chord length
C_l	-	lift coefficient
C_d	-	drag coefficient
C_n	-	C_l and C_d normal to rotor plane
C_t	-	C_l and C_d tangential to rotor plane
cog	-	center of gravity
F_l	[N]	lift force
F_d	[N]	drag force
F_n	[N]	force normal to rotor plane
F_t	[N]	force tangential to rotor plane
F_r	[N]	force radial to rotor plane
F_{bl}	[N]	force at blade root
F, f	-	Prandtl correction factor
g	[m/s^2]	gravity acceleration
H	-	hub
HB	-	hub - bearing
i,j,k	-	Factors, counters
l	[m]	length, distance
L_B	[N]	force at pitch / main bearing
$L_{eq.}$	[N]	equivalent bearing load
L_{10}	[h]	bearing life time
M_n	[Nm]	moment around normal axis
M_t	[Nm]	moment around tangential axis
M_r	[Nm]	moment around radial axis
$M_{a.f.}$	[Nm]	airfoil twist moment
M_{bl}	[Nm]	moment at blade root
m	[kg]	mass
P	[W]	power
r	[m]	(local) blade radius
R	[m]	blade tip radius
R_{cog}	[m]	Blade radius of center of gravity
u	[m/s]	circumferencial speed
v, v_w	[m/s]	speed, wind speed
V	[m^3]	volume
w	[m/s]	relative speed
α	[°]	angle of attack
β	[°]	blade twist / pitch angle
γ	[°]	rotor tilt angle
Γ	[m^2/s]	circulation
δ	[°]	blade cone angle
ε	[°]	side (shear) wind angle
λ	-	tip speed ratio
μ	-	non-dimensional radius
ρ	[kg/m^3]	air density
σ	[m]	solidity
φ	[°]	angle of relative wind
φ^*	[°]	modified angle of relative wind
χ	[°]	blade tilt angle
ψ	[°]	rotating angle of rotor
ω	[1/s]	angular speed
rtn / r't'n'	-	rotating coordinates (rotor / blade), radial, tangential, normal
xyz / x'y'z'	-	initial coordinates (rotor / main shaft)

2.1 Introduction

It is expected that installation, operation and maintenance (O&M) costs in offshore wind parks are nearly one-third of the levelized cost of energy [1]. Thus, reducing O&M costs has a significant contribution to lower levelized cost of energy. Furthermore, unplanned failures of wind turbine systems cause the majority of O&M costs of offshore wind farms [2]. Therefore, failure prediction is essential to efficiently plan maintenance activities in advance and thus, to reduce the O&M costs. Failures of wind turbine systems are commonly predicted based on failure statistics [3] which, are used for planning maintenance activities [4]. Other approaches follow data driven or model-based methods for failure prediction. Data driven methods or big data frameworks [5] directly use condition monitoring or SCADA data [6] in combination with prognostics methods like Bayesian probability theory [7][8], Wiener process [9] or artificial neural networks [10][11] to evaluate the remaining useful life (RUL). Model-based methods utilize, for example, physics of failure [12][13] to predict failures and calculate the life time of components. Note that some model-based methods are inspired by physical principles, but are statistics-based in reality. This means that a lot of approaches of life time prediction proposed in literature are statistics-based. However, statistics-based maintenance is less precise than model-based maintenance [14], especially when large variations in design, loads or operating conditions occur, as it is typical for wind turbines. As these variations cannot be adequately incorporated in statistics-based methods, this leads to large uncertainties in life predictions and conservative maintenance intervals [13]. Consequently, the accuracy of life time prediction can be increased by a model-based approach which uses purely physical equations and calculations. Djeziri et al. [15] propose a hybrid method for the prediction of the RUL in order to not apply statistics-based methods. Thereby, a wind turbine model and measurements at a real wind turbine are combined. The model simulates the system behavior under normal and faulty condition, e.g. bearing failure. The RUL is evaluated by comparing the measured and simulated, normal and faulty conditions. This means also that Djeziri et al. [15] follow the approach of condition based maintenance where maintenance decisions are based on measurements of system performance or degradation. The closer the measured condition is known to the faulty condition, the shorter is the RUL.

In this chapter a load-based maintenance approach is proposed to utilize the model-based methods based on purely physical equations. Load- and usage-based maintenance policies have already been proposed and applied by Tinga [13]. For usage-based maintenance, he proposed to translate the system usage (on the global level) to the local (internal) loads like stress, strain or temperature. But, in mechanical systems these local loads can also be retrieved from the forces and moments (global loads) acting on or inside the mechanical system. Consequently, load-based maintenance can be executed by evaluating the global loads of the mechanical system as it will be shown in the present chapter. Using load-based maintenance instead of condition based maintenance provides the advantage that the RUL can already be predicted when the system is still “healthy”, i.e. at a stage where the real system still runs at or close to (simulated) normal condition and degradation cannot be measured yet. Further, load profiles, i.e. the range of loads a specific components is subjected to, do not depend on time rather on operational and environmental conditions. If the system has, at least once, run through the range of operational and environmental conditions, then the load profile is known and the life time can be predicted from a (measured or assumed) combination of these conditions. Moreover, it is important to note that the proposed load-

based maintenance policy uses actual loads and load profiles which can differ from the loads and load profiles assumed during system design. This means that load-based maintenance has the potential to predict the system life time more accurately than as it is evaluated during the system design procedure. In addition, the evaluated actual load profile can also be used for improving new system designs by closing the design feedback loop. Scientific literature on such a load-based maintenance approach appears to be very limited, and no application in wind turbines could be found at all. Thus, the objectives of this chapter are i) to propose the general concept of load calculations that can feed into a load-based maintenance approach and ii) specifically develop a method for wind turbine components.

Before applying the approach of load-based maintenance, the physical models used for global load evaluations must be specified. Firstly, it is important to note that global loads, i.e. forces and moments, are dependent on the design (specific geometries), operation and environment of the considered system. Hence, the physical model used for global load calculations must, on the one hand, be based on a design model and, on the other hand, consider the actual (measured) operational and environmental conditions. This means that the algorithms behind the physical design model must be able to handle measurements, ideally in real time operation. A design model is a numerical model that is used for a range of calculations during the design process, like calculation of loads, life time or performance. The results govern design choices on materials and dimensions. Secondly, load-based maintenance requires a detailed analysis of loads and system behavior to select the most dominant influences of design, operation and environment on the system load profiles. The dominant effects must, at least, be incorporated in the life time prediction. Summing up, the physical model used for the global load calculation must describe the system design, operate in real time and be able to easily analyze the system behavior. After Gokhale and Trivedi [16] an analytical model fits best to these requirements.

The approach of (global) load-based maintenance is applied in this chapter to a three bladed, horizontal axis wind turbine. Thereby, the global load evaluation focuses on the wind turbine rotor because rotor loads have a significant influence on the life time of the entire wind turbine, namely on the life time of blades, pitch-, yaw- and main power train as well as the tower. The rotor and blades are described by an analytical design model. On the one hand, the design model provides, based on simple blade design data, a virtual copy of the real wind turbine rotor. On the other hand, the design model is used, after some model modifications, to evaluate load profiles based on measured operational and environmental data. This means that for every specific wind turbine the load profiles of the wind turbine rotor can be calculated individually and hence, also the life time.

The main scientific contribution of this work is the proposal of a novel load-based maintenance approach for wind turbine components, quantifying the loading of a component (and associated expected service life) from a combination of a component-specific physical model (the design model) and the actual (measured) operational and environmental conditions. The additional practical contribution is the implementation of the approach for a wind turbine rotor, demonstrating the dominant factors (and their magnitude) affecting the blade, hub and tower loads (and life time).

The outline of the chapter is as follows: in section 2.2 the physical model for quantifying the rotor loads is derived. First a basic rotor model is developed, also including a basic blade design procedure (as commonly not all blade details are available). Then the effects of a range of variations are included in the model and the calculation procedure is discussed. Section 2.3 then applies the model to the case of a 3 bladed wind turbine rotor, demonstrating and discussing the qualitative results of variations in operational conditions. Section 2.4 focuses

on the verification of the model results and contains a critical discussion. Finally, section 2.5 summarizes the main conclusions of the work.

2.2 Wind Turbine Rotor Load Calculation

This section presents the analytical models which are needed for the rotor load calculations under real time conditions. In total two models are required. One model is used for the design of the virtual wind turbine rotor, i.e. the geometry of the wind turbine rotor. This is necessary as the detailed geometry of the rotor is in most cases not available. A second model evaluates the wind turbine rotor loads during operation based on the geometry of the virtual wind turbine rotor and measurements. The second model builds on the first model and is additionally enriched with effects, which influence the rotor behavior and loads during operation. The effects that are considered in the present chapter are: wind profile over height (surface roughness), yaw misalignment and side winds, tilt and cone angle as well as tower displacement, individual blade pitching and, wind turbulences. Some equations implemented in the second model can lose their mathematical validity at specific operating conditions. These calculation limits are discussed at the end of this section.

2.2.1 Analytical Blade Model of Virtual Rotor

A model of a three bladed wind turbine rotor can easily be created by triplicating the model of one turbine blade. The Blade Element Momentum (BEM) theory provides a set of equations to analytically describe the transfer of fluid flow properties (wind) into the motion and loading of a wind turbine blade. In the BEM theory the turbine blade is divided into sections. Then, a set of analytical equations is defined for every blade section. A complete derivation of the BEM theory is beyond the scope of this chapter. Therefore, only those equations are mentioned here which are needed for the calculation procedures. Detailed descriptions of the BEM theory are given by [17], [18] and [19]. Nevertheless, two crucial points of the BEM theory shall be highlighted here.

First, the BEM theory adopts two main assumptions for every blade section: a) energy contained in the wind speed can only partially be converted to mechanical rotating energy of the turbine rotor and b) the angular rotor speed increases due to wake, i.e. due to the momentum caused by the wind on the blade surface while changing wind direction in the turbine rotor. Effect a) is expressed by an axial induction factor a and effect b) by a tangential induction factor a' [17]. Figure 2.1 shows the speed triangle including axial and tangential induction factors as well as aerodynamic forces at an airfoil (blade section). The actual wind speed v_w is scaled by the axial induction factor a and the rotor circumferential speed u by the tangential induction factor a'. Together these determine the relative wind speed w_{rel} that the airfoil is exposed to (also defined by angle φ). As a result, the lift force F_l and drag force F_d are generated, which can be decomposed into a normal (F_n) and tangential (F_t) force that cause blade bending and rotor rotation. The induction factors will be defined in detail below.

Second, in an extended version of the BEM theory air flow losses at the blade tip and root can be included by the Prandtl correction factor F respectively f_{root} and f_{tip} [19]. The losses are caused by a radial airflow due to the pressure difference between suction and pressure side of the blade [19]. In order to minimize these losses, the circulation Γ around the airfoil at the blade ends is set to zero during the blade design process which is also done by the

Prandtl correction factors as shown later. Finally, after [17], [18] and [19] the set of equations for a simple blade design are given as:

Axial induction factor:

if $a \leq a_c$ $$a = \frac{1}{\frac{4F\sin^2(\phi)}{\sigma C_n}+1} \quad (2.1a)$$

if $a > a_c$

$$a = \frac{1}{2}\left(2 + K(1-a_c)\right) - \frac{1}{2}\sqrt{(K(1-2a_c)+2)^2 + 4(Ka_c^2 - 1)} \quad (2.1b)$$

with $$K = \frac{4F\sin^2(\phi)}{\sigma C_n}$$

Note that the simple BEM theory (Eq. 2.1a) is only valid for small values of a, and breaks down at $a_c = 0.2$ [17], [18]. Therefore, the axial induction factor a must be calculated after Eq. 2.1b if $a > a_c$.

Tangential induction factor:

$$a' = \frac{1}{\frac{4F\sin(\phi)\cos(\phi)}{\sigma C_t}-1} \quad (2.2)$$

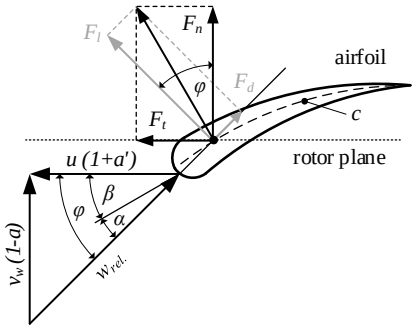

Figure 2.1 Wind speed triangle and aerodynamic forces at airfoil.

In the expressions for the two induction factors the following parameters are used:

– the angle of relative wind w.r.t rotor plane φ (cp. Figure 2.1):

$$\tan(\phi) = \frac{(1-a)}{(1+a')}\frac{1}{\mu\lambda} \quad (2.3)$$

– the tip speed ratio λ which is the ratio of the circumferential rotor speed at the blade tip and the wind speed:

$$\lambda = \frac{u_{tip}}{v_w} = \frac{\omega R}{v_w} \quad (2.4)$$

– the non-dimensional blade radius which is defined by the local blade radius r of the different blade sections and the maximum blade radius *R*, i.e. $\mu \in [0;1]$:

$$\mu = \frac{r}{R} \tag{2.5}$$

– the solidity which is the ratio of the local blade (airfoil) area and local rotor area. The airfoil area is given by the airfoil chord length *c*, the difference of local blade radii Δr and the number of blades *B*:

$$\sigma = \frac{c\Delta rB}{2\pi r\Delta r} = \frac{cB}{2\pi r} \tag{2.6}$$

– the projected lift and drag coefficient normal (C_n) and tangential (C_t) to rotor plane with C_l and C_d the airfoil lift and drag coefficients (cp. also the projection of lift (F_l) and drag (F_d) force to a tangential (F_t) and normal (F_n) force in Figure 2.1):

$$C_n = C_l \cos(\phi) + C_d \sin(\phi) \tag{2.7a}$$
$$C_t = C_l \sin(\phi) - C_d \cos(\phi) \tag{2.7b}$$

– the Prandtl correction factor: $F = f_{root} f_{tip}$ (2.8)

– the Prandtl correction factor components at blade root and tip:

$$f_{root} = \frac{2}{\pi}\cos^{-1}\left(\exp\left(-\frac{B}{2\sin(\phi)}\frac{(\mu-\mu_{root})}{\mu}\right)\right) \tag{2.8a}$$
$$f_{tip} = \frac{2}{\pi}\cos^{-1}\left(\exp\left(-\frac{B}{2\sin(\phi)}\frac{(1-\mu)}{\mu}\right)\right) \tag{2.8b}$$

The BEM theory is normally applied to calculate the optimal chord *c* for new blade designs. However, for a virtual wind turbine rotor, i.e. a copy of an existing wind turbine rotor, the chord is already defined. So two assumptions are made here: first, the maximum chord of the blade (along its span) is known from a blade data sheet and second, the circulation around the blade is constant along the blade radius ($\Gamma = const.$) except at blade tip and root where the circulation must be zero. Further, the consideration of the lift force provides a useful relation to describe the chord length *c* depending on the blade circulation, lift coefficient and relative wind speed. The lift force per blade length unit is specified by [17] as $F_l = \frac{\rho}{2} w_{rel.}^2 c C_l = \rho w_{rel.} \Gamma$ and thus, the chord length can be derived as $c = \frac{2\Gamma}{C_l w_{rel.}}$.

Based on the BEM theory an expression for a uniform circulation Γ along the blade radius including Prandtl correction factors is given by [19] as $\Gamma = \frac{4\pi}{\lambda}\frac{a}{(1-a)}F(1-Fa)^2$. From this equation, it can be seen that the circulation is only uniform along the blade radius, if the axial induction factor a is uniform, too. So it can be concluded that in this case (under the assumptions as defined before) the axial induction factor will be constant over the blade radius and the circulation at the blade root and tip only depends on the Prandtl correction factors. Furthermore, based on Figure 2.1 the relative wind speed is defined as

$$w_{rel.} = \frac{v_w(1-a)}{\sin(\phi)} \ . \tag{2.9}$$

So the chord length variation along the blade for a blade with uniform circulation (and constant axial induction factor) is given as a function of the non-dimensional radius by:

$$c(\mu) \sim \frac{F(\mu)[1-F(\mu)a]^2}{C_l(\mu)} \sin[\varphi(\mu)] \tag{2.10a}$$

Normally, variables like wind speed, induction factor etc. at the blade design point of the considered wind turbine are not available. Thus, the magnitude of the chord length at the different blade sections cannot be evaluated. However, the value of the maximum chord length $c_{max.ref.}$ is often given in the blade data sheet. Then, the blade chord lengths can be calculated by scaling Eq. 2.10a with the ratio of the given chord length maxima. Hence, the chord length c along the blade radius can be described for the virtual rotor as follows:

$$c(\mu) = \frac{c_{max.ref.}}{[max(c(\mu))]_{Eq.2.10a}} \frac{F(\mu)[1-F(\mu)a]^2}{C_l(\mu)} \sin[\varphi(\mu)] \tag{2.10b}$$

The chord length calculated after Eq. 2.10b can be used in Eq. 2.6. Then, Eq. 2.1 to 2.8 can be solved for given lift and drag coefficients, i.e. for given airfoils resulting in the actual values of the induction factors a and a', and the resulting relative wind speed w_{rel}. Furthermore, for given lift and drag coefficients as well as chord lengths the normal and tangential blade forces can be calculated (cp. also Figure 2.1) and thus, also the blade thrust force, blade bending moments and rotor power [18].

Normal and tangential blade force (per unit blade length):

$$F_n^m = \frac{\rho}{2} w_{rel.}^2 c C_n \tag{2.11}$$

$$F_t^m = \frac{\rho}{2} w_{rel.}^2 c C_t \tag{2.12}$$

Blade thrust force:

$$F_n = R \int_{\mu_{root}}^{1} F_n^m \, d\mu \tag{2.13}$$

Blade bending moments around normal and tangential axis:

$$M_t = R^2 \int_{\mu_{root}}^{1} F_n^m \, \mu d\mu \tag{2.14}$$

$$M_n = R^2 \int_{\mu_{root}}^{1} F_t^m \, \mu d\mu \tag{2.15}$$

Rotor power:

$$P_{rotor} = \sum_{i=1}^{B} (M_n)_i \, \omega \tag{2.16}$$

Note that Eq. 2.11 to 2.16 are used for both evaluating the blade design of the wind turbine rotor and for calculating the wind turbine rotor loads during operation. The blade design as well as load calculation procedures are explained in the following subsections.

2.2.2 Blade Design Procedure of Virtual Rotor

The set of analytical equations is now used to design the blades of the virtual wind turbine rotor based on a real turbine blade. In order to do so, the blade EUROS 100 is chosen [20] in the present chapter. Table 2.1 shows an extract from the data sheet of the blade EUROS 100.

Furthermore, after EUROS [20] the design of the blade EUROS 100 is based on the airfoils types DU and NACA 64. Therefore, in the present chapter it is assumed for the blade design that the airfoil DU 97-W-300LM is used at the blade root region, DU 93-W-210LM around the blade center and NACA 64-618 at the blade tip region (cp. also Table 2.2). Then, the optimal angle of attack of these airfoils is calculated based on given lift and drag coefficients [21]. The optimal angle of attack is used for the blade design and is defined by the maximum value of the glide ratio (lift/drag ratio). Table 2.2 shows the values of angle of attack, lift and drag coefficient at chosen non-dimensional radii used for the blade design of the virtual wind turbine rotor. Based on Table 2.2 lift and drag coefficients as well as angle of attacks for all other non-dimensional blade radii $\mu \in [0.05, 1.0]$ are interpolated by fifth order polynomials.

$$C_l(\mu) = a_l\mu^4 + b_l\mu^3 + c_l\mu^2 + d_l\mu + e_l \tag{2.17}$$
$$C_d(\mu) = a_d\mu^4 + b_d\mu^3 + c_d\mu^2 + d_d\mu + e_d \tag{2.18}$$
$$\alpha(\mu) = a_\alpha\mu^4 + b_\alpha\mu^3 + c_\alpha\mu^2 + d_\alpha\mu + e_\alpha \tag{2.19}$$

The polynomial constants of Eq. 2.17 to 2.19 evaluated for the blade design after Table 2.2 are shown in Table 2.3. For the load calculation, it shall be noted here that polynomial constants of Eq. 2.17 to 2.19 must be re-evaluated as soon as lift, drag coefficient or angle of attack changes during operation. Figure 2.2 shows the distribution of angle of attack, lift and drag value along the non-dimensional blade radius based on Table 2.2 and 2.3 as well as Eq. 2.17 to 2.19. The lift and drag coefficient evaluation as a function of the non-dimensional radius is necessary to proceed the calculation as proposed in section 2.2.1. Then, the virtual wind turbine rotor is described by the set of equations of section 2.2.1 and the values of Table 2.1 to 2.3.

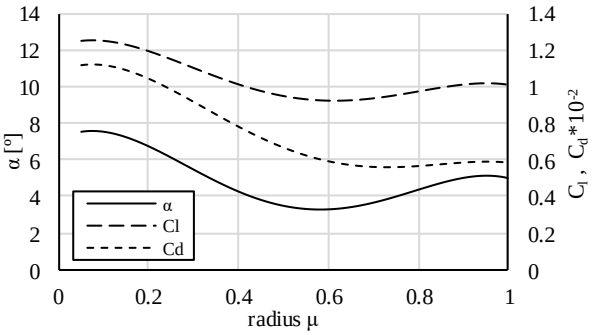

Figure 2.2 Angle of attack, lift and drag coefficients along blade radius as estimated for the selected blade EUROS 100.

Table 2.1 Euros 100 – Blade Data

Quantity	Unit	Value
Rotor diameter (approx.)	[m]	100
Rated power	[kW]	3000
Nominal wind speed	[m/s]	12.3
Mass	[kg]	12200
Design tip speed ratio	-	8.2
Max. chord length	[m]	4.15

Table 2.2 Blade Design Values

Airfoil Type	Lift coefficient	Drag coefficient	Angle of attack [°]	Radius μ
DU 97-W-300LM	1.254	0.01116	7.5	0.05
DU 97-W-300LM	1.254	0.01116	7.5	0.1
DU 93-W-210LM	0.948	0.00664	3.5	0.5
NACA 64-618	1.001	0.00581	5	0.9
NACA 64-618	1.001	0.00581	5	1.0

Table 2.3 Polynomial Constants for a Blade after Table 2

Polynomial Constant	Lift coefficient	Drag coefficient	Angle of attack
a	-5.250	-0.0540	-77.68
b	11.495	0.1268	166.8
c	-7.373	-0.0890	-104.0
d	0.915	0.0112	12.83
e	1.225	0.0108	7.098

As the induction factors and the angle of relative wind are independent (cp. Eq. 2.1a, 2.1b, 2.2 and 2.3), an iterative calculation procedure is needed. The design evaluation procedure of the virtual wind turbine rotor is visualized in Figure 2.3. One can see that forces, moments and power are calculated at the end of the calculation procedure. The forces, moments and power evaluated at the blade design point can be used to compare the virtual and real wind turbine rotor. Here it is important to remember that the usage of the BEM theory is an approximation of the real blade design. So it can occur that the calculated power at the design point deviates from the real power. Then, a correction factor may be necessary to adjust the forces, moments and power calculation of the virtual wind turbine rotor. The correction factor can be calculated by comparing the power of the real and virtual wind turbine rotor (cp. also Eq. 2.16). As the correction factor is a calculation constant, it can also be added to Eq. 2.11 to 2.15. If a correction factor is used, it is crucial to apply it also while calculating the wind turbine loads during operation (cp. section 2.2.4).

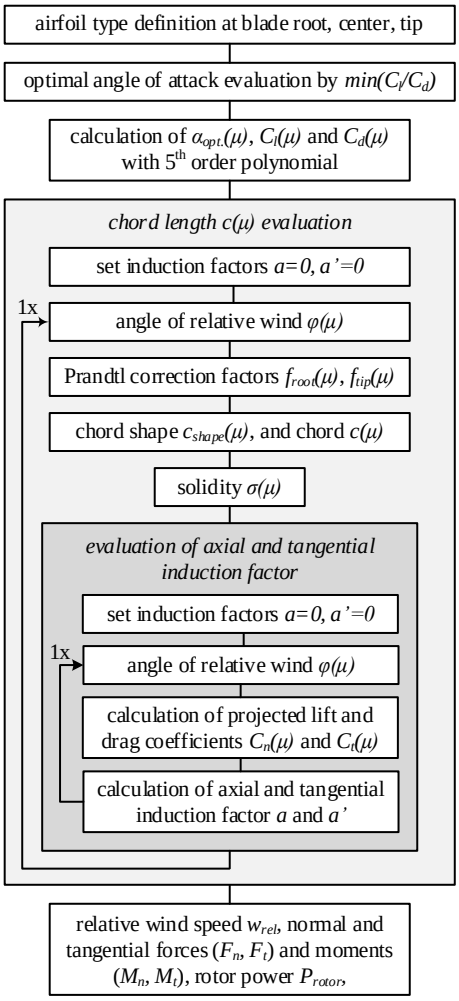

Figure 2.3 Blade design calculation procedure at design point

2.2.3 Effects on Wind Turbine Rotor Behavior

In the previous subsections the design procedure of the virtual wind turbine rotor was presented. The virtual rotor was designed based on ideal operation conditions. For example, it was assumed that the wind speed is constant over height and that the blades are not pitched during operation. However, these assumptions are not true while operating the wind turbine. Therefore, in this subsection different effects are presented which influence the behavior of the wind turbine rotor and thus, the rotor loads during operation. In the present chapter the effects are limited to wind profile over height, yaw misalignment and side winds, tilt and cone angle as well as tower displacement, individual blade pitching and, wind turbulences. However, other effects, like shear winds, can easily be added to the method. The effects are

described analytically in this section. Moreover, their influence on the rotor loads are evaluated separately by a sensitivity analysis in the next section.

The first effect to be considered is the variation of wind speed with height. The wind speed cannot be considered as constant over height because the surface roughness of the landscape around wind turbines, i.e. buildings and trees reduce the wind speed. As the latter is an input parameter for the load calculation (cp. Eq. 2.9 and 2.11 to 2.15), it must be evaluated as a function of the surface roughness and height. A logarithmic description of the wind profile as a function of the height H, surface roughness z_o and reference wind speed at a reference height is provided by [22].

$$v_w(H) = v_{w,ref} \ln\left(\frac{H}{z_o}\right) / \ln\left(\frac{H_{ref}}{z_o}\right) \tag{2.20}$$

If both the surface roughness of the area surrounding the considered wind turbine and, for example, the wind speed at the rotor hub height are known, then the wind speed distribution over height can be evaluated and taken into account by the virtual wind turbine rotor. In case a second reference wind speed is available at a second reference height (e.g. at half tower height), the surface roughness need not to be taken from a Table like [22] offers, rather, can be calculated from the second reference wind speed. Figure 2.4 shows in a simplified manner how the change of the wind speed modifies the direction of the relative wind speed and thus, the magnitude of the relative wind speed and the angle of attack. Consequently, the aerodynamic forces (cp. Figure 2.1) vary over height, too. Hence, the wind turbine rotor faces different conditions during one rotor rotation, as it is influenced by the wind speed variation over height.

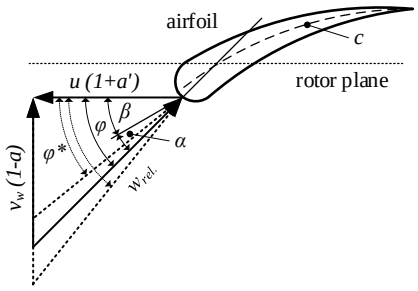

Figure 2.4 Changing the wind speed in the wind speed triangle

The second effect to be included is yaw misalignment and the associated side winds. Yaw misalignment will occur, if the wind turbine rotor is not exactly aligned to the main direction of wind whereby a side wind hits the wind turbine rotor. Figure 2.5 shows, again in a simplified way, the effect of yaw misalignment or side winds. It can be seen that a yaw misalignment is equivalent to side winds in terms of their effect on the wind turbine rotor behavior. From Figure 2.5, it is also visible that yaw misalignment and side winds again change the magnitude of the relative wind speed and angle of attack and thus, also the aerodynamic forces.

Furthermore, it is assumed in the present chapter that side winds occur purely in horizontal wind direction and that any flow in radial blade direction does not influence the aerodynamic forces and blade behavior. This means that the effects of side winds and yaw misalignment

are neglected at horizontal blade positions. Consequently, the changes of the wind speed triangle and aerodynamic forces due to side winds reach their maximum respectively minimum at upper and lower vertical blade position (see also Figure 2.6). In addition, based on the yaw misalignment or side wind angle ε (caused by a side wind of magnitude $v_{w,t}$) the modified angle φ^* of relative speed can be described over a rotor rotation (angle ψ) as follows:

$$\tan(\phi^*) = 1/\left[\frac{(1+a')}{(1-a)}\mu R\frac{\omega_{rotor}}{v_{w,n}} + \tan(\varepsilon)\sin(\psi)\right] \qquad (2.21)$$

with $\tan(\varepsilon) = \frac{v_{w,t}}{v_{w,n}(1-a)}$

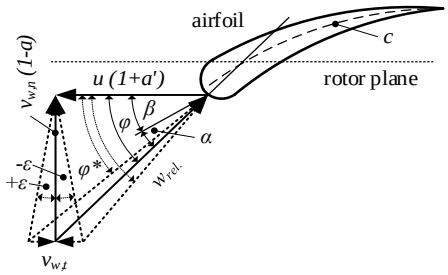

Figure 2.5 Effect of side winds and yaw misalignment

Note that the side wind angle depends on both side wind direction and rotating direction of wind turbine rotor (clock- or counterclockwise). Therefore, the sign of the side wind angle and thus also the angle of relative speed can change between upper and lower vertical blade position (cp. Figure 2.6).

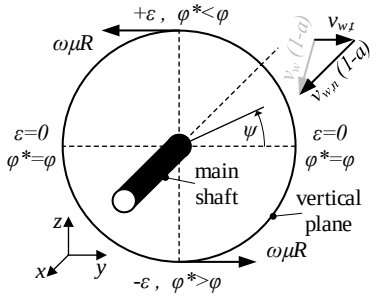

Figure 2.6 Modified relative wind angle due to side wind

Even though shear winds are not considered in the present chapter during the calculation of rotor loads, some considerations will be mentioned at this point. In principle the shear winds can be described in the same way as side winds after Figure 2.5 and Eq. 2.21. In case of shear winds a wind speed component in purely vertical direction (shear wind) must be taken into account instead of a wind speed component in purely horizontal direction (side

winds). This means that the angle ε is a shear wind angle instead of a side wind angle and that the effect of shear winds are neglected at vertical blade positions. Then, the changes of the wind speed triangle and aerodynamic forces due to side winds reach their maximum respectively minimum at horizontal blade position. So vertical shear winds have a similar effect as side winds (cp. Figure 2.6), but with a 90 degree shift of the angle ψ.

The third effect to be incorporated in the model is a variation in rotor tilt (γ) angle and blade cone (δ) angle. The modification of the angle of relative wind speed in Eq. 2.21 includes only the effect of side winds and yaw misalignment. However, wind flow deviations do not only occur because of side winds, but also because of tilt and cone angle as well as tower displacement (cp. Figure 2.7).

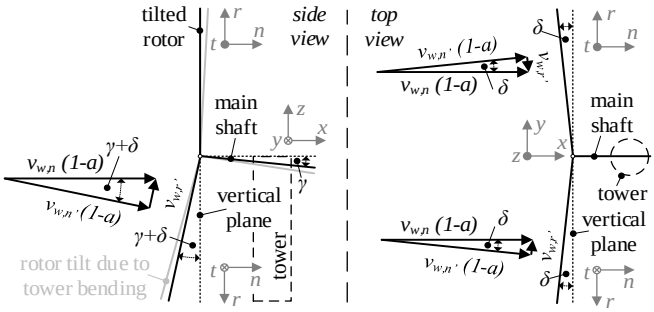

Figure 2.7 Rotor side and top view due to tilt (γ) and cone (δ) angle as well as tower displacement for $\gamma = \delta$

Note that the tilt and cone angle are chosen during wind turbine design to guarantee enough clearance between tower and rotating blades [22]. As shown in Figure 2.7 the turbine blades do not rotate anymore in the vertical plane because of the tilt and cone angle as well as tower displacement caused by tower bending. Consequently, it cannot be assumed anymore that the wind flow streams perpendicular to the rotating blade, which is a basic assumption in BEM. Instead, it is assumed that air also flows along the blade in radial direction due to the tilt angle and tower displacement. Then, the air flow and thus the wind speed can be decomposed in a modified normal $v_{w,n'}$ and radial $v_{w,r'}$ wind speed (cp. Figure 2.7). The Cartesian coordinates now refer to the blade axis instead of the vertical plane, i.e. *rtn*-coordinates change to *r't'n'*-coordinates by rotating around the *t*-axis (cp. Figure 2.8) with the angle χ (see Eq. 2.23). Using the modified, normal wind speed (*r't'n'*-coordinates) for the calculation of the aerodynamic forces means that both lift and drag forces as well as blade resulting forces are rotated by the tilt angle.

Figure 2.8 shows the wind speed triangle due to a combination of side wind, tilt and cone angle as well as the resulting aerodynamic forces. It can be seen that the reacting forces at the blades are not any longer just in the vertical plane or perpendicular to it, but an additional force is generated in the radial direction of the rotor plane (cp. Figure 2.8 – aerodynamic forces). By comparing Figure 2.1 and 2.8 one can see that the tilt and cone angle as well as tower displacement must also be considered in Eq. 2.7a, 2.7b and Eq. 2.14, 2.15. Furthermore, it is visible in Figure 2.7 that the blade – vertical plane angle and tower displacement changes over one rotor rotation. The projected lift and drag coefficients normal, tangential and radial to the rotor plane are then defined as follows:

$$C_n = [C_l \cos(\phi) + C_d \sin(\phi)] \cos(\chi) \quad (2.22a)$$
$$C_t = [C_l \sin(\phi) - C_d \cos(\phi)] \cos(\chi) \quad (2.22b)$$
$$C_r = [C_l + C_d] \sin(\chi) \quad (2.22c)$$

with the blade vertical plane angle

$$\chi = \delta - (\gamma_{tilt} + \gamma_{tower}) \sin(\psi) \quad (2.23)$$

Note that the rotating angle ψ is zero ($\psi = 0$) at the horizontal blade position and $\pi/2$ ($\psi = \pi/2$) at the top position.

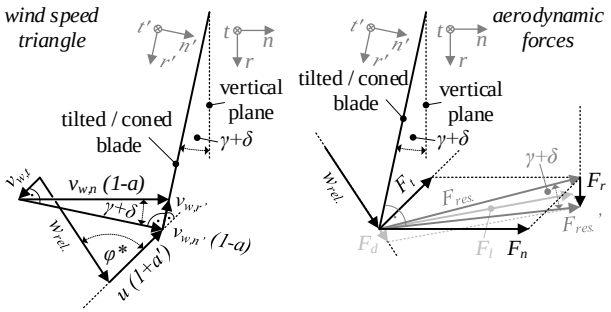

Figure 2.8 Wind speed triangle and aerodynamic forces due to tilt angle at lower blade position

Moreover, due to the radial blade force (cp. Figure 2.8 – aerodynamic forces) and the tilted respectively coned blade, an additional radial blade force and blade bending moment are generated which complement Eq. 2.11 to 2.15. On the basis of Eq. 2.22a-c, blade bending moments are specified around the tangential direction of the rotor plane as:

Radial blade force (per unit blade length):

$$F_r^m = \frac{\rho}{2} w_{rel.}^2 c C_r \quad (2.24)$$

Total blade radial force:

$$F_r = R \int_{\mu_{root}}^{1} F_r^m \, d\mu \quad (2.25)$$

Blade bending moments around tangential axis:

$$M_{t,1} = R^2 \cos(\chi) \int_{\mu_{root}}^{1} F_n^m \, \mu d\mu \quad (2.26)$$
$$M_{t,2} = R^2 \sin(\chi) \int_{\mu_{root}}^{1} F_r^m \, \mu d\mu \quad (2.27)$$

In addition, it is important to note that the tilt angle and tower displacement do not only affect the wind inflow at the leading edge of the airfoils or blade, but also the wind inflow angle, i.e. angle of attack, at horizontal blade positions (cp. Figure 2.9). In other words, tilt angle and tower displacement cause blade pitching in horizontal blade position. This means

that the blades are positively and negatively pitched during one rotor rotation. Consequently, the angle of attack changes and thus, the aerodynamic force, too, because the angle of attack directly influences lift and drag values of the airfoils. Note also that the blade cone angle does not influence the angle of attack over one rotor rotation. Figure 2.9 shows, furthermore, that the change of angle of attack at a tilted rotor is equal to the tilt angle or tower displacement. Hence, the fluctuating angle of attack due to tilt angle and tower displacement can be described over one rotor rotation by:

$$\Delta\alpha_{tilt} = [\gamma_{tilt} + \gamma_{tower}]\cos(\psi) \tag{2.28}$$

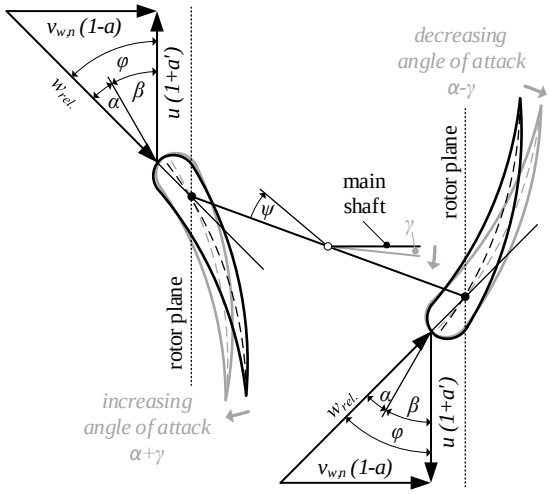

Figure 2.9 Changing angle of attack due to tilt angle

Tilt and cone angle as well as tower displacement finally also influence the blade mass forces because the blades do not rotate exactly in the vertical plane. This means that blade mass forces also occur in the direction normal to the vertical plan. If the blade is not pitched during operation, i.e. the blade does not move, then the acceleration of the blade mass due to regular rotation is specified by [23] as: $\vec{a} = -\vec{\omega} \times (\vec{\omega} \times \vec{r})$. The blade accelerations are then calculated by considering the angular main shaft speed ω_0 and circular path of the blade center of gravity (*cog*) over one rotation.

$$\vec{\omega} = \omega_0 \begin{pmatrix} \cos(\gamma) \\ 0 \\ -\sin(\gamma) \end{pmatrix}_{xyz} \tag{2.29}$$

$$\vec{r}(t) = R_{cog} \begin{pmatrix} -\sin(\chi) \\ \cos(\chi)\cos(\omega t) \\ \cos(\chi)\sin(\omega t) \end{pmatrix}_{xyz} \tag{2.30}$$

Whereas all previous equations have been defined in the (individual) blade coordinate system *rtn*, the description of the complete rotor now requires to shift to a more global rotor

coordinate system. Thus, both angular main shaft speed and circular path are expressed here in *xyz*- coordinates. The *xyz*-coordinates are inertial (Cartesian) coordinates whose origin is placed in the vertical plane and at the hub center (see Figure 2.10). For evaluating the position vector in Eq. 2.30, the radius of the blade center of gravity is required. After Grote and Antonsson [23] the center of gravity is calculated by $R_{cog} = \int_0^R r\rho dV / \int_0^R \rho dV$. To simplify the calculation of the center of gravity, it is assumed here that the blade mass is homogeneously distributed and that the blade surface is proportional to the blade volume. Hence, the center of gravity can be approximated as:

$$R_{cog} = \frac{\int_0^R r dA}{\int_0^R dA} = R\frac{\sum_i(\mu_i \Delta\mu_i c_i)}{\sum_i(\Delta\mu_i c_i)} \tag{2.31}$$

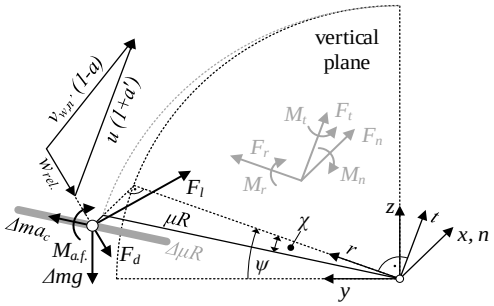

Figure 2.10 Overview of loads acting on a of blade element

Then, based on Eq. 2.29 and 2.30 the acceleration of the blade mass due to rotation around the main shaft axis is defined as:

$$\vec{a}_{c,xyz}(t) = R_{cog}\omega_0^2 \begin{pmatrix} \sin^2(\gamma)\sin(\chi) - \frac{1}{2}\sin(2\gamma)\cos(\chi)\sin(\omega t) \\ \cos(\chi)\left[\sin^2(\gamma)\sin(\omega t) + \cos^2(\gamma)\cos(\omega t)\right] \\ \cos^2(\gamma)\cos(\chi)\sin(\omega t) - \frac{1}{2}\sin(2\gamma)\sin(\chi) \end{pmatrix}_{xyz} \tag{2.32}$$

In the same way the gravitational acceleration can also be described in *xyz* coordinates.

$$\vec{g} = \begin{pmatrix} 0 \\ 0 \\ -g_0 \end{pmatrix}_{xyz} \tag{2.33}$$

Thus, the total blade mass force, which acts on the blade in addition to aerodynamic forces and moments, is given in *xyz*-coordinates as: $\vec{F}_{m,bl} = m_{bl}[\vec{a}_c(t) + \vec{g}]_{xyz}$.

The fourth effect to be included is the blade pitching effect. As already mentioned, the tilt angle pitches the blades in horizontal blade position (cp. Eq. 2.28). Blade pitching, however, is also done actively by individual blade pitch control units. This means that every blade of the wind turbine rotor can operate with an individual angle of attack. Consequently, the aerodynamic forces differ from blade to blade which makes that the aerodynamic rotor

unbalance increases. The change in angle of attack α is directly linked to the individual pitch control (pitch angle β) and does not depend on the rotor position:

$$\Delta\alpha(\psi) = \Delta\beta(\psi) \tag{2.34}$$

The fifth and final effect to be included is wind turbulence, which also affects the aerodynamic blade forces and thus, the wind turbine rotor behavior. Wind turbulences are wind speed fluctuations. Therefore, a simplified description, which is usable for the BEM theory, is the variation of wind speed v_w along the blade radius and over one rotor rotation. So wind turbulences are similarly specified as the change of wind speed over height (cp. also Figure 2.4). By introducing a wind speed correction factor, a simplified analytical description is provided for wind turbulences.

$$\begin{aligned} v_{w,turb}(\mu,\psi) &= k_{turb}(\mu,\psi) * v_w \\ k_{turb}(\mu,\psi) &= 1 + A\sin(2i\pi\mu)\sin(j\psi) \end{aligned} \tag{2.35}$$

Thereby, the amplitude *A* defines the magnitude of the wind speed fluctuation, *i* the number of wind speed fluctuations along the blade radius and *j* the number of wind speed fluctuations over one rotor rotation. Note that Eq. 2.35 is a very simplified way to describe wind turbulences. Consequently, any calculation results based on Eq. 2.35 must be interpreted carefully. However, this expression does enable to check the sensitivity of blade loads on turbulence level, as it will be shown in section 2.3.

2.2.4 Calculation Procedure for Blade Forces and Moments during Operation

In the previous two subsections the design procedure of the virtual wind turbine rotor and blades as well as the different effects on the wind turbine rotor behavior were introduced. The design of the virtual blade was described for one specific operating point (blade design point) under ideal conditions excluding any effects during operation. However, for evaluating the wind turbine rotor loads during operation it is necessary to follow a calculation procedure which considers the different effects (as discussed in section 2.2.3). This means that the calculation procedure of Figure 2.3 must be modified. It is important to note that due to these effects the angle of attack and relative speed change continuously over one rotor rotation. This means that the axial and tangential induction factor must be re-calculated for every blade position and operating condition. Figure 2.11 shows the modified calculation procedure which is used for determining the loads of the wind turbine rotor. As now the aerodynamic blade loads are calculated, the torsional blade moment generated by the airflow around the airfoil [24] is included in Figure 2.11. Note that this blade pitching moment was not considered in the design of the virtual blade and wind turbine rotor (cp. Figure 2.3). For the aerodynamic load calculation, it is assumed in the present chapter that the blade is rigid i.e. the blade does not deform due to torsional and bending moments. This assumption is not true in reality; however, it provides the advantage that the change of angle of attack and relative wind due to blade deformations can be neglected during the load calculation of the blade and wind turbine rotor.

Further, one can see by comparing Figure 2.3 and 2.11 that the purpose of the calculation procedure in Figure 2.3 is the evaluation of the chord shape (blade geometry) and axial and tangential induction factors at the blade design point. In contrary, the purpose of the

calculation procedure in Figure 2.11 is the calculation of the angle of attack during operation including the different effects described in the previous subsection. Based on the angle of attack, which is continuously calculated, the lift, drag and torque coefficients are evaluated and thus, also the resulting forces and moments during operation. By following the calculation procedure in Figure 2.11 the normal, tangential and radial forces and moments are calculated along the blades i.e. for the different blade sections (elements) needed to apply the BEM theory. To illustrate this, Figure 2.10 schematically shows the centrifugal, gravity and aerodynamic forces as well as the pitching moment acting on a blade element with a length $\Delta\mu R$ at a radius μR. The blade element forces and moments are described and calculated in the rotating rtn-coordinates. The rtn coordinates have the same origin as the xyz coordinates; however, the rtn coordinates rotate over the angle $\psi = \omega t$ (cp. also Figure 2.10). Hence, the blade root forces and moments (in rtn-coordinates) are the sum of all forces and moments of the different elements. The blade root force and moment written as time dependent vectors are specified as follows:

$$\vec{F}_{bl}(t) = m_{bl}\left[\vec{a}_c - g_0\begin{pmatrix}\sin(\omega t)\\ \cos(\omega t)\\ 0\end{pmatrix}\right]_{rtn} + \begin{pmatrix}\sum_i\left(F_r(\mu_i)\right)\\ \sum_i\left(F_t(\mu_i)\right)\\ \sum_i\left(F_n(\mu_i)\right)\end{pmatrix}_{rtn} \tag{2.36}$$

$$\begin{aligned}\vec{M}_{bl} = {} & R_{cog}\begin{pmatrix}\cos(\chi)\\ 0\\ -\sin(\chi)\end{pmatrix}_{rtn} \times m_{bl}\left[\vec{a}_c - g_0\begin{pmatrix}\sin(\omega t)\\ \cos(\omega t)\\ 0\end{pmatrix}\right]_{rtn} + \\ & + R_{bl}\begin{pmatrix}\cos(\chi)\\ 0\\ -\sin(\chi)\end{pmatrix}_{rtn} \times \begin{pmatrix}\sum_i\left(\mu F_r(\mu_i)\right)\\ \sum_i\left(\mu F_t(\mu_i)\right)\\ \sum_i\left(\mu F_n(\mu_i)\right)\end{pmatrix}_{rtn} - \\ & - \sum_i\left(M_{a.f.}(\mu_i)\right)_{rtn}\begin{pmatrix}\cos(\chi)\\ 0\\ -\sin(\chi)\end{pmatrix}_{rtn}\end{aligned} \tag{2.37}$$

with $F_r(\mu) = F_{aero}(\mu)\cdot C_r(\mu), F_t(\mu) = F_{aero}(\mu)\cdot C_t(\mu), \quad F_n(\mu) = F_{aero}(\mu)\cdot C_n(\mu)$, $F_{aero}(\mu) = \frac{\rho}{2}\cdot w_{rel.}^2(\mu)\cdot c(\mu)$, $M_{a.f.}(\mu) = F_{aero}(\mu)\cdot c(\mu)\cdot C_m(\mu)$ and

$$a_{c,rtn}(t) = \begin{pmatrix}0 & 0 & 1\\ \cos(\omega t) & -\sin(\omega t) & 0\\ \sin(\omega t) & \cos(\omega t) & 0\end{pmatrix}^{-1} a_{c,xyz}(t)$$

The blade root force and moment (loads) are calculated for every blade and rotor rotating angle ψ (or time instance t). Then, the blade root loads are transformed from the rotating *rtn*-coordinates to initial *xyz*-coordinates. The resulting loads of all (three) blades, i.e. the sum of blade root loads of all blades, constitute the loads of the wind turbine rotor hub. Note that to simplify the calculation algorithms the mass forces of the entire blade are reduced in the present chapter to a point force i.e. only aerodynamic forces are considered here as distributed forces.

In summary, based on the calculation procedure shown in Figure 2.11 and based on Eq. 2.36 and 2.37, forces and moments (loads) of the virtual blades respectively virtual wind

turbine rotor can be quantified for different operating conditions, as it will be demonstrated in the section 2.3.

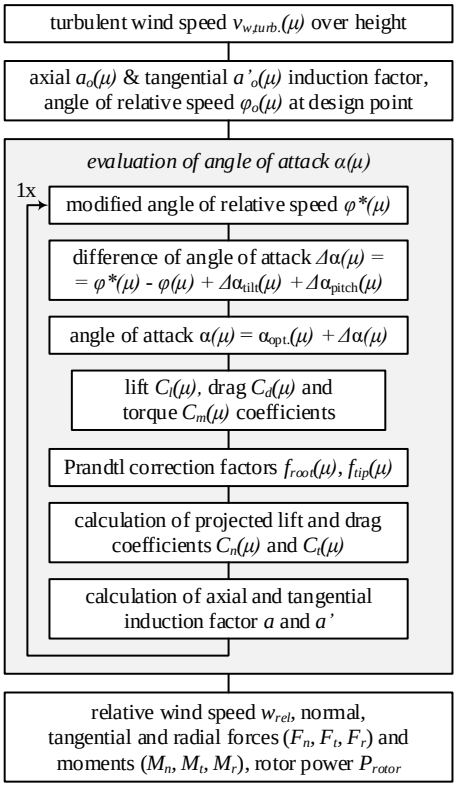

Figure 2.11 Calculation procedure of aerodynamic blade loads

2.2.5 Limitations of the Analytical Rotor Model

After introducing the calculation procedure for blade and wind turbine rotor loads, some limitations of this calculation procedures will be mentioned in this subsection. First, the BEM theory is an approximation of the real blade design implying that the load calculation results may deviate from the real loads. A correction factor was introduced to overcome this problem. Second, the effects demonstrated in section 2.2.3 are based on assumptions and simplifications while describing the wind speed triangle and its angles during different operating conditions. The accuracy of the calculation results may be reduced by these assumptions and simplifications. Third, the angle of relative speed (cp. Eq. 2.21), axial and tangential induction factor, angle of attack as well as lift and drag coefficients are not independent (cp. Figure 2.11). If the change of angle of attack is so high that values of the projected lift and drag coefficient (cp. Eq. 2.22a-c) change their sign, then the normal calculation of the induction factors (cp. Eq. 2.1a, 2.1b and Eq. 2.2) and relative angle of wind (cp. Eq. 2.21) will fail. On the other hand, it can be argued that a wind turbine should not run under conditions where the projected lift and drag values change their sign because this

means that either the lift coefficient is negative or the drag coefficient is very high. A negative lift coefficient turns the direction of the lift force by 180 degrees and a high drag coefficient is equivalent to a huge blade thrust force. So it can be assumed that the set of equations used for the calculation procedure shown in Figure 2.11 do not fail during regular operation. Nevertheless, it is important to monitor the values of the induction factors during the analyses in order to detect load calculation failures.

2.3 Load Calculations

In this section the load calculation as described by Figure 2.11, Eq. 2.36 and 2.37 is applied to a three bladed upwind wind turbine rotor which is designed based on the values of Table 2.1 to 2.3 (cp. also section 2.2.2). The virtual model of this wind turbine rotor is used for performing load sensitivity analyses in order to evaluate the influence of wind profile over height, yaw misalignment and side winds, tilt and cone angle, tower displacement, individual blade pitching and wind turbulences (cp. section 2.2.3). The loads are analyzed at three locations: at the blade root, the hub center of the wind turbine rotor as well as the tower head. All calculations are executed with an average wind speed of *8.5 m/s* at a hub height of *94* meters. An agricultural terrain is assumed with very few buildings and trees, i.e. the surface roughness z_0 is set equal to *0.03* meters (cp. also [22]). Furthermore, different scenarios are considered for the sensitivity analyses in order to demonstrate the different effects on the wind rotor behavior. Table 2.4 and 2.5 show the parameter settings of the different scenarios which take into account wind speed over height (*h*), negative and positive yaw misalignment (*y*), negative and positive pitching (*p*) of one blade and turbulences (*turb.*). The parameters of the turbulence (Eq. 2.35) are set to: $i = 33$, $j = 720$, $A=0.01$ (scenario *turb. 2%*) respectively $A = 0.025$ (*turb. 5%*). Moreover, the rotor tilt (*t*) and blade cone angles are set equally, i.e. $\gamma = \delta$. This means that the blades are in the vertical plane at the upper position (cp. Figure 2.7 and 2.10). In addition, the load sensitivity analyses are performed using equivalent loads which are calculated from the evaluated forces, moments and dimensions like radii or shaft lengths. These equivalent loads neglect the masses of the hub, main shaft, gearbox and direct drive generator because mass gravity forces act only in vertical (or radial) direction, while the dominant power train loads act in axial and circumferential direction. Further, the gravity forces only act as a load offset, i.e. they do not influence the load fluctuations and dynamic loads. The drawback of neglecting the mass gravity forces of the different drive train components is that the calculated equivalent loads may be lower than the real loads. The advantage, however, is that the results presented in this section are generic, and thus valid for any wind turbine independent of its drive train concept.

Table 2.4 Different scenarios for load calculations with a tilt and cone angle of 0°

Scenario	Surface roughness	Yaw angle ε	Pitch angle β	Tilt / cone angle γ / δ	Turbu-lences
h-t0°	0.03	0°	0°	0°	no
y -0.1°	0.03	-0.1°	0°	0°	no
y +0.1°	0.03	+0.1°	0°	0°	no
p -0.1°	0.03	0°	-0.1°	0°	no
p +0.1°	0.03	0°	+0.1°	0°	no
turb. 2%	0.03	0°	0°	0°	±1%

Table 2.5 Different scenarios for load calculations with a tilt and cone angle of 6°

Scenario	Surface roughness	Yaw angle ε	Pitch angle β	Tilt / cone angle γ / δ	Turbu-lences
h-t6°	0.03	0°	0°	6°	no
y -3°	0.03	-3°	0°	6°	no
y +3°	0.03	+3°	0°	6°	no
p -1.5°	0.03	0°	-1.5°	6°	no
p +1.5°	0.03	0°	+1.5°	6°	no
turb. 5%	0.03	0°	0°	6°	±2.5%

2.3.1 Loads at Blade Root

The forces and moments acting at the blade root must not only be carried by the blade itself but also by the pitch bearing. Therefore, the load sensitivity analysis at the blade root is performed by evaluating equivalent pitch bearing loads. Figure 2.12 schematically shows the assembly of a turbine blade, pitch bearing and rotor hub. Then, the equivalent pitch bearing load can be specified based on Figure 2.12 in the rotating coordinate frame *r't'n'*. Note that the *r'*-axis is aligned with the blade longitudinal axis and that the *r't'n'*-coordinates are obtained by rotating the *rtn*-coordinates by the blade rotor plane angle χ around the t-axis (cp. also Figure 2.10).

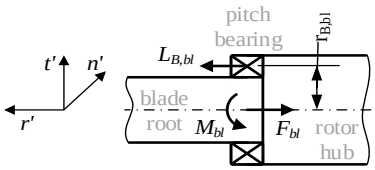

Figure 2.12 Loads of blade root at the pitch bearing

$$\vec{L}_{B,bl} = \vec{F}_{bl} + \frac{\vec{M}_{bl}}{|\vec{r}_{B,bl}|^2} \times \vec{r}_{B,bl} = \begin{pmatrix} F_{bl,r'} \\ F_{bl,t'} \\ F_{bl,n'} \end{pmatrix} + \begin{pmatrix} M_{bl,r'} \\ M_{bl,t'} \\ M_{bl,n'} \end{pmatrix} \times \begin{pmatrix} 0 \\ 1/r_{B,bl} \\ 1/r_{B,bl} \end{pmatrix} \tag{2.38}$$

The equivalent pitch bearing load as defined in Eq. 2.38 is evaluated for the different scenarios shown in Table 2.4 and 2.5. To compare the different parameter settings, the absolute values of the equivalent blade root loads are calculated with blade root / bearing radius $r_{B,bl} = 1.15m$. Figure 2.13 and 2.14 show the results for the different scenarios. It is noteworthy that pitch angle deviation of one blade, yaw misalignment or fluctuations of the lift and drag forces (turbulences) have only a minor influence on the equivalent blade root loads. An effect that cannot be neglected is caused by a variation of tilt and cone angle. One can see by comparing Figure 2.13 and 2.14 that the magnitude of the dynamic load, i.e. the load fluctuation over one rotor rotation is increased by increasing simultaneously both the tilt and cone angle. However, the most dominant load variation observed in these Figures is governed by the rotation angle. Equation 2.36 and 2.37 show that the mass forces are responsible for this variation.

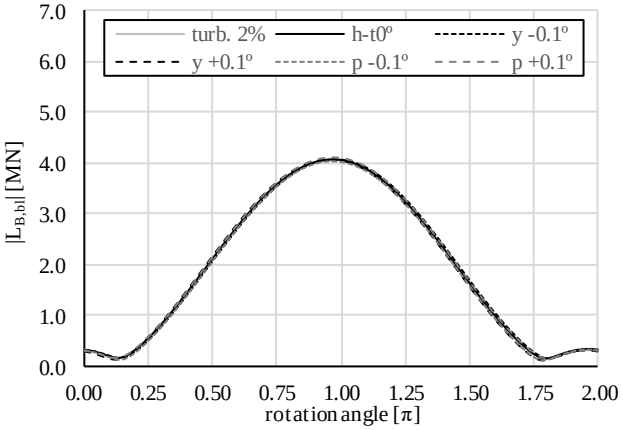

Figure 2.13 Absolute value of pitch bearing load for the scenarios in Table 2.4

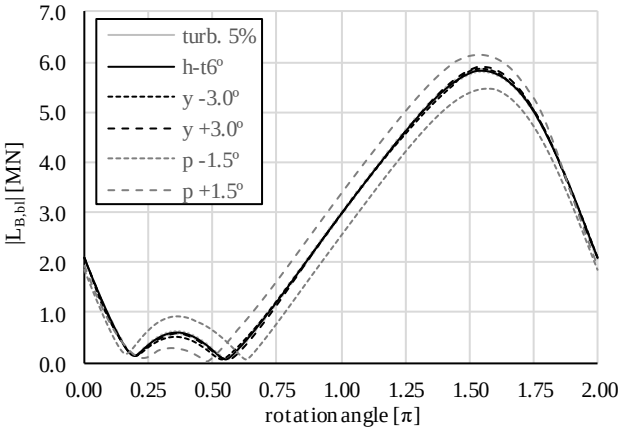

Figure 2.14 Absolute value of pitch bearing load for the scenarios in Table 2.5

The different accelerations acting on the blade mass need to be considered in more details. Until now, a rigid blade was assumed which was also not pitched during operation. But blade flapping and pitching cause additional accelerations of the blade mass because the blade rotates. Consequently, Euler and Coriolis forces also act on the blade mass. After [23] the Euler acceleration is defined as $\vec{a}_{Euler} = \vec{\omega} \times \vec{r}_{cog}$ and the Coriolis acceleration as $\vec{a}_{Coriolis} = 2\vec{\omega} \times \vec{v}_{cog}$ where $\vec{r}_{cog}$ and $\vec{v}_{cog}$ are the radial position and velocity of the blade center of gravity respectively. For evaluating the influence of Euler and Coriolis acceleration on the blade root loads, the magnitude of the Euler, Coriolis, centrifugal acceleration and gravity are compared. To do so, the blade pitch and cone angles including the effect of blade pitching and flapping are described as follows:

$$\Delta\beta(t) = \beta_0 + \Delta\alpha_h \sin(\omega t) \tag{2.39}$$

$$\delta(t) = \delta_0 + \Delta\delta \sin(k\omega t) \tag{2.40}$$

Equation 2.39 assumes that pitching is used for the change of angle of attack needed to compensate the effect of wind speed over height. Other effects that cause a change of the angle of attack over one rotor rotation are not considered here because Eq. 2.39 and 2.40 are only used to demonstrate the influence of Euler and Coriolis acceleration. In reality, Eq. 2.39 is dictated by the pitch control system and Eq. 2.40 could be derived from measurements of blade flapping. The factor k indicates the number of blade flaps per rotor rotation. The angle δ_0 is defined by the blade coning and the angle difference $\Delta\delta$ is the cone angle fluctuation due to blade flapping. Based on Eq. 2.39 and 2.40 the radius and velocity of the blade mass center as well as angular velocity and acceleration are specified in *rtn*-coordinates for a tilt angle $\gamma = 0$ as.

$$\vec{r}(t) = R_{cog}\begin{pmatrix}\cos(\delta(t))\\ -\sin(\delta(t))\sin\big(\beta+\Delta\beta_p(t)\big)\\ -\sin(\delta(t))\cos\big(\beta+\Delta\beta_p(t)\big)\end{pmatrix}_{rtn} \tag{2.41}$$

$$\vec{v}_{cog}(t) = -\omega_0 R_{cog}\begin{pmatrix}k\Delta\delta\sin\big(\delta(t)\big)\cos(k\omega_0 t)\\ k\Delta\delta\cos\big(\delta(t)\big)\cos(k\omega_0 t)\sin\big(\beta+\Delta\beta_p(t)\big)\\ k\Delta\delta\cos\big(\delta(t)\big)\cos(k\omega_0 t)\cos\big(\beta+\Delta\beta_p(t)\big)\end{pmatrix}_{rtn} + \\ + \omega_0 R_{cog}\begin{pmatrix}0\\ -\Delta\alpha_h\sin(\delta(t))\cos\big(\beta+\Delta\beta_p(t)\big)\cos(\omega_0 t)\\ \Delta\alpha_h\sin(\delta(t))\sin\big(\beta+\Delta\beta_p(t)\big)\cos(\omega_0 t)\end{pmatrix}_{rtn} \tag{2.42}$$

$$\vec{\omega}(t) = \omega_0\begin{pmatrix}\Delta\alpha_h\cos(\omega_0 t)\\ 0\\ 1\end{pmatrix}_{rtn} \tag{2.43}$$

$$\dot{\vec{\omega}}(t) = \omega_0^2\begin{pmatrix}-\Delta\alpha_h\sin(\omega_0 t)\\ 0\\ 0\end{pmatrix}_{rtn} \tag{2.44}$$

The centrifugal, Euler and Coriolis accelerations acting at the blade mass center (cp. Figure 2.15) are calculated based on Eq. 2.41 to 2.44. Furthermore, for detecting the influence of Euler and Coriolis acceleration on the blade root loads the following calculation parameters are assumed: blade cone angle $\delta_0 = 10^o$, cone angle fluctuation $\Delta\delta = 2^o$, number of blade flaps (wind gusts) per rotor rotation $k = 12$, blade pitch angle $\beta_0 = 0$ and correction of angle of attack by blade pitching $\Delta\alpha_h = 6^o$ (cp. also Eq. 2.34). The angular velocity of the main shaft is considered here as constant. In reality an unsteady angular shaft velocity would additionally cause Euler and Coriolis accelerations. In Figure 2.16 the absolute values of Euler, Coriolis, centrifugal and gravity accelerations are plotted over one rotor rotation.

It can be seen that the ratio between gravity and Euler acceleration and between centrifugal and Coriolis acceleration is approximately ten. Therefore, both Euler and Coriolis acceleration and their associated forces cannot be neglected because, for example, the ball bearing life time is proportional to bearing loads by the power three [25]. A load increase due to Euler and Coriolis acceleration by approx. 10% leads thus to a bearing life time reduction

of approx. 25%. In addition, one can see in Figure 2.16 that the Coriolis acceleration caused by blade flapping can fluctuate with a much higher frequency than the main shaft rotation frequency. This means that the Coriolis acceleration causes high-cycle loads and thus, contributes to the high-cycle fatigue of the blade and pitch bearing. For extending the life time of blade and pitch bearing the magnitude of Euler and Coriolis accelerations should be reduced to a minimum during operation. The minimization of Euler and Coriolis accelerations can only be achieved by smoothing unsteady behavior of angular shaft speed and blade pitching. However, blade flapping always occurs and even though the angular acceleration is assumed equal to zero, Coriolis acceleration still has a significant influence on the blade root load profiles and thus, the life time of the blade and pitch bearing.

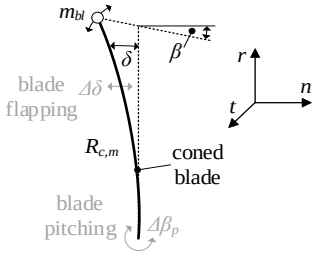

Figure. 2.15 Pitching and flapping of coned blade

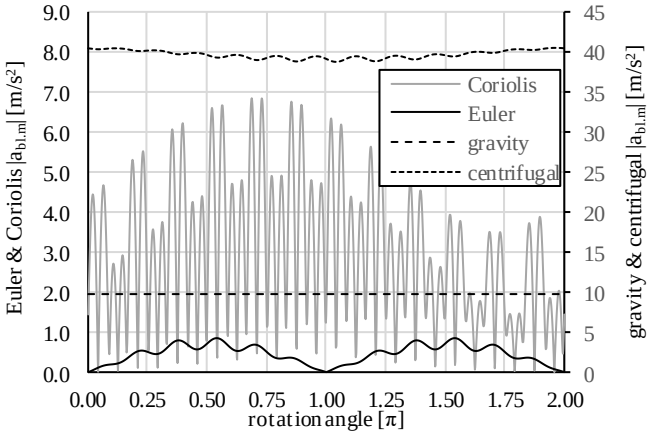

Figure 2.16 Absolute value of blade mass accelerations

2.3.2 Loads at Rotor Hub

In the previous subsection loads at the blade root were evaluated. Now, loads at the rotor hub center are analyzed and are derived from the blade root loads because hub center loads are equal to the sum of all blade root loads. This means that some blade root loads negate each other and some are additive. Furthermore, the resultant hub center loads must be absorbed by main bearings (cp. Figure 2.17).

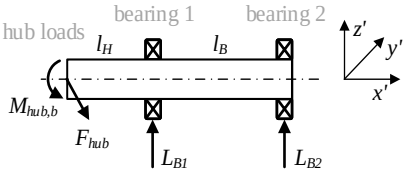

Figure 2.17 Loads of rotor hub and main bearings

So analogous to the blade and pitch bearing loads, the main bearing loads are equivalent to the hub center loads. As the mass gravity forces of the different components connected to the main shaft are neglected in the present chapter, the main bearing loads can be used as an equivalent hub center load for the load sensitivity analysis. Without considering the mass gravity forces, the loads on the two bearings (L_{B1} and L_{B2}) are described in *x'y'z'*-coordinates as follows:

$$\vec{L}_{B1} = \vec{l}_{HB}\vec{F}_{hub} + \frac{1}{l_B}\vec{M}_{hub,b} = \begin{pmatrix} 1 \\ 1+\frac{l_H}{l_B} \\ 1+\frac{l_H}{l_B} \end{pmatrix}^T \begin{pmatrix} F_{hub,x'} \\ F_{hub,y'} \\ F_{hub,z'} \end{pmatrix} + \frac{1}{l_B}\begin{pmatrix} 0 \\ M_{hub,y'} \\ M_{hub,z'} \end{pmatrix} \tag{2.45}$$

$$\vec{L}_{B2} = -\left[\vec{l}_H\vec{F}_{hub} + \frac{1}{l_B}\vec{M}_{hub,b}\right] = -\begin{pmatrix} 0 \\ \frac{l_H}{l_B} \\ \frac{l_H}{l_B} \end{pmatrix}^T \begin{pmatrix} 0 \\ F_{hub,y'} \\ F_{hub,z'} \end{pmatrix} + \frac{1}{l_B}\begin{pmatrix} 0 \\ M_{hub,y'} \\ M_{hub,z'} \end{pmatrix} \tag{2.46}$$

The *x'y'z'*-coordinates are obtained by rotating the *xyz*-coordinates over the tilt angle γ around the *y*-axis. In addition, it is assumed here that the bearing *B1* absorbs both axial and radial forces and, bearing *B2* only radial forces.

To compare again the different scenarios of Table 2.4 and 2.5, the equivalent load of the main bearing B1 is evaluated using Eq. 2.45 with shaft distances $l_B = 1.0m$ and $l_H = 0.75m$. Figure 2.18 and 2.19 show the absolute values of the equivalent loads on B1 for the different scenarios. First, one can see that the change of both tilt and cone angle from 0º to 6º (Figure 2.18 versus 2.19) increases the bearing loads (L_{B1}) by a factor of almost ten. Note that at the hub center the blade bending moments due to gravity are balanced out at a purely tilted rotor and are summed up at a purely coned rotor. This means that the bearing load increase is mainly caused by the cone angle. It is also important to remember that the tilt and cone angles are chosen while designing the wind turbine. Second, depending on the side wind direction (or yaw misalignment) a negative or positive offset is observed in the bearing loads. So side winds or yaw misalignment can either decreases or increases the average loads (and life time) of the main bearings. Third, individual blade pitching increases the dynamic part (fluctuating load amplitude) of the main bearing loads independent of negative or positive pitch angle. Consequently, the bearing peak loads also increase due to individual pitching (cp. Figure 2.19 *p-1.5º / p+1.5º* vs. *h-t6º*). Fourth, it is visible that the frequency of the main bearing loads (L_{B1}) variation, i.e. three cycles over a 2π rotation angle, equals the product of the main shaft frequency and number of blades. The origin of this relation is the wind speed difference over height causing the aerodynamic blade loads to vary over one rotor rotation (cp. also [26]). However, in Figure 2.18 and 2.19 it can also be observed that due to blade pitching the

bearing load frequency shifts from the third to the first rotor harmonic depending on the magnitude of the pitch angle variation. The shift from the third to the first harmonic is provoked by pitch angle deviation (or individual blade pitching). If one blade is pitched individually, its angle of attack and associated aerodynamic forces differ from the other two blades. Consequently, the aerodynamic imbalance (peak load) increases and becomes dominant over the initial (3rd harmonic) load variation due to wind speed fluctuation. Fifth, load fluctuations due to wind turbulences are also visible in the bearing loads (cp. Figure 2.18 and 2.19) and they increase both the peak-to-peak loads and the frequency. Therefore, wind turbulences negatively influence the life time of the main bearings.

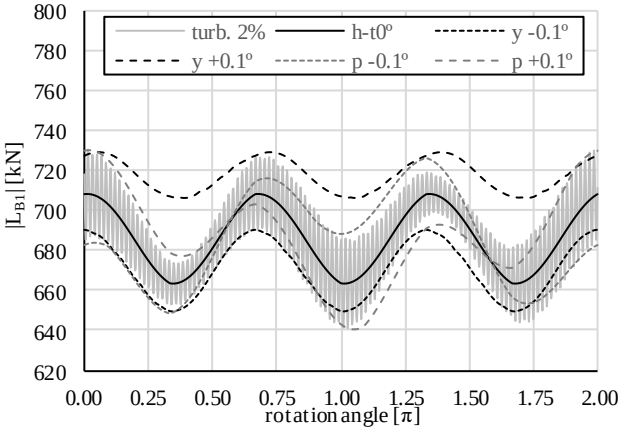

Figure 2.18 Absolute value of main bearing load (B1) for the scenarios in Table 2.4

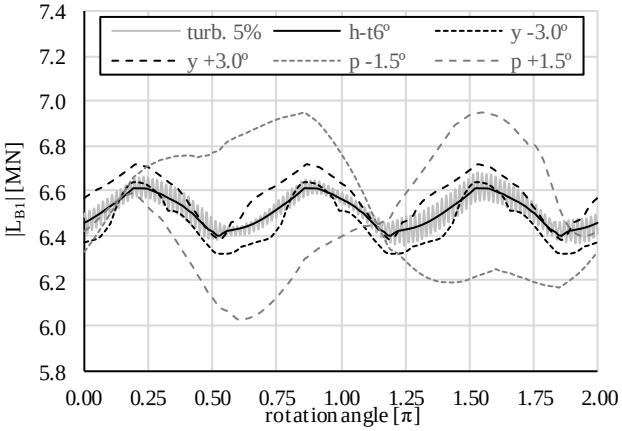

Figure 2.19 Absolute value of main bearing load (B1) for the scenarios in Table 2.5

In order to quantify the influence of yaw misalignment, pitch angle deviation and turbulences on the bearing loads (and life time), ball bearing loads are evaluated over one rotor rotation. Equivalent loads are calculated for constant shaft speeds using [27]:

$$L_{B1,eq.} = \sqrt[3]{\sum_i \left(q_i \cdot L_{B1,i}^3\right)} \tag{2.47}$$

Equation 2.47 expresses that the combination of i different loads, each with a relative occurrence q_i (in time or revolutions), leads to an equivalent load $L_{B1,eq.}$. The equivalent bearing load is calculated for one rotor rotation using $i = 720$ and for each of the six plotted curves shown in Figure 2.19 (and presented in Table 2.6). For comparing them, curve *h-t6°* is used as reference because the curve *h-t6°* only includes the effect of tilt and cone angle and wind speed over height. The relative bearing life time L_{10} is also shown, assuming that it is proportional to $1/L_{eq.}^3$ [25]. Moreover, centrifugal and aerodynamic forces, as well as aerodynamic moments, are proportional to the square of the wind speed (Eq. 2.11 to 2.15 and Eq. 2.32 and 2.36). So the life time is proportional to the 6th power of the wind speed.

$$L_{10} \sim \left(1/L_{eq.}\right)^3 \sim (1/v_w^2)^3 \sim 1/v_w^6$$

Table 2.6 demonstrates that the equivalent bearing loads are affected by both negative and positive yaw misalignment and pitch angle deviations. This means that the bearing life time is extended or reduced depending on negative or positive yaw misalignment and pitch angle deviation. Table 2.6 shows additionally that load fluctuations due to wind turbulences reduce the bearing life time, too, but the magnitude of the effect is much smaller.

Table 2.6 Equivalent load and main bearing life time for $v_{wind} = 8m/s$

Parameter setting	Equivalent load $L_{eq.}$	Bearing life time $(1/L_{eq.})^3$	Δ life time [%]
h-t6°	1.000	1.000	0.00
y -3.0°	1.027	0.924	-7.56
y +3.0°	0.984	1.050	5.01
p -1.5°	1.016	0.953	-4.73
p +1.5°	0.992	1.026	2.58
turb. 5%	1.001	0.997	-0.31

From a first point of view it seems that yaw misalignment, pitch angle deviation and wind turbulences may have minor influences on the main bearing loads (approx. 1-3%). However, it is important to note that these effects can occur simultaneously. Moreover, this demonstration calculation neglected (actively controlled) blade pitching and flapping. Further, the calculations were performed at a wind speed of 8.5 m/s, with a wind speed fluctuation of ±2.5% and a constant angular shaft speed. However, as was shown before the bearing life time is proportional to the power six of the wind speed (for wind speeds < rated wind speed). Therefore, the negative and positive life time differences calculated in Table 2.6 change with increasing wind speed. Table 2.7, with the results for a wind speed of 12 m/s, confirms that the wind speed distribution over time has a dominant effect on the main bearing life time but now also with a magnitude that cannot be neglected.

Table 2.7 Equivalent load and main bearing life time for v_{wind} = 12m/s

Parameter setting	$L_{eq.}$ at v_{wind} = 8.5 m/s	$L_{eq.}$ at v_{wind} = 12.0 m/s	$(1/L_{eq.})^3$ at v_{wind} = 12m/s	Δ life time [%]
h-t6°	1.000	1.000	1.000	0.00
y -3.0°	1.027	1.082	0.790	-21.02
y +3.0°	0.983	0.952	1.158	15.81
p -1.5°	1.013	1.050	0.865	-13.52
p +1.5°	0.989	0.975	1.079	7.93
turb. 5%	1.001	1.003	0.0991	-0.94

Summarizing the load calculation at the rotor hub center or rather at the main bearings it can be stated that the yaw misalignment (side winds), individual blade pitching (pitch angle deviation) and wind speed during operation (wind speed distribution) are the most dominant influences in the load profile and life time calculation of main bearings.

2.3.3 Tower Head Loads due to Rotor Hub Loads

After discussing the blade root (pitch bearing) and hub (main bearing) loads in the previous two subsections, finally the tower head loads are considered. These are equivalent to the yaw system loads since the main bearings are fixed on the steel base frame (nacelle) which is installed on the top of the tower. The loads of the steel base frame are transmitted via the yaw system to the tower head. Therefore, the rotor hub loads are also handled by the yaw system and tower (cp. Figure 2.20). The top of the tower has to absorb both wind rotor loads and gravity forces caused by masses of nacelle and drive train components like gearbox, generator and others. In this section the tower head loads due to the rotor hub loads are calculated. The mass gravity forces of nacelle and different drive train components are again neglected. Based on Figure 2.20, the tower head force and moment are defined as follows:

$$\vec{F}_{tower} = \vec{F}_{hub} = \begin{pmatrix} F_{hub,x} \\ F_{hub,y} \\ F_{hub,z} \end{pmatrix} \tag{2.48}$$

$$\vec{M}_{tower} = \vec{l}_{rotor} \times \vec{F}_{hub} + \vec{M}_{hub} = \begin{pmatrix} l_{rotor} \\ 0 \\ 0 \end{pmatrix} \times \begin{pmatrix} F_{hub,x} \\ F_{hub,y} \\ F_{hub,z} \end{pmatrix} + \begin{pmatrix} i_G \cdot M_{hub,x} \\ M_{hub,y} \\ M_{hub,z} \end{pmatrix} \tag{2.49}$$

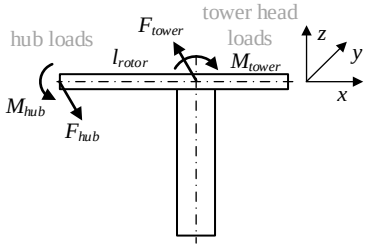

Figure 2.20 Tower head loads due to rotor hub loads

Note that the moment around the x-axis is the torque generated in the rotor shaft and the moment around the z-axis is the torque generated in the tower structure (to be counterbalanced by the yaw system). The torque ratio i_G is determined by the design of the gearbox and generator. For a drive train with a gearbox the ratio i_G depends on the number of planetary gear steps, the ratio of each planetary gear step as well as the total gearbox ratio. In the case of a direct drive train the ratio i_G is equal to one which means that the full torque generated in the rotor main shaft has to be balanced by the tower.

In order to compare the different scenarios of Table 2.4 and 2.5, the tower head moment from Eq. 2.49 is evaluated. Figure 2.21 and 2.22 show the absolute values of tower head moments calculated with the rotor to tower center distance $l_{rotor} = 1.25m$ (cp. Figure 2.20). As the neglected gravity forces of rotor hub, main shaft, gearbox, generator and other tower head components are equivalent to a load offset, the tower head moment from Eq. 2.49 can be considered as the dynamic (fluctuating) part of the tower head loads. First, one can see from Figure 2.21 and 2.22 that the change of both tilt and cone angle from 0º to 6º increases the tower head moment by a factor of approximately five. Consequently, the tilt and cone angle selection during the wind turbine design also has a significant influence on the tower head moment and thus, on the tower bending or tower torsion during operation. Second, depending on the side wind direction and yaw misalignment a negative or positive offset is caused on the tower head moment. Third, individual blade pitching, i.e. a pitch angle deviation of one blade increases the amplitude of the fluctuating tower head loads. Consequently, the dynamic peak loads of the tower head also increase due to individual pitching. Fourth, a frequency shift of the tower head loads from the third to the first rotor harmonic is observed (cp. Figure 2.22: *h-t6º* versus *p +1.5º*) because of the reasons which were already explained in section 2.3.2. The frequency of the dynamic tower head loads can again be obtained from the product of the main shaft frequency and number of blades. Tower measurements [28] showed that the tower head is, in fact, excited by the third harmonic (three bladed rotor). Fifth, it is also clear from Figure 2.21 and 2.22 that load fluctuations due to wind turbulences are visible in the dynamic loads of the tower head and, again, lead to increasing peak values as well as load frequency.

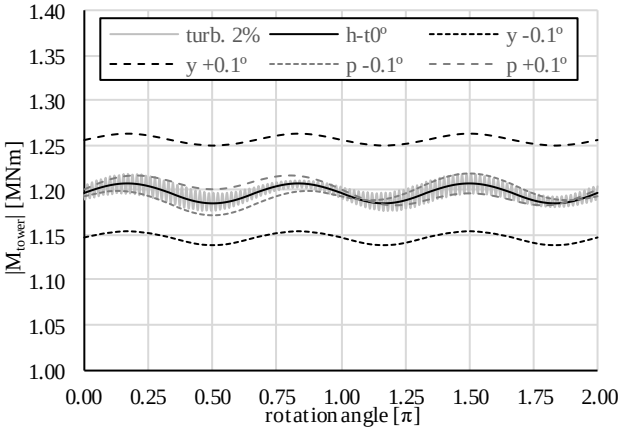

Figure 2.21 Absolute value of tower head moment for the scenario in Table 2.4

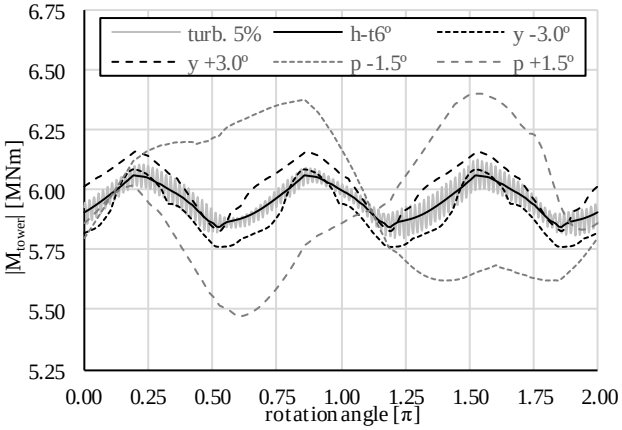

Figure 2.22 Absolute value of tower head moment for the scenario in Table 2.5

In summary, the yaw misalignment (side winds) causes an offset of the tower head loads. Pitch angle deviation increases the dynamic loads of the tower and, in addition, shifts the load frequency to lower wind turbine rotor harmonics. For the tower behavior the increase of dynamic loads and a frequency shift of the tower head loads are more critical than a load offset. Therefore, the surface roughness (wind speed over height) and individual blade pitching (pitch angle deviation) are more critical for the tower than yaw misalignment or side winds.

2.4 Verification and Discussion

Now, after the proposed method for calculating wind turbine components has been introduced and demonstrated, some issues remain for discussion. The most important issue is the verification of the load calculations, so that will be addressed first. To do so, the equivalent bearing load calculation results of section 2.3.2 are compared with measurements. However, loads (forces and moments) at the rotor hub and main bearings cannot directly be measured. An alternative way to evaluate the wind turbine rotor and main bearing loads is to consider the main shaft response to loads. The response to loads acting at one shaft end can be quantified by measuring the shaft displacement at the other shaft end assuming that the system is acting as a rigid body, not flexible. This assumption is justified because any rotating system should always run far from its resonance frequencies in order to protect it from its self-destruction. So based on the rigid body assumption, the response of the rotor hub loads can be measured as displacement at the gearbox or direct drive generator rotor. If, in addition, the main shaft loads (rotor hub loads) and load response are only compared from a qualitative point of view, then the exact shaft geometries will be unimportant for the verification of the load calculation. This means that only normalized shaft displacements are compared. Without the requirement of detailed shaft geometries and bearing positions, existing displacement measurements can be used for the verification procedure. Gearbox displacements were already measured by [29] at a three bladed rotor with a known pitch angle deviation of 1.2° at one blade. In order to compare these measured gearbox displacements with the equivalent bearing load calculated with Eq. 2.45, the load calculations are executed with the parameter

setting shown in Table 2.8. The calculation results are plotted in Figure 2.23 and 2.24. Figure 2.24 also includes the gearbox displacement measurements done by [29] at a GE 1.5XLE wind turbine equipped with a GPV 455 gearbox. Both the calculated main bearing loads and measured displacements have been normalized by its average value and evaluated over one rotor rotation. Furthermore, the loads in *x'* (axial), *y'* (lateral) and *z'* (vertical) direction are plotted separately. By comparing Figure 2.23 and 2.24, one can see that the load patterns in *x'*, *y'* and *z'*-direction, and thus the shaft displacement, are different for negative and positive blade pitching (cp. *Lz'*, *Ly'*, *Lx'* plotted in Figure 2.23 and 2.24). In Figure 2.24, it is also visible that the measured lateral (*Sy': p 1.2°*) and vertical (*Sz': p 1.2°*) gearbox displacement matches quite well with the calculated and normalized bearing load patterns *Ly' p +1.2°* and *Lz' p +1.2°*.

Table 2.8 Parameter setting for main bearing (B1) load calculations

Parameter setting	Surface roughness	Yaw angle ε	Pitch angle β	γ_{tilt} / δ + γ_{tower}	Turbu-lences
L: p -1.2°	0.03	0°	-1.2°	5° + 2°	±2.5%
L: p +1.2°	0.03	0°	+1.2°	5° + 2°	±2.5%

In summary, based on the gearbox displacement measurements and calculated load patterns plotted in Figure 2.24, it can be concluded that the calculation methods proposed and used in the present chapter adequately reflect the actual load patterns and profiles of a real wind turbine. Only the absolute values of the calculated loads could not be validated yet, as the required measurements are not (yet) available.

Now the model has been verified, some other aspects of the proposed approach will be discussed. The final aspect will be a comparison with the more commonly applied machine learning approaches.

First, it was shown that the load profiles at blade root and pitch bearing are considerably affected by inertial forces, i.e. especially by Euler and Coriolis forces. By knowing that Euler and Coriolis forces occur in rotating (coordinate) systems, it can be concluded that the mass forces, i.e. gravity, centrifugal, Euler and Coriolis do not determine only the load profile of the blade and pitch bearing but also the load profile of all components and parts installed in the rotor hub of the wind turbine. Consequently, all components of the pitch system located in the rotor hub are affected by Euler and Coriolis forces, too. This means that a pitch system realized by hydraulic cylinders and tubes must counter act Coriolis forces because these forces occur as soon as the hydraulic cylinders move and oil is pumped through the tubes (moving mass). On the other hand, a pitch system utilizing a gearbox and electrical motor must handle centrifugal and Euler forces because all rotating parts of the gearbox and electrical motor do not only have an angular speed but also an angular acceleration during every pitch cycle. One can see from this consideration, that the load profiles (and life time) of the pitch system are not only determined by aerodynamic loads (airfoil moment) but also by mass forces in the rotating (coordinate) system of the rotor hub, number of pitching cycles and pitching velocity of rotor blades. In addition, it is important to note that active stall control introduces higher loads to both rotor blades and pitch system than a regular pitch control policy. The active stall control increases the turbulences on the suction side of the blade [19]. Therefore, the blade tends to flap more often and faster. Furthermore, active stall control rises the aerodynamic airfoil moment which, again, must be absorbed by the pitch system (hydraulic cylinder or gearbox).

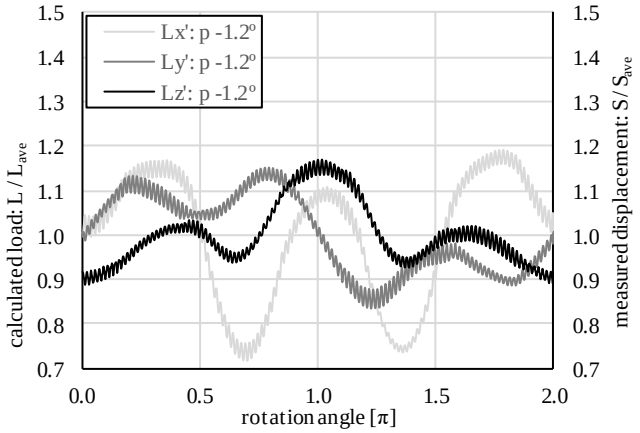

Figure 2.23 Normalized calculated bearing (B1) loads (L) with pitch angle of -1.2°

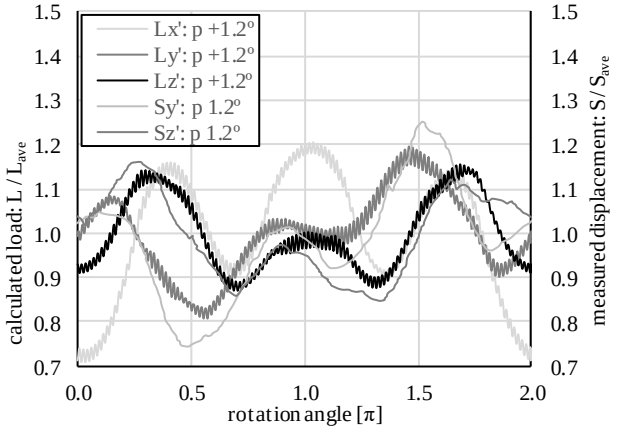

Figure 2.24 Normalized calculated bearing (B1) loads (L) and normalized measured gearbox displacement (S) with pitch angle of +1.2°

Second, from Figure 2.24, it is visible that the dynamic rotor hub loads can be evaluated by measuring the displacement of the gearbox housing. This means that the rotor hub loads also affect the load profiles of gearbox bearings and gears of the first gear step (which is realized as planetary gear set in present day wind turbines). Consequently, the life time of all bearings, shafts and gears of the first planetary gear set in a wind turbine gearbox are influenced by the rotor hub loads. Furthermore, as the rotor hub loads cause a dynamic gearbox displacement, the rotor hub loads also affect the output shaft (high speed shaft) of the gearbox. The dynamic gearbox displacement, during operation, increases the shaft end misalignment between gearbox and generator. An increasing misalignment of shaft ends reduces the life time of all high speed shaft bearings both on gearbox and generator side. If a direct drive generator is installed on the main shaft instead of a gearbox, then rotor hub loads cause a dynamic displacement of the generator rotor. In other words, due to the rotor hub loads the rotor-stator gap of the direct drive generator varies. Because of the fluctuating rotor-stator gap the

magnetic flux density varies locally and thus the current in the generator stator. The fluctuating current and current peaks must, again, be handled by the full-scale power converter i.e. by capacitors, inductors as well as semiconductors like diodes and IGBTs.

Third, the tower head loads do not only bend the tower but also excite the complete turbine structure with the third or first harmonic of the wind turbine rotor. As the wind turbine rotor typically rotates with an angular speed of 6 to 15 rpm i.e. 0.10 to 0.25 Hz, the turbine structure is excited by a frequency of approx. 0.1 Hz to 0.75 Hz depending on rotor speed (wind speed) and pitch angle deviation. Therefore, it may occur that the wind turbine structure and substructures operate close to or even at their natural frequencies. Moreover, the tower head loads must also be handled by the yaw system because the yaw system transmits the rotor hub loads to the tower head. This means that the azimuth gear and their drives (i.e. gearboxes, brakes and electrical motors) must absorb the tower head moments. Therefore, the loads due to the tower head moments are significant for the life time prediction of the yaw system.

From these considerations, it can be seen that the load profiles of rotor hub center and tower head are crucial for the life time prediction of wind turbines. For a more accurate life time prediction it is useful to calculate load profiles and predict life time based on measurements, namely: wind speed at two different heights (second wind speed used for evaluation of surface roughness), wind speed distribution, side (and shear) winds, yaw misalignment, pitch angle deviations, number of blade flaps, blade flapping speed and average wind turbulence intensity. Then, based on the set of equations proposed in the present chapter the load profiles of different wind turbine components can be calculated and therefore, the life time. By integrating the calculated load profiles and failure statistics it is possible to evaluate the life time under various environmental conditions. Moreover, the reduction of rotor hub loads is important in order to obtain an optimum life time. The rotor hub loads can be influenced either by the tilt and cone angle during the design procedure or by pitch and yaw control algorithms during operation. The control algorithms should reduce the pitch angle deviation and yaw misalignment during operation in order to lower load peaks at hub center (cp. Figure 2.19) and tower head (cp. Figure 2.22). Furthermore, blade pitching and nacelle yawing should be as smooth as possible to avoid or, at least, minimize Euler and Coriolis accelerations on blade and wind turbine rotor masses. A smooth blade pitching, however, stands in conflict with over speeding of the power train. This means that any load variation introduced into the wind turbine from the blades or rotor hub does affect the load (and associated life time) of many components of the complete wind turbine. It is, therefore, crucial for the wind turbine asset management to understand and quantify these interactions.

Finally, the proposed physics-based approach for life prediction is compared to the more commonly adopted data-driven approach. As was mentioned in the introduction (section 2.1), this load-based maintenance approach does not only allow failure and remaining useful life (RUL) predictions with higher accuracy but also enables these predictions at an early moment when the component (system) is still “healthy”. The higher accuracy is obtained because specific and representative physical component models (like virtual wind turbine blades) are used for evaluating the actual loads (at blade root, hub center and tower head) and because these actual loads are compared with design loads (like bearing load capacities). The early prediction is possible because there is no need to wait for actual failures or anomalies to occur. This means that once the component has run through the range of these operational and environmental conditions, the load profiles are known and the RUL can be evaluated. These are clear advantages in comparison to commonly used data driven or machine learning approaches which use mathematical, statistics-based models trained by learning algorithms and reference data sets [30]. The mathematical, statistics-based models are used to identify

deviations from normal operational conditions (anomaly detection) and to predict failures and the RUL. This means that the prediction i) is based on a relative reference because the relation between the training data set and the design life time (absolute reference) is unknown and ii) can only be done after a certain number of failures has occurred or clear changes of operational conditions can be measured. The principle of both approaches are visualized in Figure 2.25. However, it must also be mentioned here that the higher accuracy and early prediction of the physics and load-based approach are at the expenses of more detailed information on components (e.g. geometries, dimensions, bearing types, etc.) and on the operational and environmental conditions. Therefore, the comparison of the two approaches also demonstrates that the more detailed the input data and prediction model are, the earlier and more accurate predictions are possible.

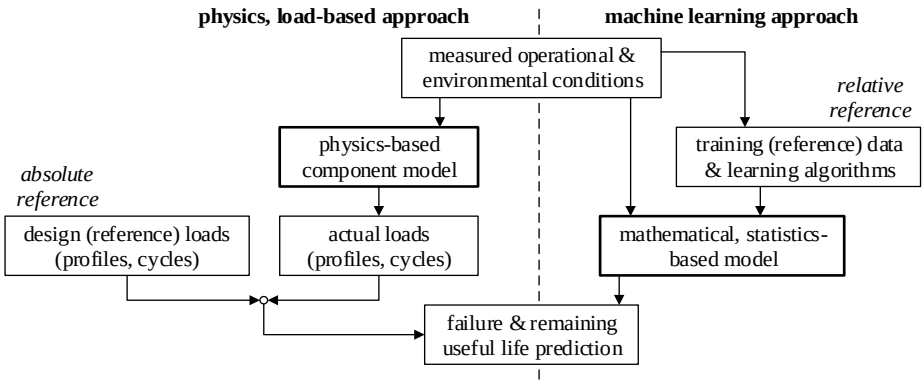

Figure 2.25 Comparison of machine learning (data driven) and physics, load-based approaches

2.5 Conclusion and Outlook

In the present chapter a model and method is introduced for load-based maintenance on a three bladed, horizontal axis, upwind wind turbine. A calculation procedure was proposed to evaluate loads (forces and moments) at blade roots, rotor hub center and tower head during wind turbine operation. The dominant influences in the load profiles were detected by performing load sensitivity analyses for different scenarios and parameters. Table 2.9 summarizes the results by providing an overview of critical parameters and their effects on load profiles. The influences are categorized in neutral, minor and major. It is recommended to consider, at least, minor and major influences when the load profiles for a specific wind turbine are calculated.

Moreover, measurements are needed to specify and take properly into account the dominant parameters in the load profile calculation. Table 2.10 gives an overview of the measurements which are required to calculate the load profiles. These measurements were derived from the sensitivity analyses performed in the present chapter. Further, the present chapter focused specifically on the calculation of load profiles under operational conditions because the resulting accurate load profiles can both enable more efficient maintenance of the system and lead to a better system design.

Table 2.9 Overview of critical / dominant calculation parameters

Parameter	Blade root loads	Hub (tower) loads	Load effect for 3 bladed rotor
Tilt, cone angle	minor	major	– High load increase – Load offset due to increasing load unbalance
Side / (shear) wind, yaw misalignment	neutral	minor	– Load offset
Pitch angle deviation	minor	major	– Increase of dynamic peak loads – Shift of load frequency from 3rd to 1st rotor harmonic
Surface roughness	neutral	minor	– Dynamic loads with 3rd rotor harmonic (3 blades)
Turbulences (wind gusts)	neutral (major)	neutral (minor)	– Neutral: small / even distributed turbulences – Minor / major: gusts, blade flapping
Mass forces	major	neutral	– neutral: initial coordinate system, mainly load offset – major: rotating coordinate system, Coriolis force due to blade flapping
Wind speed (distribution)	major	major	– loads proportional to square of wind speed (if $v_{wind} < v_{wind,rated}$)

To give a short outlook into future application of this concept in real wind turbines, three different ways of life time prediction can be distinguished. First, the most accurate way to predict the life time is the calculation of both load profiles and life time based on measurements and given component dimensions. This approach was shown by example and applied to main shaft bearings in section 2.3.2 and can also enable designers to improve their designs, because they know what loads components must bear in operation. Second, if the life time cannot be calculated, e.g. due to missing information, then a relation can be created between load profiles, number of operating hours and failure statistics. The evaluated relation is then used to predict the life time. Third, if neither the life time nor the load profiles can be calculated, then a relation between measurements of the dominant influences in the load profiles, operating hours and failure statistics can be found. The detected relation, again, is utilized to estimate the life time or number of load cycles. So it can be concluded that the evaluation and measurement of the dominant influences in the load profiles are essential for life time prediction of wind turbine components during both maintenance and design.

Finally, future works may combine the approach of physics-based component model and load-based failure prediction shown in this chapter with wind turbine control designs [31] and signal processing [32] to improve the performance of wind turbine systems.

Table 2.10 Overview of required measurements for load-based life time prediction

Load profile evaluation at / Life time of	require measurements of / is determined by
– *blade (root)* – *pitch bearing*	– angular main shaft speed – number of blade flaps – blade flapping velocity – number of blade pitches – blade pitching velocity
– *pitch system (installed in rotor hub)*	– angular main shaft speed – number of blade flaps – blade flapping velocity – number of blade pitches – blade pitching velocity – wind speed – wind speed distribution
– *rotor hub center* – *main bearings* – *gearbox + generator* – *direct drive generator* – *yaw system* – *tower (head)*	– wind speed – wind speed distribution – wind speed over height – side / shear winds – yaw misalignment to main direction of wind speed – pitch angles respectively pitch angle deviations – wind gusts – wind turbulence intensity

References

[1] B. Maples, G. Saur, M. Hand, R. van Pietermen, and T. Obdam, "Installation, Operation, and Maintenance Strategies to Reduce the Cost of Offshore Wind Energy," *Tech. Rep. Nrel/Tp-5000-57403*, no. July, pp. 1–106, 2013.

[2] M. Asgarpour and J. D. Sørensen, "State of the art in Operation and Maintenance planning of offshore wind farms," in *Safety and Reliability: Methodology and Applications - Proceedings of the European Safety and Reliability Conference, ESREL 2014*, 2015.

[3] J. Ribrant and L. M. Bertling, "Survey of Failures in Wind Power Systems With Focus on Swedish Wind Power Plants During 1997-2005," *IEEE Trans. Energy Convers.*, vol. 22, no. 1, pp. 167–173, 2007.

[4] C. Kaidis, "Wind Turbine Reliability Prediction a Scada Data Processing & Reliability Estimation Tool," no. September, pp. 1–72, 2013.

[5] M. Canizo, E. Onieva, A. Conde, S. Charramendieta, and S. Trujillo, "Real-time predictive maintenance for wind turbines using Big Data frameworks," *2017 IEEE Int. Conf. Progn. Heal. Manag. ICPHM 2017*, pp. 70–77, 2017.

[6] Y. Zhao, D. Li, A. Dong, D. Kang, Q. Lv, and L. Shang, "Fault prediction and diagnosis of wind turbine generators using SCADA data," *Energies*, vol. 10, no. 8, pp. 1–17, 2017.

[7] J. Herp, M. H. Ramezani, M. Bach-Andersen, N. L. Pedersen, and E. S. Nadimi, "Bayesian state prediction of wind turbine bearing failure," *Renew. Energy*, vol. 116, pp. 164–172, 2018.

[8] M. Asgarpour and J. Sørensen, "Bayesian Based Diagnostic Model for Condition Based Maintenance of Offshore Wind Farms," *Energies*, vol. 11, no. 2, p. 300, 2018.

[9] Y. Hu *et al.*, "A prediction method for the real-time remaining useful life of wind turbine bearings based on the Wiener process," *Renew. Energy*, vol. 127, pp. 452–460, 2018.

[10] Z. Tian, T. Jin, B. Wu, and F. Ding, "Condition based maintenance optimization for wind power generation systems under continuous monitoring," *Renew. Energy*, vol. 36, no. 5, pp. 1502–1509, 2011.

[11] L. Vera-Tudela and M. Kühn, "Analysing wind turbine fatigue load prediction: The impact of wind farm flow conditions," *Renew. Energy*, vol. 107, pp. 352–360, 2017.

[12] C. S. Gray and S. J. Watson, "Physics of failure approach to wind turbine condition based maintenance," *Wind Energy*, 2010.

[13] T. Tinga, "Application of physical failure models to enable usage and load based maintenance," *Reliab. Eng. Syst. Saf.*, vol. 95, no. 10, pp. 1061–1075, 2010.

[14] M. Engeler, D. Treyer, D. Zogg, K. Wegener, and A. Kunz, "Condition-based Maintenance: Model vs. Statistics a Performance Comparison," *Procedia CIRP*, vol. 57, pp. 253–258, 2016.

[15] M. A. Djeziri, S. Benmoussa, and R. Sanchez, "Hybrid method for remaining useful life prediction in wind turbine systems," *Renew. Energy*, vol. 116, pp. 173–187, 2018.

[16] S. S. Gokhale and K. S. Trivedi, "Analytical Modeling," *Encycl. Distrib. Syst.*, 1998.

[17] M. O. L. Hansen, *Aerodynamics of Wind Turbines, 2nd edition*. Taylor & Francis, 2013.

[18] S. Gundtoft, *Wind Turbines*. 2009.

[19] T. Burton, N. Jenkins, D. Sharpe, and E. Bossanyi, *Wind Energy Handbook*. 2011.

[20] EUROS, “Blade family EU90 | 100,” 2009.
[21] N. Timmer, “Airfoil data of NACA 64-618, DU 93-W-210ML, DU 97-W-300LM, Excel Sheet,” Delft, The Netherlands, 2009.
[22] E. Hau and H. von Renouard, *Wind Turbines: Fundamentals, Technologies, Application, Economics*. Springer Berlin Heidelberg, 2005.
[23] K. H. Grote and E. K. Antonsson, *Springer Handbook of Mechanical Engineering*, no. v. 10. Springer, 2009.
[24] J. F. Manwell, J. G. McGowan, and A. L. Rogers, *Wind Energy Explained: Theory, Design and Application*. Wiley, 2010.
[25] DIN ISO 281, “Rolling bearings - Dynamic load ratings and rating life - calculation methods,” 2009.
[26] F. D. Bianchi, H. de Battista, and R. J. Mantz, *Wind Turbine Control Systems: Principles, Modelling and Gain Scheduling Design*. Springer London, 2007.
[27] FAG, *Wälzlager Hauptkatalog*. Schweinfurt: Schaeffler KG, 2008.
[28] W. Hu, S. Said, A. Multibrid, and N. Sea, “Resonance phenomenon in a wind turbine system under operational conditions 1,2,3,4,” *9Th Int. Conf. Struct. Dyn.*, 2014.
[29] A. Heege, J. Hemmelmann, L. Bastard, J. L. Sanchez, L. Lens, and M. Omiciuolo, *Matching experimental and numerical data of dynamic wind turbine loads by modelling of defects*, vol. 3. 2009.
[30] A. Stetco *et al.*, “Machine learning methods for wind turbine condition monitoring: A review,” *Renew. Energy*, vol. 133, pp. 620–635, 2019.
[31] A. D. Wright and L. J. Fingersh, “Advanced Control Design for Wind Turbines Part I : Control Design, Implementation, and Initial Tests,” *Tech. Rep. Natl. Renew. Energy Lab.*, no. March, p. 98, 2008.
[32] S. Simani and P. Castaldi, “Adaptive Signal Processing Strategy for a Wind Farm System Fault Accommodation ∗,” *IFAC-ChaptersOnLine*, vol. 51, no. 24, pp. 52–59, 2018.

CHAPTER 3

Calculating Loads and Life Time Reduction of Wind Turbine Gearbox and Generator Bearings due to Shaft Misalignment

ABSTRACT

During the last two decades wind turbine industries have faced high failure rates, downtimes and costly repairs. Gearbox and generator have contributed to this, especially, because their high speed shaft (HSS) bearings have often failed. In this chapter an analytical method is proposed to calculate the reaction loads of flexible connecting couplings (FCC) installed between wind turbine gearbox and generator. Reaction loads are determined from joint kinematics and metal disc pack deformations as well as axial and angular shaft misalignment. The calculations are executed for both a FCC and an universal joint shaft (UJS) and applied to the gearbox high speed shaft (HSS). The performance of FCC and UJS are compared with respect to the bearing loads and life time of the gearbox HSS. It is shown that the early, unplanned bearing failures of gearbox and generator HSS can often be attributed to the FCC installed between gearbox and generator.

This chapter is reproduced from: Rommel, D. P., Di Maio, D., Tinga, T. (2020). Calculating Loads and Life Reduction of Wind Turbine Gearbox and Generator Bearings due to Shaft Misalignment. *Wind Engineering*.

Nomenclature

SYMBOL	UNIT	QUANTITY
A	-	transfer function
a	-	axial
B	-	bearing
B, b	-	bending
D	[m]	diameter
DD	-	direct drive
e	-	unity vector, factor
F	[N]	force
FCC	-	flexible connecting coupling
f_{red}	-	relative life time factor
G	[N]	gravity force
$GFRP$	-	glass fiber reinforced polymer
H	-	hub
k_{1D}	[N/m]	spring stiffness
k_t	[Nm/rad]	torsional stiffness
L, l	[m]	length, distance
L_{10}	-	life time
M	[Nm]	moment
m	[kg]	mass
N	-	nominal
n	-	number of connections
P	[N]	equivalent bearing load
P	-	pinion
p	-	pitch
R, r	[m]	radius, distance
r	-	radial
r	-	length ratio, diameter ratio
S	-	shaft
s_{dyn}	[m]	dynamic displacement
st	-	(gear) stage, steel
T	[Nm]	torque
t	-	torque, torsional
UJS	-	universal joint shaft
V	[m³]	volume
v_{vib}	[m/s]	vibration velocity
Δx	[m]	axial displacement
X	-	factor
Y	-	factor
x,y,z	-	(primary side) coordinates
x',y',z'	-	secondary side coordinates
α	[rad]	displacement angle
β	[rad]	displacement angle
γ	[rad]	displacement angle
δ	[rad]	angle
θ	[rad]	spur gear meshing angle
μ_f	-	friction coefficient
ρ	[kg/m^3]	density
φ	[rad]	shaft rotation angle
ψ	[rad]	phase angle between e_1 and e_2
ω	[1/s]	(shaft) speed

3.1 Introduction

Surveys of failures in a wind turbine system evaluated during the last decades have highlighted that wind turbine gearboxes and generators have significant failures rates and downtimes [1]–[6]. Some of these studies have also outlined which subcomponents within the gearbox and generator were damaged. Failure data showed that bearings were the main cause of gearbox [7] and generator [8] failures. Especially, the high speed shaft (HSS) bearings were identified as those with the highest failure rates [7]. It is suspected that these high failure rates of the HSS bearings are caused by increased bearing loads. These increased bearing loads are determined by the magnitude of misalignment [7] as well as by the type of connecting coupling installed between gearbox and generator shaft. However, the actual magnitude of the misalignments during operation is generally unknown. Therefore, the selection of an adequate type of connecting coupling is problematic [7]. Several multibody analyses have been applied to model the dynamics of the complete wind turbine system [9]–[12] and to evaluate the load increase on the HSS bearings [7]. But despite this, it is still unclear to which extent the loads on the HSS bearings are increased by the actual misalignments and thus, whether the used connecting couplings are suitable for the application in the wind turbine power train. Scientific literature on shaft connecting couplings seems to be very limited, and neither a load calculation nor a misalignment estimation applied to connecting couplings could be found at all. Thus, the main objectives of this chapter are i) to propose a method for the load calculation and misalignment estimation of flexible connecting couplings (FCC), which can be used for both design and maintenance prediction and ii) to evaluate the suitability of FCC in wind turbine power trains.

The approach followed is similar to previous work by the authors on the effects of variations in operational conditions [13]. Firstly, the joint kinematics of the FCC are considered in section 3.2.1. Then, the flexible joint elements of the FCC (metal disc packs) are described by 1D springs in section 3.2.2. Section 3.2.3 discusses the calculation of bearing loads. An estimation of the shaft misalignments is provided in section 3.2.4 based on shaft misalignment during installation and normal vibration data. In section 3.3.1, the reaction loads due to shaft misalignment are calculated for a FCC as well as an universal joint shaft (UJS) and applied to the gearbox high speed shaft (HSS). The bearing loads of the gearbox HSS are computed in section 3.3.2 and used to calculate a relative life time factor which indicates the performance of the FCC compared to the UJS. Finally, the performance and suitability of a FCC between gearbox and generator in wind turbines is discussed in section 3.4.

3.2 Load calculations

Flexible connecting couplings (FCC) and universal joint shafts (UJS) are often installed between the HSS ends of gearbox and generator (cp. Figure 3.1). The FCC and UJS allow axial and angular displacement of gearbox and generator shaft during operation while, at the same time, transmitting high torques.

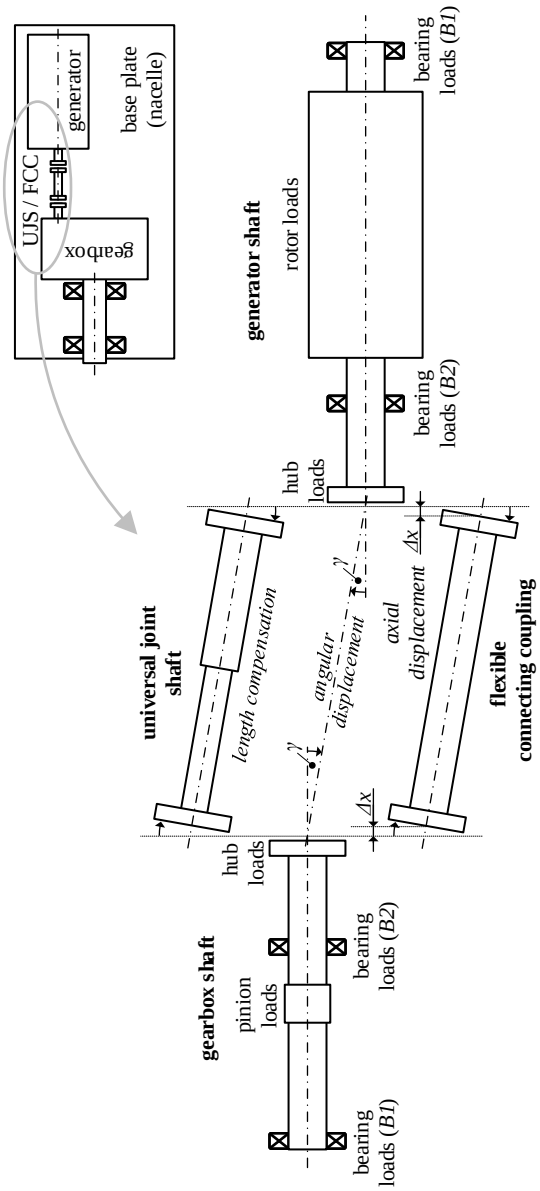

Figure 3.1 Gearbox and generator high speed shaft assembly

FCCs use flexible elements between the shaft hubs to allow axial (Δx) and angular (γ) displacement. The flexible elements are realized by rubber or metal parts depending on the transmitted torque. Due to the high transmitted torque, FCCs applied in wind turbines use metal disc packs as flexible elements (cp. Figure 3.2 from [14]). The permissible magnitude of axial and angular displacement depends on the design of the coupling joint and metal disc

pack itself determining the maximal allowable deformation and associated stresses of the metal disc pack. However, the deformation of the metal disc packs also causes reaction forces and moments which are transmitted to the primary and secondary side hubs of the coupling joint (cp. Figure 3.2) and, thus to the gearbox and generator shafts (cp. Figure 3.1 – hub loads).

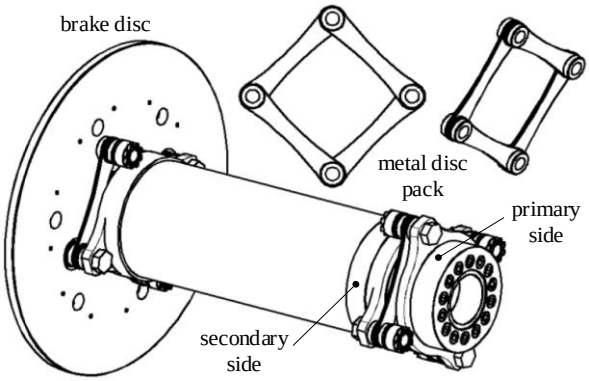

Figure 3.2 Design of flexible connecting coupling for wind turbines [14]

Further, due to the joint kinematics of connecting couplings, additional loads are generated at the primary and secondary side hub. These loads are well known for a UJS; however, they also apply for FCCs. Therefore, the hub loads at the gearbox and generator shaft end are a combination of the loads due to the joint kinematics and those due to the deformation of metal disc packs (cp. also Figure 3.3). Both types of loads can be calculated by models describing the joint kinematics and disc pack deformation as a function of axial and angular displacement. These models are developed in section 3.2.1 (loads due to joint kinematics) and in section 3.2.2 (loads due to disc pack deformations). Then, from these models the reaction forces and moments (loads) can be evaluated at the connecting coupling hub (cp. Figure 3.3). By applying the reaction loads to a shaft-bearing assembly, the bearing loads are derived as will be shown in section 3.2.3. Finally, to quantify the hub reaction and bearing loads, axial and angular displacement during installation and operation are discussed and considered in section 3.2.4.

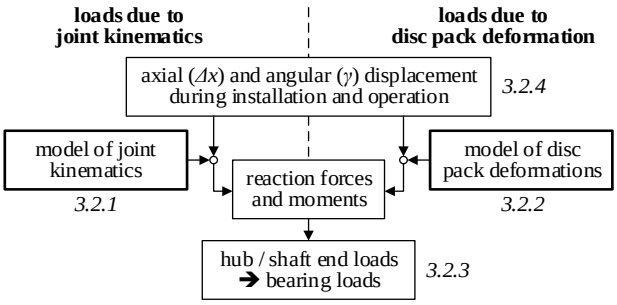

Figure 3.3 Process of load calculation

3.2.1 Loads due to joint kinematics

It is well-known that joints in UJSs and cardan shafts cause fluctuating shaft speeds, torques and bending moments [15]. These quantities can be evaluated by considering the kinematic relation between the shaft speed before (ω_1) and after (ω_2) the joint [15]. This calculation makes use of the fact that a cross connection is present in the joints (cp. Figure 3.4a), i.e. the rotating vectors e_1 and e_2 shown in Figure 3.4a and 4b are perpendicular ($\psi = \pi/2$). Therefore, their scalar product is equal to zero and a direct relation between the speeds ω_1 and ω_2 can be found (cp. [15] for the principle of the derivation of Eq. 3.1):

$$\frac{\omega_2}{\omega_1} = \frac{\frac{\cos\beta}{\cos\alpha}}{\left[1+\left(\tan\varphi\frac{\cos\beta}{\cos\alpha}+\tan\alpha\sin\beta\right)^2\right]\cos^2\varphi} \tag{3.1}$$

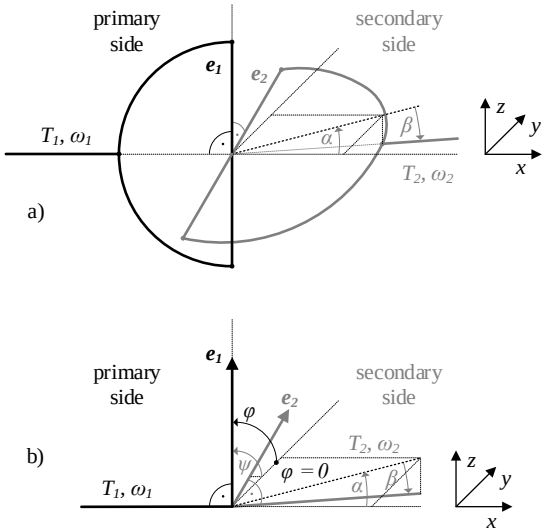

Figure 3.4 Primary and secondary side of coupling joint with a) cross connection ($\psi = \pi/2$) and b) general connection

This means that the speed ω_2 differs from the speed ω_1 depending on the displacement angles α and β and the shaft rotation (position) angle φ. The displacement angle α is the rotation of the secondary side around the z-coordinate and the displacement angle β to the rotation around the y-coordinate (cp. also Figure 3.4).

However, FCCs do not use a cross connection in the joint, i.e. the angle ψ is not necessarily equal to $\pi/2$ (cp. Figure 3.5a-c). Hence, the scalar product of the two vectors e_1 and e_2 is not always zero anymore. Consequently, the kinematic relation between the speeds ω_1 and ω_2 cannot be evaluated in a straight forward manner as it is shown in [15]. An alternative method is needed to describe the kinematic relation between primary and secondary side. As the transmitted power, i.e. the product of shaft speed ω and torque T, before and after the joint must be equal, the following relation is valid:

$$\frac{\omega_2}{\omega_1} = \frac{T_1}{T_2} \tag{3.2}$$

Therefore, the kinematic relation between the speeds ω_1 and ω_2 is equivalent to the relation of the torques T_1 and T_2. In other words, the kinematic relation after Eq. 3.1 can also be derived by evaluating the torques T_1 and T_2.

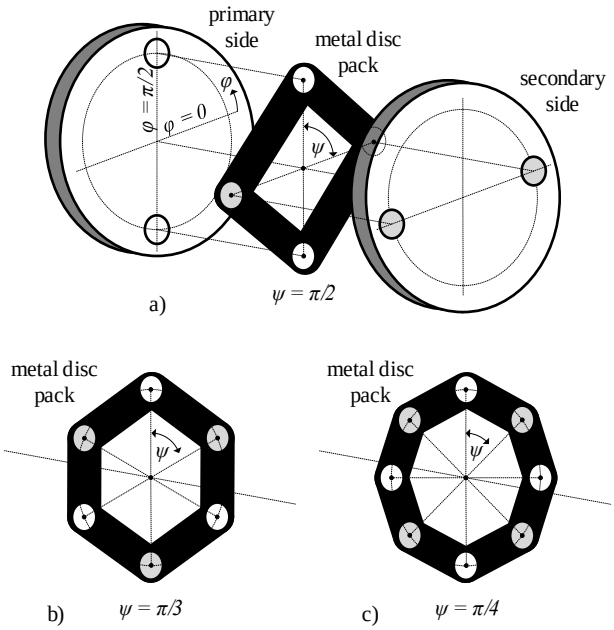

Figure 3.5 FCC joints with different angles ψ

In addition, torque is the product of a radius and force. This means that for analyzing how the torque (T_2) is changed by the FCC joint with metal disc packs (Figure 3.5), the change of the radius R_2 and force F_2 must be described. It also means that by evaluating separately the change of radius R_2 and force F_2 and then, by combining them the kinematic relation in Eq. 3.1 can be found. To do so, a simplified pre-consideration of the kinematics is discussed before looking at the general consideration. The pre-consideration evaluates the kinematic loads at the rotating angle $\varphi = 0$ (change of radius) and $\varphi = \pi/2$ (change of force) for the displacement angle $\alpha \neq 0$, but $\beta = 0$. In a third case the displacement angles are set to $\alpha = 0$ and $\beta \neq 0$. Note that the pre-considerations are valid for any angle ψ.

Pre-consideration:

As a first case, the FCC joint is schematically shown in Figure 3.6 for a rotation angle $\varphi = 0$, which represents the change of radius case. Primary and secondary side have an angular displacement (i.e. misalignment) given by the angle α, i.e. the secondary side rotates by the angle α around the z-axis. Due to this rotation the effective radius which transmits the force from the primary to the secondary side reduces from R to R_y (cp. Figure 3.6). As a consequence of this, the transmitted force should increases from F_1 to F_2 because the torque of the primary side is constant.

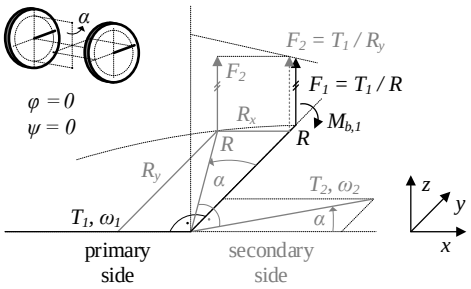

Figure 3.6 Pre-consideration case 1, change of radius: $\varphi = 0$ and $\beta = 0$

Further, because of the rotation around the z-axis the working lines of force F_1 and F_2 are still parallel; however, they do not coincide anymore, i.e. they are separated by the distance R_x. This means that a bending moment ($M_{b,1}$) is introduced to the primary side in order to transmit the force from the primary to the secondary side. Then, the torque T_2 of the secondary side is the product of the increased transmitted force F_2 and the radius R. So the equations valid for the connecting coupling position shown in Figure 3.6 are given as follows:

$$T_1 = F_1 R \tag{3.3}$$

$$F_2 = {T_1}/{R_y} = F_1 {R}/{R_y} = F_1 {1}/{A_{R,\alpha y}} \tag{3.4}$$

$$T_2 = F_2 R = {T_1}/{A_{R,\alpha y}} \tag{3.5}$$

$$M_{b,1} = -F_2 R_x = -F_1 {R_x}/{A_{R,\alpha y}} = T_1 {A_{R\alpha,x}}/{A_{R,\alpha y}} = T_1 A_{B1,\alpha} \tag{3.6}$$

In which $A_{R,\alpha}$ is the radius transfer function describing the modification of torque T_2 due to the angle α. The bending transfer function (at the primary side) due to the angle α is indicated by $A_{B1,\alpha}$. With Figure 3.6 these transfer functions can be extended to be valid for any value of the rotating angle φ by:

$$A_{R,\alpha y} = {R_y}/{R} = \sqrt{(\cos\alpha\cos\varphi)^2 + (\sin\varphi)^2} \tag{3.7}$$

$$A_{R,\alpha x} = {R_x}/{R} = -\sin\alpha\sqrt{(\cos\varphi)^2} = -\operatorname{sgn}\alpha\sqrt{(\sin\alpha\cos\varphi)^2} \tag{3.8}$$

$$A_{B1,\alpha} = {A_{R,\alpha x}}/{A_{R,\alpha y}} = -\operatorname{sgn}\alpha\sqrt{\frac{(\sin\alpha\cos\varphi)^2}{(\cos\alpha\cos\varphi)^2+(\sin\varphi)^2}} \tag{3.9}$$

In the second case, the FCC joint visible in Figure 3.6 is rotated by an angle $\varphi = \pi/2$. This leads to the joint position as shown in Figure 3.7, which represent the change of force case.

It can be seen from Figure 3.7 that due to the rotation of $\varphi = \pi/2$ the radii of the primary and secondary side coincide, as the misalignment (angle α) is in the xy-plane. This, however, means that the working lines of force F_1 and F_2 deviate with the displacement angle α (change

of force). Consequently, the force F_1 of the primary side is upon transmission split into a force F_2 and $F_{b,2}$. The force F_2 generates (with the radius R) the torsional torque T_2 of the secondary side while the force $F_{b,2}$ creates (with the radius R) the bending moment $M_{b,2}$ at the secondary side. The equations valid for the FCC joint position shown in Figure 3.7 are given as follows:

$$F_2 = F_1 \cdot A_{F,\alpha} \tag{3.10}$$

$$F_{b,2} = F_1 \cdot A_{B2,\alpha} \tag{3.11}$$

$$T_2 = F_2 R = T_1 \cdot A_{F,\alpha} \tag{3.12}$$

$$M_{b,2} = -F_{b,2} R = T_1 \cdot A_{B2,\alpha} \tag{3.13}$$

with $A_{F,\alpha}$ the force transfer function and $A_{B2,\alpha}$ the bending transfer function (at the secondary side) due to the angle α.

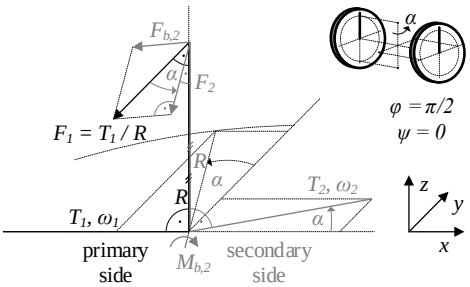

Figure 3.7 Pre-consideration case 2, change of force: $\varphi = \pi/2$ and $\beta = 0$

Based on in Figure 3.7 the transfer functions are generalized again, and can be specified as a function of the rotating angle φ by:

$$A_{F,\alpha} = {}^{F_2}/_{F_1} = \sqrt{(\cos\alpha \sin\varphi)^2 + (\cos\varphi)^2} \tag{3.14}$$

$$A_{B2,\alpha} = {}^{F_{b,2}}/_{F_1} = -\sin\alpha \sqrt{(\sin\varphi)^2} = -\operatorname{sgn}\alpha \sqrt{(\sin\alpha \sin\varphi)^2} \tag{3.15}$$

It can be seen that the secondary side torque T_2 can be modified by the transfer functions in both Eq. 3.7 (due to a change in effective radius) and Eq. 3.14 (change in force). So these two equations must be combined to obtain the total torque transfer function. From Eq. 3.5, it is visible that the primary torque is divided by $A_{R,\alpha y}$ and from Eq. 3.12 that the primary torque is multiplied by $A_{F,\alpha}$. This means that the torque transfer function $A_{T,\alpha}$ for a displacement angle α (and any rotation angle φ) is $A_{F,\alpha}$ divided by $A_{R,\alpha y}$, i.e.:

$$A_{T,\alpha} = {}^{T_2}/_{T_1} = {}^{A_{F,\alpha}}\Big/_{A_{R,\alpha y}} = \sqrt{\frac{(\cos\alpha \sin\varphi)^2 + (\cos\varphi)^2}{(\cos\alpha \cos\varphi)^2 + (\sin\varphi)^2}} \tag{3.16}$$

And finally, as a third case, in the same way as shown for the displacement angle α, the torque and bending transfer functions can be obtained for the displacement angle $\beta \neq 0$, but $\alpha = 0$. Considering that the displacement angle β is equivalent to a phase shift of $-\pi/2$ in comparison to the displacement angle α (cp. Figure 3.4b), the transfer functions are obtained as follows:

$$A_{T,\beta} = \sqrt{\frac{(\cos\beta\cos\varphi)^2+(\sin\varphi)^2}{(\cos\beta\sin\varphi)^2+(\cos\varphi)^2}} \tag{3.17}$$

$$A_{B1,\beta} = \operatorname{sgn}\beta\sqrt{\frac{(\sin\beta\sin\varphi)^2}{(\cos\beta\sin\varphi)^2+(\cos\varphi)^2}} \tag{3.18}$$

$$A_{B2,\beta} = \operatorname{sgn}\beta\sqrt{(\sin\beta\cos\varphi)^2} \tag{3.19}$$

The pre-consideration of the FCC joint demonstrates that the torque of the secondary side as well as the bending moments of the primary and secondary side can be expressed as functions of the torque of the primary side, if the displacement angles and thus, the transfer functions are known. Therefore, in the following general consideration the radius and force transfer functions are derived taking into account the angles φ, ψ, α, β (cp. also Figure 3.4b).

General consideration:

The alpha (Eq. 3.9, 3.15 and 3.16) and beta (Eq. 3.17 to 3.19) transfer functions are particular forms of the general transfer functions. This means that the general transfer functions, can be derived from them. If the displacement angles $\alpha \neq 0$ and $\beta \neq 0$, then an equivalent displacement angle γ will be calculated by (see also Figure 3.8a in combination with Table 3.1):

$$\gamma = \operatorname{sgn}(\alpha)\arccos(\cos\alpha\cos\beta)\ . \tag{3.20}$$

Further, the position of the equivalent displacement angle is specified by the phase angle φ_γ (cp. Figure 3.8a), which can be derived from the displacement angles α and β (cp. Figure 3.8a and Table 3.1) as:

$$\tan\varphi_\gamma = -\frac{\beta}{\alpha} \tag{3.21}$$

Table 3.1 Displacement angle γ and phase angle φ_γ dependent on angles α and β

angle α	**angle β**	**angle γ**	**angle φ_γ**
> 0	0	α	-0
> 0	> 0	> 0	< 0
> 0	< 0	< 0	> 0
< 0	0	α	$+0$
< 0	> 0	> 0	> 0
< 0	< 0	< 0	< 0
$+0$	> 0	β	$-\pi/2$
$+0$	< 0	β	$\pi/2$

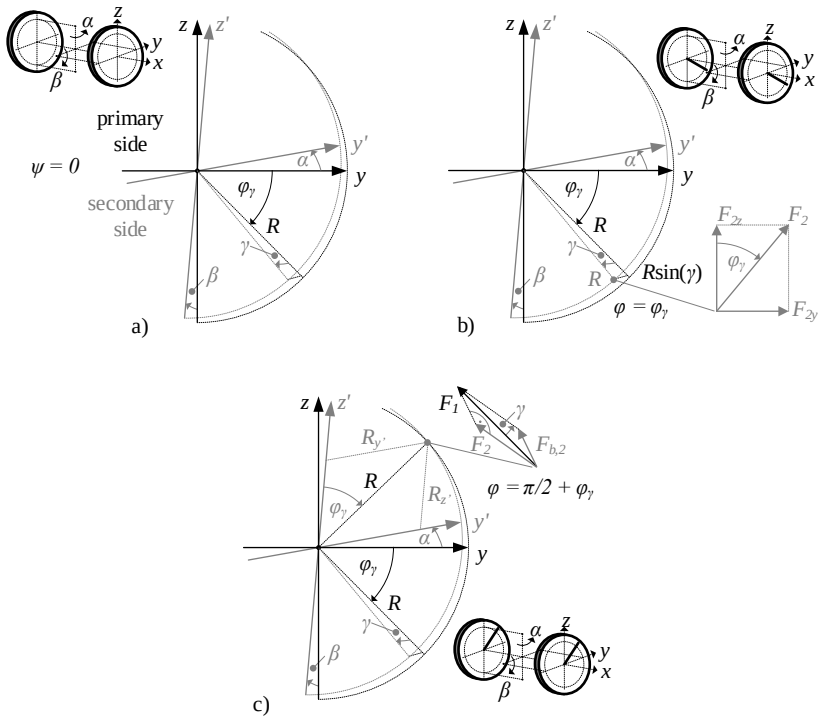

Figure 3.8 a) Displacement angle γ and phase angle φ_γ due to the combination of α and β
b) Reaction forces due to angle γ and at rotation angle $\varphi = \varphi_\gamma$ (change of radius)
c) Reaction forces due to angle γ and at rotation angle $\varphi = \pi/2 + \varphi_\gamma$ (change of force)

At the position $\varphi = \varphi_\gamma$ the reaction forces are parallel to the yz-plane and thus can be decomposed in a force component in y- and z-direction. This is shown in Figure 3.8b which is equivalent to the pre-consideration case 1, change of radius in Figure 3.6. It also means that the primary side shaft bending has also components around y- and z- direction (cp. Figure 3.8b).

Then, at the position $\varphi = \pi/2 + \varphi_\gamma$ the secondary side is in plane with the primary side, i.e. the radii of primary and secondary side coincide. This is demonstrated in Figure 3.8c which is equivalent to the pre-consideration case 2, change of force in Figure 3.7. At this position the working lines of the reaction forces cross. The reaction force $F_{b,2}$, which is parallel to the rotating axis of the secondary side (x'-axis) and normal to the rotated y'z'-plane, causes shaft bending of the secondary side (cp. Figure 3.8c). This shaft bending can, again, be split in its components because the secondary side radius can be decomposed, too.

Based on these considerations the radius $A_{R,\gamma}$ (cp. Figure 3.8b) and force $A_{F,\gamma}$ (cp. Figure 3.8c) transfer functions can be derived for the equivalent displacement angle γ. By, again, combining the radius $A_{R,\gamma}$ and force $A_{F,\gamma}$ transfer functions, the torque transfer functions is obtained. The detailed derivations of the radius ($A_{R,\gamma}$) and force ($A_{F,\gamma}$) transfer functions are not shown here for space limitation reasons. The resulting torque ($A_{T,\gamma}$) and bending transfer functions ($A_{B1,\gamma}$ and $A_{B2,\gamma}$) are:

$$A_{T,\gamma} = {A_{F,\gamma}}\Big/{A_{R,\gamma y}} = \sqrt{\frac{(\cos\gamma\sin(\varphi-\psi-\varphi_\gamma))^2+(\cos(\varphi-\psi-\varphi_\gamma))^2}{(\cos\gamma\cos(\varphi-\psi-\varphi_\gamma))^2+(\sin(\varphi-\psi-\varphi_\gamma))^2}} \tag{3.22}$$

$$A_{B1,\gamma} = -\operatorname{sgn}\gamma\sqrt{\frac{(\sin\gamma\cos(\varphi-\psi-\varphi_\gamma))^2}{(\cos\gamma\cos(\varphi-\psi-\varphi_\gamma))^2+(\sin(\varphi-\psi-\varphi_\gamma))^2}}\begin{pmatrix}0\\ \cos\varphi_\gamma\\ \sin\varphi_\gamma\end{pmatrix} \tag{3.23}$$

$$A_{B2,\gamma} = -\operatorname{sgn}\gamma\sqrt{(\sin\gamma\sin(\varphi-\psi-\varphi_\gamma))^2}\begin{pmatrix}0\\ \cos\varphi_\gamma\\ \sin\varphi_\gamma\end{pmatrix} \tag{3.24}$$

Note that the general torque and bending transfer functions in Eq. 3.22 to 3.24 are valid for every connection between primary and secondary side. The vector in Eq. 3.23 is needed to split the bending moment in its components around y- and z- direction. The same applies for Eq. 3.24, i.e. the vector splits the bending moment in its components around y'- and z'-direction

Moreover, note that the number of connections *n* is defined by the design of the FCC joint. For example, FCCs shown in Figure 3.5a to 3.5c have each two, three respectively four connections at primary and secondary side. This means that the angle ψ is related to the number of connections *n* as:

$$\psi = \frac{\pi}{n} \tag{3.25}$$

To evaluate the transfer functions of the FCC joint, Eq. 3.22 to 3.24 must be calculated for every connection (of the secondary side). It can be assumed that every of the *n* connections transmits the n-th part of the primary side torque. So the transfer functions of the connecting coupling are obtained by summing up the torques and bending moments of the *n* connections, i.e.:

$$T_2 = \sum_{i=1}^{n}\frac{T_1}{n}A_{T,\gamma,i} \tag{3.26}$$

$$M_{b,1} = \sum_{i=1}^{n}\frac{T_1}{n}A_{B1,\gamma,i} \tag{3.27}$$

$$M_{b,2} = \sum_{i=1}^{n}\frac{T_1}{n}A_{B2,\gamma,i} \tag{3.28}$$

Note that in the case of $n = 2$ connections the transfer functions for $i = 1$ and $i = 2$ are identical. This means that in this case a summation after Eq. 3.26 to 3.28 is not necessary and the torque and bending moments can be directly determined from the transfer functions. In the pre-considerations this simplification was utilized.

Further, from Eq. 3.26 to 3.28, it can be seen that torque fluctuations and shaft bending moments occur at any type of FCC joint using *n* connections at primary and secondary side. Moreover, according to Eq. 3.2 the inverse of the torque ratio in Eq. 3.22 for $n = 2$ connections, i.e. $\psi = \pi/2$, must be equivalent to Eq. 3.1. Remember that Eq. 3.1 describes the kinematic relation of the primary and secondary shaft speed with a cross connection (ψ =

$\pi/2$) in the joint. Figure 3.9 shows this comparison for one shaft rotation, demonstrating that Eq. 3.1 and 3.22 are indeed equivalent. In addition, Eq. 3.27 provides the bending moment components around the y- and z-axes and Eq. 3.28 the bending moment components around the y'- and z'-axes because Eq. 3.23 and 3.24 include a vector decomposition. This is needed for the hub / bearing load calculations in y- and z-direction. Therefore, it can be concluded that the loads due to the kinematics of the coupling joint (cp. also Figure 3.3) can be calculated by Eq. 3.22 to 3.24 respectively Eq. 3.26 to 3.28.

Figure 3.10 shows the absolute value of the primary side bending moment for connecting couplings with $n = 2$, $n = 3$ and $n = 4$ connections over one shaft rotation. For $n = 3$ and $n = 4$ the superposition of the different connections can be observed since the fluctuation (amplitude) of the bending moment reduces significantly. This demonstrates that the bending moment (over one rotation) converges to an almost constant value by increasing the number of connections at primary and secondary side. So the primary ($M_{b,1}$) and secondary ($M_{b,2}$) side bending moments of FCCs with a higher number of connections can be considered as constant in time. Note that this also applies to the secondary side torque (T_2) for even-numbered connections, i.e. $n \in \{4,6,8,..\}$, as can be derived from Eq. 3.24.

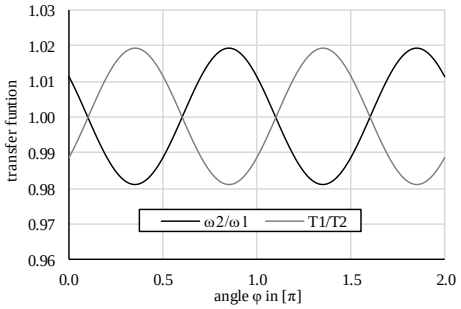

Figure 3.9 Comparison of transfer functions for $\alpha = 5°$ and $\beta = 10°$

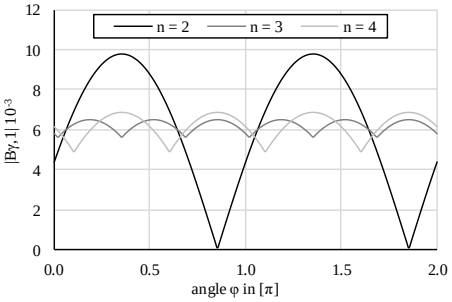

Figure 3.10 Bending of primary side shaft for $\alpha = 0.5°$ and $\beta = 0.25°$

Although the joint kinematics do not generate any axial forces, in the case of UJSs with length compensation axial forces occur which must be absorbed by the primary side shaft bearings. These axial forces are caused by the transmitted torque and friction between the flanks of the profiles while compensating the axial length [16] [17]. Based on the primary side torque, the profile pitch diameter D_p, friction coefficient μ_f as well as displacement angles

α and β respectively γ, the (maximal) reaction force at the primary side due to length compensation can be calculated as follows [16] [17]:

$$\vec{F}_{max} = \begin{pmatrix} F_x \\ F_y \\ F_z \end{pmatrix} = \mu_f T_1 \frac{2}{D_p} \begin{pmatrix} 1 \\ \tan\gamma \cos\varphi_\gamma \\ \tan\gamma \sin\varphi_\gamma \end{pmatrix} \tag{3.29}$$

Note that the axial forces and thus also the forces in Eq. 3.29 slightly increase due to the pressure built up in the length compensation during lubrication [16]. This effect, however, is neglected in this chapter.

To summarize, the kinematics of the joints result in variations (over shaft position or time) of rotational speed and transmitted torque. The equations derived in this subsection enable to quantify these variations for any misalignment angle and joint design (number of connections). Moreover, bending moments are generated in both the primary and secondary sides of the joints. Also these moments can be quantified using the proposed equations. In the next subsection, the second type of loads generated in joints will be discussed in detail.

3.2.2 Loads due to disc pack deformations

As already mentioned above, metal disc packs are commonly used in FCC joints which have to transmit high torques. The metal disc packs provide, on the one hand, a high torsional stiffness and allow, on the other hand, axial and angular shaft misalignment. This means that the metal discs have a high tension / compression stiffness and simultaneously a low bending and twist stiffness. Consequently, it can be assumed that the reaction loads, i.e. the forces that the coupling exerts on the two connected shafts, due to disc pack deformations are dominated by the tension / compression stiffness. Therefore, for the reaction load calculation the metal disc packs can be approximated by a set of one-dimensional springs which have a tension / compression stiffness k_{1D} (cp. Figure 3.11).

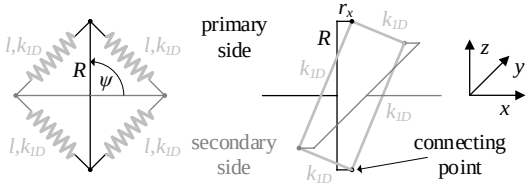

Figure 3.11 Representation of a FCC joint with $\psi = \pi/2$ by a set of 1D springs, front view (left) and 3D sketch (right)

The stiffness k_{1D} can be evaluated from the torsional stiffness k_t of the metal disc pack which is normally given in the FCC data sheet. For a FCC with each two (spring) connecting points at primary and secondary side (cp. Figure 3.11), i.e. $\psi = \pi/2$, the spring force due to the transmitted torque T_1 is given as:

$$F_{spring} = \frac{T_1}{2R}\sin\left(\frac{\psi}{2}\right) = \frac{T_1}{2\sqrt{2}R} = k_{1D}\Delta l = k_{1D}2R\left[\sin\left(\frac{\psi+\Delta\psi}{2}\right) - \sin\left(\frac{\psi}{2}\right)\right] \tag{3.30}$$

The spring extension Δl is specified by the difference between the deformed (l') and undeformed (l) length of the 1D spring. In addition, for small angles $\Delta\psi$ and for $\psi = \pi/2$ Eq. 3.30 can be simplified by using:

$$\sin\left(\frac{\psi+\Delta\psi}{2}\right) - \sin\left(\frac{\psi}{2}\right) = \\ = \sin\left(\frac{\psi}{2}\right)\cos\left(\frac{\Delta\psi}{2}\right) + \cos\left(\frac{\psi}{2}\right)\sin\left(\frac{\Delta\psi}{2}\right) - \sin\left(\frac{\psi}{2}\right) = \frac{\Delta\psi}{2\sqrt{2}} \tag{3.31}$$

Then, with the torsional stiffness k_t specified by the quotient of the torque T_1 and torsional displacement angle $\Delta\psi$, the stiffness k_{1D} can be written as follows:

$$k_{1D} = \frac{F_{spring}}{\Delta l} = \frac{T_1}{2\sqrt{2}R}\frac{2\sqrt{2}}{2R\,\Delta\psi} = \frac{1}{2R^2}\frac{T_1}{\Delta\psi} = \frac{1}{2R^2}k_t \tag{3.32}$$

Hence, based on the product of the spring stiffness k_{1D} and the spring extension Δl due to angular (γ) and axial (Δx) displacement the reaction forces and moments can be calculated at the shaft centers of the primary and secondary side. As the forces and moments are equal at the primary and secondary side, it is sufficient to calculate them at the primary side. The spring extension due to axial ($\Delta l_{\Delta x}$) and angular (Δl_γ) displacement is evaluated based on Figure 3.12. It is for small angles:

$$\Delta l_{\Delta x} = l' - l = \sqrt{l^2 + \Delta x^2} - l = \\ = \sqrt{2}R\left(\sqrt{1 + \left(\frac{\Delta x}{l}\right)^2} - 1\right) \approx \sqrt{2}R\left(\sqrt{1 + \left(\tan\frac{\delta}{\sqrt{2}}\right)^2} - 1\right) \tag{3.33}$$

$$\Delta l_\gamma = l' - l \approx \sqrt{2}R\left(\sqrt{1 + \left(\tan\frac{\gamma}{\sqrt{2}}\right)^2} - 1\right) \tag{3.34}$$

Eq. 3.33 and 3.34 can be simplified by the following trigonometric relation:

$$\sqrt{1 + (\tan\gamma)^2} = \frac{1}{\cos\gamma} \tag{3.35}$$

Then, the total spring extension due to angular (γ) and axial (Δx) displacement is approximated for small angles by (cp. Figure 3.12):

$$\Delta l = \sqrt{2}R\left(\frac{1}{\cos\left(\frac{1}{\sqrt{2}}(\delta \pm \gamma)\right)} - 1\right) \tag{3.36}$$

Note that due to the combination of angular and axial displacement the extension is not equal for the different springs. In other words, one half of the springs is tensioned until Δl_{max} while the other half of the springs only until Δl_{min}.

$$\Delta l_{max} = \sqrt{2}R\left(\frac{1}{\cos\left(\frac{\Delta x}{\sqrt{2}R} + \frac{\gamma}{\sqrt{2}}\right)} - 1\right) \tag{3.36a}$$

$$\Delta l_{min} = \sqrt{2}R\left(\frac{1}{\cos\left(\frac{\Delta x}{\sqrt{2}R} - \frac{\gamma}{\sqrt{2}}\right)} - 1\right) \tag{3.36b}$$

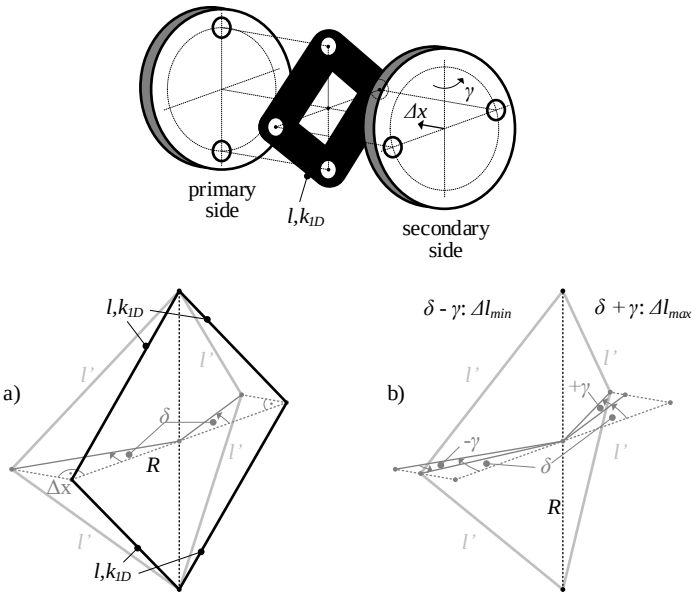

Figure 3.12 Tensioning of 1D springs due to displacement – a) axial Δx and b) combination of axial Δx and angular γ

Further, due the unequal extension, the spring forces at the connecting points are neither equal, i.e. a force difference occurs at the spring connecting points. This means that reaction forces (vector F) and moments (vector M_b) appear at the shaft center. These forces and moments are specified based on Figure 3.13 as follows:

$$F_{max} = k_{1D}\Delta l_{max} \tag{3.37a}$$

$$F_{min} = k_{1D}\Delta l_{min} \tag{3.37b}$$

$$F_{axial} = 2\left[F_{min}\sin\left(\frac{\Delta x}{\sqrt{2}R} - \frac{\gamma}{\sqrt{2}}\right) + F_{max}\sin\left(\frac{\Delta x}{\sqrt{2}R} + \frac{\gamma}{\sqrt{2}}\right)\right] \tag{3.38}$$

$$F_{radial} = 2\sin\left(\frac{\psi}{2}\right)\left[F_{min}\cos\left(\frac{\Delta x}{\sqrt{2}R} - \frac{\gamma}{\sqrt{2}}\right) - F_{max}\cos\left(\frac{\Delta x}{\sqrt{2}R} + \frac{\gamma}{\sqrt{2}}\right)\right] \tag{3.39}$$

$$\vec{F} = \begin{pmatrix} F_x \\ F_y \\ F_z \end{pmatrix} = \begin{pmatrix} F_{axial} \\ F_{radial}\cos\psi_\gamma \\ F_{radial}\sin\psi_\gamma \end{pmatrix} \tag{3.40}$$

$$\vec{M}_b = \begin{pmatrix} 0 \\ M_{b,y} \\ M_{b,z} \end{pmatrix} = \begin{pmatrix} r_x \\ 0 \\ 0 \end{pmatrix} \times \begin{pmatrix} F_x \\ F_y \\ F_z \end{pmatrix} = \begin{pmatrix} 0 \\ -r_x F_z \\ r_x F_y \end{pmatrix} \tag{3.41}$$

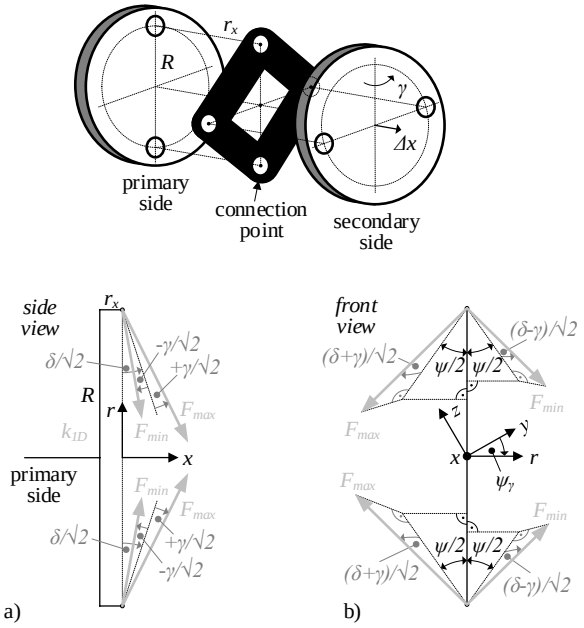

Figure 3.13 Minimal and maximal forces at spring (disc pack) connection points of primary side caused by axial (Δx) and angular (γ) displacement: a) side view b) front view seen from secondary side

To summarize, it can be seen from Eq. 3.36 to 3.39 that the hub loads (Eq. 3.40 and 3.41) at the gearbox and generator shaft end (cp. also Figure 3.1) caused by disc pack deformations can be calculated from the torsional disc pack stiffness (k_t) and by given axial (Δx) and angular (γ) displacements. It is important to note that, because of approximating the metal disc packs with 1D tension / compression springs, the calculated reaction loads are lower than the loads which occur in reality, i.e. the load calculation is non-conservative. Nevertheless, the calculated reaction loads are a proper approximation of the real loads because with the torsional stiffness the dominate disk pack stiffness is considered. It should be recalled that the metal disk packs are designed to transmit high torques (= high torsional stiffness of disc packs) and to allow simultaneously axial and angular misalignment (= low bending and twisting stiffness of disc packs).

3.2.3 Bearing load calculation

After evaluating the (hub) loads due to joint kinematics and disc pack deformation, the bearing loads are considered. To analyze the effect of axial and angular displacement on gearbox and generator shaft bearings, it is sufficient to have a closer look at one of these

shafts (cp. also Figure 3.1). As a shorter bearing spacing increases the bearing loads and the gearbox shaft is normally shorter than the generator shaft, the gearbox shaft is considered to be more critical and thus, is analyzed in this chapter. In the bearing load calculation of the gearbox shaft (cp. Figure 3.14) the following loads are taken into account: the shaft weight G_S, (radial) forces of the (spur-toothed) pinion F_P, the reaction force F_H and moment M_H at the shaft end (hub) due to the joint kinematics and metal disc pack deformation as well as the half weight G_H of the FCC (or UJS). The length l_B is the distance between bearing B1 and B2, l_P the distance between the pinion and bearing B2 and l_H the distance between bearing B2 and hub.

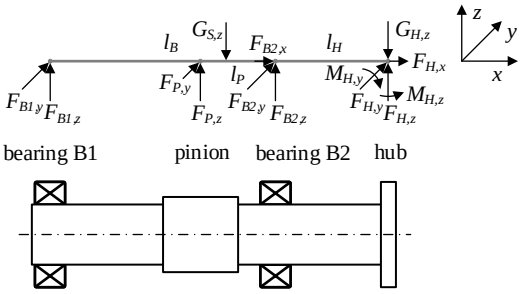

Figure 3.14 Forces and moments acting on a shaft with pinion and hub

Further, bearing loads are often calculated based on static force and moment balance considerations and can be evaluated by taking the sum of all forces and moments acting on the shaft and equating this sum to zero (force balance). So for the shaft assembly shown in Figure 3.14 the bearing forces are calculated as follows:

$$\underline{\Sigma F:}$$
$$\vec{F}_{B1} + \vec{F}_{B2} + \vec{F}_P + \vec{F}_H + \vec{G}_S + \vec{G}_H = 0 \tag{3.42}$$

$$\begin{pmatrix} 0 \\ F_{B1,y} \\ F_{B1,z} \end{pmatrix} + \begin{pmatrix} F_{B2,x} \\ F_{B2,y} \\ F_{B2,z} \end{pmatrix} + \begin{pmatrix} 0 \\ F_{P,y} \\ F_{P,z} \end{pmatrix} + \begin{pmatrix} F_{H,x} \\ F_{H,y} \\ F_{H,z} \end{pmatrix} + [m_S + m_H] \begin{pmatrix} 0 \\ 0 \\ -g \end{pmatrix} = 0 \tag{3.43}$$

and similar for the momentum balance:

$$\underline{\Sigma M:}$$
$$\vec{M}_H + \vec{l}_{B1} \times \vec{F}_{B1} + \vec{l}_{B2} \times \vec{F}_{B2} + \vec{l}_P \times \vec{F}_P + \vec{l}_S \times \vec{G}_S = 0 \tag{3.44}$$

$$\begin{pmatrix} 0 \\ M_{H,y} \\ -M_{H,z} \end{pmatrix} + \begin{pmatrix} l_B + l_H \\ 0 \\ 0 \end{pmatrix} \times \begin{pmatrix} 0 \\ F_{B1,y} \\ F_{B1,z} \end{pmatrix} + \begin{pmatrix} l_H \\ 0 \\ 0 \end{pmatrix} \times \begin{pmatrix} F_{B2,x} \\ F_{B2,y} \\ F_{B2,z} \end{pmatrix} +$$
$$+ \begin{pmatrix} l_p + l_H \\ 0 \\ 0 \end{pmatrix} \times \begin{pmatrix} 0 \\ F_{P,y} \\ F_{P,z} \end{pmatrix} + \frac{m_S}{2} \begin{pmatrix} l_B + l_H \\ 0 \\ 0 \end{pmatrix} \times \begin{pmatrix} 0 \\ 0 \\ -g \end{pmatrix} = 0 \tag{3.45}$$

Note that pinions are normally designed as small as possible, i.e. the pinion and shaft diameter are almost equal. Therefore, the pinion weight is neglected in Eq. 3.42 to 3.45 and only the shaft and hub weights are considered. By solving the system of equations in Eq. 3.43 and 3.45, the bearing forces F_{B1} and F_{B2} are obtained.

$$F_{B1,y} = \frac{1}{l_B} M_{H,z} - \frac{l_P}{l_B} F_{P,y} + \frac{l_H}{l_B} F_{H,y} \tag{3.46}$$

$$F_{B1,z} = -\frac{1}{l_B} M_{H,y} - \frac{l_P}{l_B} F_{P,z} + \frac{l_H}{l_B} F_{H,z} + g\left[\frac{m_S}{2}\left(1 - \frac{l_H}{l_B}\right) - m_H \frac{l_H}{l_B}\right] \tag{3.47}$$

$$F_{B2,x} = -F_{H,x} \tag{3.48}$$

$$F_{B2,y} = -\left[\frac{1}{l_B} M_{H,z} + \left(1 - \frac{l_P}{l_B}\right) F_{P,y} + \left(1 + \frac{l_H}{l_B}\right) F_{H,y}\right] \tag{3.49}$$

$$F_{B2,z} = \frac{1}{l_B} M_{H,y} - \left(1 - \frac{l_P}{l_B}\right) F_{P,z} - \left(1 + \frac{l_H}{l_B}\right) F_{H,z} - \\ -g\left[\frac{m_S}{2} \frac{(l_B + l_H)^2}{l_B l_H} - m_H \left(1 + \frac{l_H}{l_B}\right)\right] \tag{3.50}$$

The hub forces F_H in x-, y- and z-direction and moments M_H around y- and z-axis are caused by the joint kinematics and metal disc pack deformations due to angular and axial displacement (cp. previous sections). The pinion force can be evaluated by the transmitted torque and pinion diameter D_p (approx. shaft diameter D_S).

$$F_{P,y} = \frac{2T_1}{D_P} \tan\theta \tag{3.51}$$

$$F_{P,z} = \frac{2T_1}{D_P} \tag{3.52}$$

Therefore, the bearing loads in Eq. 3.46 to 3.50 can be derived from shaft displacement (axial Δx and angular γ), torsional metal disc pack stiffness (k_t) and transmitted torque (T_1).

In addition, the presented bearing load calculation considering the hub loads due to coupling joint kinematics and disc pack deformation will be applied to a FCC and UJS in section 3.3. To execute the calculation the hub gravity force G_{Hz} (in Figure 3.14) has to be evaluated. Due to missing detailed information of the geometry and material of FCC and UJS, the weight of FCC and UJS is estimated (in this chapter) by hollow respectively solid shafts (cylinder) as follows:

- Shaft weight with pinion, estimated by a solid cylinder

  $$m_S = \rho_{steel} V_S = \rho_{steel} \frac{\pi}{4} D_S^2 (l_B + l_H) \tag{3.53}$$

- Hub weight due to half flexible coupling weight (cp. also FCC shown in Figure 3.2 and [14]):

$$m_{H,FCC} = \rho_{steel} V_{FCC,1} + \rho_{GFRP} V_{FCC,2} \tag{3.54}$$

with the metal hub volume $V_{FCC,1}$ ($D_{out,1} = 2.5D_S$, $D_{in,1} = D_S$) and Glass Fiber Reinforced Polymer (GFRP) tube volume $V_{FCC,2}$ ($D_{out,2} = 2.5D_S$, $D_{in,2} = 1.5D_S$), estimated by hollow cylinders:

$$V_{FCC,1} = \frac{\pi}{8}\left(D_{out,1}^2 - D_{in,1}^2\right)(L_T - L_{GFRP}) \tag{3.54a}$$
$$V_{FCC,2} = \frac{\pi}{8}\left(D_{out,2}^2 - D_{in,2}^2\right)L_{GFRP} \tag{3.54b}$$

- Hub weight due to half universal joint shaft weight, estimated by solid cylinder ($D_{UJS} = 1.25D_S$):

$$m_{H,UJS} = \rho_{steel} V_{UJS} = \rho_{steel} \frac{\pi}{4} D_{UJS}^2 L_T \tag{3.55}$$

Note that inner (D_{in}) and outer (D_{out}) metal hub and GFRP tube diameters in Eq. 3.54a and 3.54b are randomly chosen. As the universal joint shaft is, due to its design, equivalent to the combination of a solid and hollow shaft, its outer diameter (D_{UJS}) can be estimated by the assumption that the polar section modulus of the solid and hollow shaft is equal. Further, the main purpose of the hub weight estimation is the consideration of the different weights of flexible coupling and universal joint shaft in the bearing load calculation because flexible couplings tend to be lighter than universal joint shafts. For this purpose a rough weight estimation shall be sufficient here.

Finally, the bearing life time calculation requires the evaluation of an equivalent bearing load. The equivalent bearing load P is defined with the radial (F_r) and axial (F_a) bearing forces using ISO 281 as follows:

$$P = F_r \qquad \text{for } F_a/F_r \leq e \tag{3.56}$$

$$P = XF_r + YF_a \qquad \text{for } F_a/F_r > e \tag{3.57}$$

Depending on the ratio e of the axial and radial (bearing) force, Eq. 3.56 or 3.57 applies. Values for the constants e , X and Y depend on bearing type and size and are provided by ISO 281 or bearing manufacturers.

3.2.4 Displacement Estimation

For the bearing load calculation the displacement between gearbox and generator shaft is needed (cp. also Figure 3.3). As the actual displacement is difficult to measure during operation, it can be estimated from installation and vibration data. During the installation of the FCC technicians align the gearbox and generator shafts within a certain tolerance, i.e. typically, within an axial displacement of approx. $\pm 1mm$ and an angular displacement of approx. $\pm 0.1°$ depending on the gearbox and generator size (cp. also [18]). Then, during operation additional displacements occur due to the reaction loads of gearbox and generator and their base frame stiffness. The reaction loads can be split in static and dynamic loads. Static reaction loads cause static displacements (a constant offset) and static base frame

deformations which, again, are difficult to measure. But, dynamic reaction loads generate dynamic displacements which can be observed as vibrations and thus, can be evaluated.

The ISO 10816 provides recommendations for the allowed vibrations severity. For large soft foundations, which are the case for a wind turbine, the ISO 10816 considers vibration velocities v_{vib} until *5m/s* (zero to peak) as good. If, in addition, the dominant shaft speed ω_S is known, then a rough estimation of the dynamic displacement Δs_{dyn} during operation is given by the following relation:

$$\Delta s_{dyn} = \frac{v_{vib}}{\omega_S} = \frac{v_{vib}[m/s]}{2\pi\, n_S[1/s]} \tag{3.58}$$

Note that Eq. 3.58 represents the amplitude of the dynamic displacement. It is calculated by the time integration of the vibration velocity $v(t) = v_{vib} \cdot cos(\omega_S t)$. This means the dynamic displacement is $s(t) = \Delta s_{dyn} \cdot sin(\omega_S t)$. In the case of the wind turbine, the dominant shaft speed seen at the gearbox housing is determined by the main shaft speed which is approx. *3-15 rpm*. For a main shaft speed of approx. *9.5 rpm* a vibration velocity of *5m/s* is equivalent to a dynamic displacement of *5mm*. By applying this consideration to the axial and angular displacement of gearbox and generator in the wind turbine, the displacement during operation can be estimated (cp. also Figure 3.1). For a moderate consideration, it is assumed in this chapter that the vibration velocities v_{vib} = *5m/s* is a peak to peak value. This lead to the following displacements:

- By assuming a lower axial (approx. *1m/s* to *3m/s*) than radial (*5m/s*) vibration level, the axial displacement during operation is approximately *1-3mm* (peak to peak). So together with the displacement during installation, a total axial displacement of the flexible connecting coupling is approx. *2-4mm*, i.e. *1-2mm* per FCC joint.

- By assuming a distance of approx. *1m* between gearbox and generator shaft (hub) (cp. also Figure 3.1) and a radial vibration velocity of *5m/s* (peak to peak), the angular displacement during operation is approx. $\gamma_{dyn} = tan(0.025) \approx 0.3°$. Together with the angular displacement during installation the total angular displacement is approx. *0.4°*.

In comparison, measurements at the wind turbine gearbox provided by [19] show a dynamic radial displacement of approx. *2.5mm* and a dynamic axial displacement of approx. *0.5mm*. Therefore, the here estimated axial (*1-2mm*) and angular (*0.4°*) displacements during operation are realistic assuming that they include the static and dynamic displacement during operation as well as the displacement during installation.

If instead of the FCC a UJS is used, an additional displacement offset will be taken into account because the UJS has to operate at an angular displacement higher than *2°* [16]. This means that the UJS will be installed with a displacement angle of approx. *2.5°*.

3.3 Performance of flexible connecting couplings

In this section the previously proposed expressions for the hub and bearing loads as well as estimations of the axial and angular shaft misalignment (displacement) are applied to a specific shaft assembly (Figure 3.14) using either a FCC or an UJS. Table 3.2 shows the parameters which are used to compute the hub and bearing loads.

Table 3.2 Values used for bearing load calculation of shaft assembly

dimension	value	unit	comment / assumption
$r_{HB} = l_H / l_B$	0.8	-	length ratio hub side
$r_{PB} = l_P / l_B$	0.3	-	length ratio pinion side
$r_{DB} = D_S / l_B$	0.35	-	Diameter to length ratio
$D_P \approx D_S \approx D_{pitch}$	120	[mm]	pinion and pitch equal to shaft diameter & uniform shaft diameter (no shaft shoulders)
L_T	1450	[mm]	total mounting length [14]
L_{GFRP}	950	[mm]	GFRP tube length [14]
R_{FCC}	228	[mm]	metal disc pack radius of FCC [14]
r_x	20	[mm]	estimated disc pack hub plane distance
T_N	21000	[Nm]	nominal transmitted torque [14]
k_t	$15*10^6$	[Nm/rad]	torsional metal disc pack stiffness, recommended by [14]
μ_f	0.12	-	friction coefficient for steel on steel lubricated [17]
θ	20	[°]	spur gear meshing angle (pinion)
ρ_{steel}	$7.8*10^3$	[kg/m³]	steel density
ρ_{GFRP}	$1.2*10^3$	[kg/m³]	Glass Fiber Reinforced Polymer density [20]

3.3.1 Hub loads calculation

At first, the hub loads are considered, i.e. the forces that the joints exert onto the shaft hub(s). This is done for 50% nominal torque, an axial displacement of $\Delta x = 1mm$ per FCC joint and an angular displacement angle $\beta = 0$. The FCC is aligned at $\alpha_{FCC} = 0°$ and the UJS at $\alpha_{UJS} = 2.5°$. For both FCC and UJS a dynamic displacement angle of $\pm 0.4°$ is considered. Further, the hub loads include the effects of joint kinematics (FCC and UJS), metal disc pack deformation (FCC), length compensation (UJS) and weights (FCC and UJS).

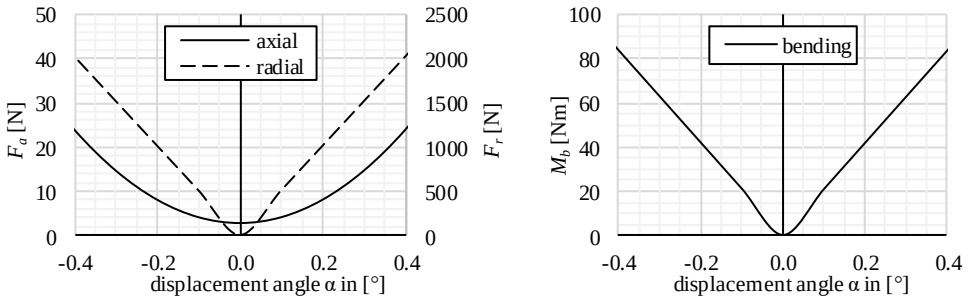

Figure 3.15 FCC hub forces (left) and bending moment (right) for a range of misalignment angles

Figure 3.15 shows the hub loads of the FCC and Figure 3.16 the hub loads of the UJS over the displacement angle α, i.e. the gearbox-generator misalignment angle in the horizontal plane. It is visible that the dominant hub load of the FCC is the radial force ($F_a / F_r \approx 0.01$ to 0.02) while the dominant hub load of the UJS is the axial force ($F_a / F_r \approx 20$ to 30). The radial force of the FCC increases significantly with the displacement angle α. This increase is mainly caused by load asymmetry at the connection points (cp also Figure 3.13) and thus, by the loads due to disc pack deformation. In contrast, the axial force of the UJS remains almost

constant over the displacement angle α. Further, this axial force can be decreased by changing the friction coefficient μ_f in Eq. 3.29. Using an UJS with a PTFE (Teflon) coating (cp. also Figure 3.16) leads to a reduction of the friction coefficient and thus, to a decrease of axial and radial hub forces by a factor of three ($\mu_{f,PTFE} = 0.04$ [16]). The friction factor can further be reduced from sliding to rolling friction by installing a tripod UJS [16].

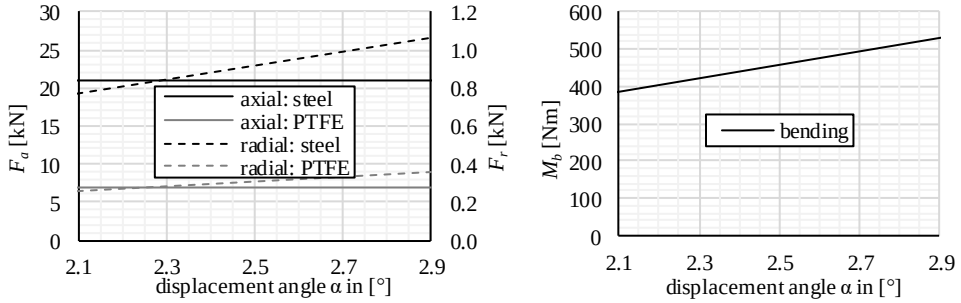

Figure 3.16 UJS hub forces (left) and bending moment (right) for a range of misalignment angles and an uncoated (steel) vs. a PTFE coated UJS

3.3.2 Bearing life time calculation

The bearing loads are calculated for the shaft assembly in Figure 3.14 using either a FCC or an UJS. Due to the high pinion loads the radial force on the bearing is much larger than the axial force. Hence, Eq. 3.56 should be used, even for the UJS. To compare the bearing loads, i.e. the performance of the shaft assembly with a FCC and an UJS, a relative life time factor is applied in this chapter. As the (roller) bearing life time L_{10} is proportional with the power 10/3 of the inverse value of the equivalent bearing load P (ISO 281), the relative life time factor f_{rel} is defined as follows:

$$L_{10} \sim \left(\frac{1}{P}\right)^{10/3} \tag{3.59}$$

$$L_{10,FCC} = f_{rel,FCC} L_{10,ref} \tag{3.60a}$$
$$L_{10,UJS} = f_{rel,UJS} L_{10,ref} \tag{3.60b}$$

$$f_{rel,FCC} = \left(\frac{P_{ref}}{P_{FCC}}\right)^{10/3} \tag{3.61a}$$
$$f_{rel,UJS} = \left(\frac{P_{ref}}{P_{UJS}}\right)^{10/3} \tag{3.61b}$$

The relative life time factors compare the equivalent bearing loads P_{FCC} and P_{UJS} with a reference load P_{ref}. The reference load P_{ref} is equal to the ideal FCC case where no misalignment occurs, i.e.:

$$P_{ref} = P_{FCC}(\alpha = 0, \beta = 0, \Delta x = 0) \tag{3.62}$$

This means that the reference load P_{ref} only considers pinion loads and the weights of shaft and FCC (cp. also section 3.2.3). Note also that a relative life time factor greater than one ($f_{rel} > 1$) means that a bearing life time for the FCC case ($L_{10,FCC}$) respectively UJS case ($L_{10,UJS}$) exceeds the life time of the reference case ($L_{10,ref}$), and vice versa. Next, the relative life time factor $f_{rel,FCC}$ will be presented for four different scenarios. Thereafter, the relative life time factor $f_{rel,UJS}$ is discussed.

First, the effect of angular displacement is studied by evaluating the relative life time factor at 50% nominal torque for an axial displacement of $\Delta x = 1mm$ per FCC joint (cp. Figure 3.1). It can be seen in Figure 3.17 that an increase of the displacement angles α and β of the flexible coupling increases respectively decreases the relative life time factor depending on the sign of the displacement angle α and β. Note that Figure 3.17 shows this only for the more critical bearing B2 and that the relative life time factor of bearing B1 behaves opposed to the one of bearing B2 (cp. also later Figure 3.19 and 3.20). This, however, means that angular displacements cause a variation of the bearing life time (B1 and B2). Depending on the magnitude and sign of the displacement angle α and β the life time can vary several percent.

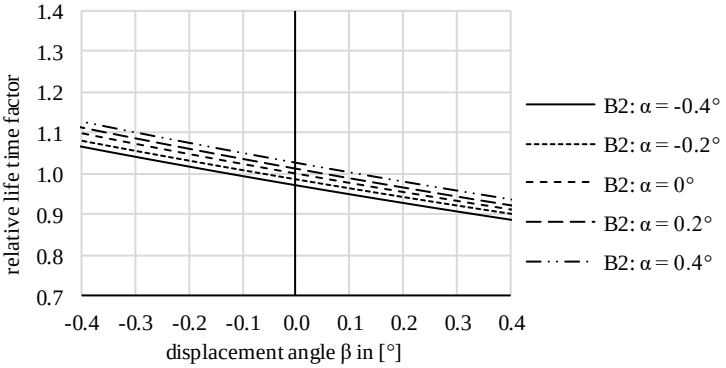

Figure 3.17 Bearing relative life time factor as a function of displacement angles α and β and at $\Delta x = 1mm$ for an FCC

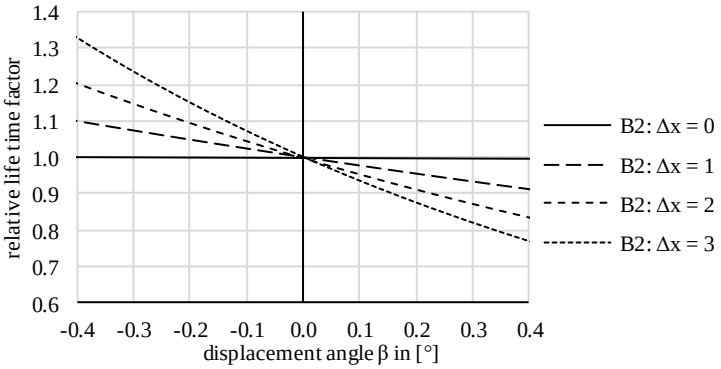

Figure 3.18 Bearing relative life time factor depending on axial displacement Δx [mm] and displacement angle β for displacement angle $\alpha = 0$ for an FCC

Second, the influence of an axial displacement is checked by calculating the relative life time factor at 50% nominal torque for an angular displacement $\alpha = 0°$ (cp. Figure 3.18). It is shown (for the bearing B2) that depending on the axial displacement Δx (per joint) of the FCC the relative life time factor increases respectively decreases several tens of percent. This means that the life time of one bearing increases significantly with an increasing axial displacement Δx, while the life time of the other bearing decreases. That is because the relative life time factor of bearing B1 and B2 behave opposed to each other (see later Figure 3.19 and 3.20). Further, the combination of axial and angular displacement causes significant reaction loads at the shaft end (hub loads) and bearing loads. This can be seen from Figure 3.18 by comparing line *B2:* $\Delta x = 0$ and *B2:* $\Delta x = 3$ plotted over the displacement angle β.

Third, the relative life time factor is evaluated at 50% nominal torque for an angular displacement $\alpha = 0°$ and an axial displacement $\Delta x = 1mm$. The effect of the disc pack stiffness is investigated for different displacement angles β (cp. Figure 3.19). By changing the torsional stiffness k_t of the metal disc pack with a factor two, it can be seen that the relative life time factor increases and decreases again several percent. This means that a high torsional stiffness of the metal disc pack, which is required to transmit high torques and to avoid torsional vibration, has drawbacks for the bearing loads and their life time.

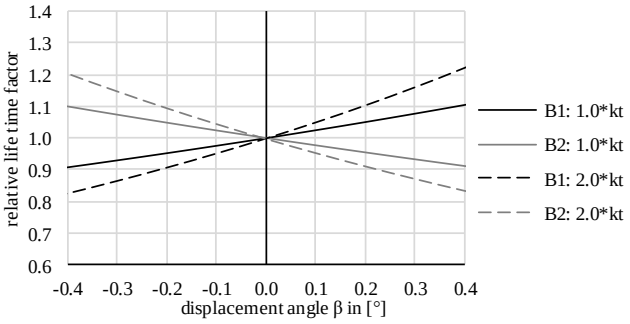

Figure 3.19 Bearing relative life time factor depending on torsional stiffness k_t of the metal disc pack for an FCC

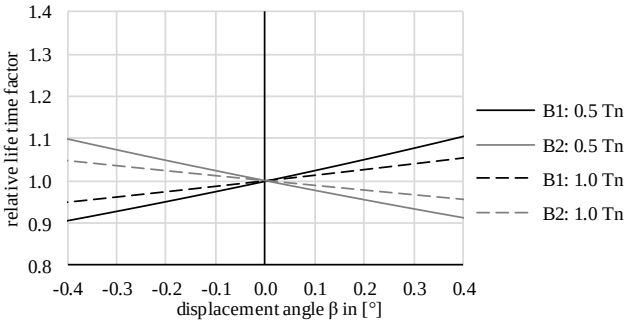

Figure 3.20 Bearing relative life time factor depending on nominal transmitted torque T_n for an FCC

Fourth, the relative life time factor is calculated at 50% and 100% nominal torque for an angular displacement $\alpha = 0°$ and an axial displacement $\Delta x = 1mm$ (cp. Figure 3.20). Increasing

the nominal torque means that the reference load increases, too. Consequently, the relative life time factor decreases because the hub loads due to disc pack deformation (cp. section 3.2.2) are torque independent. Nevertheless, it can be seen from Figure 3.20 that the hub loads due to disc pack deformation are still notable at nominal torque.

Now, the relative life time factor for an UJS ($f_{rel,UJS}$) is considered. It is evaluated for the displacement angle range $\alpha_{UJS} = 2.5° \pm 0.4°$. By executing the hub and bearing load calculation (cp. section 3.2) with 50% nominal torque, it can be seen that bearing loads vary less than ±1% within this displacement angle range. This is because of the almost constant hub loads of the UJS (cp. Figure 3.16). It also means that the bearing loads of the gearbox shaft with a UJS are independent from small dynamic angular displacements during operation and depend only on the transmitted torque (cp. section 3.2.1). Then, the relative life time factor is calculated at a displacement angle $\alpha_{UJS} = 2.5°$ and at 50% nominal torque. It is:

$$f_{rel,UJS} \approx 0.99 \tag{3.63}$$

It can be seen that the UJS provides an almost constant relative life time factor $f_{rel,UJS}$ whose value is close to one. This means that the UJS performs similar to an FCC at ideal operation conditions, where neither axial ($\Delta x = 0$) nor angular ($\alpha = 0, \beta = 0$) misalignments occur.

3.4 Discussion

By considering the relative life time factor, it can be seen that using a FCC causes a large variation of HSS bearing loads while using a UJS provides almost constant bearing loads. The reaction loads of the FCC are dominated by the metal disc pack deformation, i.e. they are mainly influenced by the axial and angular displacement between gearbox and generator HSS. The reaction loads of the UJS, however, depend mainly on the transmitted torque, i.e. the influence of small displacements during operation can be neglected. Due to the high variation of the HSS bearing loads, the bearing life time varies, too. This means that bearing life time predictions are difficult and that the bearings fail rather randomly which leads to unplanned downtimes. In contrary, constant and torque dependent bearing loads allow a more accurate bearing life time prediction which may result in planned instead of unplanned downtimes.

Furthermore, for typical combinations of axial and angular displacements during operation, i.e. *1-2mm* axial displacement per FCC joint and approx. *0.3°* to *0.4°* angular displacement (cp. also section 3.2.4), the FCC causes relative life time factors of approx. 0.75. It can be expected that even lower relative life time factors occur because FCC suppliers allow higher displacements than considered in this chapter. In the case of the FCC shown in Figure 3.2, the maximal permissible displacements, given by the supplier, are *5mm* axial (per joint) and *1.0°* angular [14]. Suppliers also state that the flexible connecting coupling should not operate simultaneously at the maximal permissible axial and angular displacement. So assuming that the flexible connecting coupling operates around the half of the permissible displacements, i.e. *2-3mm* axial (per joint) and approx. *0.5°* angular, which is likely after section 3.2.4, relative life time factors of approx. 0.6-0.7 can still occur. In other words, the usage of the FCC can reduce the gearbox bearing life time to approx. 60-70% of the designed life time.

Moreover, it can be seen (from Figure 3.17) that the displacement angle β has a larger effect on the relative life time factor than the displacement angle α. The reason for this effect is the

direction of the reaction force due to metal disc pack deformations. The reaction force due to the displacement angle β is parallel to the main reaction force of the pinion while the reaction force due to the displacement angle α is perpendicular (cp. section 3.2.2 and 3.2.3). Consequently, the reaction force due to the displacement angle β has a larger influence on the bearing loads than the reaction force due to the displacement angle α. In a wind turbine, the displacement angle α and β are caused by main shaft or base frame bending. However, as the wind turbine gearbox is fixed in rubber bushes, the displacement angle β is also generated by the deformation of the rubber bushes due to the gearbox counter torque. The counter torque is equal to the ring gear torque of the planetary gears used in wind turbine gearboxes at the first (and second) gear step. This means that the magnitude of the counter torque is similar to the magnitude of the wind turbine rotor torque depending on the stationary gear ratio of the planetary gear(s). Consequently, significant (static and dynamic) displacement angles β can occur during operation depending on the rubber bushes stiffness, i.e. operation at a displacement angle β around $\pm 0.4°$ seems likely.

In addition to improving wind turbine designs, the calculation method for hub (coupling joint) and bearing loads proposed in this chapter can also be used to predict the remaining useful life time of gearbox (and generator) bearings. The transmitted torque can be derived from SCADA data, i.e. from the speed of the gearbox high speed shaft and transmitted power. The axial and angular misalignment is estimated i) with the alignment protocol filled in by technician during installation and ii) with the dimensions of the FCC, the speed of the main shaft (from SCADA) and gearbox vibration data measured by the condition monitoring (CM) system (cp. also section 3.2.4). Then, the hub and bearing loads are determined with the torsional disc pack stiffness (available in data sheets) and the high speed shaft (HSS) dimensions (cp. section 3.2.1 to 3.2.3). Based on these loads and the bearing type (load capacity) the bearing life time can be calculated using ISO 281 and therefore also the remaining useful life time. This process is shown schematically in Figure 3.21.

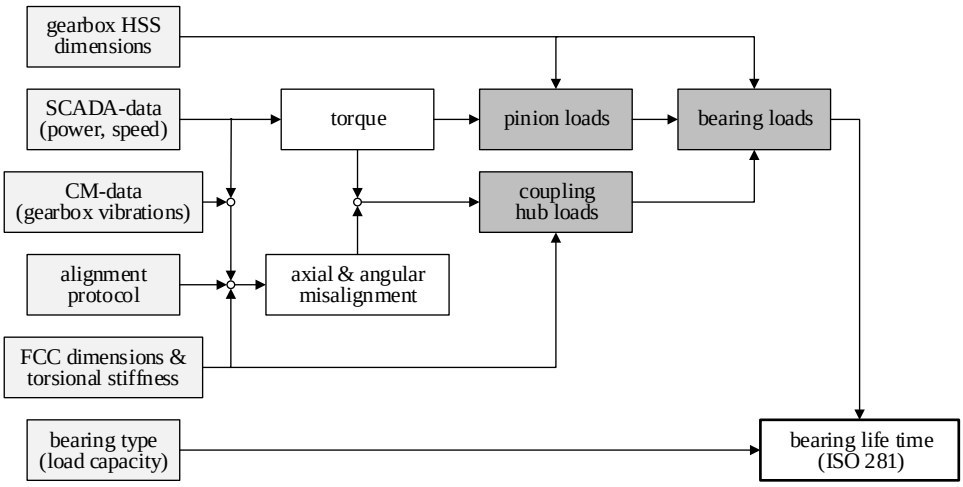

Figure 3.21 Prediction of remaining useful bearing life time based on SCADA, CM-data and component dimensions

Finally, as at present no explicit equations to calculate the coupling hub loads were available, the bearing loads could not be calculated accurately. This has led to big deviations between predicted / expected (during design) wind turbine gearbox life times and the actual (much shorter) life times observed in the field. The method proposed in this work enables a quick and accurate calculation of these hub loads, leading to much more accurate gearbox bearing life times.

3.5 Conclusion

The present chapter provides a calculation method to evaluate the bearing load increase (life time reduction) caused by shaft connecting couplings and the axial and angular misalignment of gearbox and generator high speed shafts (HSS). The method takes into account the reaction loads of the coupling joints due to both kinematics (UJS and FCC) and metal disc pack deformations (FCC). The metal disc packs are modeled as 1D tension / compression springs whose stiffness is obtained from the torsional stiffness of the metal disc pack (given in data sheets). The shaft misalignment is estimated based on HSS alignment during installation and on vibration data during operation. The load calculations are shown to be part of the remaining useful life prediction of gearbox (and generator) HSS bearings considering SCADA, condition monitoring data as well as HSS component dimensions.

To demonstrate the proposed approach, the load calculations are applied to a specific flexible connecting coupling (FCC) and universal joint shaft (UJS). By comparing their performance it is shown that the usage of FCCs can significantly increase the bearing loads of gearbox and generator HSS in wind turbine drive trains. The bearings can fail at 60-70% of the design life time because high bearing load fluctuations occur, caused by the displacement during operation. Further, it is demonstrated that the reaction loads of FCCs are dominated by metal disc pack deformations, i.e. they are dependent on small displacements during operation. In contrast, the reaction loads of UJS are governed by the transmitted torque and independent of small displacements during operation. This means that (in the case of the UJS) the gearbox and generator bearing loads are not affected by small shaft displacements during operation. Finally, it is discussed that the usage of an UJS i) allows a more accurate prediction of bearing life time because the loads of UJS are torque dependent and displacement independent and therefore, ii) avoids costly, unplanned gearbox and generator failures as well as downtimes.

References

[1] J. Ribrant, “Reliability performance and maintenance - A survey of failures in wind power systems,” 2006.

[2] J. Ribrant and L. M. Bertling, “Survey of Failures in Wind Power Systems With Focus on Swedish Wind Power Plants During 1997-2005,” *IEEE Trans. Energy Convers.*, vol. 22, no. 1, pp. 167–173, 2007.

[3] Noordzee Wind CV, “Operations Report 2008,” 2009.

[4] Noordzee Wind CV, “Operations Report 2009,” 2010.

[5] M. Wilkinson *et al.*, “Methodology and results of the reliawind reliability field study,” 2010.

[6] Tavner, *Offshore Wind Turbines: Reliability, availability and maintenance*. 2013.

[7] D. Infield, N. Barltrop, J. Coultate, K. Scott, and A. Shahaj, “Effects of Extreme and Transient Loads on Wind Turbine Drive Trains,” pp. 1–24, 2014.

[8] K. Alewine and W. Chen, “A review of electrical winding failures in wind turbine generators,” *IEEE Electr. Insul. Mag.*, vol. 28, no. 4, pp. 8–13, 2012.

[9] J. Peeters, D. Vandepitte, and P. Sas, “Flexible multibody model of a three-stage planetary gearbox in a wind turbine,” *Isma*, pp. 3923–3942, 2004.

[10] J. Peeters, “Simulation of dynamic drive train loads in a wind turbine,” 2006.

[11] J. Peeters, D. Vandepitte, and P. Sas, “Structural analysis of a wind turbine and its drive train using the flexible multibody simulation technique,” 2006.

[12] J. Wang, D. Qin, and Y. Ding, “Dynamic Behavior of Wind Turbine by a Mixed Flexible-Rigid Multi-Body Model,” *J. Syst. Des. Dyn.*, vol. 3, pp. 403–419, 2009.

[13] D. P. Rommel, D. Di Maio, and T. Tinga, “Calculating wind turbine component loads for improved life prediction,” *Renew. Energy*, vol. 146, 2020.

[14] J. H. Kang, J. Bae, H. On, and H. W. Lee, “The design of a flexible wind turbine coupling structure considering torsional vibration,” *Int. J. Appl. Eng. Res.*, vol. 11, no. 16, pp. 9093–9098, 2016.

[15] D. Thoma, “Das Kräftespiel im Kreuzgelenk,” *Schweizerische Bauzeitung*, 1920.

[16] Voith, “High-Performance Universal Joint Shaft,” 2015. [Online]. Available: https://www.masino.fi/wp-content/uploads/2013/06/Voith_Nivelakselit.pdf. [Accessed: 09-Apr-2019].

[17] Elbe-Group, “Cardan Drive-Shafts,” 2014. [Online]. Available: https://www.elbe-group.de/fileadmin/user_upload/images/produkte/ELBE_Programm_D.pdf. [Accessed: 09-Apr-2019].

[18] PRUFTECHNIK, “A Practical Guid to Shaft Alignment,” 2002. [Online]. Available: https://www.plantservices.com/assets/knowledge_centers/ludeca/assets/A_Practical_Guide_to_Shaft_Alignment.pdf. [Accessed: 09-Apr-2019].

[19] A. Heege, J. Hemmelmann, L. Bastard, J. L. Sanchez, L. Lens, and M. Omiciuolo, *Matching experimental and numerical data of dynamic wind turbine loads by modelling of defects*, vol. 3. 2009.

[20] P. Ephraim M. E., Adetiloye A.Harcourt, “Mechanical Properties of Glass Fibre Reinforced Polymer Based on Resin from Recycled Plastic.,” *Int. J. Sci. Eng. Res.*, vol. 6, no. 3, pp. 145–152, 2015.

CHAPTER 4

Transformer Hot Spot Temperature Prediction based on basic Operator Information

ABSTRACT

A power transformer is an important component in power trains and electrical distribution networks. Predicting its life time, which is determined by the winding temperature, is desirable, especially, if a zero downtime policy is applied. However, component owners and users often have to deal with a lack of information and cannot always use the established methods for life time prediction. Therefore, the present chapter provides an alternative way to calculate the hot spot temperature and thus, the life time of power transformers based on limited information, i.e. transformer rating information and rms current and voltage measurements (including phase angles). The transformer hot spot temperature is derived from the transformer losses and a virtual twin. Therefore, the chapter provides methods i) to evaluate the separate transformer losses, i.e. core, winding and stray losses, ii) to create a simple virtual transformer twin and iii) to calculate the temperature distribution in the transformer windings and thus, the hot spot temperature. The methods are applied to one phase of a 154kV, 15MVA power transformer. It is shown that the calculated losses and hot spot temperature matches with winding measurements available in literature.

This chapter is based on: Rommel, D. P., Di Maio, D., Tinga, T. (n.d.). Transformer Hot Spot Temperature Prediction based on basic Operator Information. revision submitted

Nomenclature

SYMBOL	UNIT	QUANTITY
A	[m²]	area, cross section
b	[m]	core dimension
B	[T]	magnetic field
C_1, C_2	-	integration constants
ed	-	eddy current
E	[J]	energy
F_{AA}	-	ageing acceleration factor
h	[m]	core dimension
H	[A/m]	magnetic field strength
$hyst$	-	hysteresis
i	[A]	current
k	[W/mK]	thermal conductivity
k_f	-	fill factor
K	-	correction factor
L	[WΩ/K²]	Lorenz number, life time
l	[m]	length
mag	-	magnetization
N	-	number of turns
n	-	turn ratio
p	-	primary side
p,m	-	primary side measured
P	[W]	power
Q	[W]	heat flow
q_V	[W/m³]	specific heat flow
R, r	[m]	radius
R	[Ω]	resistance, resistance
s	-	secondary side
th	-	theta (Θ)
T	[K]	temperature
u	[V]	voltage
V	[m³]	volume
w	-	winding
X	[Ω]	reactance
Z	[Ω]	impedance
θ	[°C]	temperature
Θ, Θ^+	[A]	magnetomotive force
κ	[S/m]	electrical conductivity
μ	[H/m]	permeability
ρ	[Ωmm²/m]	specific resistance
ρ	[kg/m³]	density
σ	-	stray (field)
φ	[rad]	phase angle
Φ	[Wb]	magnetic flux
Φ_σ	[Wb]	flux leakage
χ	[rad]	angle in triangle
Ψ	[Wb]	flux linkage
ψ	[rad]	angle in triangle
ω	[1/s]	angular frequency

4.1 Introduction

Surveys of failures in wind turbine systems evaluated during the last decades have shown that power transformers have non-negligible failures rates and downtimes [1]. Although these failure rates and downtimes are relatively low in comparison to other power train components, the recent trend to a zero downtime policy also requires the consideration of the power transformer. To achieve maintenance with zero or, at least, close to zero downtime maintenance prediction becomes important. This means that end customers (transformer owners and operators) or consultancy companies seek for methods to evaluate the remaining useful life time based on actual operating conditions (see e.g. [2] and [3] for a similar approach for bearings). However, these two stakeholders normally deal with the problem that only limited information about the component and actual operating conditions are available to them. Therefore, methods are needed that can predict the remaining useful life time of components based on limited information, for example, based on component ratings information and simple measurements only.
To predict the transformer life time models provided by IEEE Std C57.91 [4], IEEE Std C57.100 [5] and IEC 60354 [6] are used [7]. Alternative and improved models are proposed by [8]–[11]. These models calculate the insulation's aging rate as a function of its temperature [7], since the temperature is the basic factor affecting the thermal loss of life [7]. This means that the highest temperature (also called hot spot temperature) to which the insulation is exposed is used to predict the transformer life time. The relation of insulation deterioration to changes in time and temperature is specified by the ageing acceleration factor F_{AA} [7]:

$$F_{AA} = e^{\left[\frac{15000}{\theta_{HS,ref}+273} - \frac{15000}{\theta_{HS}+273}\right]} \tag{4.1}$$

where $\theta_{HS,ref}$ is a hot spot temperature of $110°C$.

The actual transformer life time (L) is then obtained by dividing the normal insulation life L_n (at $110°C$) by F_{AA}:

$$L = \frac{L_n}{F_{AA}} \tag{4.2}$$

Alternatively, following [7], the Loss of Life (LoL) in a certain period of operation time (t_{op}) yields the fraction of the normal insulation life that is consumed in t_{op}. This allows to calculate the remaining useful life of the transformer for scenarios in which the hot spot temperature is not constant over time.

$$LoL = \frac{F_{AA}\, t_{op}}{L_n} \tag{4.3}$$

Hence, to quantify the life time, the hot spot temperature θ_{HS} (°C) in the transformer windings must be calculated. It can be estimated from (oil) temperature measurements using IEEE / IEC loading guides [4]–[6] as follows:

$$\theta_{HS} = \theta_{TO} + K \cdot \Delta\theta_{HR} \left(\frac{I}{I_R}\right)^{2m} \tag{4.4}$$

where θ_{TO} (°C) is the oil temperature measured at the top of the transformer and $\Delta\theta_{HR}$ (°C) is the temperature difference between the hot spot and the top oil temperature as measured during a heat run test at the rated power. The winding exponent m is an empirical parameter recommended by the IEEE / IEC loading guide. Then, based on these measurements, the actual load current I and the rated current I_R, the hot spot temperature is interpolated (cp. [12][13]). In addition to the interpolation, a correction factor K is used which depends on the transformer design [13]. A modified approach is proposed by [8] and [14] taking into account heat convection respectively environmental variables. However, calculating the hot spot temperature according to IEEE / IEC loading guides always requires information about the correction factor (transformer design) and measured temperature drops (e.g. from winding to oil) for rated load conditions. An end customer or consultancy company may not have access to this kind of information, which means that they cannot apply this method to evaluate the transformer hot spot temperature and remaining life. Furthermore, the winding exponent is an empirical factor and the design dependent correction factor value given in the standard underestimates the actual winding temperature measurements [15].

Further, the transformer temperature depends on the actual losses generated in the transformer. This means that for determining the winding temperature the separate transformer core and winding losses are needed. The transformer losses can be estimated by the standard IEEE C.57.120 [16]. However, to evaluate the actual winding temperature the actual losses are needed, i.e. the losses must be evaluated based on measurements. Arri *et al.* [17] provide an online loss measurement of transformers requiring an extensive measurement effort. An improved real time monitoring method of the transformer losses is developed by Lin and Fuchs [18] distinguishing between iron core and copper losses. They combine eddy current and hysteresis losses to quantify the iron core losses and use ohmic winding and stray losses to determine the copper losses. However, a further separation between ohmic winding and stray losses is necessary because the stray losses occur in different transformer parts [19] and thus, have only minor effect on the winding temperature. The temperature is therefore mainly affected by ohmic winding losses.

It seems that scientific literature i) evaluating separately transformer core, stray and ohmic winding losses based on voltage and current measurements and ii) calculating the winding hot spot temperature based on these transformer losses, i.e. without design dependent correction factors and measured temperature drops is very limited. Simple online monitoring methods for specifying the different transformer losses and for estimating the winding hot spot temperature based on the actual losses could not be found at all. Therefore, the main objective of this chapter is to propose methods to evaluate i) the actual separate transformer losses, i.e. core, stray and ohmic winding losses and ii) the actual winding hot spot temperature. The proposed methods use measured oil temperature and measured (input and output) rms voltage and current, including their phase angles, as this information is readily available, also to owners and service providers. Further, a simple virtual twin of the transformer is utilized to estimate the temperature distribution in the transformer windings and thus, to determine the winding hot spot temperature. The virtual twin is created based on only transformer ratings information which is typically available on the transformer nameplate and therefore available for any operator. Figure 4.1 provides an overview of the transformer loss and winding hot spot temperature calculation. In section 4.2 the calculation of the losses and the estimation of the transformer dimension for the simple virtual twin are discussed. Then, the winding temperature distribution is determined in section 4.3. Finally, in section 4.4 the loss and temperature calculations are applied to a case study and validated

with measurements available in literature as well as with the hot spot temperature evaluated by the IEEE / IEC loading guides.

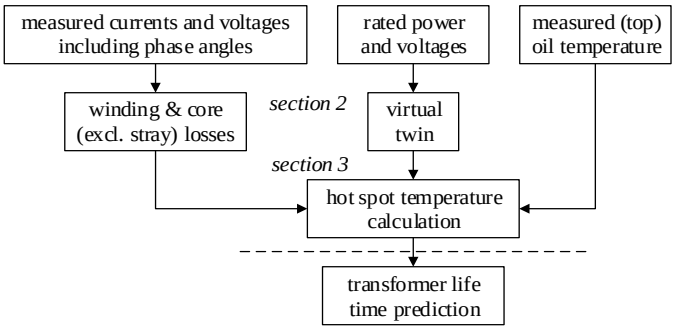

Figure 4.1 Hot spot temperature calculation procedure

4.2 Evaluation of transformer losses and creation of the virtual twin

In this section, the calculations of the different transformer losses, i.e. ohmic winding, core and stray losses, are derived and discussed in details. To simplify the calculations one transformer phase is considered. A general transformer model including losses is analyzed in section 4.2.1. The calculation of ohmic resistances as well as the core hysteresis needed for the loss calculation are discussed in section 4.2.2. Then, the calculation procedure to evaluate the transformer losses is explained in section 4.2.3. Finally, the creation of the virtual transformer twin, i.e. the estimation of the transformer dimensions, is presented in section 4.2.4.

4.2.1 Transformer model

First, to simplify the theoretical considerations and calculations the common transformer phase where the primary (high voltage) winding is placed around the secondary (lower voltage) winding (cp. Figure 4.2a) is approximated by a simple transformer with separate windings around the two sides of the transformer core (cp. Figure 4.2b).

Then, to evaluate ohmic winding, core and stray losses, the simple transformer is considered as a real transformer. This means that the transformer shown in Figure 4.2b must include the following characteristics of a real transformer [20]:

- The permeability of the magnetic circuit is not infinite, i.e. $\mu_{Fe} \neq \infty$ and is also a function of the magnetic field strength H, i.e. $\mu_{Fe} = f(H)$. This means that the relation between the magnetic field B and magnetic field strength H is not linear anymore, i.e. a hysteresis and thus core losses occur as will be discussed in more detail in section 4.2.2. Further, considering the eddy current i_{ed} induced in an iron core (cp. Figure 4.2b), the magnetomotive force Θ is given with the core length element ds and total core length l as follows [20]:

$$\Theta = \oint H\, ds = Hl = i_p N_p + i_s N_s + i_{ed} \neq 0 \tag{4.5}$$

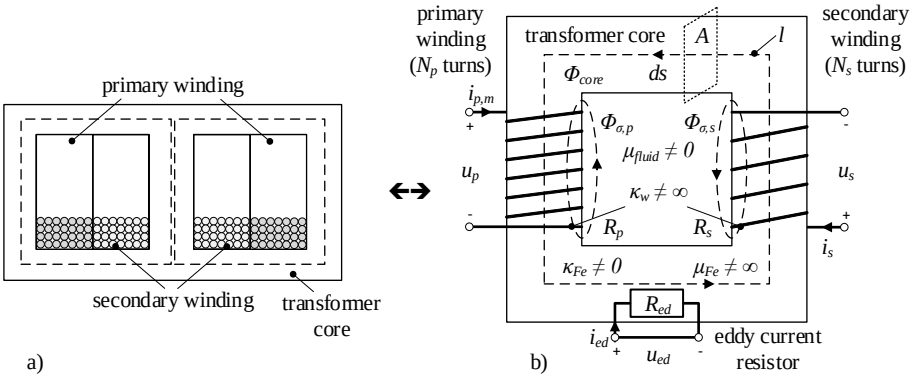

Figure 4.2 Schematic presentation of a) common and b) simplified transformer phase

Note that the magnetomotive force Θ is the cause of the magnetic flux in the magnetic circuit [21]. It is determined by the product of the number of turns N and the current i through the circuit.

- The electrical conductivity of the magnetic circuit is non-zero, i.e. $\kappa_{Fe} \neq 0$. So eddy currents appear in the transformer core causing further losses. The magnitude of these losses are given by the eddy current i_{ed} and the resistance R_{ed} placed in the core (cp. Figure 4.2b). Moreover, the magnetic flux of the transformer core (Φ_{core}) is obtained from the law of induction and Eq. 4.5.

$$\Phi_{core} = \int B dA = \int \mu_{Fe}(H) H \, dA = \frac{A}{l} \mu_{Fe}(H) \left[i_p N_p + i_s N_s + i_{ed} \right] \qquad (4.6)$$

- The permeability of the surrounding fluid (e.g. oil) is non-zero, i.e. $\mu_{fluid} \neq 0$. Hence, a field outside the core (stray field) occurs causing the flux leakage (Φ_σ). It is assumed here that the considered transformer phase has separable stray fields (cp. Figure 4.2b). This means that the flux leakage of the primary and secondary side does not affect each other and that the magnetic flux of the primary and secondary side is given by:

$$\Phi_p = \Phi_{core} + \Phi_{\sigma,p} \qquad (4.7)$$
$$\Phi_s = \Phi_{core} + \Phi_{\sigma,s} \qquad (4.8)$$

Note that a separation of the stray fields is normally not applicable for real transformers [20]. However, the assumption (of separable stray fields) is acceptable for the simple transformer shown in Figure 4.2b and provides some calculation benefits as it will be shown in section 4.2.3.

- The electrical conductivity of the windings is not infinite, i.e. $\kappa_w \neq \infty$. Thus, the resistance of the primary and secondary side winding has to be taken into account, i.e. resistance losses occur. Then, the primary (u_p) and secondary (u_s) side voltages are obtained from the current i, the resistance R, the magnetic flux linkage Ψ respectively the number of turns N and magnetic flux Φ.

$$u_p = R_p i_{p,m} + \frac{d\Psi_p}{dt} = R_p i_{p,m} + N_p \left(\frac{d\Phi_{core}}{dt} + \frac{d\Phi_{\sigma,p}}{dt}\right) \tag{4.9}$$

$$u_s = R_s i_s + \frac{d\Psi_s}{dt} = R_s i_s + N_s \left(\frac{d\Phi_{core}}{dt} + \frac{d\Phi_{\sigma,s}}{dt}\right) \tag{4.10}$$

In the same way, a voltage u_{ed} caused by eddy currents can be defined. The voltage u_{ed} is equal to zero because the eddy current is short-circuited in the transformer core (cp. also section 4.2.2). As the eddy currents are caused by the changing magnetic flux Φ over time this implies [20]:

$$u_{ed} = 0 = R_{ed} i_{ed} + \frac{d\Phi_{core}}{dt} \tag{4.11}$$

Note that there is a difference between the primary side current (i_p) and the transformer input current ($i_{p,m}$) in Eq. 4.9. The input current $i_{p,m}$ contains both the primary side current i_p and the current i_{mag} needed to magnetize the transformer core. The distinction between $i_{p,m}$ and i_p will be elaborated in section 4.2.3.

Further, based on Eq. 4.5 and 4.9 to 4.11 the vector diagram[1] of the (real) transformer (with separable stray fields) can be created. This is needed later for the loss calculations (in section 4.2.3) and is visualized in Figure 4.3 for the transformer in Figure 4.2b. Figure 4.3a shows the voltages (Eq. 4.9 to 4.11) and Figure 4.3b the currents (Eq. 4.5). The voltages $u_{core,p}$ and $u_{core,s}$ coincide with the real axis and the core flux Φ_{core} with the negative imaginary axis. This is equivalent to the ideal transformer where the primary and secondary side voltages are i) parallel and ii) perpendicular to the magnetic flux in the vector diagram [20]. Hence, the core voltages $u_{core,p}$ and $u_{core,s}$ are defined (with ω the fundamental angular frequency) as follows:

$$u_{core,p} = N_p \frac{d\Phi_{core}}{dt} = j\omega\, N_p \Phi_{core} \tag{4.12}$$

$$u_{core,s} = N_s \frac{d\Phi_{core}}{dt} = j\omega\, N_s \Phi_{core} \tag{4.13}$$

The voltage drops due to ohmic winding ($u_{R,p}$ and $u_{R,s}$) and stray ($u_{\sigma,p}$ and $u_{\sigma,s}$) losses are specified as:

$$u_{R,p} = R_p i_{p,m} \tag{4.14}$$

$$u_{R,s} = R_s i_s \tag{4.15}$$

$$u_{\sigma,p} = N_p \frac{d\Phi_{\sigma,p}}{dt} \tag{4.16}$$

$$u_{\sigma,s} = N_s \frac{d\Phi_{\sigma,s}}{dt} \tag{4.17}$$

By adding these losses to the (ideal) core voltages in the vector diagram, the resulting u_p and u_s are obtained (cp. Figure 4.3a).

Then, the core losses are determined by the eddy currents and the hysteresis effect [20]. This is shown in Figure 4.3b. In an ideal transformer the magnetomotive force Θ is equal to zero and thus, the primary and secondary side currents are i) opposed to each other and ii)

[1] Alternating quantities like currents and voltages can be represented by a (rotating) arrow in a vector diagram. The length of the arrow specifies the magnitude (i.e. the rms value) of the alternating quantity. The phase (difference) is represented by the relative position of a vector with respect to another vector, i.e. by the angular position.

parallel in the vector diagram [20]. Therefore, the core losses are governed by the magnetomotive force Θ and the eddy currents i_{ed} causing a current drop and a phase shift between primary and secondary side current, i.e. $i_pN_p \neq -i_sN_s$ (cp. Figure 4.3b). Note that additional losses in the transformer are caused, for example, by current displacement phenomena in the windings [20]. These losses are not explicitly considered here. On the other hand, they are already included in the winding, core and stray losses because the input and output voltages and currents are used for the loss calculation.

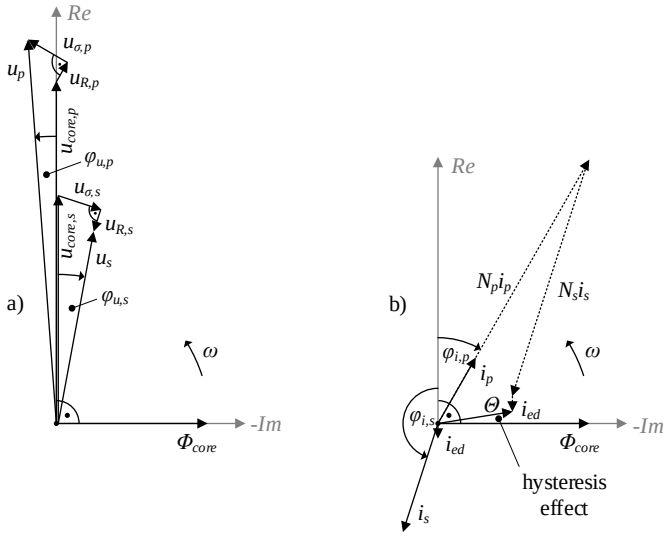

Figure 4.3 Vector diagram of a) voltages and b) currents in a real transformer

In addition, winding losses are calculated in a straightforward manner because they are given by the (measured) input ($i_{p,m}$) and output (i_s) current and by the ohmic resistances R_p and R_s (cp. Figure 4.2b). The ohmic winding resistances can either be measured or taken from data sheets or estimated by calculations. However, the evaluation of the stray and core losses require some more effort. To specify the eddy current, the hysteresis effect and the stray voltages ($u_{\sigma,p}$ and $u_{\sigma,s}$) in the vector diagram shown in Figure 4.3 must be solved. This will be demonstrated in section 4.2.3. But first, some fundamental considerations which are needed to solve the vector diagram are discussed in section 4.2.2.

4.2.2 Ohmic resistances, core hysteresis and stray field

In this section, the ohmic resistance (R_p, R_s) calculation, the hysteresis effect, i.e. the conversion of the magnetomotive force Θ to the magnetic flux Φ_{core} as well as the power losses are discussed. Simple analytical considerations and equations are used to determine them. The equations are developed for the simple transformer shown in Figure 4.2b.

First, an ohmic resistance R_Ω is defined by the specific resistance ρ [Ωmm²/m], the length l_Ω and the cross section A_Ω of the ohmic conductor [22], i.e.:

$$R_\Omega = \rho \frac{l_\Omega}{A_\Omega} \tag{4.18}$$

The specific resistance ρ is determined by the conductor material, i.e. for copper $\rho_{Cu} = 1.68 \cdot 10^{-8}\ \Omega m$ [23]. The length l_Ω is given by the number of turns N and the average winding circumferences, i.e. with the inner (C_{in}) and outer (C_{out}) winding circumferences:

$$l_\Omega = \frac{C_{in} + C_{out}}{2} N \tag{4.19}$$

In the case of a squared ($C = 4h$) or circular ($C = 2\pi R$) winding, the length l_Ω is with the edge length h respectively radius R is defined as:

$$l_{\Omega,\text{square}} = 2(h_{in} + h_{out})N \tag{4.20}$$
$$l_{\Omega,\text{round}} = \pi(R_{in} + R_{out})N \tag{4.21}$$

The conductor cross section A_Ω is obtained from the ratio between the rms current I_{rms} and rms current density J_{rms} (in [A/mm²]) at rated operation.

$$A_\Omega = \left(\frac{I_{rms}}{J_{rms}}\right)_{rated} \tag{4.22}$$

Then, the ohmic power losses are obtained from the (measured) transformer input current $i_{p,m}$ and output current i_s:

$$P_{\Omega,p} = R_p i_{p,m}^2 \tag{4.23}$$
$$P_{\Omega,s} = R_s i_s^2 \tag{4.24}$$

Second, before discussing the core hysteresis, some essential comments must be made first. A (laminated) transformer core with a magnetic field B is considered (cp. Figure 4.4a and 4.4b). Due to the magnetic field B eddy currents occur in the transformer core respectively core laminates.

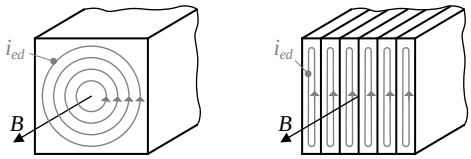

a) b)

Figure 4.4 Eddy currents generated by the magnetic field B in a) solid and b) laminated transformer core

This means that eddy currents can be included in the hysteresis effect, i.e. the core hysteresis is modified so that the calculated hysteresis losses represent the total core losses. This is proposed by Müller and Ponick [20] and applied in this chapter. To do so the effective magnetomotive force Θ^+ is defined based on Eq. 4.5 as follows:

$$\Theta^+ = \Theta - i_{ed} = i_p N_p + i_s N_s \tag{4.25}$$

This is shown in the vector diagram in Figure 4.5 which is an extension of Figure 4.3b, i.e. the magnetomotive force Θ^+ is included. Further, Figure 4.5 shows the magnetization current i_{mag}, hysteresis current i_{hyst} and eddy current i_{ed}. The current i_{hyst} could be used to describe the hysteresis losses. However, this is not further considered here.

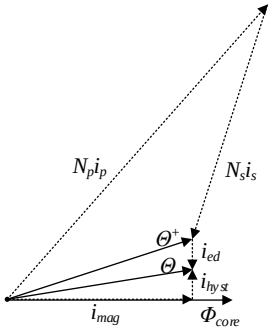

Figure 4.5 Magnetomotive force Θ^+

Now, the hysteresis effect is elaborated. The magnetization and demagnetization of a steel transformer core follows a hysteresis (cp. Figure 4.6). The hysteresis is caused, on the one hand, by the permeability μ_{Fe} which is a function of the magnetic field strength H, i.e. $\mu_{Fe} = f(H)$ and, on the other hand, by the residual magnetism of the core material. As the permeability μ_{Fe} depends on the magnetic field strength H, the relation between the magnetic field B and the magnetic field strength H is nonlinear, i.e.:

$$B = \mu_{Fe}(H)\, H \tag{4.26}$$

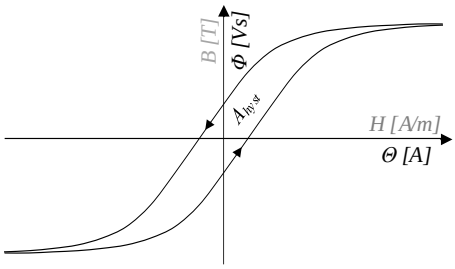

Figure 4.6 Hysteresis of transformer core

This leads to the flattening of the hysteresis, i.e. magnetic core saturation, for higher values of H (cp. Figure 4.6). The residual magnetism causes a remaining magnetic field (B) at a magnetic field strength (H) equal to zero. This means that the magnetization and demagnetization curve of the transformer core differ and the hysteresis occur. It also means that the residual magnetism influences the enlargement of the hysteresis. Further, with Eq. 4.5 and 4.6 the hysteresis (B-H diagram) can also be shown in a Φ-Θ (magnetic flux - magnetomotive force) diagram (cp. Figure 4.6).

As the magnetization and demagnetization curve of the transformer do not coincide (hysteresis effect), energy is dissipated in the transformer core removing the residual magnetism (every hysteresis cycle). This energy is equivalent to the area A_{hyst} in Figure 4.6. The dissipated energy of the hysteresis is calculated for the one (hysteresis) cycle based on Eq. 4.5 and 4.6 as follows [20]:

$$E_{hyst} = A\ l\ \int BdH = \int \Phi d\Theta \tag{4.27}$$

Taking into account Eq. 4.25 the total energy lost in the transformer core during one cycle is given by:

$$E_c = \int \Phi d\Theta^{+} \tag{4.28}$$

Then, with the number of cycles per second given by the angular frequency ω the total power losses in the core are:

$$P_c = \frac{\omega}{2\pi}\ E_c = \frac{\omega}{2\pi} \int \Phi d\Theta^{+} \tag{4.29}$$

It can be seen that the magnetic flux Φ_{core} and magnetomotive force Θ^{+} must be known to calculate the total core losses. This means that Eq. 4.9, 4.10 and 4.25 must be solved. However, solving these equations is not a straight forward procedure. Its solution is shown in section 4.2.3.

Third, the stray fields occur in the transformer because the permeability of the materials and fluids surrounding the transformer core is non-zero (cp. section 4.2.1). This means that the stray fields are generated in different transformer components [19]. It also means that the stray losses are distributed over several parts in the transformer and that they rather influence the temperature of the entire transformer than the temperature of one particular transformer component. Consequently, the stray losses cannot be assigned to one specific transformer component like the windings. Therefore, in this chapter the stray losses are not considered in the calculation of the winding hot spot temperature because i) the portion of stray losses occurring in the windings cannot be evaluated by simple methods and ii) the stray losses are significantly smaller than the ohmic winding losses [15][19] and thus are non-dominant for the winding hot spot temperature. Nevertheless, for the sake of completeness, the stray loss calculation is briefly shown here.

From Figure 4.3a it can be seen that the stray fields cause a voltage drop given by the stray voltages $u_{\sigma,p}$ and $u_{\sigma,s}$. Due to the assumption of separable stray fields, the power losses are computable individually for the primary and secondary side. The power losses are defined by the product of stray voltage and current, i.e.:

$$P_{\sigma,p} = u_{\sigma,p} i_{p,m} \tag{4.30}$$
$$P_{\sigma,s} = u_{\sigma,s} i_s \tag{4.31}$$

Then, the total transformer losses are given with Eq. 4.23, 4.24 and Eq. 4.29 to 4.31:

$$P_{loss} = P_c + P_{\Omega,p} + P_{\Omega,s} + P_{\sigma,p} + P_{\sigma,s} \tag{4.32}$$

To verify the loss calculation result, i.e. Eq. 4.23, 4.24 and Eq. 4.29 to 4.31, the total transformer losses according to Eq. 4.32 must coincide with losses $P_{loss,m}$ evaluated by the measured input and output currents and voltages [18], i.e.:

$$P_{loss,m} = i_{p,m}u_p - i_s u_s \tag{4.33}$$

This will be demonstrated for a literature case in section 4.4.

4.2.3 Loss calculation procedure

Before explaining the calculation procedure used to evaluate the magnetic flux Φ_{core}, magnetomotive force Θ^+ and thus, the total transformer losses, the data required for the calculation, i.e. the calculation inputs, are specified. To solve the voltage and current vector diagram (cp. Figure 4.3), at the least, the rms values of currents, voltages and phase angles are needed (cp. Figure 4.7). This means that the following transformer input and output measurements are required:

- primary (u_p) and secondary (u_s) side voltages
- input current ($i_{p,m}$) and secondary (output) current (i_s)
- phase angle φ_u between u_p and u_s
- phase angle φ_p between u_p and $i_{p,m}$
- phase angle φ_i between $i_{p,m}$ and i_s
- phase angle φ_s between u_s and i_s (determined by φ_u, φ_p and φ_i)

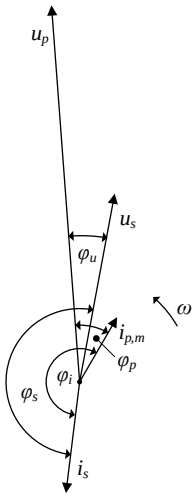

Figure 4.7 Vector diagram of calculation input measurements

An overview of the calculation procedure is provided in Figure 4.8. The magnetic flux Φ_{core} is calculated based on the vector diagram of voltage (cp. Figure 4.3a) and the magnetomotive force Θ^+ based on the vector diagram of currents (cp. Figure 4.3b or 4.5). (Note that the

definition of the angles φ, χ and ψ is given while presenting the calculation procedure for Θ^+.)

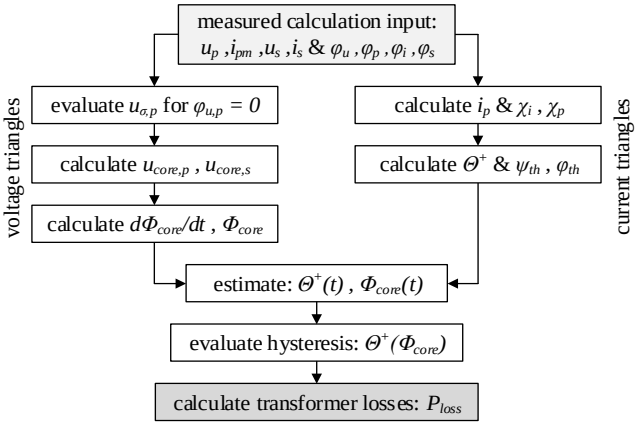

Figure 4.8 Calculation procedure for transformer losses

The procedure sketched in Figure 4.8 is as follows. First, the magnetic flux Φ_{core} is considered. The time derivative of the magnetic flux $d\Phi_{core}/dt$ must comply with both Eq. 4.9 and 4.10. This means that the vector diagram of voltages visible in Figure 4.9 is determinable (cp. also Figure 4.3a). The voltages u_p and u_s as well as the phase angles φ_u (sum of $\varphi_{u,p}$ and $\varphi_{u,s}$), φ_p and φ_s are directly measured. The voltages $u_{R,p}$ and $u_{R,s}$ are specified by the measured current $i_{p,m}$ and i_s and ohmic resistances R_p and R_s (cp. also Eq. 4.14 and 4.15). Further, for a linearized core permeability, i.e. $\mu_{Fe} = const.$ and sinusoidal currents with the fundamental angular frequency ω, i.e.

$$i(t) = \hat{I}\sin(\omega t) \tag{4.34}$$

$$\frac{di(t)}{dt} = \omega\hat{I}\cos(\omega t) \tag{4.35}$$

the time derivative of the (stray) flux is with Eq. 4.6 [20]:

$$\frac{d\Phi_\sigma}{dt} \sim \frac{di(t)}{dt} \sim j\omega\,\hat{I} \tag{4.36}$$

This means that in the vector diagram the stray voltages $u_{\sigma,p}$ and $u_{\sigma,s}$ are perpendicular (phase shift of $\pi/2$ due to $j\omega$) to the currents i_p and i_s (cp. Figure 4.9). Note that this is valid for ideal conditions and thus, implies that an approximation is made for the real transformer.

Further, to solve the voltage vector diagrams directly, it is assumed that the phase angle $\varphi_{u,p}$ is equal to zero ($\varphi_{u,p} = 0$). This means that the voltages u_p and $u_{core,p}$ are parallel and that the phase angle $\varphi_{u,s}$ is equal to the measured voltage phase angle φ_u. It also means that the minimum stray voltage $u_{\sigma,p}$ and the maximum core voltage $u_{core,p}$ are calculated. With the measured voltage u_p current $i_{p,m}$, phase angle φ_p and ohmic resistance R_p this yields:

$$u_{\sigma,p} = u_{R,p}\tan(\varphi_p) = R_p i_{p,m}\tan(\varphi_p) \tag{4.37}$$

$$u_{core,p} = u_p - u_{R\sigma,p} = u_p - \sqrt{u_{R,p}^2 + u_{\sigma,p}^2} = u_p - R_p i_{p,m} \sqrt{1 + \left(\tan(\varphi_p)\right)^2} \quad (4.38)$$

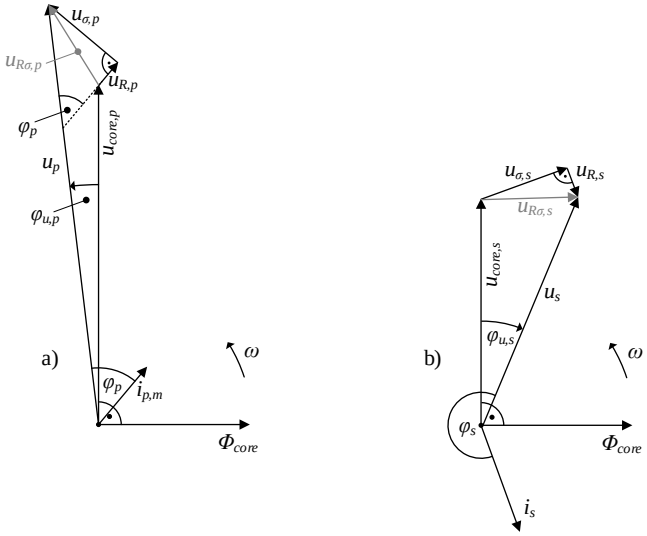

Figure 4.9 Vector diagram of voltages at the a) primary and b) secondary side for $\varphi_i > \pi$ and $\varphi_s > \pi$

Moreover, the core voltages $u_{core,p}$ and $u_{core,s}$ are equivalent to the primary and secondary side voltages of an ideal transformer which are perpendicular to the magnetic flux Φ_{core} [20]. This means that the ratio of the core voltages $u_{core,s}$ is given by the voltage $u_{core,p}$ and the transformer turns ratio $n = N_s / N_p$.

$$u_{core,s} = n\, u_{core,p} = \frac{N_s}{N_p} u_{core,p} \quad (4.39)$$

Then, with the measured secondary side voltage u_s, current i_s and phase angle φ_u, the stray voltage $u_{\sigma,s}$ of the secondary side can be evaluated. With the law of cosines applied to Figure 4.9b and $\varphi_{u,s} = \varphi_u$ this yields:

$$u_{R\sigma,s} = \sqrt{u_s^2 + u_{core,s}^2 - 2u_s u_{core,s} \cos(\varphi_u)} \quad (4.40)$$

$$u_{\sigma,s} = \sqrt{u_{R\sigma,s}^2 - u_{R,s}^2} = \sqrt{u_s^2 + u_{core,s}^2 - 2u_s u_{core,s} \cos(\varphi_u) - (R_s i_s)^2} \quad (4.41)$$

Finally, after calculating the core and stray voltages, the time derivative of the magnetic flux $d\Phi_{core}/dt$ and the magnetic flux Φ_{core} must still be evaluated. With the fundamental angular frequency ω of the vector diagram it follows (cp. Eq. 4.12 and 4.13) that:

$$\frac{d\Phi_{core}}{dt} = \frac{1}{N_p} u_{core,p} = \frac{1}{N_s} u_{core,s} \quad (4.42)$$

$$\Phi_{core} = \frac{1}{\omega} \frac{d\Phi_{core}}{dt} \quad (4.43)$$

From this, it can be seen that the calculation of the core voltages $u_{core,p}$ and $u_{core,s}$ based on transformer input and output measurements provides the actual magnet flux Φ_{core} in the transformer core. Knowing the actual magnet flux Φ_{core} is the first of two pieces which are needed to calculate the transformer core losses.

Second, the magnetomotive force Θ^+ is evaluated. To do so the primary side current i_p has to be calculated based on the measured transformer input current $i_{p,m}$ and the secondary side current i_s. Remember that in the previous section it was stated that the input current $i_{p,m}$ contains the magnetization current i_{mag}, hysteresis current i_{hyst} and eddy current i_{ed} while the primary side i_p current does not. This will become clear when the transformer is considered at idling operation where $i_p = i_s = 0$ and $i_{pm} \neq 0$. In other words, at idling operation an input current is measured which is needed for the core magnetization and losses, i.e. for i_{mag}, i_{hyst} and i_{ed} [20]. Therefore, the current i_p and $i_{p,m}$ can be distinguished as it is shown in the current vector diagram visible in Figure 4.10a.

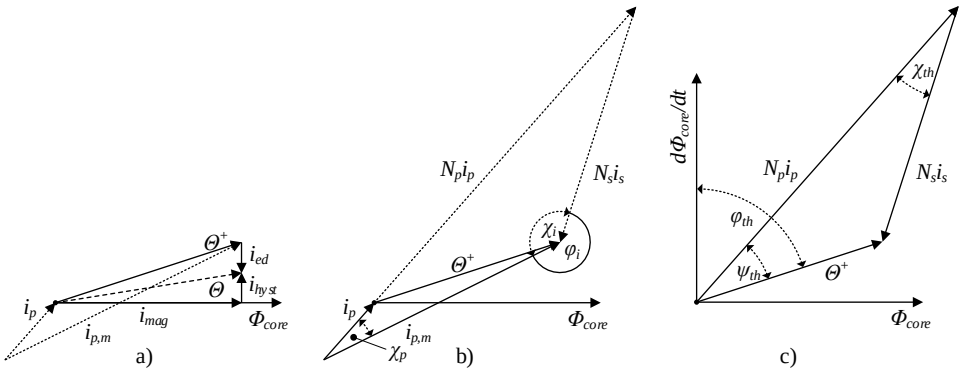

Figure 4.10 Current vector diagrams: a) currents i_p and $i_{p,m}$ b) triangle for calculating current i_p and c) magnetomotive force Θ^+

This means that the primary side current i_p can be calculated from the current triangle determined by i_p, $N_p i_p$, $N_s i_s$ and $i_{p,m}$ as demonstrated in Figure 4.10b. By applying the law of cosines to this triangle, the current i_p is given with the measured current phase angle φ_i as follows:

$$i_p = \frac{1}{N_p+1}\sqrt{i_{p,m}^2 + N_s^2 i_s^2 - 2N_s i_{p,m} i_s \cos(\chi_i)} \tag{4.44}$$

with

$$\chi_i = 2\pi - \varphi_i \tag{4.45}$$

Using further the law of sines for this current triangle, the angle χ_p between the currents i_p and $i_{p,m}$ is evaluated with the calculated current i_p and measured current i_s (cp. Figure 4.10b).

$$\sin(\chi_p) = \frac{N_s}{N_p+1}\frac{i_s}{i_p}\sin(\chi_i) \tag{4.46}$$

Then, the magnetomotive force Θ^+ can be determined based on Figure 4.10c. Again, by applying the law of cosines to the current triangle $N_p i_p$, $N_s i_s$ and Θ^+, the magnetomotive force Θ^+ is specified.

$$\Theta^+ = \sqrt{N_p^2 i_p^2 + N_s^2 i_s^2 - 2N_p N_s i_p i_s \cos(\chi_{th})} \tag{4.47}$$

with (cp. also Figure 4.10b and 4.10c)

$$\chi_{th} = \varphi_i - \chi_p - \pi \tag{4.48}$$

Furthermore, with the law of sines the angle ψ_{th} between the current i_p and the magnetomotive force Θ^+ is given and thus, also the angle φ_{th} (cp. Figure 4.9a and 4.10c).

$$\sin(\psi_{th}) = \frac{N_s i_s}{\Theta^+} \sin(\chi_{th}) \tag{4.49}$$

$$\varphi_{th} = \varphi_p - \varphi_{u,p} - \chi_p + \psi_{th} \tag{4.50}$$

From these considerations of the current vector diagram (cp. Figure 4.10), it can be seen that based on transformer input and output measurements the actual magnetomotive force Θ^+ in the transformer core can be calculated. Knowing the actual magnetomotive force Θ^+ is the second piece needed to calculate the transformer core losses.

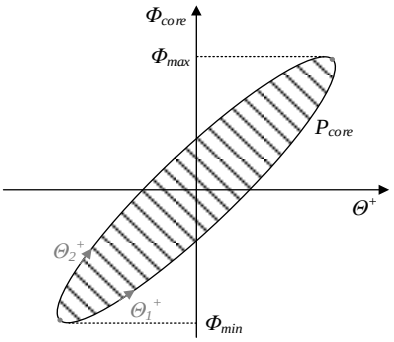

Figure 4.11 Hysteresis (core losses P_{core}) approximated by an ellipse

Finally, if the hysteresis is approximated by an ellipse (cp. Figure 4.11), then the magnetomotive force Θ^+ and magnetic flux Φ_{core} can be estimated as a function of the time t and the angular frequency ω, i.e.:

$$\Theta^+(t) = \sqrt{2}|\Theta^+| \sin(\omega t + 0.5\pi - \varphi_{th}) \tag{4.51}$$

$$\Phi_{core}(t) = \sqrt{2}|\Phi_{core}| \sin(\omega t) \tag{4.52}$$

Then, by describing the hysteresis with two function $\Theta_1^+(\Phi_{core})$ and $\Theta_2^+(\Phi_{core})$ as it is shown in Figure 4.11, the total core (hysteresis) losses are calculated as follows:

$$P_c = \frac{\omega}{2\pi}\int_{\Phi_{min}}^{\Phi_{max}}[\Theta_1^+(\Phi_{core}) - \Theta_2^+(\Phi_{core})]d\Theta^+ =$$
$$= \frac{\omega}{2\pi}\sum_{i=1}^{n-1}\frac{(\Phi_{core,i+1}-\Phi_{core,i})}{2}\left[\left(\Theta_{1,i+1}^+ + \Theta_{1,i}^+\right) - \left(\Theta_{2,i+1}^+ + \Theta_{2,i}^+\right)\right] \quad (4.53)$$

In addition, it is important to note that the presented calculation procedure to determine the magnetomotive force Θ^+ and magnetic flux Φ_{core} is only valid for ideal working conditions, i.e. a sinusoidal regime. This means that the presented method is applicable for transformers where harmonics are avoided by protection and filtering devices.

4.2.4 Virtual transformer twin

Now, the virtual transformer twin is evaluated, i.e. a rough estimation of the number of turns and transformer dimensions is presented. The numbers of turns N_p and N_s are necessary to solve the current vector diagram shown in Figure 4.10. Further, the number of turns and the transformer dimension are needed to calculate the temperature distribution in the windings and thus to evaluate the hot spot temperature as it will be shown in section 4.3.

The transformer dimensions and number of turns can be determined from a few fundamental considerations and equations which must be fulfilled by any transformer and which can be derived from the theory discussed in section 4.2.1. First, the number of turns N_p of the primary side is related to the primary side voltage. With Eq. 4.6 and neglecting the voltage drops due to ohmic resistance R_p and stray flux $\Phi_{\sigma,p}$ in Eq. 4.9 (cp. ideal transformer [20]), the magnetic flux $\Phi(t)$ as a function of the primary side voltage, is given by:

$$u(t) = \hat{U}\sin(\omega t) = \sqrt{2}U_{rms}\sin(\omega t) \quad (4.54)$$

$$\Phi(t) = \int B(t)dA = \frac{1}{N_p}\int u(t)dt \quad (4.55)$$

Based on Eq. 4.54 and 4.55 the number of turns N_p is obtained from with the primary side voltage $u(t)_p$, the core cross section A, the magnetic field B and fundamental angular frequency ω. Using the rms value for the primary side voltage $U_{p,rms}$ at rated operation, which is available on the transformer nameplate, and assuming the rms value of the magnetic field B_{rms} (at rated operation), the number of turns N_p is calculated as follows:

$$N_p = \frac{1}{\omega A}\left(\frac{U_{rms}}{B_{rms}}\right)_{rated} \quad (4.56)$$

Second, a similar equation is obtained for calculating the number of turns N_p with the ratio of winding window area A_w multiplied by the fill factor k_f and the wire cross section A_Ω (cp Figure 4.12). The wire cross section area A_Ω is obtained from the rms current I_{rms} and rms current density J_{rms} (in [A/mm²]) at rated operation (cp. Eq. 4.22). The winding window is specified by the winding length l_w and height difference Δh (cp. Figure 4.12). The fill factor k_f describes the ratio of wire cross section area A_Ω to the provided winding space in the window area A_w. For example, the ratio of a circular area (round wire) and a square (winding space) leads to a fill factor $k_f = \pi/4$. Then, the number of turns N_p is:

$$N_p = \frac{k_f A_w}{A_\Omega} = k_f l_w \Delta h \left(\frac{J_{rms}}{I_{rms}}\right)_{rated} \tag{4.57}$$

Third, combining Eq. 4. 56 and 4.57 provides a simple relation for the product of the transformer core cross section A and winding window area A_w, i.e.:

$$A\, A_w = \frac{1}{\omega\, k_f} \left(\frac{U_{rms}\, I_{rms}}{B_{rms}\, J_{rms}}\right)_{rated} \tag{4.58}$$

Further, if it is assumed that the ratio of the transformer lengths b and h (cp. Figure 4.12) is fixed, e.g. $b/h = 3$, the main transformer dimensions, i.e. the virtual twin, are determined with $A = h^2$ and $A_w = (b - 2h)b$:

$$b = \sqrt[4]{\frac{2}{\omega\, k_f \left(1-\frac{2h}{b}\right)\left(\frac{h}{b}\right)^2} \left(\frac{U_{rms}\, I_{rms}}{B_{rms}\, J_{rms}}\right)_{rated}} \approx \sqrt[4]{\frac{2}{\omega \left(1-\frac{2h}{b}\right)\left(\frac{h}{b}\right)^2} \left(\frac{U_{rms}\, I_{rms}}{B_{rms}\, J_{rms}}\right)_{rated}} \tag{4.59}$$

Note that i) the current density J_{rms} (approx. *1.5-2 A/mm²*) and the magnetic field B_{rms} (approx. *1 T*) are estimated and that ii) the fourth root of the fill factor k_f is approx. one. Therefore, the fill factor is neglected in Eq. 4.59.

Fourth, after calculating the core cross section area A based on Eq. 4.59 and then, the number of turns N_p based on Eq. 4.57, the number of turns N_s (secondary side) is determined by:

$$N_s = nN_p \tag{4.60}$$

Note that both numbers of turns N_p and N_s must be integers. This means that N_p must be rounded downwards appropriately. The transformer ratio n is obtained from the rated voltages of primary and secondary side which, again, are available on the transformer nameplate.

Finally, assuming a squared wire cross section with the edge length h_Ω, i.e. a fill factor k_f of approx. one, the number of turns $N_{p,l}$ along the length l_w and $N_{p,\Delta h}$ along the height difference Δh can be estimated as follows (cp. Figure 4.12):

$$N_{p,l} = \frac{l_w}{h_\Omega} = l_w \sqrt{\frac{J_{rms}}{I_{rms}}} \tag{4.61}$$

$$N_{p,\Delta h} = \frac{\Delta h}{h_\Omega} = \Delta h \sqrt{\frac{J_{rms}}{I_{rms}}} \tag{4.62}$$

The latter two equations also apply for the secondary side winding by using the secondary side rms current.

These considerations and equations show that the transformer main dimensions and the number of turns of the primary and secondary side winding can be estimated, i.e. a simple virtual twin can be created based on the transformer rating information (rated power and

voltages) only. Based on the simple virtual twin the current vector diagram (cp. Figure 4.10) and the winding temperature can be calculated. The latter is shown in the next section.

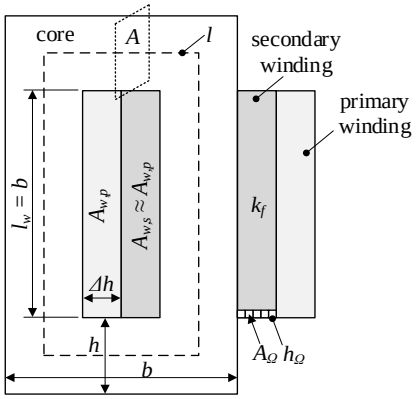

Figure 4.12 Virtual twin (dimensions) of common transformer phase

4.3 Calculation of transformer temperature

For the life time prediction of the transformer it is necessary to know the temperature in the transformer windings. Therefore, it is important to describe the conversion of the dissipated power (winding and core losses) to an actual temperature. In order to do so, winding and core losses are assumed to be evenly distributed over the (copper) winding ($V_{p,Cu}$, $V_{s,Cu}$) respectively core volume (V_c). With Eq. 4.23, 4.24, 4.29 and Figure 4.12 this leads to the following definition of the volumetric heat generation in the primary ($q_{V,p}$) and secondary ($q_{V,s}$) side windings as well as core ($q_{V,c}$):

$$q_{V,p} = \frac{Q_p}{V_{p,Cu}} = \frac{R_p i_{p,m}^2}{4\,(h+3\Delta h)\,A_{w,p}\,k_f} \tag{4.63}$$

$$q_{V,s} = \frac{Q_s}{V_{s,Cu}} = \frac{R_s i_s^2}{4\,(h+\Delta h)\,A_{w,s}\,k_f} \tag{4.64}$$

$$q_{V,c} = \frac{Q_c}{V_c} = \frac{2\pi}{\omega\,A\,l} \int \Phi d\Theta^+ \tag{4.65}$$

Note that the volumetric heat generation q_V is in [W/m³] and the heat flow Q in [W].

Then, to simplify the temperature calculation a few assumptions are made here:

- The windings and core have square cross sections, i.e. $A = h^2$.
- The circumferences of the squared winding ($4h$) is described by an equivalent circular circumferences ($2\pi R$) as shown in Figure 4.13, i.e.

$$R = 2h/\pi \qquad \text{or} \qquad r = 4x/\pi \tag{4.66}$$

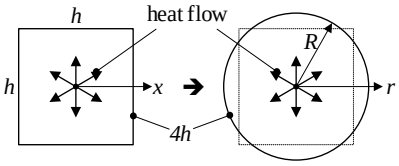

Figure 4.13 Cross section approximation

- The heat flow is uniform and only occurs in radial direction. This means that 1D considerations are sufficient.

- The transformer operates under quasi-stationary conditions, i.e. the change of the volumetric heat generation q_v and winding temperature T over time does not have a significant effect on the spatial temperature distribution in the windings. This means that the general 1D (radial direction) heat equation in cylinder coordinates [24]

$$\frac{1}{r}\frac{d}{dr}\left(kr\frac{dT}{dr}\right) + q_V = \rho c_p \frac{dT}{dt} \tag{4.67}$$

with the density ρ, heat capacity c_p and thermal conductivity k can be simplified to

$$\frac{1}{r}\frac{d}{dr}\left(kr\frac{dT}{dr}\right) + q_V = 0 \tag{4.68}$$

as the temporal variation in temperature is assumed to be approx. zero, i.e. $dT/dt \approx 0$, steady state. It also means that the winding temperature T, apart from the amount of heat (q_V) generated, will only depend on the winding radius r (cp. Eq. 4.68).

- The transformer windings are assumed to consist of consecutive circumferential layers of copper and insulation (including oil) and the magnitude of q_V depends on their different thermal conductivities in the radial heat flow (cp. Figure 4.14). This means that the $N_{p,l}$ (or $N_{s,l}$) turns along the winding length l_w merge to one solid copper layer with the following thickness (primary side winding):

$$\Delta r_{Cu} = \Delta h \frac{k_f}{N_{p,\Delta R}} \tag{4.69}$$

Then the insulation layer thickness is:

$$\Delta r_{ins} = \Delta h \frac{1-k_f}{N_{p,\Delta R}} \tag{4.70}$$

Note that the number of turns $N_{p,\Delta R}$ and $N_{s,\Delta R}$ along the radius difference ΔR are equal to the number of turns $N_{p,\Delta h}$ and $N_{s,\Delta h}$ along the height difference Δh (cp. Figure 4.12 and 14). The approximated transformer windings (cp. Figure 4.14) have $N_{p,\Delta R}$ respectively $N_{s,\Delta R}$ layers of both copper and insulation in radial direction. Further, the number of layers will have to be rounded to an integer, if the number of turns $N_{p,\Delta R}$ respectively $N_{s,\Delta R}$ are evaluated based on Eq. 4.61 and 4.62. In addition, as the thermal

conductivities of insulation material, e.g. Enamel ($k_{en.}$ = 0.26-0.54 W/mK [25]) and oil (k_{oil} = 0.3714 W/mK [26]) are similar, they are merged into one insulation layer.

- The ambient oil temperature ($T_{oil,amb}$) of the windings is available, i.e. it is measured during operation (cp. Figure 4.14). It is used as boundary condition to approximate the windings temperature, i.e. copper layers temperature.

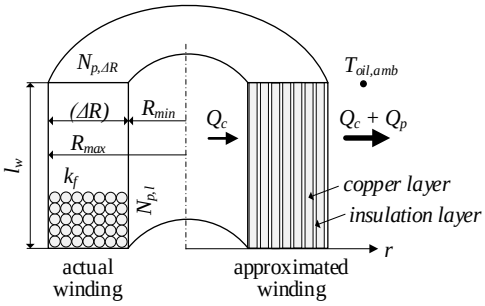

Figure 4.14 Winding approximation by layers (primary side)

Now, the radial temperature distribution for the different winding layers is defined. The layers can be categorized in two types: copper and insulation layers. Although, these layers have different radial heat flow gradients, the radial temperature calculation can be developed simultaneously for both type of layers because the gradient *dQ/dr = 0* (insulation layer) is a special case of the gradient *dQ/dr = const.* (copper layer).

In general, the heat flow Q in the layers is expressed by the product of the specific radial heat flow q_r in [W/m²] and the surface area A_r, i.e. for a cylindric layer with the winding length l_w:

$$Q = q_r A_r = q_r 2\pi r l_w \tag{4.71}$$

The specific heat flow in radial direction is given by the Fourier's law of conduction, i.e. with thermal conductivity *k*.

$$q_r = -k\left(\frac{dT}{dr}\right) \tag{4.72}$$

Further, rearranging and integrating Eq. 4.68 yields to:

$$dT = -\frac{q_V}{2k} r dr + \mathrm{C}_1 \frac{dr}{r} \tag{4.73}$$

$$T(r) = -\frac{q_V}{4k} r^2 + \mathrm{C}_1 \ln(r) + \mathrm{C}_2 \tag{4.74}$$

The constants C_1 and C_2 are determined by boundary conditions, i.e. by the temperatures at the inner (T_{in}) and outer (T_{out}) side of the layers. Hence, the constants C_1 and C_2 are specified with the inner (r_{in}) and outer (r_{out}) layer radii (cp. Figure 4.15) by:

$$T_{in} = -\frac{q_V}{4k} r_{in}^2 + \mathrm{C}_1 \ln(r_{in}) + \mathrm{C}_2 \tag{4.75}$$

$$T_{out} = -\frac{q_V}{4k} r_{out}^2 + \mathrm{C}_1 \ln(r_{out}) + \mathrm{C}_2 \tag{4.76}$$

Moreover, with Eq. 4.71 to 4.73 this yields to:

$$Q^* = -2\pi r l_w k \left(\frac{dT}{dr}\right) = 2\pi l_w k \frac{(T_{in} - T_{out}) + \frac{q_V}{4k}(r_{in}^2 - r_{out}^2)}{\ln\left(\frac{r_{out}}{r_{in}}\right)} \tag{4.77}$$

with the modified radial heat flow Q^* specified by the radial heat flow Q and volumetric heat generation q_V:

$$Q^* = Q - q_V \pi r^2 l_w \tag{4.78}$$

As the ambient oil temperature is measured, i.e. T_{out} is known and the modified heat flow Q^* through the winding is calculated based on the transformer losses (cp. previous section), the inner layer temperature T_{in} can be evaluated as follows:

$$T_{in} = T_{out} + \frac{Q^*}{2\pi l_w k} \ln\left(\frac{r_{out}}{r_{in}}\right) - \frac{q_V}{4k}(r_{in}^2 - r_{out}^2) \tag{4.79}$$

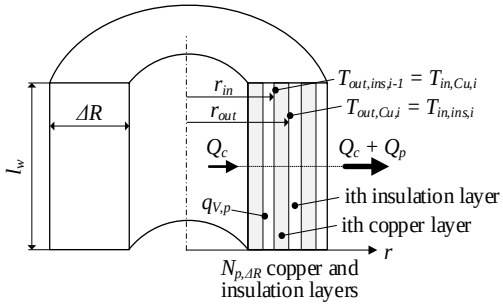

Figure 4.15 Inner and outer layer radii and temperatures (primary side)

Note that the winding temperature is evaluated from the winding outside to its inside, i.e. from the outermost to the innermost winding layers. This means that the outer temperature of the ith copper layer is equal to the inner temperature of the ith insulation layer (cp. Figure 4.15). Therefore, the outer layer temperature is known and the inner layer temperature must be determined. Further, note that Eq. 4.78 and 4.79 apply to copper layers for $q_V > 0$ and to insulation layers for $q_V = 0$.

In addition, to solve Eq. 4.79 for every layer, the inner ($r_{in,i}$) and outer ($r_{out,i}$) radii and the heat flow (Q_i) are needed for every ith copper and insulation layer. These quantities are determined as follows for $i \in [1, N_{p,\Delta R}]$ and with Figure 4.14 and 4.15 (primary side winding):

$$r_{in,Cu,i} = R_{max} - i\frac{\Delta R}{N_{p,\Delta R}} \tag{4.80}$$

$$r_{out,Cu,i} = r_{in,Cu,i} + k_f \frac{\Delta R}{N_{p,\Delta R}} \tag{4.81}$$

$$r_{out,ins,i} = r_{in,Cu,i} + \frac{\Delta R}{N_{p,\Delta R}} \tag{4.82}$$

$$r_{in,ins,i} = r_{out,ins,i} - \left(1 - k_f\right)\frac{\Delta R}{N_{p,\Delta R}} \tag{4.83}$$

$$Q_c = q_{V,c}\pi R_{min}^2 l_w \tag{4.84}$$
$$Q_p = R_p i_{p,m}^2 \tag{4.85}$$
$$Q_i = Q_c + Q_p - \sum_{i=1}^{N_{p,\Delta R}} q_{V,p}\pi l_w\left(r_{out,Cu,i}^2 - r_{in,Cu,i}^2\right) \tag{4.86}$$
$$Q_i^* = Q_i - q_{V,p}\pi l_w r_{out,Cu,i}^2 = Q_c + Q_p - \sum_{i=1}^{N_{p,\Delta R}} q_{V,p}\pi l_w\left(2r_{out,Cu,i}^2 - r_{in,Cu,i}^2\right) \tag{4.87}$$

Finally, from these considerations, it can be seen that based on the main transformer dimensions (virtual twin) and winding and core losses the temperature distribution in the transformer windings can be evaluated. The hot spot temperature is the highest winding temperature. It is normally the winding temperature closest to the core, i.e. at the innermost copper layer. Further, if the primary side winding is placed around the secondary side winding (cp. Figure 4.12), then the heat flow through the primary side winding does not only contain the heat flow from the core but also from the secondary side winding.

4.4 Case study and validation

In this section, the losses and winding hot spot temperature are calculated for a single phase of a 154kV, 15MVA power transformer. Kwean *et al.* [15] provide loss and winding temperature measurements as well as the hot spot temperature calculated according to the IEEE / IEC loading guide for this transformer. The available transformer information are shown in Table 4.1 [15].

First, the main transformer dimensions of the virtual twin are estimated based on Table 4.1 and section 4.2.4. Table 4.2 shows the properties of the virtual twin. Note that the turn ratio $n = N_s / N_p$ is estimated based on Eq. 4.18 and 4.19 (cp. section 4.2.2) and the ratio of the measured winding resistances (cp. Table 4.1). For three parameters in Table 4.2 values need to assumed, i.e. B_{rms}, J_{rms} and b/h. The magnetic field B_{rms} is estimated based on the magnetic field saturation of the transformer core, which is typically $B_s \approx 1.5 - 1.7\ T$ [27]. This means that a magnetic field of $B_{rms} = 1\ T$ of one phase at nominal transformer operation leads to a magnetic field peak of $B_{peak} = 1.4\ T$. In other words, the magnetic field is chosen such that the transformer core almost reaches saturation at nominal operation. Then, the current density J is typically in the range of $2\text{-}5\ A/mm^2$ [28]. Due to the compact transformer windings, for safety reasons lower values of the current density are chosen. Therefore, a current density peak for one phase at nominal operation of $J_{peak} = 2.5\ A/mm^2$, i.e. $J_{rms} = 1.75\ A/mm^2$, is assumed here. In addition, the dimension ratio $b/h = 3$ is obtained by minimizing the length b using Eq. 4.59. This might not yield the optimal transformer dimensions where the sum of core and winding losses is minimized. However, as the core losses are proportional to the core volume, i.e. the product of core cross section A and length l (cp. Figure 4.12), and the winding losses are a function of the window area A_w (cp. Eq. 4.18 and 4.57), i.e. the dimensions h and b, the optimization of the transformer volume provides a rough estimation of the dimension ratio b/h.

By comparing the winding resistances in Table 4.1 and 4.2, it can be seen that the calculated resistances are between the cold and hot measured resistances. This means that the virtual

twin is an adequate approximation of the actual transformer because the winding resistances (lengths, cp. Eq. 4.18) are also a function of the transformer dimensions, i.e. winding radii.

Second, to calculate the transformer losses rms currents and voltages including phase angles are needed. This is shown in Table 4.3.

The transformer loss calculations are executed with the calculated winding resistances available in Table 4.2. Further, as the phase angles were not available, they are estimated here such that the calculated transformer losses match with the measurements provided by [15], assuming an inductive load impedance, i.e. $\varphi_i > \pi$, connected to the transformer output. The stray losses determine the phase angle φ_u (cp. Eq. 4.30 and 4.31 as well as Eq. 4.40 and 4.41), while the core losses determine the phase angles φ_p and φ_i (cp. Eq. 4.45, 4.48 and 4.50). Finally, the phase angle φ_s is derived from the phase angles φ_u, φ_p and φ_i (cp. Figure 4.7). Note that this means that the comparison of the measured and calculated losses (cp. Table 4.4) demonstrates the feasibility of the loss calculation with the proposed method, but it does not quantify the calculation errors.

Table 4.1 Available information of 154kV, 15MVA power transformer

parameter	value	unit	description
S	15	[MVA]	rated power
U_{rms}	77,798	[V]	rated voltage (measured)
I_{rms}	206.1	[A]	rated current
$R_{p,cold}$	0.79277	[Ω]	HV winding resistance (cold measured)
$R_{p,hot}$	0.98997	[Ω]	HV winding resistance (hot measured)
$R_{s,cold}$	0.017228	[Ω]	LV winding resistance (cold measured)
$R_{s,cold}$	0.021456	[Ω]	LV winding resistance (hot measured)

Table 4.2 Properties of virtual transformer twin

parameter	value	unit	description
B_{rms}	1	[T]	magnetic field (assumed)
J_{rms}	1.75	[A/mm²]	current density (assumed)
f	50	[Hz]	operating frequency
b/h	3	-	dimension ratio (assumed)
b	1.11	[m]	length
R	0.20875	[m]	core radius
n	5	-	turn ratio
N_p	1800	-	number of turns (primary side)
$N_{p,l}$	100	-	number of turns (along length)
$N_{p,\Delta R}$	18	-	number of turns (along radius)
N_s	360	-	number of turns (secondary side)
$N_{s,l}$	45	-	number of turns (along length)
$N_{s,\Delta R}$	8	-	number of turns (along radius)
$R_{p,calc}$	0.807552	[Ω]	HV winding resistance (calculated)
$R_{s,calc}$	0.0197352	[Ω]	LV winding resistance (calculated)

On the other hand, the calculated losses shown in Table 4.4 depend differently on the estimated phase angles. The stray losses are sensitive to the phase angle φ_u because it is used

to calculate the secondary side stray voltage in Eq. 4.41. Doubling the phase angle φ_u from $3.47 \cdot 10^{-4}\pi$ to $6.94 \cdot 10^{-4}\pi$ increases the stray losses from *16,180W* to *39,594W*. The core losses are much less sensitive to the phase angles (cp. Eq. 4.44 and the followings). Reducing the phase angle φ_i from 1.46π to 1.36π decreases the core losses from *11,023W* to *8,931W*. Then, the winding losses do not depend at all on the phase angles. Rather, they are determined by the calculated winding resistances, i.e. they depend on the estimation of the virtual transformer twin and its dimensions. This means that estimating the phase angles is non-critical here because the stray losses will not be considered in the winding hot spot temperature calculation. As already mentioned in the section introduction, the stray losses occur in different transformer parts and thus, only a minor portion of them can be assigned to the heat flow through the windings. This portion is difficult to evaluate and therefore, it is not considered in the winding hot spot temperature calculation.

Table 4.3 Input data for transformer loss calculations

parameter	value	unit	description
u_p	77,798	[V]	primary side rms voltage
i_{pm}	206.1	[A]	primary side rms current
u_s	15,513	[V]	secondary side rms voltage
i_s	960.4	[A]	secondary side rms current
φ_u	$3.47 \cdot 10^{-4}\pi$	[rad]	phase angle between u_p and u_s
φ_p	0.1π	[rad]	phase angle between u_p and i_p
φ_i	1.46π	[rad]	phase angle between i_p and i_s
φ_s	1.36π	[rad]	phase angle between u_s and i_s

Table 4.4 Calculated and measured transformer losses

loss [W]	calculated	measured
core	11,023	11,280
winding	65,091	62,769
stray	16,180	16,277

Furthermore, the core losses do neither flow entirely through the windings. The part of the transformer core that is surrounded by the windings generates the heat which must flow through the windings (cp. Figure 4.12 and 4.14). In addition, the part of transformer core which is outside the windings affects the temperature distribution, too (cp. Figure 4.16) because the heat is not directly dissipated (in radial direction) to the surrounding fluid (oil). Rather, before it is absorbed by the oil, it has to flow, at least to a certain extent, through the transformer core causing a higher winding temperature. This is demonstrated by the heat flow path A and path B in Figure 4.16 which shows the schematically the top view of the transformer used by Kwean *et al.* [15]. On path A the heat is directly dissipated to the surrounding fluid, while on path B the heat must flow through the outer transformer part which also generates additional heat (core losses). To consider the latter in the winding temperature calculation, a fictive shell around the windings can be assumed through which the heat must flow (cp. Figure 4.16). Note that this only applies for path B and is a rough approximation describing the worst case scenario.

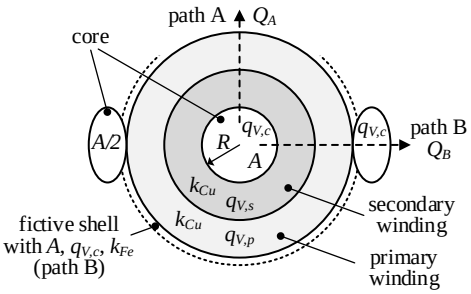

Figure 4.16 Transformer top view with different paths of radial heat flow

Moreover, from Table 4.4 it can be seen that the core losses are significantly lower than the winding losses. Using in addition to that only a part of the core losses means that small deviations in the core losses calculations have an insignificant influences on the winding hot spot calculations. On the other hand, as the winding losses are the main losses, they are crucial for the winding temperature. Consequently, a proper evaluation of the winding resistances is important for the hot spot temperature calculation.

Third, based on the properties of the virtual transformer twin (Table 4.2) and the calculated core and winding losses (Table 4.4) the temperature distribution in the windings is calculated along path A and B. The calculations are executed for a measured oil temperature of *73.7°C* [15] and a thermal conductivity of copper k_{Cu} = *385W/mK* [25], wire insulation (Epoxy impregnation) k_{ins} = *1W/mK* [25] and iron k_{Fe} = *80W/mK* [29].

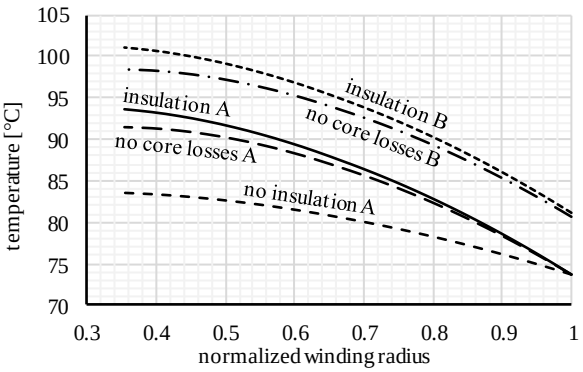

Figure 4.17 Winding temperature distribution

The winding temperature distribution is calculated for a fill factor k_f = *1* and k_f = *0.9974* along path A (cp. Figure 4.17). A fill factor equal to one (k_f = *1*) means that the wire insulation is neglected (cp. “no insulation A” in Figure 4.17) and that the heat is only transmitted via the copper. A fill factor k_f = *0.9974* means that there are small layers of insulation in between the windings through which the heat must flow (cp. Figure 4.14 and 4.15). As the insulation material has a significantly lower thermal conductivity than the copper, very thin layers of insulation cause a notable increase of the calculated winding temperature, i.e. up to *10K* (cp. “no insulation A” and “insulation A” in Figure 4.17). Further, the winding temperature

distribution is calculated neglecting the core losses including the insulation (cp. “no core losses” in Figure 4.17). It is visible that the maximum calculated temperature (hot spot temperature) will be approx. *2K* lower on path A respectively approx. *2.5K* on path B, if the core losses are neglected. Moreover, due to the fictive shell around the windings the temperature distribution on path B is increased by an offset of approx. *7.5K* in comparison to path A (cp. “insulation” in Figure 4.17). This increase is caused by i) the heat (core losses) generated in the fictive shell and ii) the thermal conductivity of iron which is lower than that of copper. In addition, note that the winding radius in Figure 4.17 is normalized with the maximum radius of the primary side winding and that in this case study the secondary side winding is surrounded by the primary side winding (cp. also [15] and Figure 4.16). The low normalized winding radii thus represent the windings that are a the inside of the transformer, and Figure 4.17 shows that the temperature reaches its maximum at these windings.

From Figure 4.17, it is visible that the calculated winding hot spot temperature (at the inner side of the secondary winding) considering the insulation is *93.6°C* on path A and *101.0°C* on path B. For comparison, Kwean *et al.* [15] measured a temperature of *98.0°C* on path A, *105.9°C* on path B and calculated a temperature of *92.6°C* based on the IEEE / IEC loading guide. So the hot spot temperature calculated with insulation approximates the measured hot spot temperatures. The hot spot temperature according to the loading guide is lower than evaluated with the method proposed in this chapter (cp. path B). So values of the correction factor *K* (cp. Eq. 4.4) provided by the IEC standard appear to be too small. This confirms the Kwean *et al.* [15] findings and concerns that higher correction factors should be applied in the IEEE and IEC standards. The results also confirm that the proposed method allows to quite accurately determine the winding temperatures.

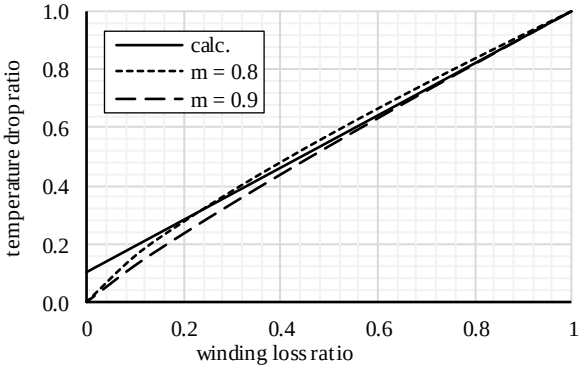

Figure 4.18 Evaluation of empirical winding exponent (insulation A)

Fourth, the winding temperature calculation with the proposed method also provides the evaluation of the winding exponent *m* (cp. Eq. 4.4). To do so, the calculated differences between hot spot and oil temperature are normalized by the rated difference, i.e. the temperature drop ratio is evaluated. Then, this ratio is plotted over the winding loss ratio (cp. “calc.” Figure 4.18). The winding loss ratio is defined by the ratio of the actual winding losses to rated winding losses. Note that the core losses are considered in the temperature drop ratio. Therefore, the temperature drop ratio is not zero at zero winding losses in Figure 4.18. For comparison the winding loss ratio, which is equivalent to the power two of the current ratio in Eq. 4.4, is calculated for a winding exponent $m = 0.8$ and $m = 0.9$ (cp. Figure 4.18). It is

visible that a winding exponent of *0.8* fits better to the calculated temperature drop ratio. Kwean *et al.* [15] used based on the IEC standard recommendations a winding exponent of *0.8* for the considered transformer. This means that the calculated and empirically evaluated winding exponents coincide.

4.5 Discussion

Now, after the proposed methods for calculating the transformer losses and hot spot temperature has been introduced and demonstrated, some issues remain for discussion.

First, the case study and validation reveal that with the proposed method the hot spot temperature can be estimated for an effective fill factor $k_f = 0.9974$, i.e. considering small layers of insulation. This means on the one hand that the winding insulation cannot be neglected and, on the other hand, that the actual fill factor, which is significantly smaller than one (e.g. $\pi/4$), does not apply. The effective fill factor is derived here from the ratio of the thermal conductivity of the insulation ($k_{ins} = 1W/mK$) and the copper ($k_{Cu} = 385W/mK$) as follows:

$$k_f = 1 - \frac{k_{ins}}{k_{Cu}} = 1 - \frac{1}{385} = 0.9974 \tag{4.88}$$

For explaining Eq. 4.88, two wires are considered in radial winding direction (cp. Figure 4.19). It is assumed that heat is only transported through the parts of the (insulated) wires that are in contact, i.e. the gaps between the wire cross sections do not contribute to the heat transport. This assumption is motivated by the significant difference in thermal conductivity of the wires and the gaps (oil), $k_{Cu} >> k_{oil}$.

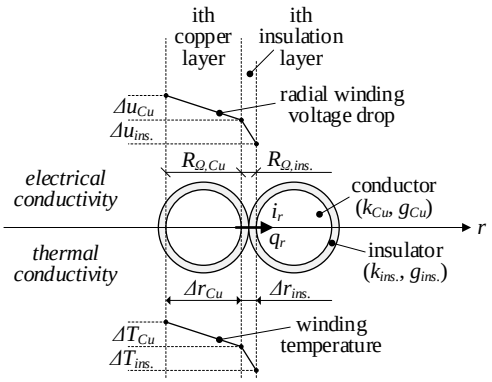

Figure 4.19 The cross section of two circular wires in radial winding direction

It is assumed that the specific heat flow q_r in radial direction is equal in the ith insulation and copper layer. Then, it follows with Eq. 4.72:

$$\frac{k_{ins}}{k_{Cu}} = \frac{\Delta r_{ins}}{\Delta r_{Cu}} \frac{\Delta T_{Cu}}{\Delta T_{ins}} \tag{4.89}$$

Further, the Wiedemann-Franz law applies. It defines the ratio of the thermal and electrical conductivity with the (material) temperature T and the Lorenz number $L = 2.44 \cdot 10^{-8}\ W\Omega/K^2$.

$$\frac{k}{g} = LT \tag{4.90}$$

with the electrical conductivity g is specified by (cp. Eq. 4.18):

$$g = \frac{1}{R_\Omega}\frac{l_\Omega}{A_\Omega} \tag{4.91}$$

If small temperature drops ΔT across ith layers are assumed, the temperature T in the ith layers is almost constant and hence, the ratio of the thermal and electrical conductivity (cp. Eq. 4.90). With a constant specific heat flow q_r in the ith layers and with $l_\Omega = \Delta r$ and $A_\Omega = A_r$ (cp. Eq. 4.71), this yields the following relation for the temperature drop and radial ohmic resistance of the insulation and copper layers:

$$\frac{k_{ins}}{k_{Cu}} = \frac{\Delta r_{ins}}{\Delta r_{Cu}}\frac{\Delta T_{Cu}}{\Delta T_{ins}} = \frac{l_{\Omega,ins}}{A_{\Omega,ins}}\frac{R_{\Omega,cu}}{R_{\Omega,ins}}\frac{A_{\Omega,Cu}}{l_{\Omega,Cu}} = \frac{g_{ins}}{g_{Cu}}$$

$$\frac{\Delta T_{ins}}{\Delta T_{Cu}} \approx \frac{R_{\Omega,ins}}{R_{\Omega,Cu}} \tag{4.92}$$

This means that a high radial ohmic layer resistance $R_{\Omega,ins}$ leads to a high temperature drop ΔT_{ins}. Both $R_{\Omega,ins.}$ (cp. Eq. 4.91) and ΔT_{ins} (cp. Eq. 4.72) increase with the insulation layer thickness Δr_{ins}. A high radial ohmic layer resistance $R_{\Omega,ins}$ is desired to minimize the radial current i_r across the windings caused by the radial winding voltage drop. The latter is determined by the winding terminal voltages and thus, is given by external transformer conditions. On the other hand, a low temperature drop ΔT_{ins} is preferred to reduce the temperature increase in the windings, i.e. the hot spot temperature and eventually the insulation aging process. However, this is a dilemma and requires the optimal insulation layer thickness to satisfy both a high radial resistance $R_{\Omega,ins}$ and a low temperature drop ΔT_{ins}.

To do so, it is assumed here that the radial current i_r across the windings is equal in the ith copper and insulation layer. Further, the total radial voltage drop across the ith copper and insulation layer is evenly distributed, i.e. $\Delta u_{Cu} \approx \Delta u_{ins}$. With Eq. 4.92 this yields to $\Delta T_{Cu} \approx \Delta T_{ins}$ The even distribution of both voltage and temperature drop provides the benefit that the mechanical stresses (i.e. deformation due to the voltage drop [30][31]) and thermal stresses (due to the temperature trop) are limited in the insulation layer. As the total radial voltage drop is given by external conditions a minimum insulation layer thickness is needed to limit the mechanical stresses level. On the other hand, this minimum thickness determines the thermal stress level. So the conditions $\Delta u_{Cu} \approx \Delta u_{ins}$ and $\Delta T_{Cu} \approx \Delta T_{ins}$ define a balance point of mechanical and thermal stress levels in the insulation layer. Based on these considerations Eq. 4.89 can be simplified and Eq. 4.88 is obtained again assuming that only the ratio between the radial dimensions (Δr) of copper and insulation determine the (effective) fill factor (and the gaps can be neglected). This also explains the high k_f value.

In addition, as the calculated hot spot temperature ($93.6°C$) (cp. “insulation A” in Figure 4.17) is between the measured ($98.0°C$) and calculated ($92.6°C$) temperature based on the IEEE / IEC loading guide [15], it appears that the here assumed voltage and temperature drop distribution across the ith copper and insulation layer are appropriate. However, to limit the

scope of this chapter the optimal insulation layer thickness and balance point of mechanical and thermal stress levels are not further discussed. This is left for future research.

Second, the accuracy in creating the virtual transformer twin also influences the hot spot temperature. If the dimensions of the virtual twin are smaller than the actual transformer, then a higher hot spot temperature will be calculated because the winding volume affects the calculations (cp. Eq. 4.63 and 4.64). To validate whether the dimensions of the virtual twin are estimated properly, the measured and calculated winding resistances are compared. Remember that the winding resistances depend on the winding lengths (cp. Eq. 4.18), i.e. winding radii. Hence, if the measured and calculated winding resistances coincide, then it can be concluded that the dimensions of the virtual twin and actual transformer match. As this is the case here (cp. Table 4.1 and 4.2), the calculated temperature distribution (cp. Figure 4.17) and hot spot temperature can be considered to be representative for the actual transformer. Furthermore, the assumption of radial heat flow leads to a deviation between the calculated and measured hot spot temperatures. Although the heat mainly flows in radial direction, multiple directional heat flows occur in reality. This means that the winding temperature is not only determined by the losses generated in the windings and in the transformer core surrounded by the windings. Rather, the losses of the entire core as well as the stray losses, which are not considered here at all, additionally affect the winding temperature distribution. Consequently, higher local temperatures occur in the transformer windings. This makes that the measured temperature is higher than the calculated hot spot temperature, which matches with the results presented in the previous section. From this perspective, the presented method leads to a non-conservative prediction.

Third, the core losses are determined by the vector diagram and the approximation of the core hysteresis by an ellipse. The latter applies only for ideal working conditions where harmonics are not present. However, as the core losses are significantly smaller than the winding losses and, in addition to that, the core losses are only partly considered in the winding temperature calculation, the proposed method can still be used with the presence of harmonics. This would then mean that the harmonics are neglected in the core loss calculation, but they are considered in the winding loss calculation. This yields a slightly less conservative temperature prediction, as the core losses have a minor influence on the winding temperature distribution (cp. Figure 4.17).

Fourth, to demonstrate the significance of the hot spot temperature on the winding life time, Eq. 4.1 is applied for a specific temperature range. The inverse of the ageing acceleration factor ($1/F_{AA}$) is shown in Figure 4.20. It is visible that the higher the hot spot temperature, the lower the inverse value $1/F_{AA}$. This means for an increase of the hot spot temperature by $1K$, the winding life time is reduce by approx. 10% (Eq. 4.2). Therefore, a proper determination of the hot spot temperature is essential to predict the transformer life time.

Fifth, the here proposed method uses Eq. 4.79 to evaluate the hot spot temperature (i.e. T_{in}) while the IEEE / IEC load guides apply Eq. 4.4. Comparing these equations yields the following:

$$\frac{Q^*}{2\pi l_w k}\ln\left(\frac{r_{out}}{r_{in}}\right) - \frac{q_V}{4k}\left(r_{in}^2 - r_{out}^2\right) \leftrightarrow K \cdot \Delta\theta_{HR}\left(\frac{I}{I_R}\right)^{2m} \tag{4.93}$$

It can be seen that both Eq. 4.4 and 4.79 consider the transformer dimensions. The proposed method uses the inner (r_{in}) and outer (r_{out}) winding radius as well as the winding length (l_w). In the IEEE / IEC load guide the correction factor K, exponent m and measured temperature drop $\Delta\theta_{HR}$ depend on the transformer type and design (dimensions). Then, the generated heat (q_V) in as well as the heat flow (Q) through the windings is determined by the core and winding losses. As the winding losses dominate, the generated heat and the heat flow are almost proportional to the square of the winding currents (cp. ohmic winding losses in Eq. 4.23 and 4.24). This is equivalent to the exponent two of the current ratio used in the IEEE / IEC loading guide. Further, the proposed method use the thermal conductivity of the windings (copper) and insulation material. The IEEE / IEC loading guide includes the thermal conductivity in the measured temperature drop $\Delta\theta_{HR}$. This comparison shows that the proposed method utilizes the same elements as the IEEE / IEC loading guide and thus, is general and representative for many transformers.

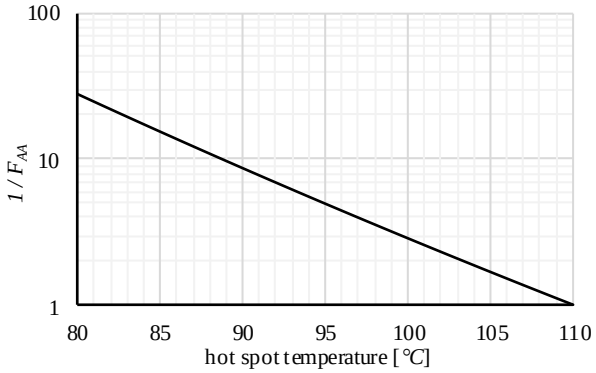

Figure 4.20 Winding ageing as a function of the hot spot temperature

Sixth, the input parameters for calculating the transformer losses rely on (phase angle) estimations. It was already discussed in the previous section that this has a minor influence on the calculated hot spot temperature because core losses are only slightly affected and winding losses are not at all affected by these estimations. However, if the proposed method is used to evaluate not only core and winding losses but also the stray losses, then further validations will be necessary as the stray losses are sensitive to these estimations. This is left for future research and is thus outside the scope of this chapter.

4.6 Conclusion

End customers and consultancy companies often deal with a lack of information and cannot always use the established methods for life time prediction. Therefore, the present chapter provides an alternative way to evaluate the life time of power transformers based on limited information. The approach is applied to one phase of a 154kV, 15MVA power transformer and the results are compared with loss and winding temperature measurements as well as temperature calculations according to the IEEE / IEC loading guides which are available in literature.

- The transformer losses are calculated based on rms current and voltage measurements (including phase angles). Then, the temperature distribution in the transformer windings is evaluated using i) core and winding losses and ii) a virtual transformer twin. Stray losses are not considered in the winding temperature calculation because only a minor portion of them can be assigned to the windings. The virtual transformer twin is created based on the transformer rating information.
- Depending on the considered path of heat flow, the hot spot temperature calculated with the proposed methods deviates from the temperature calculated according to the IEEE / IEC loading guides. Hot spot temperature measurements provided in literature show a similar deviation: higher temperatures are measured than those calculated according to the IEEE / IEC loading guides. Therefore, it appears that values of the hot spot factor recommended in these standards are too small, leading to an underestimation of the hot spot temperature. Moreover, the proposed method yields temperature values that are closer to the measured values.
- It is shown that the consideration of the winding insulation is crucial to properly determine the hot spot temperature. The factor used to indicate the winding insulation thickness is slightly smaller than one, but significantly higher than the actual fill factor. It appears that the insulation thickness factor must be determined from the thermal conductivity of the insulation material and copper (winding). An even distribution of the radial voltage and temperature drop over the copper and insulation layer appears to specify the optimal insulation (layer) thickness.
- It has been demonstrated that the hot spot temperature prediction of power transformers based on limited information is not only feasible but also provides a calculation accuracy equivalent to the established methods. Therefore, the proposed methods are an alternative way to calculate the transformer hot spot temperature and thus, to predict the transformer life time.

References

[1] R. Bi, K. Qian, C. Zhou, D. M. Hepburn, and J. Rong, "A survey of failures in wind turbine generator systems with focus on a wind farm in China," *Int. J. Smart Grid Clean Energy*, pp. 366–373, 2014.

[2] D. P. Rommel, D. Di Maio, and T. Tinga, "Calculating wind turbine component loads for improved life prediction," *Renew. Energy*, vol. 146, 2020.

[3] D. P. Rommel, D. Di Maio, and T. Tinga, "Calculating Loads and Life Time Reduction of Wind Turbine Gearbox and Generator Bearings due to Shaft Misalignment," *Wind Eng.*, 2020.

[4] IEEE Std C57.91, *IEEE Guide for Loading Mineral-Oil- Immersed Transformers*. 1999.

[5] IEEE Std C57.100, "IEEE Standard Test Procedure for Thermal Evaluation of Liquid-Immersed Distribution and Power Transformers," 1999.

[6] IEC 60354, *Loading guide for oil-immersed power transformers*. 1991.

[7] K. Najdenkoski, G. Rafajlovski, and V. Dimcev, "Thermal aging of distribution transformers according to IEEE and IEC standards," *2007 IEEE Power Eng. Soc. Gen. Meet. PES*, no. January 2017, 2007.

[8] M. H. Roslan, N. Azis, M. Z. A. Ab Kadir, J. Jasni, Z. Ibrahim, and A. Ahmad, "A simplified top-oil temperature model for transformers based on the pathway of energy transfer concept and the thermal-electrical analogy," *Energies*, vol. 10, no. 11, 2017.

[9] M. Srinivasan and A. Krishnan, "Prediction of Transformer Insulation Life with an Effect of Environmental Variables," *Int. J. Comput. Appl.*, vol. 55, no. 5, pp. 43–48, 2012.

[10] B. Gorgan *et al.*, "Calculation of the remaining lifetime of power transformers paper insulation," *Proc. Int. Conf. Optim. Electr. Electron. Equipment, OPTIM*, no. 2012, pp. 293–300, 2012.

[11] Y. Biçen, F. Aras, and H. Kirkici, "Lifetime estimation and monitoring of power transformer considering annual load factors," *IEEE Trans. Dielectr. Electr. Insul.*, vol. 21, no. 3, pp. 1360–1367, 2014.

[12] M. T. Ishak and Z. Wang, "Transformer hotspot temperature calculation using IEEE Loading Guide," *Proc. 2008 Int. Conf. Cond. Monit. Diagnosis, C. 2008*, no. May, pp. 1017–1020, 2007.

[13] S. Ghosh, "Calculation of Hot Spot Temperature and Aging of a Transformer," *Int. J. Tech. Res. Appl.*, vol. 4, no. 1, pp. 140–143, 2016.

[14] M. Srinivasan, "Prediction and Simulation of Hot Spot Temperature with an Effect of Environemntal driving variables," vol. 3, no. 6, pp. 59–63, 2012.

[15] D. J. Kweon, K. S. Koo, J. W. Woo, and J. S. Kwak, "A study on the hot spot temperature in 154kV power transformers," *J. Electr. Eng. Technol.*, vol. 7, no. 3, pp. 312–319, 2012.

[16] IEEE Std C57.120, "IEEE Guide for Loss Evaluation of Distribution and Power Transformers and Reactors," pp. 1–53, 2017.

[17] E. F. Fuchs, T. Stensland, W. M. Grady, and M. Doyle, "Measurement of harmonic losses of pole transformers and single-phase induction motors," *Proc. 1994 IEEE Ind. Appl. Soc. Annu. Meet.*, vol. 1, pp. 128–134, 1994.

[18] D. Lin and E. F. Fuchs, "Real-time monitoring of iron-core and copper losses of transformers under (non)sinusoidal operation," *IEEE Trans. Power Deliv.*, vol. 21,

no. 3, pp. 1333–1341, 2006.
[19] L. Kralj and D. Miljavec, “Stray losses in power transformer tank walls and construction parts,” *19th Int. Conf. Electr. Mach. ICEM 2010*, 2010.
[20] G. Müller and B. Ponick, *Grundlagen elektrischer Maschinen*. Wiley, 2012.
[21] J. Hopkinson, “VIII. Magnetisation of iron,” *Philos. Trans. R. Soc. London*, vol. 176, pp. 455–469, 1885.
[22] P. Bhatt, *ICSE Physics Book-II For Class-X*. S. Chand Publishing.
[23] R. A. Matula, “Electrical resistivity of copper, gold, palladium, and silver,” *J. Phys. Chem. Ref. Data*, vol. 8, no. 4, pp. 1147–1298, 1979.
[24] V. Barbu, *Partial Differential Equations and Boundary Value Problems*. Springer Netherlands, 1998.
[25] R. Wrobel, S. Ayat, and J. L. Baker, “Analytical methods for estimating equivalent thermal conductivity in impregnated electrical windings formed using Litz wire,” *2017 IEEE Int. Electr. Mach. Drives Conf. IEMDC 2017*, no. May, 2017.
[26] Y. Lv, C. Li, Q. Sun, and M. Huang, “Effect of Dispersion Method on Stability and Dielectric Strength of Transformer Oil-Based TiO 2 Nanofluids,” *Nanoscale Res. Lett.*, vol. 11, 2016.
[27] Y. S. Kim, “Magnetic saturation effect of the iron core in current transformers under lightning flow,” *Trans. Electr. Electron. Mater.*, vol. 18, no. 2, pp. 97–102, 2017.
[28] T. Vaimann, O. Kudrjavtsev, A. Kilk, A. Kallaste, and A. Rassolkin, “Design and prototyping of directly driven outer rotor permanent magnet generator for small scale wind turbines,” *Adv. Electr. Electron. Eng.*, vol. 16, no. 3, pp. 271–278, 2018.
[29] W. M. Haynes, *CRC Handbook of Chemistry and Physics*. CRC Press, 2011.
[30] P. R. Mamy, L. Boudou, and J. Martinez-Vega, “Correlation between electrical conduction and mechanical deformation induced by an electrical field to PET,” in *Energy Procedia*, 2004, vol. 2, pp. 615-618 Vol.2.
[31] P. R. Mamy, J. Martinez-Vega, J. C. Dupre, and N. Bretagne, “Quantification of mechanical deformations induced by an electric field in a semicrystalline organic insulator,” *J. Appl. Polym. Sci.*, vol. 93, no. 5, pp. 2313–2321, 2004.

CHAPTER 5

Wind Turbine Power Train Reliability from a Physics-based Design Perspective

ABSTRACT

The interest of wind turbine industries in wind turbine power train reliability has increased during the last years because component failures are associated with high cost and long downtime. In this chapter the wind turbine power train reliability is considered from a physics- and design-based perspective, i.e. reliability is increased by reducing loads. To improve the reliability, principles for load reduction are used, namely: minimization of load magnitude, prevention of load superposition, specification of system excitation and evaluation of transfer function. These principles are applied to the mechanical subsystem of the wind turbine power train. Therefore, the load magnitudes of a wheel-two-pinion and planetary gear stage are quantified. Methods to evaluate shaft bending and tilting during operation are proposed to minimize mesh misalignment, i.e. to prevent load superposition. Further, a simple specification of the drive train excitation by the wind turbine rotor and generator is derived. It is demonstrated that being able to determine the (relative) reliability using the proposed methods provides benefits to a system designer, owner or service provider. Finally, the proposed methods prove that the system design, maintenance and reliability are interconnected and that improvements of system maintenance and reliability are related to the system design.

This chapter is based on: Rommel, D. P., Di Maio, D., Tinga, T. (n.d.). Wind Turbine Power Train Reliability from a Physics Based Design Perspective. submitted.

Nomenclature

SYMBOL	UNIT	QUANTITY
A	-	transfer function
a	[m/s²]	acceleration
B	-	bearing
C_d	-	drag coefficient
C_l	-	lift coefficient
c	-	planet carrier
c	[m], [N/m]	chord length, stiffness
D	[m]	diameter
d	-	drag
E	[N/m²]	elastic modulus
F	[N]	force
F, f	-	function
G	-	function, gear
GB	-	gearbox
Ge	-	generator
GM	-	gear mesh
H	-	function, hollow
I	[m⁴]	area moment of inertia
I_R	[A]	generator rotor current
I_S	[A]	generator stator current
i	-	(stage) transmission ratio
i_0	-	stationary gear ratio
i_D	-	diameter ratio
K_A	-	application factor
K_V	-	dynamic factor
K_H, K_F, K_B	-	load distribution factors
k_l	-	non-dimensional length
k_S	-	solid shaft geometry factor
k_H	-	hollow shaft geometry factor
k_p	-	number of pinions
k_{pl}	-	number of planets
L, l	[m]	length
l	-	lift
M	[Nm]	moment
m	[kg]	mass
n	[rad/s], -	shaft speed, normal (direction)
P	-	reliability
p	-	pitch, pinion
pl	-	planet gear
q	-	multiple
R	[m]	radius
r	[m]	radius
rg	-	ring gear
Δr	[m]	blade section length
rot	-	wind turbine rotor
S	-	shaft
s	-	sun gear
st	-	(gear) stage
T	[Nm]	torque
THD	-	total harmonic distortion
t	-	tangential (direction)
u	[m/s]	circumferencial velocity
v	[m/s]	velocity
w	[m], -	displacement, wheel, wind
$w_{rel.}$	[m/s]	relative velocity
x	[m]	coordinate
dX / dt	-	normalized velocity
dx / dt	[m/s]	time derivative of coordinate (velocity)
Z	-	number
α	[rad]	angle of attack
β	[rad]	blade twist / pitch angle
Θ	-	inertia tensor
κ	-	ratio
λ_r	-	speed ratio
ρ	[kg/m³]	density
σ	[MPa], -	stress, standard deviation
τ	[N/m²]	torsional stress
φ	[rad]	angle of relative wind
ω	[1/s]	angular speed, excitation frequency

5.1 Introduction

Surveys of failures in wind turbine systems evaluated during the last decades have highlighted that wind turbine subsystems like gearboxes, generators and power converters have significant failures rates and downtimes [1]–[6]. To avoid the costly failures and high downtimes of gearboxes, especially in offshore wind turbines, direct drive wind turbines are often favored. However, reliability analyses of wind turbine subassemblies show that direct drive wind turbines are not necessarily more reliable than geared wind turbines [7]. Failure rates of (permanent magnet) generators and (fully rated) converters in direct drive wind turbines are greater than those of gearboxes, (double fed induction) generators and (partly rated) converters in geared wind turbines [7][8]. Further, the failure frequencies of larger direct drive generators are significantly higher than those of geared drive generators [7].

To improve the reliability of wind turbine systems, literature often proposes the usage of new design tools [9], the rigorous (field) testing of the different wind turbine subassemblies [7][9], the substitution [10] or modification [11][12] of particular drive train components, the consideration of the wind load uncertainty [13] and failure mechanism [14] or simply the identification of critical components combined with condition monitoring [15][16]. However, system reliability already begins at early concept stages while designing the system [17]. This means that the wind turbine reliability starts before using new design tools, testing components or installing condition monitoring systems. It also means that reliability improvements will be most effective, if the entire (wind turbine) system is considered instead of substituting or modifying particular components. Further, to address and identify reliability concerns during design and development processes, a physics of failure approach is proposed [18]. It demonstrates a better accuracy than the traditional experience based approach because it is based on identifying the critical failure modes and on quantifying the impact of contributing environmental factors [18]. This means that physics- and design-based methods are needed to quantify and qualify the reliability during early system concept stages. Methods determining the reliability based on the system concept provide benefits for system designer, owner and service provider because these methods cannot only be used for new system developments but can also be applied to already installed systems. System concept considerations are possible using basic information to which system owners and service providers normally have access. This is particularly advantageous for them because they often deal with a lack of information and thus, cannot use the same methods as system designers.

Scientific literature analyzing the wind turbine power train reliability from a physics-based design conceptual point of view seems to be very limited. The reason for design-based approaches not being present in scientific literature is probably that OEMs have developed these, but do not want to share (for competitive reasons). Reliability evaluations and estimations considering the concepts and designs of wind turbine power trains could not be found at all. Therefore, the main objective of this chapter is to develop methods to assess the reliability of wind turbine power trains adopting a physics-based design perspective. The developed methods should be i) accessible to both system designer, owner and service provider, ii) assess the reliability of existing (wind turbine power train) designs and iii) increase the reliability of new designs.

To achieve that, a few essential (design) requirements are derived to increase the wind turbine power train reliability (in section 5.2). Then, the principle of load reduction is used for developing reliability assessment methods and improvements because the reliability is

defined by the interference between system stresses (loads) and strengths [19]. This is applied and discussed in sections 5.3 to 5.5 for some design aspects of the wind turbine drive train (i.e. the mechanical subsystem of the power train). The minimization of the load magnitude is analyzed in section 5.3. This is of particular importance for low speed and high torque applications like the wind turbine. Then, in section 5.4 methods are shown to prevent load superposition in the drive train, particularly at the gear meshing. Furthermore, a simple definition of drive train excitation (additional loads) due to wind turbine rotor and generator is developed in section 5.5. The (drive train) excitation is quantified by application factors similar to the DIN 3990 standard [20] for the calculation of load capacity of cylindrical gears in driving and driven machines. In addition, the transfer behavior and thus the (dynamic) loads of the drive train are considered. However, due to its extent, the transfer functions (behavior) are developed and discussed in a separate chapter.

5.2 Increasing the reliability by system load reduction

From a physical perspective, system reliability is equivalent to the probability that the distribution of the system loads (stresses) is smaller than the distribution of the system strength [19]. This means that the system reliability can be enhanced by either increasing the system strength or by decreasing the system loads (cp. Figure 5.1a). An increase of the system strength, i.e. an increase of the load capacity of the system components, typically leads to bigger system (component) dimensions and thus to a rise of the system weight. The latter, however, must be avoided in wind turbine power trains to minimize the tower head weight. So system reliability should preferably be raised by decreasing system (component) loads. This can be achieved by reducing the mean value of the load distribution μ_L or the load standard deviation σ_L (cp. Figure 5.1b). A decrease of the mean value is obtained by either reducing the load magnitude or preventing the superposition of different types of loads. Minimizing the effects of load variations decreases the standard deviation.

Further, the reliability is quantified by the load (μ_L, σ_L) and strength (μ_S, σ_S) mean values and standard deviations as follows [19]:

$$R = P(load < strength) = \Phi(Z) \tag{5.1}$$

with the probability P, the cumulative distribution function Φ and the standard (normal) deviate Z.

$$Z = \frac{\mu_L - \mu_S}{\sqrt{\sigma_L^2 + \sigma_S^2}} = \frac{\mu_L}{\sigma_L} \frac{1 - \frac{\mu_S}{\mu_L}}{\sqrt{1 + \left(\frac{\sigma_S}{\sigma_L}\right)^2}} \tag{5.2}$$

From Eq. 5.2, it is visible that the standard deviate Z depends on the ratios μ_L / σ_L, μ_S / μ_L and σ_S / σ_L. Then, the standard normal distribution can be applied to evaluate the influence of these ratio on the reliability. This is presented in Figure 5.1c. It can be seen that the mean value ratio μ_S / μ_L provides the most effective way to influence the reliability followed by the ratio of mean value and standard deviation μ_L / σ_L. The ratio of the standard deviations σ_S / σ_L has a minor influence.

These considerations demonstrate that decreasing the system loads will provide substantial improvements of the reliability assuming that the system strength remains constant. More specifically, a 10% load reduction that increases the ratio μ_S / μ_L (i.e. the safety factor) from *1.1* to *1.2*, increases the system reliability from 78% to 94%. It also means that reducing the load magnitude, preventing load superposition, i.e. increasing the mean value ratio μ_S / μ_L, or minimizing load variation, i.e. increasing the ratio μ_L / σ_L, are important principles to achieve a high system reliability.

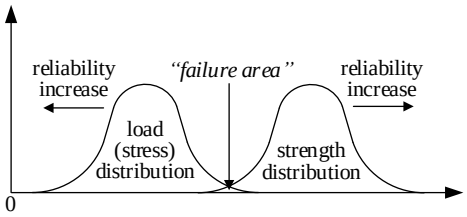

a) Reliability due to stress strength interference

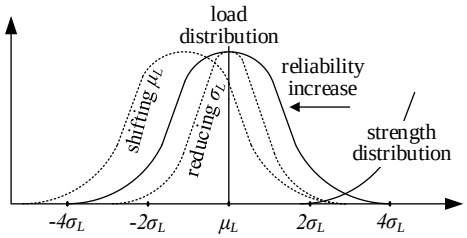

b) Reliability increase by shifting the mean value μ_L or reducing the standard deviation σ_L

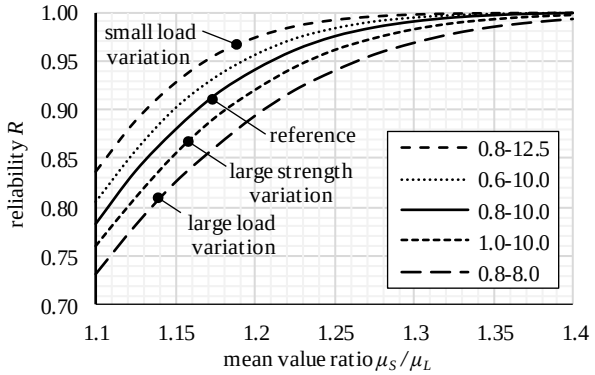

c) System reliability as function of the strength to load the mean value ratio μ_S / μ_L depending on the ratios $\mu_L / \sigma_L \in \{8.0;10;12.5\}$ and $\sigma_S / \sigma_L \in \{0.6;0.8;1.0\}$

Figure 5.1 System reliability from a load reduction perspective

Furthermore, the consideration of (system) loads is not only related to the design and reliability but also to maintenance. For example, the authors previously proposed [21] to use system loads for maintenance prediction. This means that system design, maintenance and reliability are interrelated. This interrelation is created by the system loads which are

specified during design, evaluated based on actual measurements for (load-based) maintenance [21] and which, at the end, are decisive for the system reliability (cp. Figure 5.2).

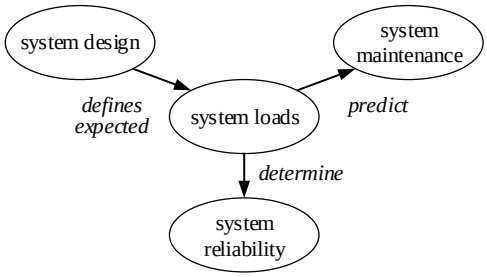

Figure 5.2 Interconnection of system design, maintenance and reliability by system loads

From this perspective, it can be seen that the system maintenance and reliability both depend on the system design. Design choices affect the system performance, strengths and loads (stresses). These aspects, specify the maintenance intensity of a system as well as its reliability. So if a system shall have a low maintenance intensity and high reliability, then the system design will have to be such that low system loads (and simultaneously high system strength) can be guaranteed. This means on the other hand that physics- and design-based methods cannot only be used to specify system design and to quantify and qualify system reliability but also to predict maintenance. This will be shown later in this chapter.

Moreover, system loads can be divided into primary and secondary loads. Primary loads are normally needed to convert the system input to the system output. This means that it is challenging to reduce the magnitude of these loads and that a load reduction is easier to achieve by avoiding load superposition. On the other hand, the secondary (oscillating) loads do not participate in the system input-output conversion, but only interfere with it, and thus are unwanted. Consequently, system load reduction (reliability increase) is most effectively achieved by avoiding, or at least by minimizing, secondary system loads. If the system is nevertheless exposed to unavoidable secondary loads (e.g. due to external system excitation via the system input or output), then the system will have to be designed such that the secondary loads are absorbed, i.e. that they disappear on the internal system path between input and output (cp. Figure 5.3).

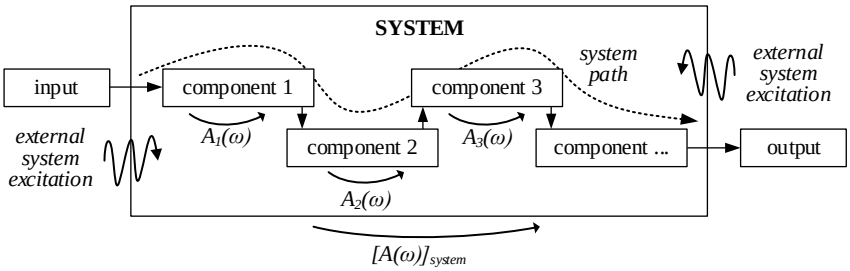

Figure 5.3 System with external excitation where the component transfer functions $A_i(\omega)$ determine whether the external excitations are damped or propagated through the system

In this chapter these considerations are applied to the system “wind turbine power train”, which can be divided in a mechanical and electrical subsystem. The two subsystems are connected by the electro-mechanical conversion realized by the generator. The system input (wind turbine rotor) includes secondary loads which are generated by unsteady, asymmetric wind flow and thus are unavoidable [21]. The system output is specified by the (electrical) interface between power train and electrical grid. If the electrical power transformer is considered as interface, then the electrical subsystem will also contain secondary loads due to current and voltage harmonics caused by i) non-linear switches like power diodes or IGBTs in frequency converters [22] or ii) grid disturbances [23][24] (cp. Figure 5.4).

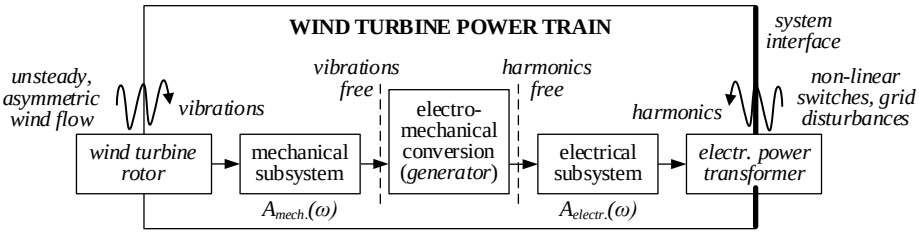

Figure 5.4 Excitation of a wind turbine power train system by mechanical vibrations and electrical harmonics

In order to achieve a high power train reliability, the electro-mechanical conversion (generator) must be free from secondary loads like (torsional) vibrations and (current and voltage) harmonics (cp. Figure 5.4). If this is guaranteed, then i) the loads on the components involved in the electro-mechanical conversion process are minimized and ii) the superposition of secondary loads (vibrations and harmonics) in the mechanical or electrical subsystems will be avoided. In other words, the generator shaft should be free from (torsional) vibrations and the generator terminals free from (current and voltage) harmonics so that the secondary loads of the mechanical and electrical subsystem cannot interfere. This means that vibrations should be absorbed as much as possible in the mechanical subsystem and harmonics in the electrical subsystem to reduce the load magnitude in these subsystems.

Furthermore, it is essential for a high reliability that the system is only exposed to the secondary loads which cannot be avoided at all. This is, for example, the case for the secondary loads (vibrations) due to unsteady, asymmetric wind flow. Hence, the mechanical subsystem of the wind turbine power train must absorb these (torsional) vibrations, i.e. behave as a “filter” in order to avoid torsional vibration at the generator shaft. On the other hand, the secondary loads (harmonics) of the electrical subsystem could, partly be avoided, if, instead of the frequency converter, an alternative component for compensating speed variability were installed in the power train. This means that the mechanical subsystem is more critical than the electrical subsystem because it is exposed to unavoidable external excitation. Therefore, the scope of the present chapter is limited to the mechanical subsystem.

The mechanical subsystem of the wind turbine power train, also called drive train, includes all components which are necessary to transmit the power of the wind turbine rotor to the generator shaft. These components can be reduced to three essential parts, namely: shafts, bearings and gears. Shafts supported by bearings transmit mechanical power from the wind turbine rotor to the generator and gears are used to convert the mechanical power, i.e. to adjust torque and speed. This means that the interaction of shafts (bearings) and gears must comply with two requirements: i) perform with a high reliability despite of excitation loads

due to unsteady, asymmetric wind flow and ii) absorb torsional vibrations, i.e. behave as "filter" to avoid load superposition in the electrical subsystem. Due to their extent, these aspects are discussed in two separate chapters. The performance with a high reliability is presented in this chapter.

Now, to determine the drive train reliability and to eventually improve it, the loads of shafts, bearings and gears must be quantified. As shafts in combination with bearings do not only transmit power, but also support the individual gears inside a gearbox, shaft and bearing loads (forces and moments) are directly related to the gear (mesh) loads. This means that shaft and bearings loads inside a gearbox are determined by the gear mesh reaction loads. It also means that the full drive train reliability can be quantified by the gear mesh loads, i.e. the gear tooth stresses. This is demonstrated by [25][26] providing a detailed reliability calculation of gear transmission systems based on the stress strength interference (cp. Figure 5.1). Given this reliability analysis, the focus of the present work is the improvement of drive train reliability by analyzing different ways to reduce the gear tooth stresses, which implicitly reduces the shaft, bearing and gear loads.

The gear tooth stress calculations in this work will be based on the standard DIN 3990. For example, the tooth (root) bending stress σ_F is given as follows:

$$\sigma_F \sim F_t \, K_F \, K_A \, K_V \tag{5.3}$$

with the rated tangential tooth force F_t, load distribution factor K_F, application factor K_A and dynamic load factor K_V.

The various load factors (K) incorporate the effects of various aspects, and will be quantified for specific applications later. So, to summarize, methods are developed in this chapter to assess the reliability based on the following principles:

- *Minimization of load magnitude*: the gear (and thus also shaft and bearing) loads are determined by the tangential tooth forces F_t. Reducing their magnitude has a direct influence on the actual stresses. The minimization of the load magnitude is evaluated in this chapter for wheel-pinion and planetary gear stages. This will enable the comparison of different gear stages in terms of reliability, as well as quantifying the reliability for different gear dimensions.
- *Prevention of load superposition*: superimposing the loads caused by different effects increases the total loads and stresses. This is discussed in the context of the gear load distribution factors affecting tooth face (K_H), root (K_F) and scuffing (K_B) stresses (DIN 3990). The load distribution factors are influenced by the gear mesh misalignment. So methods are developed to quantify the effects of shaft bending and tilting during operation on the gear loads and system reliability. As the gear mesh misalignment can fluctuate during operation, the introduced methods also include the minimization of load variation.
- *Specification of (sub)system excitation*: the application or service factor K_A of a wind turbine rotor, which specifies the relative increase of the loads in components due to in-service variations and unexpected events, is not defined in DIN 3990 and is not available according to [27]. Therefore, methods are proposed to calculate the drive train

excitation based on simple considerations, i.e. the application factor of a wind turbine rotor as well as generator.

- *Evaluation of transfer function*: the dynamic drive train behavior is governed by the transfer functions *A(ω)* (cp. Figure 5.2). The transfer functions determine how the dynamic loads are propagated through the system and thus, are related to the dynamic load factor K_V applied in DIN 3990. They are also used to derive the drive train "filter characteristic", i.e. the capacity to absorb torsional vibrations and thus, to decouple wind turbine rotor and generator. As already mentioned, this aspect is discussed in a separate chapter.

5.3 Minimization of load magnitudes

The first way to increase (wind turbine drive train) reliability is the minimization of the load magnitude. In this section, this principle is applied to two types of gear stages, i.e. wheel-pinion and planetary gear stages. The design of these stages determines the magnitude of gear, bearing and shaft loads. By comparing the loads of the wheel-pinion and planetary gear stages, it can be decided which stage provides lower load magnitudes (stresses) and thus, a higher reliability of the transmission system.

First, the gear, bearing and shaft loads (forces) are calculated for the wheel-pinion and wheel-two-pinion assemblies (index: *wp*). These assemblies transmit the torque from the low speed rotor shaft to the high speed generator shaft, and only differ by the number of pinions $k_p \in \{1, 2\}$. Therefore, the same equations are valid for these assemblies and a further distinction is not necessary. The shaft (index: *S*), bearing (index: *B*) and gear mesh (index: *GM*) forces for a given transmitted torque *T* are calculated for a spur toothed gear mesh based on Figure 5.5 as follows [28]:

$$F_{S,wp} = \frac{T}{R_{p,p}} \frac{i_{st}}{k_p} \sqrt{1 + (\tan\alpha)^2} = \frac{T}{R_{p,p}} f_{S,wp} \tag{5.4}$$

$$F_{B,wp} = \frac{F_{S,wp}}{2} = \frac{T}{R_{p,p}} \frac{i_{st}}{2\,k_p} \sqrt{1 + (\tan\alpha)^2} = \frac{T}{R_{p,p}} f_{B,wp} \tag{5.5}$$

$$F_{GM,wp} = F_{S,wp} = \frac{T}{R_{p,p}} \frac{i_{st}}{k_p} \sqrt{1 + (\tan\alpha)^2} = \frac{T}{R_{p,p}} f_{GM,wp} \tag{5.6}$$

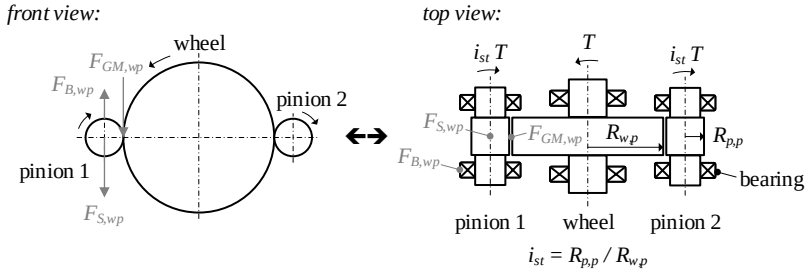

Figure 5.5 Torque and forces at wheel-two-pinion gear assembly

It can be seen from Eq. 5.4 to 5.6 that the shaft, bearing and gear mesh forces depend, on the one hand, on the ratio of the wheel input torque *T* and pinion pitch radius $R_{p,p}$ and, on the

other hand, on the stage transmission ration i_{st}, tooth flank angle α and number of pinions k_p. The three latter gear characteristics can be combined into the functions f_{wp}.

Second, the gear, bearing and shaft loads (forces) are derived for the planetary gear stage (index: *pl*) with a fixed ring gear. This configuration is selected because it provides the highest transmission ratio and is applied in current wind turbine gearboxes as first gear stage. In this case, the low speed rotor shaft is connected to the planet carrier, transmitting the torque to the high speed shaft connected to the sun gear. The shaft, bearing and gear mesh forces are determined for a spur toothed gear mesh (see Figure 5.6) as follows [29]:

$$F_{S,pl} = \frac{T}{R_{s,p}} \frac{1-i_0}{(1+i_0)^2} \frac{1}{k_{pl}} = \frac{T}{R_{s,p}} f_{S,pl} \tag{5.7}$$

$$F_{B,pl} = \frac{F_{S,pl}}{2} = \frac{T}{R_{s,p}} \frac{1-i_0}{(1+i_0)^2} \frac{1}{2\,k_{pl}} = \frac{T}{R_{s,p}} f_{B,pl} \tag{5.8}$$

$$F_{GM,pl} = F_{S,wp} = \frac{T}{R_{s,p}} \frac{1-i_0}{(1+i_0)^2} \frac{\sqrt{1+(\tan\alpha)^2}}{2\,k_{pl}} = \frac{T}{R_{s,p}} f_{GM,pl} \tag{5.9}$$

Again, it is visible from Eq. 5.7 to 5.9 that the shaft, bearing and gear mesh forces at the planet gears depend, on the one hand, on the ratio of the planet carrier input torque T and sun gear pitch radius $R_{s,p}$ and, on the other hand, on the stationary gear ratio i_0 of the planetary gear, tooth flank angle α and number of planet gears k_{pl}. As already done before, the three latter gear characteristics can be combined into the functions f_{pl}.

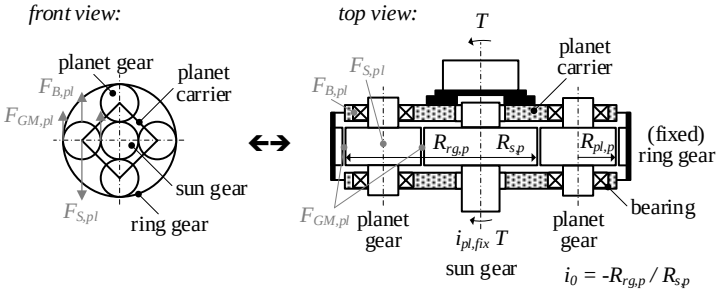

Figure 5.6 Torque and forces at planetary gear assembly

Now, to compare the gear, bearing and shaft loads (forces) of the wheel-pinion(s) and planetary gear assemblies it is assumed that i) all assemblies have the same torque T at their input and ii) pinion and sun gear pitch radius are equal, i.e. $R_{p,p} = R_{s,p}$. This means that the forces of the wheel-pinion(s) and planetary gear assemblies just differ by the functions f_S, f_B and f_{GM}. Consequently, by comparing these functions for the wheel-pinion and planetary gear assembly, it can be identified which assembly faces the lower load magnitudes. This is shown in Figure 5.5 for the number of planets $k_{pl} = 4$ and number of pinions $k_p \in \{1, 2\}$. The stationary gear ratio i_0 varies between *-3* and *-6* and the gear stage ratio i_{st} between *1/3* and *1/12*. Note that Figure 5.7 includes only six curves because $f_{S,wp} = f_{GM,wp}$ and $f_{B,pl} \approx f_{GM,pl}$.

Figure 5.7 shows that the loads for a one pinion gear are a factor two higher than for a two pinion gear (with the same dimensions). Similarly, the loads in the shafts are always a factor two higher than in the bearings assuming symmetric pinion dimensions and even

distributions of the gear mesh loads. The capacity of shaft, bearings and gear will determine which is critical, but that does not change upon changes in gear ratios or gear dimensions.

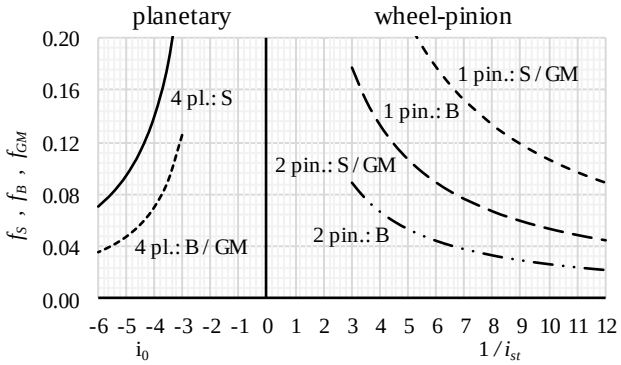

Figure 5.7 Functions f_S (shaft), f_B (bearing) and f_{GM} (gear mesh) for $k_{pl} = 4$ and $k_p \in \{1,2\}$
(Note that plot "1 pin.: B" is equal to "2 pin.: S / GM")

Furthermore, Figure 5.7 demonstrates that with increasing transmission ratios (i_0 or $1/i_{st}$), the shaft, bearing and gear mesh loads of the sun and pinion gear decrease. In fact, a gear stage ($1/i_{st} > 8$) with one wheel and two pinions provides lower shaft and bearings forces and similar gear mesh forces as a planetary gear stage with four planets and a stationary gear ratio i_0 of approx. -5. Realizing planetary gear stages with a stationary gear ratio $i_0 < -5$ is unlikely because the number of planet gears k_{pl}, i.e. their radii (diameters), limit among other influences the stationary gear ratio. Therefore, the wheel-two-pinion assembly with a transmission ratio $i_{st} < 1/8$ provides lower load magnitudes, i.e. it reduces the tangential tooth forces F_t and thus the tooth stresses (cp. Eq. 5.3). Consequently, it also shifts the load distribution to lower magnitudes which leads to a reliability improvement (cp. Figure 5.1).

However, a drawback of the wheel-two-pinion assembly is the power splitting from one to two shafts. This means that a power summation (from two to one shafts) will be necessary at the second gear stage, i.e. a rotating planetary gear stage. It also means that the planetary gear cannot be avoided in a wind turbine transmission system. A planetary gear stage has more parts than a wheel-pinion gear stage and thus, tends to have a lower reliability than the wheel-pinion gear stage. However, shifting the planetary gear from stage one to two in the wind turbine transmission system provides also benefits. At the second stage the planetary gear is exposed to lower load magnitudes. This means that its dimensions and weight can be reduced or that its strength is increased which, again, leads to a reliability improvement (cp. Figure 5.1).

Further, these considerations cannot only be used by gearbox designer but also by owners or service providers. They provide insight in the reliability and maintenance of different gear stages and gearbox designs. In addition to the higher loads (than a wheel-two-pinion gear stage with a transmission ratio $i_{st} < 1/8$) the planetary gear stage is more complex, requires more parts and provides limited installation space, i.e. limits the component strength (cp. limited planet bearing space in Figure 5.6). Further, the usage of the planetary gear stage (with a fixed ring gear) at the first stage leads to low planetary gear speeds. This has a negative influence on the load distribution factor (cp. Eq. 5.3) as will be discussed in the following section. Therefore, the usage of a planetary gear at the first stage of a (wind turbine)

transmission system causes a higher failure area (cp. Figure 5.1), reduces the reliability and increases the maintenance intensity. This is a crucial insight for system owners selecting a transmission system and for service provider maintaining the transmission system. Moreover, these results align with the reliability calculations provided by Ukonsaari and Bennstedt [30]. They compared wind turbine gearboxes with a planetary gear and a wheel-pinion gear assembly at the first stage. The wheel-pinion gear assembly showed 20-65% higher reliability depending on the operating hours and hence, is favored by them for future wind turbine gearbox designs.

Finally, from Eq. 5.4 to 5.9 it can be derived that a torque increase has the same effect as a gear radius decrease. This allows owners and service providers to compare different gear stages and gearboxes of different power ranges. The gear tooth stress, i.e. the tangential tooth force per gear width and module (cp. DIN 3990) should thus be similar, assuming that the gears have similar material characteristics. The gear module is the ratio of the circular pitch and the circle constant π. This also means that a deviation of the tangential force per gear width and module is a first indicator that the assessed gear stages and gearboxes (of different power ranges) will vary in their reliability. A high reliability can be expected for lower values of the tangential force per gear and module and vice versa. The tangential force can be calculated with the provided equations and the transmitted torque and gear radius. Gear width and module can be measured during visual inspection.

5.4 Prevention of load superposition

Avoiding the superposition of different types of loads is the second way to achieve a higher system reliability. This principle is discussed here for the gear mesh misalignment. At the gear mesh different effects are superimposed causing additional loads. Two of these effects are shaft bending and tilting during operation. To achieve a high reliability minimizing or even avoiding these two effects is important so that the gear tooth stresses are kept at an acceptable level. Therefore, in this section simple methods are presented to calculate shaft displacements due to bending and tilting.

5.4.1 Shaft bending

To determine the shaft bending, a shaft with length L and diameter D is analyzed (cp. Figure 5.8). On the shaft the transverse gear reaction load F_S is acting, which could be given, for example, by Eq. 5.4. From Eq. 5.4 it can also be seen that the shaft force can be described as a multiple q of the ratio of the transmitted torque T and shaft diameter D, i.e.:

$$F_S = \frac{T}{R_{p,p}} \frac{i_{st}}{k_p} \sqrt{1 + (\tan \alpha)^2} = \frac{T}{D} q \tag{5.10}$$

where the factor q contains the dimensional details of the specified gear.

With the Euler-Bernoulli beam theory the displacement in z-direction $w(x)$ of this shaft is obtained by considering the sum of all forces and moments with the non-dimensional location of F_S being $k_l \in [0,1]$ boundary conditions $w(0) = w(1) = 0$, E-modulus, area moment of inertia I_y, torsional stress τ and Macaulay brackets:

$$w(x) = \frac{F_S L^3}{E I_y 6} k_x = q k_x \frac{64}{\pi E D^4} \frac{T}{D} \frac{L^3}{6} = \frac{2}{3} q k_x \frac{\tau}{E} \left(\frac{L}{D}\right)^2 L \tag{5.11}$$

with

$$k_x = -\left(x^3(1-k_l) + x(1-k_l)((1-k_l)^2 - 1) - \underbrace{\langle x - k_l \rangle^3}_{Macaulay} \right) \tag{5.12}$$

$$\tau = \frac{16}{\pi} \frac{T}{D^3} \tag{5.13}$$

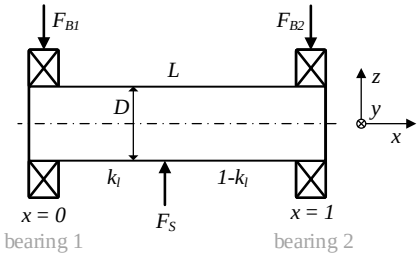

Figure 5.8 Shaft with transverse load F_S

From Eq. 5.11 it can be seen that the shaft displacement *w(x)* for a specific shaft length *L* depends on the value of k_l (position of load F_L), the shaft material (*E*-modulus), applied torsional stress τ and diameter length ratio D / L. Considering these variables a reference shaft displacement can be specified by removing the gear specific factor *q*.

$$w(x)_{ref} = \frac{2}{3} k_x \frac{\tau}{E} \left(\frac{L}{D}\right)^2 L \tag{5.14}$$

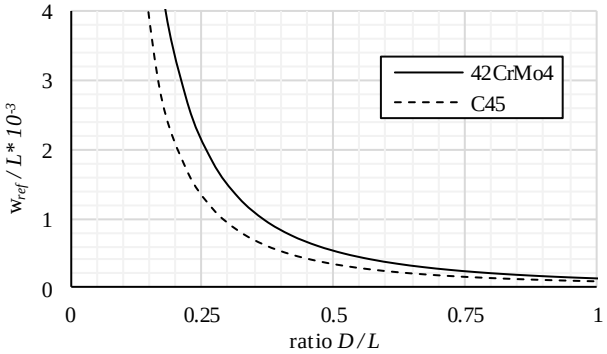

Figure 5.9 Reference shaft displacement w_{ref} per shaft length *L*

Figure 5.9 shows a plot of the reference shaft displacement with the *E*-modulus of steel (210,000 N/mm²). For the shear stress τ, the upper limit is applied by using the torsional (fatigue) strength of C45 (210 N/mm²) and 42CrMo4 (330 N/mm²) according to EN 10083.

The force position is $k_l = 0.5$. Although the fatigue strength should never be reached, using it as an equivalent of the maximum shaft force F_S allows a determination of the upper limit of the shaft displacement in z-direction $w(x)$.

It is visible from Figure 5.9 that the diameter length ratio of the shaft should be larger than *0.25-0.3* to avoid a drastic increase of the shaft displacement. As in Figure 5.9 the ratio of the multiple q and a shaft safety factor is not taken into account the actual shaft bending might be higher. So slender shafts with ratios lower than *0.3* require special attention in transmission systems.

To demonstrate the effect of shaft bending, a shaft with a gear pinion F_S and a hub load (force) F_H is considered (cp. Figure 5.10a). The hub force can, for example, be caused by shaft connecting couplings [31].

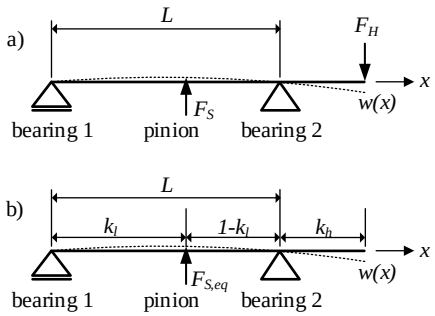

Figure 5.10 Shaft with a) hub load F_H and b) equivalent shaft load F_S

Again, the displacement in z-direction $w(x)$ can be calculated including the hub force as follows:

$$w(x) = w_s(x) + w_h(x) = \frac{L^3}{E\, I_y\, 6}\left(F_S k_{x,s} + F_H k_{x,h}\right) \tag{5.15}$$

with

$$k_{x,s} = -\left(x^3(1-k_l) + x(1-k_l)((1-k_l)^2 - 1) - \underbrace{\langle x-k_l\rangle}_{Macaulay}^{3} + k_l \underbrace{\langle x-1\rangle}_{Macaulay}^{3}\right) \tag{5.16}$$

$$k_{x,h} = -\left(k_h(x^3 + x) - (1+k_h)\underbrace{\langle x-1\rangle}_{Macaulay}^{3}\right) \tag{5.17}$$

Further, the shaft displacement $w_h(x)$ caused by the hub force (cp. Figure 5.10a) can also be approximated by an equivalent shaft force $F_{S,eq.}$ placed at the gear pinion (cp. Figure 5.10b). With Eq. 5.15 to 5.17 and $w_s(x) = w_h(x)$ the equivalent shaft force is determined by:

$$F_{S,eq} = \frac{k_{x,h}}{k_{x,s}} F_H \tag{5.18}$$

This means that the considerations of Figure 5.8 as well as Eq. 5.11 and 5.14 also apply to Figure 5.10. So for a hub loaded shaft with a diameter length ratio (*D/L*) of *0.3*, a maximum shaft displacement of approx. $10^{-3}\,L$ can be expected (cp. Figure 5.9) as τ is the fatigue limit.

For comparison according to DIN 867, the gear tooth tip clearance c_p is approx. *0.1-0.4* times the gear module *m*. The gear module is given by the ratio of pitch diameter D_p and number of teeth *z* (DIN 1829). Approximating the pinion pitch diameter by the shaft diameter, i.e. $D_p \approx D$, and assuming $z = 20$ teeth and a shaft diameter length ratio of *0.3*, the gear tooth tip clearance can be estimated.

$$c_p \approx 0.2m = 0.2\frac{D_p}{z} = 0.01D = 3.0 \cdot 10^{-3}L \tag{5.19}$$

Note that the tooth tip clearance must be considered as maximum shaft displacement at which the tip of the gear teeth touches the gear body. Such high values of shaft displacement should never occur during operation. Nevertheless, from this comparison it can be seen that the shaft displacement and gear tooth clearance can be of the same magnitude. This also includes the tooth flank clearance which is reduced by the shaft displacement and which disappears first (before the tooth tip clearance) because it is smaller than the tooth tip clearance. If these tooth clearances are lost during operation, the teeth will be pushed together and forced wear will occur. On the other hand, the shaft displacement can increase these tolerances and thus, the pitch diameter. Operating at a larger pitch diameter means that the effective tooth thickness is reduced and that the teeth are more likely to break. In other words, the shaft displacement causes a gear mesh misalignment which affects the tooth load distribution factors and thus the reliability (cp. Eq. 5.5 and Figure 5.1).

In addition to this rough worst case scenario, gearbox owners and service provider can calculate the actual shaft displacement. To determine the shaft displacement for a high speed shaft, Figure 5.10a or 5.10b can be used. In the case of Figure 5.10b this means that the equivalent shaft force must be derived from the hub force of the shaft connecting coupling. The hub force, i.e. the reaction loads of the shaft connecting coupling, can be computed based on the connecting coupling stiffness and gearbox misalignments as proposed in previous work by the authors [31]. Then, the calculated shaft displacement can be compared to the gear mesh clearance measured, for example, during visual inspections.

Moreover, the failure analysis of the NREL field test gearbox [32][33] demonstrates the practical relevance and effect of shaft bending. Severe scuffing was detected at the high speed gear set due to gear mesh misalignment. Looking at the high speed shaft diameter length ratio, which is approx. *0.14* [34], in combination with the hub forces due to the disc pack connecting coupling often installed between wind turbine gearbox and generator [31][35], gear mesh misalignment could be accepted (cp. also Figure 5.9). This means that it is not surprising that the high speed gear set suffers early failures.

From these considerations, it can be seen that determining the shaft displacement is important to avoid early gear mesh failures and thus, to ensure a high reliability of the transmission system. This also means that the shaft displacements (during operation) is an indicator for the transmission system reliability. The equations provided in this subsection allow a quick calculation of these displacements for a given gear design.

5.4.2 Shaft tilting

Then, to determine shaft tilting, the gyroscopic effect (self-centering effect) of the gear shaft assembly shown in Figure 5.11 is quantified.

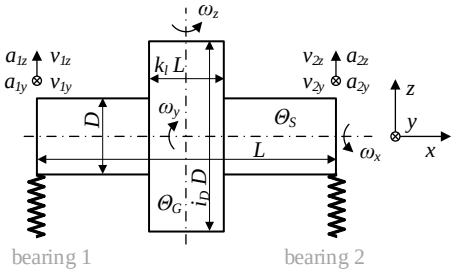

Figure 5.11 Shaft with gear for analyzing the gyroscopic effect

The mass moment of inertia tensor of the shaft (Θ_S) and gear (Θ_G) are defined relative to their mass balance point and with their masses m_s and m_G as follows [28]:

$$\vec{\Theta}_S = m_S \begin{pmatrix} \frac{D^2}{8} & 0 & 0 \\ 0 & \frac{D^2}{16}+\frac{L^2}{12} & 0 \\ 0 & 0 & \frac{D^2}{16}+\frac{L^2}{12} \end{pmatrix} = \frac{\pi}{32}\varrho_{St} D^4 L \begin{pmatrix} 1 & 0 & 0 \\ 0 & \frac{1}{2}+\frac{2}{3}\left(\frac{L}{D}\right)^2 & 0 \\ 0 & 0 & \frac{1}{2}+\frac{2}{3}\left(\frac{L}{D}\right)^2 \end{pmatrix} \quad (5.20)$$

$$\vec{\Theta}_G = m_G \begin{pmatrix} D^2\frac{i_D^2+1}{8} & 0 & 0 \\ 0 & D^2\frac{i_D^2+1}{16}+\frac{k_l^2 L^2}{3} & 0 \\ 0 & 0 & D^2\frac{i_D^2+1}{16}+\frac{k_l^2 L^2}{3} \end{pmatrix} =$$

$$= \frac{\pi}{32}\varrho_{St} D^4 L \begin{pmatrix} (i_D^4-1)k & 0 & 0 \\ 0 & (i_D^4-1)\frac{k_l}{2}+\frac{8}{3}(i_D^2-1)k_l^3\left(\frac{L}{D}\right)^2 & 0 \\ 0 & 0 & (i_D^4-1)\frac{k_l}{2}+\frac{8}{3}(i_D^2-1)k_l^3\left(\frac{L}{D}\right)^2 \end{pmatrix} \quad (5.21)$$

Where ρ_{st} is the mass density (of steel), and i_D (>1) and k_L (,1) are the factors to relate the gear dimension to the shaft dimensions L and D (cp. Figure 5.11).

The mass moment of inertia tensor of the shaft gear assembly is the sum of these tensors, i.e.:

$$\vec{\Theta}_{SG} = \vec{\Theta}_S + \vec{\Theta}_G = \frac{\pi}{32}\varrho_{St} D^4 L \begin{pmatrix} G & 0 & 0 \\ 0 & H & 0 \\ 0 & 0 & H \end{pmatrix} \quad (5.22)$$

with

$$G = (1 + (i_D^4 - 1)k_l) \tag{5.23}$$

$$H = \left(\frac{1}{2} + (i_D^4 - 1)\frac{k_l}{2}\right) + \frac{2}{3}(1 + 4(i_D^2 - 1)k_l^3)\left(\frac{L}{D}\right)^2 \tag{5.24}$$

Furthermore, the shaft angular velocity (which also holds for the rigidly connected gear) and its time derivative are specified in terms of the bearing transverse velocities v_{1y}, v_{1z}, v_{2y}, v_{2z}, accelerations a_{1y}, a_{1z}, a_{2y}, a_{2z} and constant shaft speed n_S [Hz]:

$$\vec{\omega}_S = \begin{pmatrix} \omega_x \\ \omega_y \\ \omega_z \end{pmatrix} = \frac{2}{L}\begin{pmatrix} L\pi n_S \\ v_{1z} - v_{2z} \\ v_{2y} - v_{1y} \end{pmatrix} \tag{5.25}$$

$$\dot{\vec{\omega}}_S = \frac{2}{L}\begin{pmatrix} 0 \\ a_{1z} - a_{2z} \\ a_{2y} - a_{1y} \end{pmatrix} \tag{5.26}$$

Then, the (external) shaft moment M_S around the mass balance point must be in balance with the moments due to the mass moment of inertia and the conservation of the angular moment.

$$\vec{M}_S = \vec{\Theta}_{SG}\dot{\vec{\omega}}_S + \vec{\omega}_S \times \vec{\Theta}_{SG}\vec{\omega}_S \tag{5.27}$$

$$\vec{M}_S = \frac{\pi}{16}\varrho_{St}L^4 \underbrace{\left[\left(\frac{1}{2} + (i_D^4 - 1)\frac{k_l}{2}\right)\left(\frac{D}{L}\right)^4 + \frac{2}{3}(1 + 4(i_D^2 - 1)k_l^3)\left(\frac{D}{L}\right)^2\right]}_{k_{S,geo}} \begin{pmatrix} 0 \\ a_{1z} - a_{2z} \\ a_{2y} - a_{1y} \end{pmatrix} +$$
$$+ \frac{\pi}{16}\varrho_{St}L^4 \underbrace{\left[\left(\frac{1}{2} + (i_D^4 - 1)\frac{k_l}{2}\right)\left(\frac{D}{L}\right)^4 - \frac{2}{3}(1 + 4(i_D^2 - 1)k_l^3)\left(\frac{D}{L}\right)^2\right]}_{k_{S,gyro}} \pi n_S \begin{pmatrix} 0 \\ v_{2y} - v_{1y} \\ v_{2z} - v_{1z} \end{pmatrix} \tag{5.28}$$

The first term $k_{S,geo}$ specifies the influence of the shaft assembly geometry on the mass moment of inertia, i.e. on the moment due to the rotation of the shaft mass. The second term $k_{S,gyro}$ determines the influence of shaft geometry on the gyroscopic effect, i.e. the change of the angular moment. Note that the accelerations of the first term (Δa_y and Δa_z) are perpendicular to the acceleration of the second term ($\pi n_S \Delta v_y$ and $\pi n_S \Delta v_z$).

This means that a moment (around the z-axis at the mass balance point, cp. Figure 5.11) caused, for example, by hub loads (cp. Figure 5.10) generates an acceleration and thus also a velocity in y-direction (cp. Figure 5.12a). Due to the velocity in y-direction (and a factor $k_{S,gyro}$ unequal to zero) a moment around the y-axis is provoked at the mass balance point (cp. Eq. 5.28 and Figure 5.12b). This means that the shaft does not move in y-direction, rather in z-direction (cp. Figure 5.12c). A motion of the shaft in z-direction causes an acceleration and velocity (in z-direction) and thus, a moment around the z-axis (cp. Figure 5.12d). This, again, causes with the factor $k_{S,gyro}$ a (shaft) move in the y-direction and thus, a reduction of the original moment (around the z-axis). Consequently, the shaft maintains itself centered like a spinning top. However, this is governed by the shaft speed n_S and the factor $k_{S,gyro}$. If these

two quantities are too small, the self-centering process will not start and the shaft will tilt due to the moment around the z-axis, i.e. the shaft will not shift from Figure 5.12a to 5.12b.

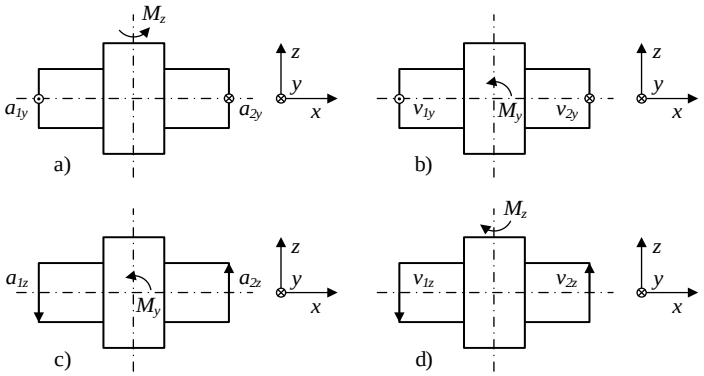

Figure 5.12 Shaft self-centering process due to the gyroscopic effect

The shaft speed depends on the gear stage designs and transmission ratios (cp. also previous section). This means, for example, that in a low speed application (like wind turbines), using a planetary gear with a fixed ring gear at the first (low speed) gear stage is not very suitable because of the low planet gear speed and thus, the risk of tilting and increased mesh misalignment. Further, the factor $k_{S,gyro}$ depends on the shaft and gear dimensions. To evaluate the critical dimension, i.e. where the factor $k_{S,gyro}$ becomes negligible, the ratio κ_S of the factor $k_{S,gyro}$ and $k_{S,geo}$ is considered, i.e. $\kappa_S = k_{S,gyro} / k_{S,geo}$.

This is presented in Figure 5.13 and 5.14 for different relative gear diameter (i_D) and gear width (k_l) (cp. Figure 5.11). It reveals that for certain gear and shaft dimensions the ratio κ_S becomes zero, i.e. the factor $k_{S,gyro}$ is negligible. To favor the shaft self-centering process the absolute value of ratio κ_S should be as high as possible so that dominance of the factor $k_{S,geo}$ is avoided. Therefore, in the case $|k_{S,geo}| >> |k_{S,gyro}| > 0$, the shaft will also tend to tilt because the gyroscopic effect can be neglected.

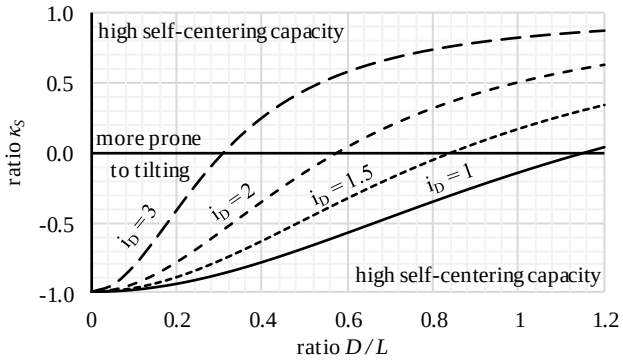

Figure 5.13 Relative influence of gyroscopic effect (ratio κ_S) for shaft gear assemblies with various gear diameters (i_D) and a fixed gear width $k_l = 0.25$

Figure 5.13 also shows that for slender assemblies (low D / L ratio), there is always a considerable self-centering effect. However, such assemblies are prone to shaft bending (cp. previous section). Assemblies with larger gear diameter ($i_D = 2, 3$) will also be self-centering at high low D / L ratio (>1). They are like a spinning disc. In the D / L range from *0.3-1.1*, all assemblies have a critical ratio at which they are prone to tilting ($\kappa_S = 0$). For low i_D this is close to $D / L = 1$, for high i_D it is close to $D / L = 0.3$. Note that assemblies typically used in gearboxes are in this range ($D / L = 0.3\text{-}1.1$). Further, Figure 5.14 demonstrates that the effect of the gear width on the self-centering capacity of the assembly is rather limited. For slender assemblies (low D / L ratio), there is always a considerable self-centering effect, independent of the gear width. For high D / L ratio, the assembly will always be prone to tilting.

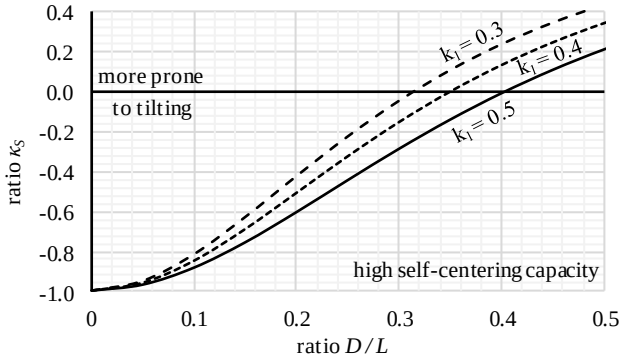

Figure 5.14 Relative influence of gyroscopic effect (ratio κ_S) for shaft gear assemblies with various gear widths (k_l) and a fixed diameter $i_D = 3$

Moreover, for hollow gears and shafts the (external) moment M_H can be derived by neglecting the mass inertia of the shaft (Eq. 5.20) and the length of the shaft (setting $k_l = 1$) in Eq. 5.21, i.e.:

$$\vec{M}_H = \vec{\Theta}_G \dot{\vec{\omega}}_S + \vec{\omega}_S \times \vec{\Theta}_G \vec{\omega}_S \tag{5.29}$$

$$\vec{M}_H = \frac{\pi}{16} \varrho_{St} L^4 \underbrace{\left[\frac{1}{4}(i_D^4 - 1)\left(\frac{D}{L}\right)^4 + \frac{8}{3}(i_D^2 - 1)\left(\frac{D}{L}\right)^2\right]}_{K_{H,geo}} \begin{pmatrix} 0 \\ a_{1z} - a_{2z} \\ a_{2y} - a_{1y} \end{pmatrix} +$$

$$+ \frac{\pi^2}{16} \varrho_{St} L^4 n_S \underbrace{\left[\frac{1}{4}(i_D^4 - 1)\left(\frac{D}{L}\right)^4 - \frac{8}{3}(i_D^2 - 1)\left(\frac{D}{L}\right)^2\right]}_{K_{H,gyro}} \begin{pmatrix} 0 \\ v_{2y} - v_{1y} \\ v_{2z} - v_{1z} \end{pmatrix} \tag{5.30}$$

Figure 5.15 demonstrates the ratio κ_H of the factor $k_{H,gyro}$ and $k_{H,geo}$, i.e. $\kappa_H = k_{H,gyro} / k_{H,geo}$. By comparing the ratio κ_H (Figure 5.15, $i = 1.2$) with the ratio κ_S (Figure 5.13, $i = 1$), it can be seen that the usage of hollow gears and shafts favors the self-centering effect for assemblies in the range ($D / L = 0.3\text{-}1.1$) because hollow assemblies become prone to tilting ($\kappa_H \approx 0$) at $D / L \approx 1.7$, while solid assemblies face that problem already at $D / L \approx 1$ ($\kappa_H \approx 0$ in Figure 5.13).

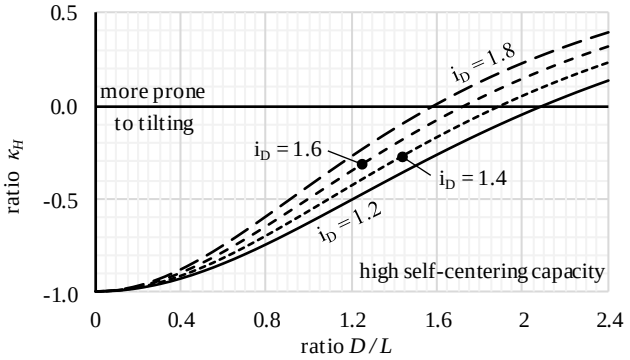

Figure 5.15 Relative influence of gyroscopic effect (ratio κ_H) for hollow gears (shafts) with various gear diameters (i_D)

Further, shaft tilting is not only reduced by the gyroscopic effect, but also by high bearing (and gearbox housing) stiffness (cp. also Figure 5.11). The bearing stiffness depends on the type, size and clearance during operation and increases with the number of rolling elements which transmit the load [36]. Further, rolling elements with a line contact are stiffer than those with point contact [36]. This means that bigger bearing sizes as well as types which have rolling elements with line contact should be preferred. In addition, using bigger sizes provides the advantage that the bearings can handle higher loads or have a longer life time. It also means that the bearing shaft gear assembly becomes more reliable (due to higher system strength). However, using bigger bearing sizes requires more installation space and yields additional weight.

As was discussed before, shafts with low speed n_S and small absolute values of the ratios κ_S and κ_H tend to tilt during operation. This, again, affects the gear mesh negatively, i.e. favors improper gear meshing. To demonstrate the significance of reducing the gear mesh misalignment during operation, i.e. of reducing shaft tilting, typical values of bearing clearance and gear mesh misalignment are considered. The bearing clearance indicates the allowable radial displacement and tilting of the shaft. Based on the bearing clearance values provided by [36] the standard bearing clearance *CN* can be described as a function of the inner diameter *D* of the inner bearing race. Then, with a shaft diameter length ratio of approx. *0.3* it follows:

$$CN \approx 0.28 \cdot 10^{-3} D = 8.4 \cdot 10^{-5} L \tag{5.31}$$

Typical shaft lengths are *0.5-1.0* meters. This means that the bearing clearances are in the range of 40 to 80 micro meters. Note that the bearing clearance will allow the shaft to wobble, if the gyroscopic effect is negligible. This causes a runout, i.e. the shaft does not rotate in line with the main axis, as well as gear mesh misalignment. Depending on the shaft length the latter has a similar magnitude as the bearing clearances. In comparison, typical values of mesh misalignment are in the range of several tens of micro meters according to DIN 3990. Mesh misalignment of this magnitude already affect the tooth load distribution factors, i.e. the contact pattern and tooth traces (cp. DIN 3964 and DIN 3990). Therefore, runouts due to bearing clearances and negligible gyroscopic effect can cause gear mesh misalignments which significantly affect the gear life time.

Finally, to demonstrate this, i.e. the practical relevance and effect of shaft tilting, the failure analysis of the NREL field test gearbox [32] is considered that was already mentioned in section 5.4.1. The scuffing at the high speed gear set was not only severe, but also varied in a sinusoidal pattern around the pinion and gear, indicating that there was a runout [33]. Looking at the intermediate shaft, a relative width $k_l = 0.17$, a diameter length ratio of approx. $D/L = 0.22$ and a gear shaft diameter ratio of approx. $i_D = 3.25$ [34] can be determined. Figure 5.13 was calculated with a relative width $k_l = 0.25$ and shows the effect of an increasing diameter ratio i_D. Figure 5.14 shows the influence of reducing the relative width k_l. By combining both Figures, it can be seen that the ratio κ_S approximates to zero ($\kappa_S \approx 0$) for $k_l = 0.17$, $D/L = 0.22$ and $i_D = 3.25$. This means that the gyroscopic effect almost disappears. Therefore, it seems possible that the runout and thus the sinusoidal pattern was caused by continuous shaft tilting during operation.

So minimizing the mesh misalignment by reducing shaft tilting during operation is a crucial part to decrease the gear mesh loads and thus, to increase the gear life time and improve the reliability. In other words, by calculating the ratio κ_S or κ_H using the proposed expressions it can be quantified how likely a shaft will tilt during operation. It can be expected that shafts with low absolute values of these ratios as well as low speeds n_S tend to tilt during operation and thus will have a lower reliability. Therefore, the quantification of the gyroscopic effect for the different gears and shafts is an indicator of the transmission system reliability (cp. Eq. 5.3).

5.5 Specification of system excitation

The third important aspect for obtaining a high system reliability is the quantification of the system excitation as well as its minimization. A wind turbine drive train can be excited (externally) by both the wind turbine rotor and generator which means that additional (dynamic) loads occur on top of the steady state load. So to specify the additional loads due to this excitation, a simple specification of the application factors (cp. Eq. 5.3) of the wind turbine rotor and generator are developed in the following subsections.

5.5.1 Excitation due to wind turbine rotor

To determine the application factor of the wind turbine rotor, the blade forces, and especially their fluctuations during operations must be considered. When secondary effects like blade pitching, nacelle yawing as well as the blade gravity forces are neglected the blade forces are determined by the aerodynamic (lift and drag) forces. Based on Figure 5.16 the aerodynamic forces are defined at a blade section, i.e. for a 2D airfoil as follows [37][38]:

$$F_l = \frac{\rho}{2} w_{rel}^2 C_l(\alpha)\, c\, \Delta r \tag{5.32}$$

$$F_d = \frac{\rho}{2} w_{rel}^2 C_d(\alpha)\, c\, \Delta r \tag{5.33}$$

with the air density ρ, relative wind speed w_{rel}, the airfoil chord length c, the blade section length Δr and lift C_l and drag C_d coefficients which are a function of the angle of attack α.

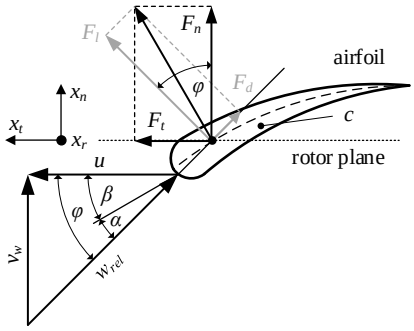

Figure 5.16 Blade sections with aerodynamic forces

As the wind flow in the wind turbine is unsteady and asymmetric the velocity triangle (cp. Figure 5.16) varies [21], i.e. the wind velocity component v_w in normal direction and the circumferential velocity u in tangential direction change. Consequently, the relative velocity w_{rel}, the angle φ and angle of attack α change, too. If blade twisting is neglected, i.e. the pitch angle β is constant during operation, and the influence of the changing angle of attack on the lift and drag coefficient is neglected, then the aerodynamic forces will only depend on the relative velocity:

$$w_{rel}^2 = (v_w + \dot{x}_n)^2 + (u + \dot{x}_t)^2 \tag{5.34}$$

with the velocity variation in normal (dx_n / dt) and tangential (dx_t / dt) direction.

Then, according to DIN 3990 the application factor is the ratio of the peak to the rated (constant) force or torque. This means that the application factor at the blade section is defined as follows:

$$K_{A,sec} = \frac{(v_w+\dot{x}_n)^2+(u+\dot{x}_t)^2}{v_w^2 + u^2} = 1 + \frac{1}{1+\lambda_r^2}\left(2\dot{X}_n + \dot{X}_n^2 + 2\lambda_r \dot{X}_t + \dot{X}_t^2\right) \tag{5.35}$$

with the speed ratio λ_r (at the blade section)

$$\lambda_r = \frac{u}{v_w} \tag{5.36}$$

and the normalized velocities in normal direction

$$\dot{X}_n = \frac{\dot{x}_n}{v_w} \tag{5.37}$$

and tangential direction

$$\dot{X}_t = \frac{\dot{x}_t}{v_w} \tag{5.38}$$

For small velocity fluctuations, the quadratic terms of dX_n / dt and dX_t / dt are close to zero, so the expression reduces to:

$$K_{A,sec} \approx 1 + \frac{2}{1+\lambda_r^2}\left(\dot{X}_n + \lambda_r \dot{X}_t\right) \tag{5.35a}$$

Further, to calculate the application factor for the entire wind turbine rotor, the tangential force distribution along the blade radius must be taken into account. Note that the tangential force (cp. Figure 5.16) generates the torque at the wind turbine rotor hub and thus, is used to determine the application factor. Based on the work provided by [39] the tangential force can be assumed as constant over the blade radius. This means that the application factor of the wind turbine rotor is the averaged application factor of the blade sections. This yields:

$$K_{A,rot} = \frac{1}{k}\sum_{i=1}^{k} K_{A,sec}(\mu_i) = \frac{1}{k}\sum_{i=1}^{k}\left[1 + \frac{2}{1+\lambda_{tip}^2\,\mu_i^2}\left(\dot{X}_n + \lambda_{tip}\dot{X}_t\mu_i\right)\right] \tag{5.39}$$

with *k* the number of blade sections, the tip speed ratio

$$\lambda_{tip} = \frac{u_{tip}}{v_w} \tag{5.40}$$

and the non-dimensional blade radius μ

$$\mu = \frac{r}{R_{tip}} \tag{5.41}$$

So, by assuming a normalized normal velocity $dX_n / dt \approx 0.0\text{-}0.2$, i.e. wind gusts and turbulence up to 20% of the wind speed, and a normalized tangential velocity $dX_t / dt \approx 0.0\text{-}0.1$, i.e. side and shear winds up to 10% of wind speed, the application factor $K_{A,rot}$ is quantified to be approx. *1.12* with a typical tip speed ratio of $\lambda_{tip} = 8$. As comparison, an application factor of *1.1* means light shocks and *1.25* moderate shocks according to DIN 3990. Therefore, the wind turbine rotor can be positioned in between steam and gas turbines (light shocks) and multiple cylinder internal combustion engines (moderate shocks).

Moreover, as the application factor directly influences the drive train loads (cp. Eq. 5.3) and thus, the reliability (cp. Figure 5.1), a wind turbine owner or service provider can use the application factor to quantify the wind turbine reliability. With the tip speed ratio, often provided by the blade manufacturer [40], and the measured normal and tangential (wind) velocity variation, an application factor can be quantified for different wind turbine locations. Wind turbines exposed to higher application factors will tend to fail earlier and will demonstrate a lower reliability, assuming that the assessed wind turbines have the same power train components. This also means that wind turbine owners and service providers can assess the reliability and maintenance intensity of the different wind turbines in a wind park. By quantifying the application factor for each wind turbine, they can estimate which wind turbine will probably fail first and will require more maintenance. This also aligns with the research identifying that the failures rates of wind turbines vary depending on the local environmental conditions [41].

Finally, to demonstrate the practical usage of the application factor $K_{A,rot}$, the wind speed effects on wind turbine reliability provided by Reder and Melero [42] are considered. Based on SCADA measurements from 544 modern operating WTs, with a rated power between 0.85 and 2 Megawatts each, they calculated the mean maximum and the total maximum wind speed within periods of one year and 30 days before failure of different wind turbine components. The mean maximum is determined by taking the maxima of particular time

series and calculating their mean value. The result of this study is shown in Table 5.1 and 5.2. Both Tables include the ratio (K_{wind}) of the total maximum and mean maximum wind speed. This ratio is similar to the application factor $K_{A,rot}$ which is determined by the ratio of the peak to the rated (constant) force (cp. also Eq. 5.39). Note that the ratio of the total maximum and mean maximum does not indicate the instantaneous wind speed fluctuations as the application factor does. The total maximum and mean maximum wind speed are determined by SCADA which provide wind speed measurements in ten minutes time steps [42]. Measuring the wind speed every ten minutes does not reflect the instantaneous wind speed fluctuations caused for example by wind gusts or turbulences. However, it provides insight in the wind speed fluctuations to which a wind turbine is exposed.

Table 5.1 Wind speed during one year before failure [42]

component	mean maximum [m/s]	total maximum [m/s]	K_{wind}
pitch system	29.1	36.7	1.26
generator	26.9	33.7	1.25
gearbox	26.0	34.9	1.34
converter	26.8	33.9	1.26
yaw system	27.3	34.8	1.27

Table 5.2 Wind speed during 30 days before failure [42]

component	mean maximum [m/s]	total maximum [m/s]	K_{wind}
pitch system	21.3	36.7	1.72
generator	20.7	27.5	1.32
gearbox	21.8	34.3	1.58
converter	20.5	33.9	1.65
yaw system	21.4	34.8	1.63

Table 5.1 and 5.2 show that the ratio K_{wind} is approx. *1.25* in the one year period before failure and increases to approx. *1.6-1.7* in the 30 days before failure (except at the generator). This increase of K_{wind} is caused by the drop of the mean maximum. Therefore, it appears that the wind fluctuations, which yield the dynamic or additional loads, are higher in the 30 days period leading to a component failure than in the full one year period before that failure. This strongly suggests that these failures are triggered by high wind (and load) fluctuations, which confirms the importance of quantifying this fluctuation with the proposed application factor $K_{A,rot}$.

5.5.2 Excitation due to wind turbine generator

The wind turbine drive train is not only excited by the wind turbine rotor, but also by the generator. As the generator provides the coupling of the mechanical and electrical power train subsystem, harmonics in the electrical power train subsystem may cause a drive train excitation. The electro-mechanical coupling can roughly be described as follows [43][44]:

$$T_{Ge} \sim I_R I_S \tag{5.42}$$

The generator torque (T_{Ge}) is proportional to the RMS rotor (I_R) and stator (I_S) currents. This means that alternating torques, i.e. mechanical drive train excitations, are provoked by

harmonics in the rotor and stator current. In the case of a permanent magnet synchronous generator (PMSG) or a grid connected synchronous generator (SG) the rotor current can be considered as constant and the alternating torques are proportional to the stator current harmonics. However, in the case of a doubly fed induction generator (DFIG) both rotor and stator current vary. Hence, the alternating torques are proportional to the superposition of rotor and stator current harmonics.

Based on these considerations an application factor $K_{A,Ge}$ can be quantified determining the additional loads caused by the current harmonics ($h \geq 2$). The nominal torque is given by $I_{R,1}$ and $I_{S,1}$ while the alternating torque, i.e. the excitation of the drive train, is specified by the current harmonics $I_{R,h}$ and $I_{S,h}$. The total harmonic distortion (*THD*) is the ratio of the RMS current of the higher harmonics I_h to the rms current of the first harmonic I_1 [22].

$$THD = \sqrt{\sum_{h=2}^{\infty} I_h^2}/I_1 \tag{5.43}$$

Further, considering the higher harmonics [45] in the RMS rotor and stator currents the generator torque is defined by:

$$T_{Ge} \sim I_{R,1}\sqrt{1+\frac{\sum_{h=2}^{\infty} I_{R,h}^2}{I_{R,1}^2}}\; I_{S,1}\sqrt{1+\frac{\sum_{h=2}^{\infty} I_{S,h}^2}{I_{S,1}^2}} = I_{R,1}I_{S,1}\sqrt{1+THD_R^2}\sqrt{1+THD_S^2} \tag{5.44}$$

Therefore, the application factor, which is the ratio of the maximum to the rated torque, is determined for the different generator types as follows:

- Synchronous Generator (SG), $I_R = I_{R,1}$.:
  $K_{A,SG} = \sqrt{1+THD_S^2}$ (5.45)

- Doubly Fed Induction Generator (DFIG):
  $K_{A,DFIG} = \sqrt{1+THD_R^2}\sqrt{1+THD_S^2}$ (5.46)

Note that for variable speed Permanent Magnet Synchronous Generators (PMSG) Eq. 5.45 also applies. Figure 5.17 shows the application factor of SG (PMSG) and DFIG depending on *THD*.

The *THD* of a DFIG is in the range of 5-20% depending on operational and control conditions [46]. This means that DFIGs have an application factor up to $K_{A,DFIG} = 1.04$. If a higher *THD* is detected at the generator terminals, then the application factor will increase further (cp. Figure 5.17). Figure 5.17 also shows that the application factor of the (PM)SG is lower than the one of the DFIG. As a smaller application factor means lower loads (cp. Eq. 5.3), it can be expected that the reliability of the DFIG will be lower than that of a (PM)SG, if all other loads are assumed to be equal. This also confirms the work provided by [8]. Further, frequency converters contribute to the *THD* in the electrical subsystem. This means that grid connected SGs (without a frequency converter) experience a lower application factor than PMSGs combined with a fully rated frequency converter, i.e. the application factor of SGs is almost one. Therefore, the generator type used as electro-mechanical coupling in the wind turbine power train also determines the reliability.

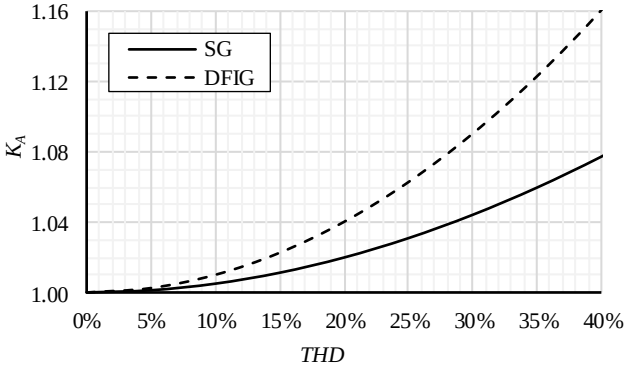

Figure 5.17 Generator application factor for two types of generators (assuming $THD_R = THD_S$)

Again, wind turbine owners and service providers can use the application factor to determine the reliability of the wind turbine and its components. By measuring the current harmonics at the generator terminals, they can determine the *THD* in the rotor and stator current. Then, based on the evaluated *THD* they can quantify the application factor of the generator. Generators exposed to higher application factors will tend to fail earlier and will demonstrate a lower reliability.

This also includes the drive train, electrical power converter and power transformer because the generator is connected to these components. This also means that wind turbine owners and service providers can assess the reliability and maintenance intensity of the different power train components and compare them, for example, within a wind park. By quantifying the application factor for each generator, they can estimate which power train will probably fail first and will require more maintenance.

Furthermore, the combination of the generator ($K_{A,Ge}$) and the wind turbine rotor ($K_{A,rot}$) application factors (cp. previous section) provides wind turbine owners and service providers insight in the wind turbine control conditions. For example, an increase of both generator and wind turbine rotor application factor in a certain period of time seems logical because an increase of unsteady, asymmetric wind flow might result in an increase of the *THD*. However, if the wind turbine rotor application factor decreases while the generator application factor increases, then the generator is affected by a *THD* which is not related to the unsteady, asymmetric wind flow rather to the wind turbine power control. The latter regulates the electromagnetic (counter)torque in the generator by adjusting, for example, the rotor current in a DFIG. This means that the THD in the generator can be caused not only by the unsteady, asymmetric wind flow but also by the power control. Consequently, the application factors can also be used to identify critical control conditions.

Finally, an example is presented to demonstrate the practical usage of the generator application factor $K_{A,Ge}$. A *THD* of 20% is assumed. Based on Eq. 5.45 and 5.46 (cp. also Figure 5.17) this leads to an application factor ratio $\kappa_{A,Ge} = K_{A,DFIG} / K_{A,SG} = 1.02$. This ratio indicates that the mean load value of the DFIG is shifted 2% more towards the mean strength value than the mean load value of the (PM)SG (Figure 5.1a and 5.1b). A load shift towards the strength causes an increase of the failure area (cp. Figure 5.1a). Further, assuming for both (PM)SG and DFIG the same ratio of mean load value and standard deviation μ_L / σ_L and the same ratio of the standard deviations σ_S / σ_L, the failure probability increase is determined by the strength to load mean ratio μ_S / μ_L (cp. Eq. 5.2). The latter differs for the (PM)SG and

DFIG by the application factor ratio $\kappa_{A,Ge}$. With Eq. 5.1 and 5.2 the failure probability increase (ΔP_f) is determined as follows:

$$\Delta P_f = 1 - \frac{1 - \Phi(Z_{SG})}{1 - \Phi(Z_{DFIG})} = 1 - \frac{1 - \Phi\left(Z\left(\frac{\mu_{S,SG}}{\mu_{L,SG}}\right)\right)}{1 - \Phi\left(Z\left(\frac{\mu_{S,SG}}{\mu_{L,SG}}\frac{1}{\kappa_{A,Ge}}\right)\right)} \tag{5.47}$$

Based on Figure 5.1c and the ratio $\kappa_{A,Ge} = 1.02$, the failure probability increase is quantified to be approx. 30-50%. To verify, the reliability study provided by [8] demonstrates that the DFIG has a 40% higher failure rate than the PMSG. This shows that the (generator) application factor can conveniently be used to quantify the reliability. In addition, note that Eq. 5.47 can also be executed with the wind turbine rotor application factor, e.g. to compare the failure probability of wind turbines at different locations.

5.6 Discussion

In the previous sections the system (wind turbine power train) reliability was discussed from a load-based perspective. Crucial principles like minimization of load magnitude, prevention of load superposition and specification of system excitation were applied to transmission systems and wind turbine drive trains. Based on these principles methods were developed to quantify the loads, which enables to reduce the loads and thus, to increase the reliability (cp. Figure 5.1). Although these methods are related to gear loads, i.e. to the tangential tooth force and tooth load factors used to determine the tooth stresses according to DIN 3990, they do not provide an absolute and direct quantification and qualification of the reliability. However, they do enable a relative reliability assessment which is very useful for the comparison of different transmission and power train designs.

Further, the determination of the (relative) reliability provides benefits for the system designer, owner and service provider. It demonstrates a designer which concept will provide a higher reliability and is preferable. An owner can use the relative reliability to assess different system solutions and then choose the one he prefers. A solution showing a higher reliability might also include a higher investment. However, looking at the total cost of ownership, he may chose the solution with the higher reliability. Similarly, a service provider can utilize the calculation of the relative reliability. Comparing the (relative) reliability of different system solutions identifies which solution is the most or least maintenance intense solution. Based on these insights, he can adjust and plan more efficiently the maintenance activities.

Another aspect, which demonstrates the physics- and design-based or load-based perspective, is the interrelation of reliability, maintenance and design. This means that the root cause of an unacceptable high maintenance intensity and low reliability is related to the design. Applying this insight to the wind turbine power train means that a reconsideration of the power train system as a whole will be needed in order to significantly reduce the maintenance intensity and improve the reliability. This includes both the mechanical and electrical power train subsystem and eventually even the interaction between wind turbine power train and electrical grid. In other words, improvements of a wind turbine power train will be effective and successful, if they are realized from the system perspective, i.e. if the power train (and even the electrical grid) are considered in its entirety.

5.7 Conclusion

The present chapter considers the reliability of the wind turbine power train from a physics- and design-based perspective. This means that the reliability is quantified by the load-strength interference. Reliability improvements based on the increase of the latter should be avoided to minimize wind turbine tower head weight. Therefore, some crucial principles are proposed to assess and reduce the loads, leading to a reliability improvement, namely: minimization of (static) load magnitude, prevention of load superposition and specification of system excitation. These principles are applied in this chapter to the drive train, i.e. the mechanical subsystem of the wind turbine power train. The following specific conclusions can be drawn:

- The load magnitude is calculated for wheel-two-pinion and planetary gear stages. It is demonstrated that the wheel-two-pinion gear stage with a high transmission ratio provides lower load magnitudes than planetary gear stages. This is especially beneficial for applications with low shaft speeds and high torques like the wind turbine rotor.
- The load superposition principle is applied to the gear mesh. Shaft bending and tilting during operation cause mesh misalignment and hence, additional loads. Therefore, methods are developed to evaluate and assess shaft bending and tilting. It is shown that both of them can be influenced by the fundamental dimensions of the shaft-gear assembly.
- The system excitations are quantified by application factors based on the DIN 3990 standard. The wind turbine drive train is excited by the wind turbine rotor and the generator. It is demonstrated that the wind turbine rotor causes light to moderate shocks in the wind turbine drive train. The excitation due to the generator depends on the generator type, i.e. a synchronous generator provides a lower application factor and thus a higher reliability than a doubly fed induction generator.
- The proposed methods determine the relative reliability, thus enabling a comparison between different system designs. The relative reliability provides benefits for system designer, owner and service provider, as it assists them in selecting the best system solution with the lowest maintenance intensity.
- The proposed methods also prove that the system design, maintenance and reliability are interconnected. This means that the reduction of maintenance intensity and the increase of reliability are related to the system design. Applying this insight to the wind turbine power train, design reconsiderations will offer effective and successful reliability improvements.

References

[1] J. Ribrant, “Reliability performance and maintenance - A survey of failures in wind power systems,” 2006.

[2] J. Ribrant and L. M. Bertling, “Survey of Failures in Wind Power Systems With Focus on Swedish Wind Power Plants During 1997-2005,” *IEEE Trans. Energy Convers.*, vol. 22, no. 1, pp. 167–173, 2007.

[3] Noordzee Wind CV, “Operations Report 2008,” 2009.

[4] Noordzee Wind CV, “Operations Report 2009,” 2010.

[5] M. Wilkinson *et al.*, “Methodology and results of the reliawind reliability field study,” 2010.

[6] Tavner, *Offshore Wind Turbines: Reliability, availability and maintenance*. 2013.

[7] F. Spinato, P. J. Tavner, G. J. W. van Bussel, and E. Koutoulakos, “Reliability of wind turbine subassemblies,” *IET Renew. Power Gener.*, vol. 3, no. 4, p. 387, 2009.

[8] J. Carroll, A. Mcdonald, and D. Mcmillan, “Reliability comparison of wind turbines with DFIG and PMG drive trains,” *Energy Conversion, IEEE Trans.*, vol. 30, pp. 663–670, 2015.

[9] W. Musial, S. Butterfield, and B. Mcniff, “Improving wind turbine gearbox reliability,” *Eur. Wind Energy Conf. Exhib. 2007, EWEC 2007*, vol. 3, pp. 1770–1779, 2007.

[10] F. Wang, J. Chen, B. Xu, and K. A. Stelson, “Improving the reliability and energy production of large wind turbine with a digital hydrostatic drivetrain,” *Appl. Energy*, vol. 251, no. December 2018, p. 113309, 2019.

[11] R. Bergua, J. Jove, and E. Javier, “Pure torque drivetrain design: A proven solution for increasing the wind turbine reliability,” *Brazil Wind. 2014 Conf. Exhib.*, no. August 2014, p. 15, 2014.

[12] M. Whittle, J. Trevelyan, W. Shin, and P. Tavner, “Improving wind turbine drivetrain bearing reliability through pre-misalignment,” *Wind Energy*, vol. 17, no. 8, pp. 1217–1230, 2014.

[13] H. Li, H. Cho, H. Sugiyama, K. Choi, and N. Gaul, “Reliability-based design optimization of wind turbine drivetrain with integrated multibody gear dynamics simulation considering wind load uncertainty,” *Struct. Multidiscip. Optim.*, 2017.

[14] A. Beržonskis and J. D. Sørensen, “Reliability Analysis of Fatigue Fracture of Wind Turbine Drivetrain Components,” *Energy Procedia*, vol. 94, pp. 146–154, 2016.

[15] C. Peeters *et al.*, “Drivetrain reliability improvements from long-term field data processed in the cloud,” *J. Phys. Conf. Ser.*, vol. 1222, no. 1, 2019.

[16] E. Artigao, S. Martín-Martínez, A. Honrubia-Escribano, and E. Gómez-Lázaro, “Wind turbine reliability: A comprehensive review towards effective condition monitoring development,” *Appl. Energy*, vol. 228, no. May, pp. 1569–1583, 2018.

[17] M. Silverman and A. Kleyner, “What is design for reliability and what is not?,” *Proc. - Annu. Reliab. Maintainab. Symp.*, no. November, 2012.

[18] Z. Matić and V. Sruk, “The Physics-of-Failure approach in reliability engineering,” *Proc. Int. Conf. Inf. Technol. Interfaces, ITI*, no. May, pp. 745–750, 2008.

[19] S. Kotz, Y. Lumelskii, and M. Pensky, *The Stress-strength Model and Its Generalizations: Theory and Applications*. World Scientific, 2003.

[20] DIN 3990, *Calculation of Load Capacity of Cylindrical Gears*. 1987.

[21] D. P. Rommel, D. Di Maio, and T. Tinga, “Calculating wind turbine component loads

for improved life prediction," *Renew. Energy*, vol. 146, 2020.
[22] N. Mohan, T. M. Undeland, and W. P. Robbins, *Power electronics: converters, applications, and design*. Wiley, 1995.
[23] H. D. Giesecke, "Steam turbine-generator torsional response due to interaction with the electrical grid," *IEEE Power and Energy Society General Meeting*. 2012.
[24] C. Liu, D. Jiang, and J. Chen, "Coupled torsional vibration and fatigue damage of turbine generator due to grid disturbance," *J. Eng. Gas Turbines Power*, vol. 136, no. 6, 2014.
[25] F. J. Zuo, L. Yu, J. Mi, Z. Liu, and H. Z. Huang, "Reliability analysis of gear transmission with considering failure correlation," *Eksploat. i Niezawodn.*, vol. 17, no. 4, pp. 617–623, 2015.
[26] E. Bai, L. Xie, H. Ma, J. Ren, and S. Zhang, "Reliability Modeling and Estimation of the Gear System," *Math. Probl. Eng.*, vol. 2018, no. 1, 2018.
[27] R. Errichello and J. Muller, "Application Requirements for Wind Turbine Gearboxes," Albany, California, 1994.
[28] K. H. Grote and E. K. Antonsson, *Springer Handbook of Mechanical Engineering*, no. v. 10. Springer, 2009.
[29] H. W. Müller, *Die Umlaufgetriebe: Berechnung, Anwendung, Auslegung*, no. v. 27-30. Springer-Verlag, 1971.
[30] J. Ukonsaari and N. Bennstedt, "Wind Turbine Gearboxes - Maintenance Effect on Present and Future Gearboxes for Wind Turbines," 2016.
[31] D. P. Rommel, D. Di Maio, and T. Tinga, "Calculating Loads and Life Time Reduction of Wind Turbine Gearbox and Generator Bearings due to Shaft Misalignment," *Wind Eng.*, 2020.
[32] R. Errichello and J. Muller, "Gearbox Reliability Collaborative Gearbox 1 Failure Analysis Report: December 2010 - January 2011," *Relat. Inf. Work performed by Gear Work. Seattle, Washingt.*, no. January 2011, 2012.
[33] R. Errichello, "Failure Analysis of NREL Field Test Gearbox No. 1," 2011.
[34] H. Link, W. Lacava, J. Van Dam, and B. Mcniff, "Gearbox Reliability Collaborative Project Report : Findings from Phase 1 and Phase 2 Testing," *Nrel/Tp-5000-51885*, no. June, p. 85, 2011.
[35] J. H. Kang, J. Bae, H. On, and H. W. Lee, "The design of a flexible wind turbine coupling structure considering torsional vibration," *Int. J. Appl. Eng. Res.*, vol. 11, no. 16, pp. 9093–9098, 2016.
[36] FAG, *Wälzlager Hauptkatalog*. Schweinfurt: Schaeffler KG, 2008.
[37] M. O. L. Hansen, *Aerodynamics of Wind Turbines, 2nd edition*. Taylor & Francis, 2013.
[38] T. Burton, N. Jenkins, D. Sharpe, and E. Bossanyi, *Wind Energy Handbook*. 2011.
[39] A. Hassanzadeh, J. W. Naughton, C. L. Kelley, and D. C. Maniaci, "Wind Turbine Blade Design for Subscale Testing," *J. Phys. Conf. Ser.*, vol. 753, no. 2, 2016.
[40] EUROS, "Blade family EU90 | 100," 2009.
[41] P. J. Tavner, D. M. Greenwood, M. W. G. Whittle, R. Gindele, S. Faulstich, and B. Hahn, "Study of weather and location effects on wind turbine failure rates," *Wind Energy*, vol. 16, no. 2, pp. 175–187, 2013.
[42] M. Reder and J. J. Melero, "Assessing Wind Speed Effects on Wind Turbine Reliability," *Wind Eur. Conf.*, pp. 15–18, 2016.
[43] G. Müller and B. Ponick, *Grundlagen elektrischer Maschinen*. Wiley, 2012.
[44] A. Kremser, *Elektrische Maschinen und Antriebe: Grundlagen, Motoren und*

Anwendungen. Vieweg+Teubner Verlag, 2013.

[45] W. M. Grady and R. J. Gilleskie, “Harmonics and how they relate to power factor,” *EPRI Power Qual. Issues Oppor. Conf.*, no. November, pp. 1–8, 1993.

[46] S. M. Nosratabadi and E. Gholipour, “Power system harmonic reduction and voltage control using DFIG converters as an active filter,” *Turkish J. Electr. Eng. Comput. Sci.*, vol. 24, no. 4, pp. 3105–3122, 2016.

CHAPTER 6

Dynamic Load Absorption in Drive Trains for an Improved Wind Turbine Reliability

ABSTRACT

The present chapter considers the dynamic load absorption of a wind turbine drive train and its effect on the wind turbine reliability by considering the load-strength interference. The potential dynamic load absorption is quantified by calculating the drive transfer function using analytical equations and basic dimensions which are readily available in assembly plans. The transfer functions are calculated as examples for a direct drive and geared drive wind turbine. It is shown that the geared drive provides a higher absorption of the dynamic load and a more stable dynamic behavior than the direct drive. This means that the geared drive emits lower dynamic loads to the (electrical) power train components like generator and converter. Consequently, in a geared drive these components are expected to have a higher reliability and a lower maintenance intensity. In addition, it is discussed that the proposed methods do not only provide benefits to system designers but also to system owners and service providers, as the methods also facilitate maintenance and reliability assessments and improvements of existing systems.

This chapter is based on: Rommel, D. P., Di Maio, D., Tinga, T. (n.d.). Dynamic Load Absorption in Drive Trains for an Improved Wind Turbine Reliability. submitted.

Nomenclature

SYMBOL	UNIT	QUANTITY
A	-	transfer function
b	[m]	gear width
C	-	sitffness matrix
C_B	-	basic rack tooth profile correction factor
C_M	-	correction factor
C_R	-	wheel bland correction factor
c	-	planet carrier
c	[N/m]	stiffness
c_t	[Nm/rad]	torsional stiffness
D	[m]	diameter
DD	-	direct drive
d	[Ns/m]	damping
dyn	-	dynamic
F	[N]	force
F	-	function
G	[N/m²], -	shear modulus of elasticity
GB	-	gearbox
Ge	-	generator
gg	-	gear-gear assembly
h	[m]	tooth height
I	[m^4]	area moment of inertia
i	-	(stage) transmission ratio
i_0	-	stationary gear ratio
is	-	inertia-shaft assembly
J	[kgm^2]	mass moment of inertia
j	-	complex number
k	-	number of drive train assemblies
k_p	-	number of pinions
k_{pl}	-	number of planets
l	[m]	length
M	-	mass matrix
m	-	module
n	[rad/s], -	shaft speed, counter
p	-	pitch, pinion
pl	-	planet gear
R	[m]	radius
r	[m]	radius
rg	-	ring gear
rot	-	wind turbine rotor
S	-	shaft
SG	-	synchronouse generator
s	-	sun gear, complex number
st	-	(gear) stage, steel
T	[Nm]	torque
THD	-	total harmonic distortion
w	-	wheel
z	-	number of teeth
α	[rad]	flank angle
ζ	-	damping ratio
ρ	[kg/m^3]	density
τ	[N/m²]	torsional stress
φ	[rad]	torsional angle
ω	[1/s]	excitation frequency
ω_0	[1/s]	natural freuquency

6.1 Introduction

Literature often highlights that wind turbine aggregates like gearboxes, generators and power converters have significant failures rates and downtimes [1]–[6]. Direct drive wind turbines are often preferred in order to avoid the costly failures and high downtimes of gearboxes. However, failure rates of (permanent magnet) generators and (fully rated) converters in direct drive wind turbines are greater than those of gearboxes, (double fed induction) generators and (partly rated) converters in geared wind turbines [7][8]. This means that a direct drive wind turbine is not implicitly more reliable than a geared wind turbine.

For enhancing the reliability of wind turbine power trains, literature often recommends the identification of critical components combined with condition monitoring [9][10], the rigorous (field) testing of the different wind turbine subassemblies [7][11], the consideration of the wind load uncertainty [12] and failure mechanism [13], the substitution [14] or modification [15][16] of particular drive train components or the usage of new design tools [11]. However, system reliability is already determined while designing the system at early concept stages [17]. Further, the approach of physics of failure is suggested to consider and identify reliability concerns during design and development processes [18]. It enables the identification of the critical failure modes and the impact estimation of the contributing environmental factors and hence, provides a better accuracy [18].

This means that methods are needed to consider the reliability from a physics-based design perspective. These methods should also be applicable during early concept stages where complex models, for example based on multi body dynamics, are not available yet. So these models should provide a reliability estimation based on essential information and basic dimensions in order to support the design and development processes. Analyzing the wind turbine power train reliability from a physics-based design perspective appears to get very little attention in scientific literature. Methods determining the wind turbine power train reliability during early concept stages and design processes could not be found at all.

As the reliability is governed by the interference between system stresses (loads) and strengths [19], reliability improvements are either based on load reduction or on strength increase. The principle of load reduction is preferred in wind turbine systems, as it contributes to minimizing the tower head weight. Therefore, in previous work by the authors [20], methods have already been proposed to improve the reliability i) by reducing the load magnitude, ii) by preventing load superposition and iii) by quantifying the subsystem excitations. The present chapter will focus on load absorption[2] as an additional way to assess the reliability of existing (wind turbine power train) designs and to increase the reliability of new designs. The original contribution in this work will be the proposal of a computationally efficient and accessible analytical method to quantify the drive train load absorption. Since the proposed method does not require detailed design information, it can readily be applied by system designers, wind turbine owners and service providers.

The outline of the chapter is as follows: based on the principle of load reduction a few essential (design) requirements are derived to increase the wind turbine power train reliability (section 6.2). To quantify the load reduction, the drive train transfer behavior is determined, i.e. the transfer function is calculated, in section 6.3. Then, in a case study the transfer functions of a direct drive and gear wind turbine are presented and compared in section 6.4.

[2] Note that in this chapter the term “absorption” is used because vibrations and their related dynamic loads are handled by structural parts, leading eventually to dissipation of (part of) the associated energy.

Based on the gained insights from the drive train transfer function, reliability assessments and improvements are discussed in section 6.5. Finally, the conclusions of the work are summarized in section 6.6.

6.2 Increasing the reliability by system load reduction

Based on the load-strength interference, system reliability is improved either by reducing the system loads or by increasing the system strength (cp. Figure 6.1a) [19]. As the latter typically leads to bigger system (component) dimensions and thus to a rise of the system weight, the system load reduction is preferred in wind turbine power trains. Reducing the system loads can be achieved by decreasing the mean value of the load distribution (μ_L) or by reducing the load standard deviation (σ_L) (cp. Figure 6.1b), as both measures reduce the overlap with the strength distribution. A decrease of the mean value can be obtained by reducing the load magnitude. Minimizing the (effects of) load variations decreases the standard deviation.

Further, with the load (μ_L, σ_L) and strength (μ_S, σ_S) mean values and standard deviations the reliability R is quantified as follows [19]:

$$R = P(load < strength) = \Phi(Z) \tag{6.1}$$

with the probability P, the cumulative distribution function Φ and the standard (normal) deviate Z:

$$Z = \frac{\mu_L - \mu_S}{\sqrt{\sigma_L^2 + \sigma_S^2}} = \frac{\mu_L}{\sigma_L} \frac{1 - \frac{\mu_S}{\mu_L}}{\sqrt{1 + \left(\frac{\sigma_S}{\sigma_L}\right)^2}} \tag{6.2}$$

Equation 6.2 shows that the ratios μ_L / σ_L, μ_S / μ_L and σ_S / σ_L determine the standard deviate Z. Then, by applying the standard normal distribution the influence of these ratio on the reliability can be quantified. From Figure 6.1c it can be derived that the strength-load mean value ratio μ_S / μ_L (i.e. the safety factor) has the greatest influence on the reliability, followed by the ratio of load mean value and standard deviation μ_L / σ_L. The ratio of the standard deviations σ_S / σ_L only has a minor influence. Assuming that the system strength remains constant, these considerations demonstrate that decreasing the system load magnitude, i.e. increasing the mean value ratio μ_S / μ_L, will provide substantial improvements of the reliability. For example, a 10% load decrease that raises the ratio μ_S / μ_L from *1.1* to *1.2*, increases the system reliability from 78% to 94%. Therefore, the focus of this chapter is on the load magnitude reduction, i.e. reducing the load mean value μ_L.

Moreover, systems are often exposed to unavoidable and unreducible (secondary) loads, like external system excitations via the system input or output. Note that primary loads are those normally needed to convert the system input to the system output, while secondary (oscillating) loads do not participate in the system input-output conversion, but only interfere with it (cp. Figure 6.2). Because a system must be capable of handling these secondary loads, it will be necessary to consider which system component could absorb these loads, and thus reduce their propagation through the rest of the system load path.

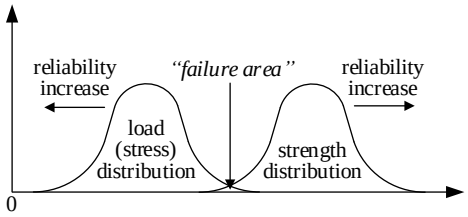

a) Reliability due to load-strength interference

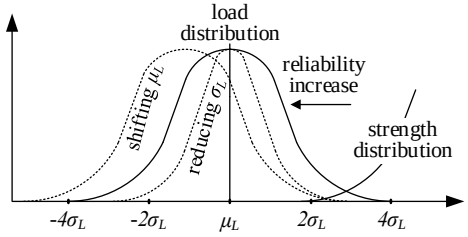

b) Reliability increase by shifting the mean value μ_l or reducing the standard deviation σ_l

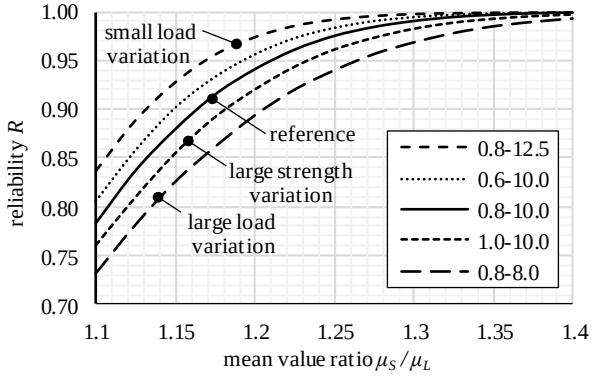

c) System reliability as function of the strength to load mean value ratio μ_S / μ_L , depending on the ratios $\mu_L / \sigma_L \in \{8.0;10;12.5\}$ and $\sigma_S / \sigma_L \in \{0.6;0.8;1.0\}$

Figure 6.1 System reliability from a load reduction perspective

Further, it must be quantified to what extent the selected component reduces the (dynamic) load magnitude, so that the effects on other system components are minimized and a high reliability of these components can be achieved. One way to reduce the dynamic load magnitude is to make use of (active) damping, because it dissipates energy. However, from a conservative point of view the selected component must be able to reduce the dynamic load magnitude by its design, even without damping. This means that in this chapter the component transfer function $A_i(\omega)$ is mainly dominated by the stiffness and inertia terms and thus, is determined excluding damping (cp. Figure 6.2). If a component is able to sufficiently reduce the dynamic load magnitude just by its design, i.e. by its stiffness and inertia, then it will provide a robust performance in absorbing (dynamic) load magnitudes. If then in practice there is some damping, the performance will only be better. In addition, note that the goal is

not to calculate the frequency response over a range of frequencies but just at one or few values, i.e. the frequency response is not quantified close to or at resonance.

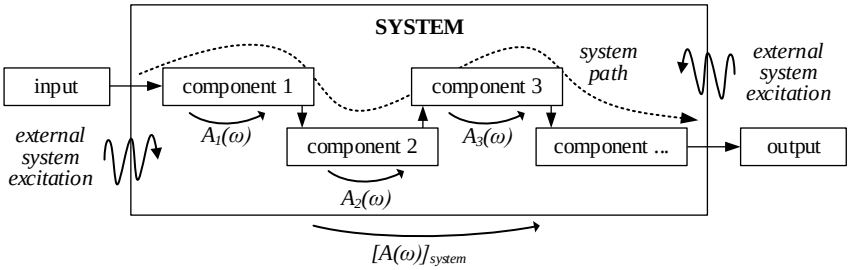

Figure 6.2 System with external excitation where the component transfer functions $A_i(\omega)$ determine whether the external excitations are absorbed or propagated through the system

Now, this concept is applied to the system "wind turbine power train" in this chapter. This system can be divided in a mechanical and electrical subsystem. The two subsystems are connected by the electro-mechanical conversion realized by the generator. The system input (wind turbine rotor) includes the unavoidable and unreducible secondary loads caused by unsteady, asymmetric wind flow [21]. The system output is specified by the (electrical) interface between power train and electrical grid. If the electrical power transformer is considered as interface, then the electrical subsystem will also contain secondary loads due to current and voltage harmonics caused by i) non-linear switches like power diodes or IGBTs in frequency converters [22] or ii) grid disturbances [23][24] (cp. Figure 6.3). The secondary loads of the electrical subsystem could be reduced and, partly also be avoided, if, instead of the frequency converter, an alternative component for compensating speed variability were installed in the power train [25]. This means that the unavoidable and unreducible secondary loads of the wind turbine power train system are mainly related to and caused by the wind turbine rotor. From Figure 6.3, it can be seen that these loads can either be absorbed by the mechanical or electrical subsystem.

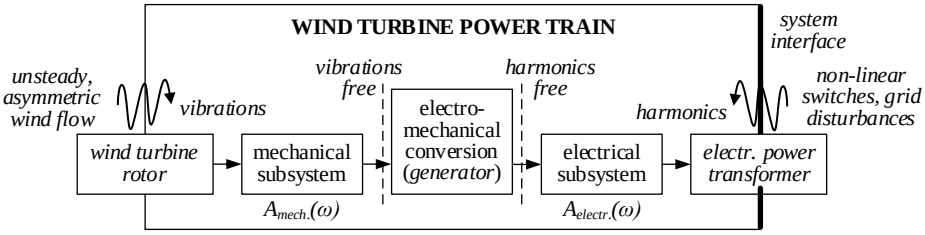

Figure 6.3 Excitation of a wind turbine power train system by mechanical vibrations and electrical harmonics

Depending on the load absorption in the mechanical subsystem, the electro-mechanical conversion and electrical subsystem are exposed to dynamic loads caused by the wind turbine rotor. If the mechanical subsystem transmits the dynamic loads, then higher load magnitudes will occur in the electro-mechanical conversion and electrical subsystem affecting their reliability. In previous work by the authors [20], methods have been proposed to reduce the load magnitude in general, prevent load superposition and quantify the subsystem excitations.

The present chapter will focus on load absorption as an additional way to reduce loads. Therefore, methods are developed to assess the reliability based on the following principle:

Evaluation of the transfer function: the dynamic drive train (i.e. mechanical power train subsystem) behavior is governed by the transfer functions $A(\omega)$ (cp. Figure 6.2). The transfer functions are used to derive the drive train "filter characteristics", i.e. the capacity to absorb dynamic loads in the drive train between input and output. The lower the load magnitude at the drive train output, the higher the reliability of the electro-mechanical conversion and electrical subsystem (assuming that their strengths remain constant).

Note that for choosing an adequate drive train configuration, the load magnitude absorption, i.e. the calculation of the transfer function, should be possible in early concept and design stages where a multi body analysis is not available yet. Therefore, in this chapter the transfer function calculation is performed by i) using analytical equations including simplifications and assumptions and ii) using the main system dimensions. Although this does not provide a highly accurate quantification of the transfer behavior, it will lead to a reasonable estimation of the mechanical subsystem design and thus, to insights for design decisions and reliability assessments. This is shown in the following sections.

6.3 Evaluation of the transfer function

In general, the transfer function $A(\omega)$ of any system is defined by the ratio of the (frequency domain) system output $Y(\omega)$ and input $X(\omega)$ [26], i.e.:

$$A(\omega) = \frac{Y(\omega)}{X(\omega)} \tag{6.3}$$

The term "transfer function" is common in electrical engineering. It is used in linear time invariant (LTI) systems. A good example of LTI systems are electrical circuits made up of resistors, capacitors, and inductors [27]. This means in mechanical engineering terms that LTI systems are created from dampers, springs and masses (inertias) and that the latter also determine the transfer function of the mechanical (sub)system. Further, most real systems have non-linear input/output characteristics; however, many of them, when operated within nominal parameters, demonstrate behavior close enough to linear. Consequently, the LTI system theory is an acceptable representation of the input/output behavior. In addition, to determine the gain (magnitude) of the transfer functions, its absolute value $|A(\omega)|$ is often presented in a Bode plot.

Now, applying these insights to the mechanical power train subsystem, i.e. the drive train, the reduction of the load magnitude from the wind turbine rotor (input) to the generator (output) can be determined. The drive train input contains oscillating torques and the output oscillating shaft speeds (torsional vibrations). The oscillating torques are caused by the wind turbine rotor due to unsteady, asymmetric wind flow. The drive train transfer behavior is governed by the drive train elements transmitting the oscillating torque, i.e. by the transfer functions of shafts, gear stages and rotating masses like generator or wind turbine rotor. To quantify these transfer functions, the damping, stiffness and inertia characteristics of the different (drive train) elements are needed.

Further, as was discussed before, only considering the stiffness and inertia terms in the transfer function calculations leads to a more conservative result. This means that the calculated output magnitude is higher than the actual one. In other words, the load absorption of the mechanical subsystem is in reality higher than calculated. From this perspective, it is beneficial not to consider damping in the transfer function calculation.

Finally, the transfer function is derived for rotating masses interconnected by shafts and gear stages. Although shafts are also rotating masses, they are described here as torsional stiffness. Their masses are added to the rotating masses (inertias) as gear bodies. In addition, the simplest gear stage is a gear-gear (wheel-pinion) assembly. More complex gear stages are wheel-two-pinion or planetary gear stages. Such gear stages are common in drive trains and thus are also considered in the following sections.

6.3.1 Inertia-shaft and gear-gear assembly

The inertia-shaft and gear-gear assemblies, and thus their transfer functions, can be defined as a mass (inertia)-spring system [28]. The mass is given by the inertia, like wind turbine rotor or gear wheels, and the spring is determined by the shaft and gear mesh stiffness. This is shown in Figure 6.4 for the n^{th} inertia-shaft and gear-gear assembly in the drive train as it is also applied by [29]. The transmission of the n^{th} gear stage is i_n.

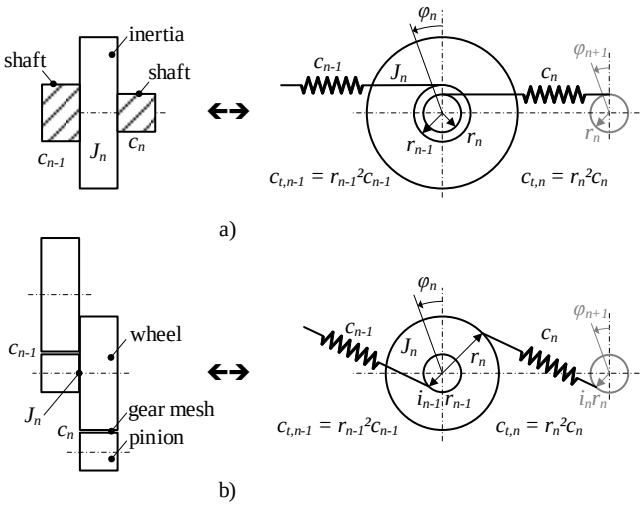

Figure 6.4 a) Inertia-shaft and b) Gear-gear assemblies

With the sum of all moments, the following expressions hold for these assemblies, thus connecting the gear stage n to the previous (n-1) and following (n+1) gear stages:

- Inertia-shaft assembly:
  $$J_n \ddot{\varphi}_n = c_{t,n-1} (\varphi_{n-1} - \varphi_n) - c_{t,n} (\varphi_n - \varphi_{n+1}) \quad (6.4)$$
- Gear-gear assembly:
  $$J_n \ddot{\varphi}_n = -c_{t,n-1} (i_{n-1}\varphi_{n-1} + i_{n-1}^2 \varphi_n) - c_{t,n} (\varphi_n + i_n \varphi_{n+1}) \quad (6.5)$$

where the torsional stiffness c_t for each shaft is obtained from the regular shaft stiffness c by multiplication by the square of the respective shaft radius r.

The (first and) second time derivative of the (sinusoidal) torsion angle φ are given by the following relation of the angle φ and the excitation frequency ω, i.e.

$$\dot{\varphi} = j\omega\,\varphi \tag{6.6}$$
$$\ddot{\varphi} = -\omega^2\varphi \tag{6.7}$$

Then, the transfer function A_n is found by considering Eq. 6.4 and 6.5 in the frequency domain. Further, the natural frequencies $\omega_{0,n}$ of the inertia-shaft or gear-gear assembly are defined as:

$$\omega_{0,n} = \sqrt{\frac{c_{t,n}}{J_n}} \tag{6.8}$$

This yields the following expressions for the transfer function A_n, i.e. the ratio between the torsion angles at the output ($n+1$) and input (n) of the n^{th} gear stage:

- Inertia-shaft assembly:

$$\varphi_{n+1} = \left(1 + \frac{c_{t,n-1}}{c_{t,n}}\left(1 - \frac{\varphi_{n-1}}{\varphi_n}\right) - \omega^2\,\frac{J_n}{c_{t,n}}\right)\varphi_n = A_n\varphi_n \tag{6.9}$$
$$A_n = \left(1 + \frac{c_{t,n-1}}{c_{t,n}}\left(1 - \frac{1}{A_{n-1}}\right) - \frac{\omega^2}{\omega_{0,n}^2}\right) \tag{6.10}$$

- Gear-gear assembly:

$$\varphi_{n+1} = -\frac{1}{i_n}\left(1 + \frac{c_{t,n-1}}{c_{t,n}}\left(i_{n-1}^2 + i_{n-1}\,\frac{\varphi_{n-1}}{\varphi_n}\right) - \omega^2\,\frac{J_n}{c_{t,n}}\right)\varphi_n = -\frac{1}{i_n}A_n\varphi_n \tag{6.11}$$
$$A_n = \left(1 + i_{n-1}^2\,\frac{c_{t,n-1}}{c_{t,n}}\left(1 - \frac{1}{A_{n-1}}\right) - \frac{\omega^2}{\omega_{0,n}^2}\right) \tag{6.12}$$

Now, Eq. 6.10 and 6.12 are the transfer functions of one inertia-shaft respectively gear-gear assembly. A drive train consists of several assemblies, normally arranged in series connection. This means that the transfer functions of the k drive train assemblies must be multiplied to obtained the total drive train transfer function $A_i(\omega)$, i.e.:

$$A_i = \prod_{n=0}^{k} A_n \tag{6.13}$$

It is important to note that the separate assembly transfer functions A_n do not only depend on the ratio of excitation and natural frequency $\omega/\omega_{0,n}$, but also on the preceding assembly transfer function A_{n-1}. Hence, the assembly transfer functions A_0 to A_k must be calculated iteratively, before evaluating the total drive train transfer function in Eq. 6.13.

6.3.2 Wheel-two-pinion and planetary gear stage

Similar to the gear-gear assembly (wheel-pinion stage), the transfer function of a wheel-two-pinion and planetary gear stage can be derived. First, the transfer function of the wheel-

two-pinion gear stage is evaluated based on Figure 6.5. The wheel is connected to a shaft stiffness.

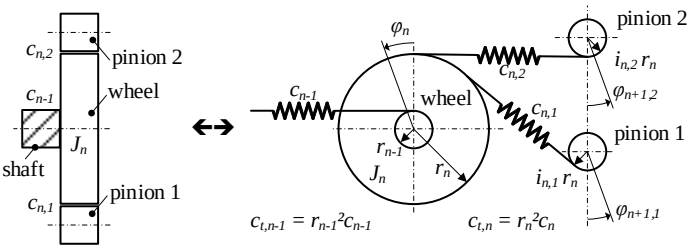

Figure 6.5 Wheel-two-pinion gear stage

Considering the sum of all moments, the following expression is derived for the wheel-two-pinion gear stage:

$$J_n\, \ddot{\varphi}_n = c_{t,n-1}\,(\varphi_{n-1} - \varphi_n) - c_{t,n,1}\,(\varphi_n + i_{n,1}\varphi_{n+1,1}) - c_{t,n,2}\,(\varphi_n + i_{n,2}\varphi_{n+1,2}) \tag{6.14}$$

By transforming Eq. 6.14 to the frequency domain and considering the special case that pinion 1 and 2 are equal, i.e. $c_{t,n,1} = c_{t,n,2} = c_{t,n}$ and $i_{n,1} = i_{n,2} = i_n$, it follows that:

$$\varphi_{n+1,1} + \varphi_{n+1,2} = -\frac{1}{i_n}\left(2 + \frac{c_{t,n-1}}{c_{t,n}}\left(1 - \frac{\varphi_{n-1}}{\varphi_n}\right) - \omega^2\,\frac{J_n}{c_{t,n}}\right)\varphi_n = -\frac{1}{i_n} A_n \varphi_n \tag{6.15}$$

$$A_n = \left(2 + \frac{c_{t,n-1}}{c_{t,n}}\left(1 - \frac{1}{A_{n-1}}\right) - \frac{\omega^2}{\omega_{0,n}^2}\right) \tag{6.16}$$

To solve Eq. 6.15, an additional boundary condition is necessary to determine both $\varphi_{n+1,1}$ and $\varphi_{n+1,2}$. It is obtained by the transmission system configuration taking into account that the wheel-two-pinion gear stage splits power from one to two shafts. In other words, two individual power paths are interconnected by the wheel-two-pinion gear stage. This means that the specific details on how the power is distributed over these two power paths provide the missing boundary condition.

Second, the transfer function of the planetary gear stage is analyzed based on Figure 6.6a. The transfer behavior from the planet carrier to the sun gear is evaluated. So the inertia J_n is determined by the planet carrier and planet gears. Further, the planet carrier is connected to a shaft stiffness.

Again, by considering the sum of all moments at the planet carrier, this yields for the planetary gear stage with k_{pl} planet gears:

$$\begin{aligned} J_n\, \ddot{\varphi}_{c,n} = {} & c_{n-1}\big(\varphi_{n-1} r_{n-1} - \varphi_{c,n} r_{c,n}\big) r_{c,n} + \\ & + k_{pl} c_{n,1}\big(\varphi_{s,n} r_{s,n} + \varphi_{pl,n} r_{pl,n}\big) r_{s,n} + k_{pl} c_{n,2}\big(\varphi_{rg,n} r_{rg,n} - \varphi_{pl,n} r_{pl,n}\big) r_{rg,n} \end{aligned} \tag{6.17}$$

Then, with the radius

$$r_{n-1} = r_{c,n} \ , \tag{6.18}$$

the torsional stiffness

$$c_{t,n-1} = c_{n-1} r_{n-1}^2 \tag{6.19}$$

$$c_{t,n,1} = c_{n,1}\left(r_{pl,n} + r_{s,n}\right)^2 \tag{6.20}$$

$$c_{t,n,2} = c_{n,2}\left(r_{pl,n} + r_{s,n}\right)^2 \tag{6.21}$$

and the ratios given by the stationary gear ratio $i_0 < -1$ of the planetary gear

$$i_n = \frac{1}{1-i_{0,n}} \tag{6.22}$$

$$i_{rg,n} = \frac{r_{rg,n}}{(r_{pl,n}+r_{s,n})} = \frac{2i_{0,n}}{i_{0,n}-1} = -2i_{0,n}i_n \tag{6.22a}$$

$$i_{pl,n} = \frac{r_{pl,n}}{(r_{pl,n}+r_{s,n})} = \frac{1+i_{0,n}}{i_{0,n}-1} = -\left(1+i_{0,n}\right)i_n \tag{6.22b}$$

$$i_{s,n} = \frac{r_{s,n}}{(r_{pl,n}+r_{s,n})} = 2i_n \tag{6.22c}$$

it follows for Eq. 6.17:

$$J_n\,\ddot{\varphi}_{c,n} = c_{t,n-1}\left(\varphi_{n-1} - \varphi_{c,n}\right) + k_{pl}c_{t,n,1}i_n^2\left(4\varphi_{s,n} - 2\varphi_{pl,n}\left(1+i_{0,n}\right)\right) + \\ + k_{pl}c_{t,n,2}i_n^2\left(4\varphi_{rg,n}i_{0,n}^2 - 2\varphi_{pl,n}i_{0,n}\left(1+i_{0,n}\right)\right) \tag{6.23}$$

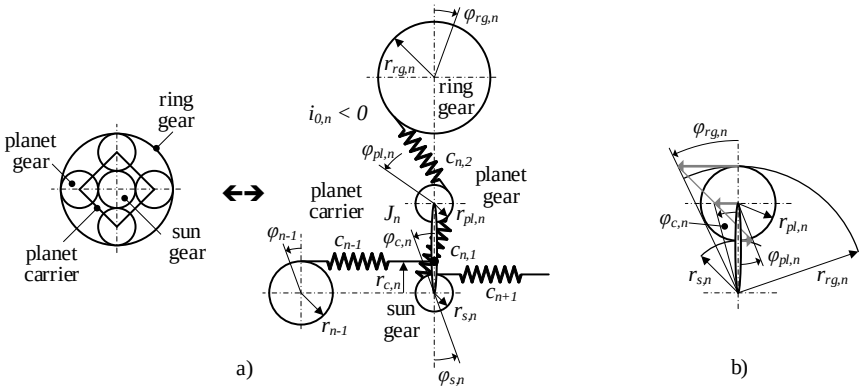

Figure 6.6 a) Planetary gear stage and b) Kinematic relation

Similar to the wheel-two-pinion gear stage, the planetary gear stage can be used for power splitting from one to two shafts or for power summation from two to one shaft [30]. So the configuration of the transmission system provides one boundary condition for Eq. 6.23. If the ring, sun gear or planet carrier are fixed, then this boundary condition is also determined by $\varphi = 0$. However, to solve Eq. 6.23 another boundary condition is necessary for the angle $\varphi_{pl,n}$. It can be obtained by the kinematic relation of the planetary gear (cp. Figure 6.6b).

$$\varphi_{pl,n}r_{pl,n} = -2\varphi_{c,n}\left(r_{pl,n} + r_{s,n}\right) + \varphi_{rg,n}r_{rg,n} \tag{6.24}$$

Implementing this condition in Eq. 6.17 or 6.23 and transferring it to the frequency domain yields:

$$J_n \ddot{\varphi}_{c,n} = c_{t,n-1}\left(\varphi_{n-1} - \varphi_{c,n}\right) + \\ + 4k_{pl}c_{t,n,1}i_n\left(\varphi_{s,n}i_n - \varphi_{c,n} - \varphi_{rg,n}i_n i_{0,n}\right) + 4k_{pl}c_{t,n,2}\varphi_{c,n}i_n i_{0,n} \quad (6.25)$$

$$\varphi_{s,n} - \varphi_{rg,n}i_{0,n} = \\ = \frac{1}{i_n^2}\left(i_n + \frac{c_{t,n-1}}{4k_{pl}c_{t,n,1}}\left(1 - \frac{\varphi_{n-1}}{\varphi_n}\right) - \frac{c_{t,n,2}}{c_{t,n,1}}i_n i_{0,n} - \omega^2\frac{J_n}{4k_{pl}c_{t,n,1}}\right)\varphi_{c,n} = \frac{1}{i_n^2}A_{c,n}\varphi_{c,n} \quad (6.26)$$

$$A_{c,n} = \left(i_n + \frac{c_{t,n-1}}{4k_{pl}c_{t,n,1}}\left(1 - \frac{\varphi_{n-1}}{\varphi_n}\right) - \frac{c_{t,n,2}}{c_{t,n,1}}i_n i_{0,n} - \omega^2\frac{J_n}{4k_{pl}c_{t,n,1}}\right) \quad (6.27)$$

Note that the angle $\varphi_{rg,n}$ is obtained by applying the boundary condition related to the transmission system configuration. Further, Eq. 6.27 determines the transfer function for the case that the planetary carrier is connected to the shaft spring stiffness $c_{t,n-1}$, i.e. to the input shaft of the planetary gear (cp. Figure 6.6a). However, if the ring or sun gear are connected to the input shaft of the planetary gear, then the transfer function in Eq. 6.27 must be re-evaluated based on the sum of all moments at the ring or the sun gear (cp. Eq. 6.17 for the sum of all moments at the planet carrier).

In addition, the transfer function derived here for the planetary gear stage (Eq. 6.27) is based on the assumptions that i) all k_{pl} planet gears have the same angle $\varphi_{pl,n}$ and ii) the angle $\varphi_{pl,n}$ is coupled to the angles $\varphi_{c,n}$ and $\varphi_{rg,n}$ by the kinematic relation (boundary condition) in Eq. 6.24. This means that the individual torsional vibrations of the planet gears are synchronized respectively coupled to the planetary carrier and sun gear. It also means that the transfer function $A_{c,n}$ (Eq. 6.27) determines the input (planetary carrier) / output (sun gear) characteristic only for those specific conditions where these assumptions are fulfilled.

6.3.3 Active drive train damping

In the previous sections any damping is neglected in the transfer function calculation because it leads to a more conservative result. This can also be done for low Coulomb or structural damping (cp. [31]), which is normally present in a drive train. However, viscous damping elements can be incorporated in the drive train, providing significant active damping due to the fluid-structure interaction. They are typically realized by torsional vibration absorbers, pumps or turbines. Their behavior in the drive train is comparable with the behavior of shock absorbers in vehicles. An essential reduction of the transfer function magnitude, i.e. of the dynamic loads, can be achieved by these active damping elements. This means that the transfer function reflects the benefits of active damping elements like torsional vibration absorbers, pumps or turbines in the drive train performance. Knowing these benefits is advantageous for system designers, owners or service providers, because it provides a possibility for additional load absorption in the drive train. This yields a high power train reliability, as will be shown later. Therefore, in this section it is demonstrated how (active) damping can be implemented in the drive train transfer functions derived in the previous sections.

The transfer function including damping can be developed based on Figure 6.4a. The (spring) stiffness $c_{t,n-1}$ and the angle φ_{n-1} are neglected. Then, a damper with damping $d_{t,n}$ is implemented in parallel to the (spring) stiffness $c_{t,n}$. In the case of a wind turbine rotor or

torsional vibration absorber, this damper is connected to the inertia J_n and to the surrounding so that the damper represents the fluid-structure interaction. The damper is not connected to the inertia J_{n+1} as the stiffness $c_{t,n}$. With Eq. 6.6 this yields:

$$J_n \ddot{\varphi}_n = -d_n \dot{\varphi}_n - c_{t,n} (\varphi_n - \varphi_{n+1}) \tag{6.28}$$

$$\varphi_{n+1} = \left(1 + j\omega \frac{d_{t,n}}{c_{t,n}} - \omega^2 \frac{J_n}{c_{t,n}}\right) \varphi_n = A_n \varphi_n \tag{6.29}$$

$$A_n = \left(1 + j\omega \frac{d_{t,n}}{c_{t,n}} - \frac{\omega^2}{\omega_{0,n}^2}\right) \tag{6.30}$$

Note that for the wind turbine rotor $n = 0$ in this chapter, i.e. the inertia J_0 is determined only by the wind turbine rotor mass (inertia), the damping $d_{t,0}$ by the fluid-blade interaction and the stiffness $c_{t,0}$ only by the main shaft stiffness.

Further, it is visible from Eq. 6.30 that the complex term $j\omega d_{t,n}/c_{t,n}$ is added in the transfer function A_n. The ratio $d_{t,n}/c_{t,n}$ is related to the dimensionless damping ratio ζ (zeta) often used in literature [26]. The damping ratio distinguishes underdamped ($\zeta < 1$), critically damped ($\zeta = 1$) and overdamped ($\zeta > 1$) system behavior. It is specified by the ratio of actual ($d_{t,n}$) and critical ($d_{t,n,c}$) damping [26]. With the natural frequency $\omega_{0,n}$ (cp. Eq. 6.14) the damping ratio ζ_n is defined as follows:

$$\zeta_n = \frac{d_{t,n}}{d_{t,n,c}} = \frac{d_{t,n}}{2\sqrt{J_n c_{t,n}}} = \frac{\omega_{0,n}}{2} \frac{d_{t,n}}{c_{t,n}} \tag{6.31}$$

This means that the damping ratio is determined by the ratio $d_{t,n}/c_{t,n}$ and the natural frequency $\omega_{0,n}$. It also means that the magnitude of active drive train damping can roughly be estimated based on the damping ratio ζ_n, or on the ratio $d_{t,n}/c_{t,n}$ if the actual damping $d_{t,n}$ is unknown or too complex to quantify. For example, the wind turbine rotor damping $d_{t,0}$ can be estimated by assuming a ratio $d_{t,0}/c_{t,0}$ of 0.05 seconds. Although this does not provide an exact quantification of the active damping effect on the transfer function, it does estimate the effect of the active damping on the drive train transfer function.

Further, Eq. 6.30 and 6.31 provide another crucial insight for wind turbine drive trains. The active damping (i.e. the damping ratio) can be increased by decreasing the stiffness $c_{t,n}$. So depending on the main shaft stiffness $c_{t,0}$, a lower or higher damping ratio ζ_0 is achieved, assuming a constant wind turbine rotor inertia J_0 and actual damping $d_{t,0}$. This means, for example, that using the same wind turbine rotor on a direct drive and geared wind turbine leads to different damping ratios ζ_0, because the main shaft in a direct drive wind turbine is shorter and thus stiffer than in a geared wind turbine. Consequently, the damping ratio of the direct drive wind turbine rotor is lower than the one of the geared wind turbine rotor, i.e. $\zeta_{0,DD} < \zeta_{0,GB}$. From this, it can already be seen that the active damping characteristics of the wind turbine rotor are more effectively used in the geared wind turbine (with a lower main shaft stiffness). A higher damping ratio reduces the transfer function and thus increases the dynamic load absorption, as will be shown later.

6.3.4 Gear mesh stiffness approximation

For calculating the transfer function, the inertia (of rotating masses) and stiffness (of shaft and gear mesh) must be known. Ideally, the inertia and stiffness are derived from dimensions

like radii, lengths and widths. That is the case for rotating masses described as a disk (inertia) and shafts (torsional stiffness) [32], i.e.:

$$J = \frac{\pi}{2}\rho b R^4 \tag{6.32}$$

$$c_{t,shaft} = \frac{\pi}{2}\frac{G}{l}r^4 \tag{6.33}$$

with the mass density ρ, width b and radius R of the rotating mass, respectively shaft length l, radius r and shear modulus G.

Similar expressions for the gear mesh stiffness are not readily available. However, determining this stiffness from the gear radius, width or length would be convenient for the transfer function calculation, i.e. for specifying the stiffness ratio $c_{t,n-1}/c_{t,n}$ and natural frequencies $\omega_{0,n}$ (cp. Eq. 6.12). For example, for an inertia-shaft assembly, including Eq. 6.32 and 6.33 in Eq. 6.8 leads to a simple definition of the natural frequency ω_0:

$$\omega_0 = \sqrt{\frac{c_{t,shaft}}{J}} = \frac{r^2}{R^2}\sqrt{\frac{G}{\rho\, b\, l}} \tag{6.34}$$

This demonstrates that a simple linear description of the gear mesh stiffness based on fundamental gear dimensions would be very useful for the transfer function calculation. Therefore, the gear mesh stiffness will be approximated here by a linear torsional stiffness similar to that of a shaft. To do so, a trapezoidal (spur) tooth loaded by a contact force F is assumed. This contact force depends on the transmitted torque T and pitch radius R_p (cp. Figure 6.7).

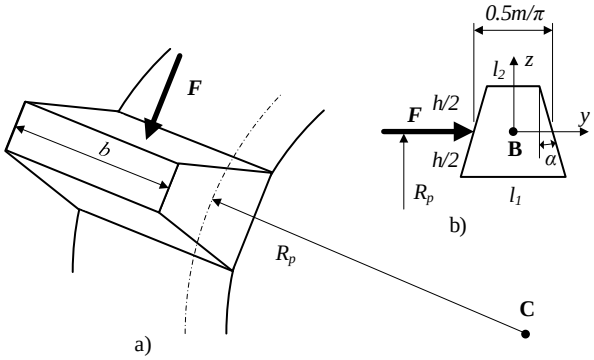

Figure 6.7 Trapezoidal spur gear tooth

With the flank angle α and module m (the gear size, defined as reference diameter ($2R_p$) divided by number of teeth) given, the tooth height (h) and inner (l_1) and outer tooth length (l_2) are, according to DIN 3960, given by:

$$h = 2m \tag{6.35}$$

$$l_1 = m\left(\frac{\pi}{2} + 2\tan\alpha\right) \tag{6.36}$$

$$l_2 = m\left(\frac{\pi}{2} - 2\tan\alpha\right) \tag{6.37}$$

The area (A) and moments of inertia (I_y and I_z) of the trapezoidal tooth in reference to the tooth center point B are specified by [32]:

$$A_{tooth} = \frac{h}{2}(l_1 + l_2) = \pi m^2 \tag{6.38}$$

$$I_{yA,tooth} = \frac{h^3}{36}\frac{(l_1+l_2)^2+2l_1l_2}{(l_1+l_2)} = m^4\left(\frac{\pi}{3} - \frac{16}{9\pi}(\tan\alpha)^2\right) \tag{6.39}$$

$$I_{zA,tooth} = \frac{h}{48}(l_1 + l_2)\left({l_1}^2 + {l_2}^2\right) = m^4\left(\frac{\pi^3}{48} + \frac{\pi}{3}(\tan\alpha)^2\right) \tag{6.40}$$

With Steiner's theorem the torsional moment of inertia of the trapezoidal tooth in reference to the gear center (point C) is given by:

$$I_{pC,tooth} = I_{yC,tooth} + I_{zC,tooth} + A_{tooth}R_p^2 =$$
$$= m^4\left(\frac{\pi^3}{48} + \frac{\pi}{3}(1 + (\tan\alpha)^2) - \frac{16}{9\pi}(\tan\alpha)^2\right) + \pi R_p^2 m^2 \tag{6.41}$$

The torsional moment of inertia of the gear body with reference to the gear center C is defined with the number of teeth z and the gear radius R_p (neglecting tooth clearance).

$$z = 2\frac{R_p}{m} \tag{6.42}$$

$$I_{pC,body} = \frac{\pi}{2}\left(R_p - m\right)^4 = \frac{\pi}{2}R_p^4\left(1 - \frac{2}{z}\right)^4 \tag{6.43}$$

Then, the torsional moment of inertia of the gear is obtained by summing up the moments of inertia of the gear body and trapezoidal tooth:

$$I_{p,gear} = I_{pC,body} + I_{pC,tooth} =$$
$$= \frac{\pi}{2}R_p^4\left(1 - \frac{2}{z}\right)^4 + \pi R_p^2 m^2 + m^4\left(\frac{\pi^3}{48} + \frac{\pi}{3}(1 + (\tan\alpha)^2) - \frac{16}{9\pi}(\tan\alpha)^2\right) \tag{6.44}$$

Further, based on Eq. 42, $R_p >> m$ for higher teeth numbers (e.g. $z > 20$). This is the case for gear wheels and often also for gear pinions. Hence, the torsional moment of inertia of the gear can be approximated by taking only the torsional moment of inertia of the gear body $I_{pC,body}$.

$$I_{p,gear} \approx I_{pC,body} = \frac{\pi}{2}R_p^4\left(1 - \frac{2}{z}\right)^4 \tag{6.45}$$

Moreover, the torsional gear or tooth stiffness $c_{t,tooth}$ in [Nm/rad] is defined by the torsional angle φ and the torque T, or by the moment of inertia, shear modulus G and gear width b.

$$c_{t,tooth} = \frac{T}{\varphi} = \frac{G}{b}I_{p,gear} = \frac{\pi}{2}\frac{G}{b}R_p^4\left(1 - \frac{2}{z}\right)^4 \tag{6.46}$$

The torsional tooth stiffness [Nm/rad] is then converted into a tooth (spring) stiffness c_{tooth} in [N/m] using the pitch radius R_p, as was also explained after Eq. 6.4 and 6.5 related to Figure 6.4b.

$$c_{tooth} = \frac{c_{t,tooth}}{{R_p}^2} = \frac{\pi}{2}\frac{G}{b}{R_p}^2\left(1-\frac{2}{z}\right)^4 \tag{6.47}$$

The tooth stiffness c_{tooth} can also be written per unit face width in [N/m²], i.e.:

$$c'_{tooth} = \frac{c_{tooth}}{b} = \frac{\pi}{2}G\left(\frac{R_p}{b}\right)^2\left(1-\frac{2}{z}\right)^4 \tag{6.48}$$

In addition, for evaluating the mesh stiffness c'_{mesh} (per unit face width), the tooth stiffness of a wheel (w) and pinion (p) gear must be combined. This means that the stiffness of the spring (c_n) or gear mesh shown in Figure 6.4b is determined by the series connection of two teeth stiffness values (pinion and wheel).

$$\frac{1}{c'_{mesh}} = \frac{1}{c'_{tooth,p}} + \frac{1}{c'_{tooth,w}} \tag{6.49}$$

So finally, with Eq. 6.48 and 6.49, as well as the stage transmission ratio $i_{st} = z_p / z_w < 1$, the mesh stiffness c'_{mesh} is specified as follows:

$$c'_{mesh} = \frac{c'_{tooth,p}\,c'_{tooth,w}}{c'_{tooth,p} + c'_{tooth,w}} = \frac{\pi}{2}G\left(\frac{R_{p,p}}{b}\right)^2\left(k(i_{st},z_p)\right)^2\left(1-\frac{2}{z_p}\right)^4\frac{1}{1+f_{pw}(i_{st},z_p)} =$$
$$= \frac{\pi}{2}G\left(\frac{R_{p,p}}{b}\right)^2\left(k(i_{st},z_p)\right)^2 F_{pw}(i_{st},z_p) \tag{6.50}$$

with

$$f_{pw}(i_{st},z_p) = i_{st}^2\left(\frac{1-\frac{2}{z_p}}{1-\frac{2\,i_{st}}{z_p}}\right)^4 \tag{6.51}$$

In principle, the mesh stiffness can now be estimated (cp. Eq. 6.50) using only the basic gear characteristics (i.e. shear modulus G, gear pitch radius R_p, width b, number of teeth z_p and stage transmission ratio i_{st}). These basic parameters are typically easy to obtain, e.g. from assembly plans. If the resulting accuracy would be insufficient, the correction factor $k(i_{st},z_p)$ in Eq. 6.50 can be used to adjust the simplified description of the mesh stiffness to that of a more accurate reference mesh stiffness. In such a case, it is sufficient to evaluate the reference mesh stiffness based on one (similar) gear stage for different transmission ratios, especially if all gearbox stages have a similar tooth and mesh geometry. Therefore, in combination with a reference mesh stiffness, Eq. 6.50 provides the benefit of calculating the (gearbox) mesh stiffness based on very limited information, but with a relatively high accuracy.

A references mesh stiffness (per unit face width) can be calculated, for example, with DIN 3990-1 (Method B). For spur gears with helical gear angle $\beta = 0$ and a teeth overlap $\varepsilon_\alpha > 1.2$ this yields

$$c'_{mesh,DIN} = c'_{th}C_M C_B C_R(0.75\,\varepsilon_a + 0.25) \tag{6.52}$$

For a solid disc wheel and a basic standard rack profile the correction factors are: $C_M = 0.8$, $C_B = 1$, $C_R = 1$. Thus, for a teeth overlap $\varepsilon_\alpha = 1.33$ this yields

$$c'_{mesh,DIN} = c'_{th} \tag{6.53}$$

where c'_{th} equals $1/q'$, with q' defined as a function of the numbers of teeth z on the pinion and wheel (DIN 3990-1):

$$q' = 0.04723 + 0.15551\frac{1}{z_p} + 0.25791\frac{1}{z_w} \tag{6.54}$$

Then, the correction factor $k(i_{st},z_p)$ is specified by:

$$k(i_{st}, z) = \sqrt{\frac{c'_{mesh,DIN}}{\frac{\pi}{2}G\left(\frac{R_{p,p}}{b}\right)^2 F_{pw}(i_{st},z_p)}} \tag{6.55}$$

Figure 6.8 shows the correction factor $k(i_{st},z_p)$ for a pitch radius gear width ratio $R_{p,p} / b = 0.5$ as a function of stage transmission ratios i_{st}. It can be seen that for higher number of teeth z_p the correction factor $k(i_{st},z_p)$ is almost constant. This means that the derived mesh stiffness c'_{mesh} fits with the reference stiffness $c'_{mesh,DIN}$ from a qualitative point of view, as an offset is the only difference. Further, for stage transmission ratios $i_{st} < 0.25$ the correction factor $k(i_{st},z_p)$ is almost independent of the stage transmission ratio i_{st}. Consequently, the reference mesh stiffness, i.e. the correction factor $k(z_p)$, can be evaluated just depending on the number of teeth z_p.

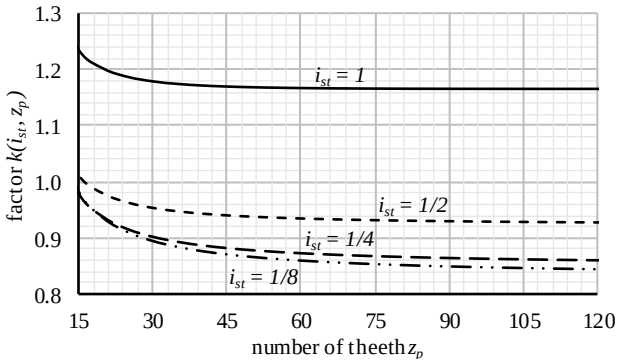

Figure 6.8 Correction factor $k(i_{st},z_p)$ for $R_{p,p} / b = 0.5$ and different stage transmission ratio i_{st}

Based on the evaluated correction factor $k(i_{st},z_p)$, the product of $(k(i_{st},z_p))^2$ and $F_{pw}(i_{st},z)$ is calculated. This product can be considered as a non-dimensional or normalized mesh stiffness $c'_{n,mesh}$.

$$c'_{n,mesh} = \frac{c'_{mesh,DIN}}{\frac{\pi}{2}G\left(\frac{R_{p,p}}{b}\right)^2} = (k(i_{st}, z))^2 F_{pw}(i_{st}, z) \tag{6.56}$$

This normalized mesh stiffness $c'_{n,mesh}$ is shown in Figure 6.9 (for spur gearing), and appears to increase with the number of teeth.

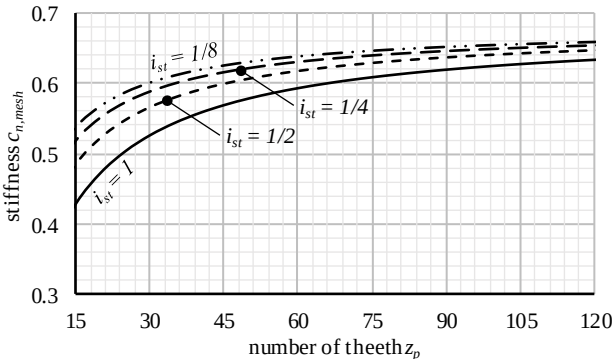

Figure 6.9 Non-dimensional mesh stiffness $c'_{n,mesh}$ for different stage transmission ratio i_{st}

Once the mesh stiffness $c'_{n,mesh}$ (per unit face width) is evaluated, it can be used to estimate the torsional stiffness [Nm/rad] of any wheel-pinion gear stage, if the pitch radius R_p and width b of the wheel and pinion are known (cp. also Eq. 6.46 to 6.48).

$$c_{t,p-w} = \frac{\pi}{2}\frac{G}{b} R_{p,p}^2 R_{p,w}^2 c'_{n,mesh} = \frac{\pi}{2}\frac{G}{b} i_{st}{}^2 R_{p,w}^4 c'_{n,mesh} \tag{6.57}$$

In addition, note that three different stiffness are calculated here. First, the stiffness c' (per unit face width) in [N/m²] is needed for the comparison with the reference stiffness provided by the DIN 3990. Second, the stiffness c in [N/m] represents the spring (gear mesh) stiffness shown in Figure 6.4b and third, the (torsional) stiffness c_t in [Nm/rad] is used for the transfer function calculation, i.e. for the stiffness ratio $c_{t,n-1}/c_{t,n}$ and natural frequencies $\omega_{0,n}$.

6.4 Case study

Now, the transfer functions derived in the previous sections for different assemblies and active damping are applied to a direct drive (Figure 6.10) and geared (Figure 6.11) wind turbine. Active damping is modeled at the wind turbine rotor (d_{rot}) and at the generator high speed shaft (d_{HSS}) of the geared wind turbine (cp. Figure 6.11).

The drive train input is specified by the dynamic rotor torque $T_{dyn,rot}$ and the drive train output by the torsional generator stiffness $c_{t,5}$ and the torsion angle φ_5. Figure 6.10 and 6.11 also show a dynamic torque ($T_{dyn,Ge}$) at the generator. This torque is caused by current and voltage harmonics at the generator terminals (cp. Figure 6.3). This yields the following relations between input and output (~ the transfer function) for the direct drive wind turbine

$$c_{t,5}\,\varphi_5 = \frac{T_{dyn,rot}}{A_0\,A_1} + \frac{T_{dyn,Ge}}{A_1} \tag{6.58}$$

and for the geared wind turbine

$$c_{t,5}\,\varphi_5 = \frac{i_{GB}\,T_{dyn,rot}}{A_0\,A_1\,A_2\,A_3\,A_4\,A_5} + \frac{T_{dyn,Ge}}{A_5} \tag{6.59}$$

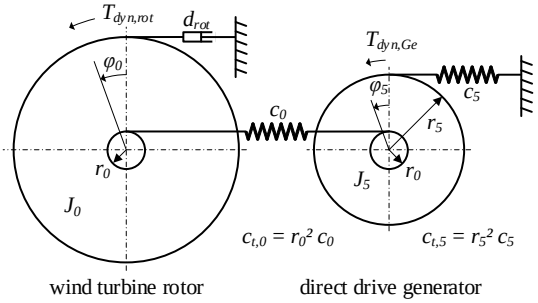

Figure 6.10 Direct drive wind turbine drive train representation

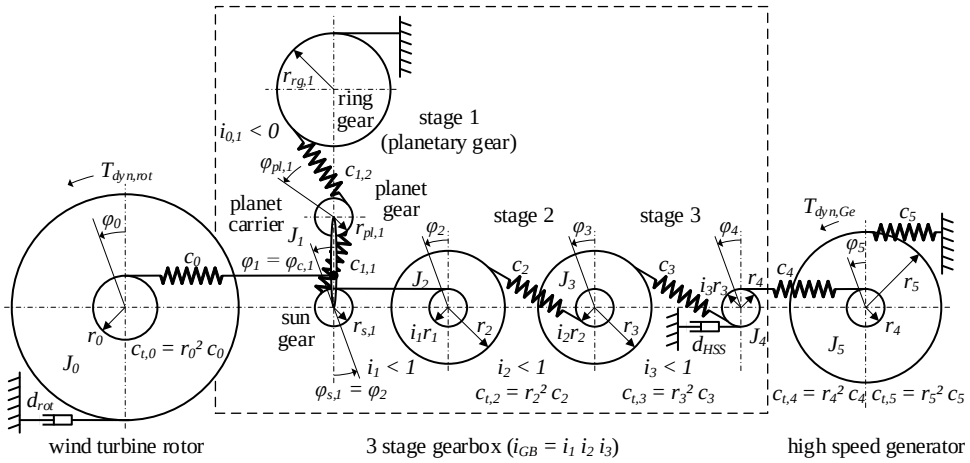

Figure 6.11 Schematic representation of a geared wind turbine with one planetary gear stage and a high speed generator

The functions A_n with $n \in [0,5]$ specify the transfer behavior of the different drive train assemblies and gear stages (cp. Figure 6.10 and 6.11). The detailed derivations of the functions A_n, and thus of the transfer functions of the direct drive (Eq. 6.58) and geared (Eq. 6.59) wind turbine, are provided in Appendix A6.7.1 and A6.7.2, respectively.

Further, the nominal direct drive generator torque is i_{GB} times larger than the geared drive generator torque. Based on this, it is assumed that the torsional generator stiffness $c_{t,5}$ of the geared wind turbine is approx. i_{GB} times (total gearbox ratio) smaller than the stiffness $c_{t,5}$ of the direct drive wind turbine. In addition to that, the dynamic generator torque is neglected. This yields the transfer functions of the direct drive (*DD*) and geared (*GB*) wind turbine:

$$DD = \prod_{n=0}^{1} \frac{1}{A_n} = \frac{1}{A_0\,A_1} \tag{6.60}$$

$$GB = \prod_{n=0}^{5} \frac{1}{A_n} = \frac{1}{A_0\,A_1\,A_2\,A_3\,A_4\,A_5} \tag{6.61}$$

To quantify the transfer functions *DD* and *GB*, the scenarios shown in Table 6.1 and 6.2 are assumed.

Table 6.1 Scenario used for direct drive wind turbine in Figure 10

parameter	unit	value	comments
P	[W]	$2.5*10^6$	rated power
m_5	[kg]	$\approx 5*10^4$	generator rotor mass
D_5	[m]	≈ 8	generator rotor diameter
l_{LSS}	[m]	0.5	main (low speed) shaft length
$d_{t,0}/c_{t,0}$	[s]	0.05	damping stiffness ratio (rotor)
τ	[N/mm²]	75	shear stress in shaft
φ_{load}	[rad]	20°	generator load angle
ω_{LSS}	[1/s]	0.4π	wind turbine rotor speed

Table 6.2 Scenario used for geared wind turbine in Figure 11

parameter	unit	value	comments
P	[W]	$2.5*10^6$	rated power
m_5	[kg]	$\approx 7.5*10^3$	generator rotor mass
D_5	[m]	≈ 0.75	generator rotor diameter
l_{LSS}	[m]	3	main (low speed) shaft length
l_{HSS}	[m]	1	high speed shaft length
$i_{0,1}$	-	-5	stationary gear ratio
i_2	-	0.24	stage 2 gear ratio
i_3	-	0.25	stage 3 gear ratio
k_{pl}	-	4	number of planets
k_S	-	2	shaft inertia factor
$c_{n,mesh}$	-	0.55	non-dimensional stiffness
$d_{t,0}/c_{t,0}$	[s]	0.3	damping stiffness ratio (rotor)
$d_{t,4}/c_{t,4}$	[s]	0.1	damping stiffness ratio (HSS)
ρ_{st}	[kg/m³]	$7.85*10^3$	density of steel
τ	[N/mm²]	75	shear stress in shafts
φ_{load}	[rad]	20°	generator load angle
ω_{LSS}	[1/s]	0.4π	wind turbine rotor speed

The transfer functions *DD* and *GB* are calculated including and excluding damping (cp. Figure 6.12). They represent the approximate direct drive and geared drive transfer behavior, because of the many assumptions made in the previous sections. This means that the absolute values of the transfer functions *DD* and *GB* deviate from reality. Theoretically, without any damping, the resonance peaks would tend to infinity. However, in Figure 6.12 they appear to attain finite magnitudes. Nevertheless, crucial insights can still be gained from these transfer functions.

It is expected that the dynamic properties of individual drive train components or stages will appear in the total drive train transfer functions. At the same time, the interaction between the components is expected to cause shifts in the high-response frequencies.

In the results excluding damping, the natural frequencies $\omega_{0,0}$ governed by the wind turbine rotor and main shaft stiffness, and $\omega_{0,5}$ governed by generator rotor inertia and generator stiffness can be associated to the peaks observed in the spectrum. The (calculated) natural frequency (cp. Eq. 6.8) of the wind turbine rotor $\omega_{0,0}$ is approx. *1.74 Hz* (*DD*) respectively *0.71 Hz* (*GB)*. The (calculated) natural frequency of the generator $\omega_{0,5}$ is approx. *0.6 Hz* (*DD*) respectively *1.65 Hz* (*GB*). This means that in Figure 6.12 the peak associated to the natural frequencies $\omega_{0,5}$ is shifted to higher frequencies in both *DD* and *GB*. The peak related to the

natural frequencies $\omega_{0,0}$ is shifted to lower frequencies in *DD*, while it is not shifted at all in *GB*. The wind turbine rotor excites the drive train with the first and third rotor harmonics [20], i.e. with excitation frequencies in the range of *0.05-0.75 Hz*, when assuming a rotor speed of approx. *3-15 rpm*. This means that a shift to higher frequencies is advantageous because the peak associated to the natural frequency is moved away from the excitation frequencies. Consequently, not shifting the peak of the natural frequency is better than moving it closer to the excitation frequencies. Therefore, by considering the peak shifting in the transfer function (relative to the original component natural frequencies), it can already be identified which drive train configuration is prone to higher dynamic loads. This means that the direct drive (*DD*) will be exposed to higher dynamic loads than the geared drive (*GB*) because its transfer function shows a shift of the resonance frequencies closer to the rotor excitation frequencies.

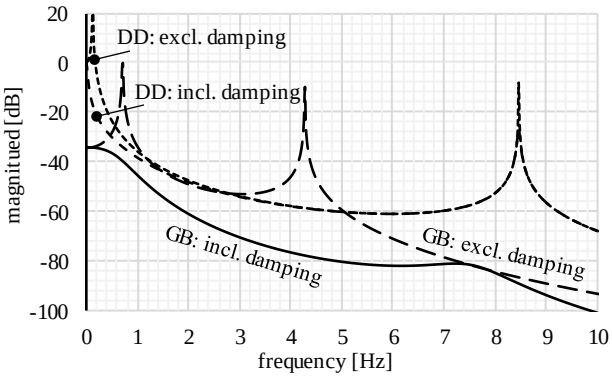

Figure 6.12 Drive train transfer functions *DD* and *GB* for the scenarios in Table 1 and 2
(Note that *DD: excl. damping* and *DD: incl. damping* overlap at higher frequencies)

Further, only considering stiffness and inertia terms, i.e. excluding damping in the transfer function calculation leads to a more conservative result, i.e. the calculated magnitude is higher than the actual one. When the peaks of the natural frequencies are ignored, the plot provides insight in whether the direct or geared drive shows a greater potential of absorbing dynamic loads. By comparing the transfer functions *DD* and *GB* excluding damping, it can be seen that the transfer function *GB* starts at minus *34.5 dB*, while the transfer function *DD* starts above *0 dB*. This reveals an essential advantage of the geared drive (transfer function *GB*), because in the frequency range of *0.05-0.75 Hz* where the wind turbine rotor excites the drive train, the geared drive (*GB*) demonstrates a lower transfer function, i.e. a higher load absorption, than the direct drive (*DD*). The geared drive achieves this by its lower global stiffness (than the direct drive). In addition, the transfer function *GB* declines faster with increasing frequencies than the transfer function *DD*. These aspects indicate that the geared drive has a greater potential to absorb dynamic loads than the direct drive. As damping is excluded in these consideration, this potential is achieved solely by the drive design, i.e. by the assembly of different shafts and gears. This also demonstrates that load absorption can not only be achieved by active damping, but also by selecting the proper drive configuration.

When the results including damping are considered, it is observed that the peaks of the natural frequencies are reduced, except for the natural frequency $\omega_{0,5}$ of the direct drive generator. This is explained by the fact that the technical realization of active (mechanical)

damping at the direct drive generator is difficult, and thus is not considered in Figure 6.10. The damping of the wind turbine rotor ($d_{t,rot}$) and the vibration absorber at the high speed shaft ($d_{t,HSS}$) are estimated based on the ratios $d_{t,0}/c_{t,0}$ respectively $d_{t,4}/c_{t,4}$ (cp. Table 6.1 and 6.2). It is assumed that the actual damping ($d_{t,rot} = d_{t,0}$) of the wind turbine rotor is equal in the transfer functions *DD* and *GB*. However, as the main shaft stiffness ($c_{t,0}$) of the direct drive and geared drive differ due to different main shaft lengths (cp. Table 6.1 and 6.2: l_{LSS}), their ratios $d_{t,0}/c_{t,0}$ also differ, i.e. by a factor of six. This yields a higher damping ratio ζ_0 in the transfer function *GB* than in *DD*, i.e. $\zeta_{0,GB} = 0.67$ and $\zeta_{0,DD} = 0.27$ with Eq. 6.37. Therefore, a higher reduction of the transfer function *GB* is achieved by wind turbine rotor damping. This means that wind turbine rotor damping is more effective in the geared wind turbine (with a low main shaft stiffness) than in a direct drive wind turbine. Further, in the geared drive (cp. Figure 6.11) an active damper (d_{HSS}) is implemented at the high speed shaft (HSS). It damps the drive train in addition to the damping (d_{rot}) of the wind turbine rotor, i.e. it reduces the transfer function *GB* at higher frequencies.

In addition to that, the transfer function GB cannot only be influenced by the drive configuration or active damping, but also by the gear mesh stiffness (cp. the assembly transfer functions A_n derived in the previous section). To demonstrate the influence of the gear mesh stiffness on the transfer function *GB* (including damping), the non-dimensional mesh stiffness $c'_{n,mesh}$, derived in the previous section, is doubled and tripled simultaneously for all gear stages. The result is shown in Figure 6.13, revealing that the transfer function drops at low frequencies when increasing the gear mesh stiffness. This means that a high gear mesh stiffness increases the load magnitude absorption provided by the geared drive. As a reference, also the *DD* transfer function is plotted in Figure 6.13, showing that the load absorption is again much smaller than for the *GB*.

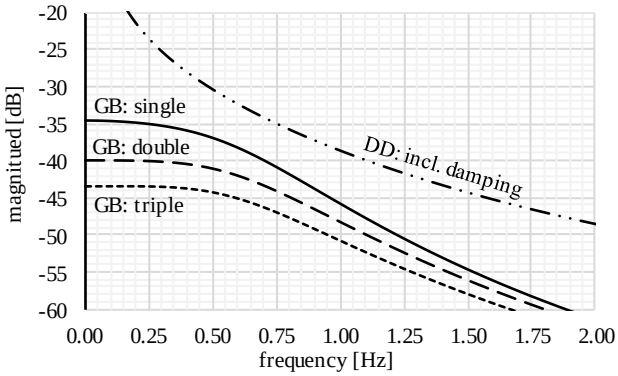

Figure 6.13 Effect of gear mesh stiffness increase on the transfer function *GB* including damping

Moreover, by quantifying the gain margin of the transfer functions *DD* and *GB*, the dynamic behavior of the direct and geared drives can be determined. The gain margin is defined by the smallest distance of the transfer function from *0 dB*. In control theory, as a rule of thumb, a gain margin of *20 dB* is often recommended to ensure the stability of a system (despite external excitations). From Figure 6.12, it is visible that the transfer function *DD* approximates *0 dB* at low frequencies, while the transfer function GB already starts with *-34.5 dB* and decreases further with increasing frequencies. This means that the direct drive is prone to an instable dynamic (oscillating) behavior at low excitation frequencies, while the

geared drive is stable. In other words, the generator rotor is more likely to oscillate, i.e. to show torsional vibrations, in a direct than in a geared drive. An oscillating generator rotor causes (current and voltage) harmonics [33], increasing the dynamic loads in the electro-mechanical conversion and electrical power train subsystem.

These considerations demonstrate that a geared drive provides a higher dynamic load absorption (lower transfer function) than a direct drive. A geared drive achieves this by its configuration, active damping and high gear mesh stiffness. Further, a higher dynamic load absorption by the drive train increases the reliability of the electro-mechanical conversion and the electrical power train subsystem (cp. Figure 6.3). This means that the drive train configuration, active damping and gear mesh stiffness can be used to assess the reliability of the electro-mechanical conversion and electrical subsystem in different power trains. Note that this is a relative reliability assessment, because it is determined by comparing two systems instead of quantifying the absolute reliability of one specific system.

For example, it is assumed that a wind turbine rotor spins at 12 *rpm* (*0.2 Hz*) and excites the drive train with its first harmonic and with a dynamic torque equal to 10% of the nominal torque, i.e. $T_{dyn} = 0.1T_{nom}$. The total drive train input load is the sum of the nominal and dynamic torque, i.e. $1.1T_{nom}$. Further, at a frequency of *0.2 Hz* the direct and geared drive reduce the dynamic torque magnitude from 100% to approx. 8.7% (*-21.2 dB*) respectively 1.8% (*-34.8 dB*) (cp. Figure 6.12). This means that the total load magnitude is approx. 0.7% lower at the geared than at the direct drive. In other words, the strength to load ratio μ_S / μ_L (safety factor) is a factor $k_L = 1.007$ higher for the geared drive than for the direct drive. This yields a higher reliability of the geared drive by approx. 0.5-1%, or a higher failure probability of the direct drive by approx. 5-10% (cp. Figure 6.1c: reference). With Eq. 6.1 and 6.2 the failure probability increase (ΔP_f) is determined as follows:

$$\Delta P_f = 1 - \frac{1 - \Phi(Z_{GB})}{1 - \Phi(Z_{DD})} = 1 - \frac{1 - \Phi\left(Z\left(k_L \frac{\mu_S}{\mu_L}\right)\right)}{1 - \Phi\left(Z\left(\frac{\mu_S}{\mu_L}\right)\right)} \tag{6.62}$$

So from the perspective of total load magnitude (load mean value) it can already be seen that the geared drive provides a higher reliability than the direct drive. This difference will even be larger, if only the dynamic load magnitudes are considered. From Figure 6.12, it is visible that the geared drive provides a dynamic load magnitude reduction approx. 2 to 10 times higher than the direct drive. This means that the geared drive causes significantly lower dynamic load magnitudes and thus, reduces the number of fatigue failures related to these cyclic loads. For example, applying this to a S-N curve means that a magnitude (stress) reduction by a factor of 2 to 10 yields a significant increase of load cycles until failure. This increase can be in the range of 10^6 to 10^7 cycles or even higher, depending on the material and its properties. Note that in a S-N diagram the cyclic stress (S), i.e. dynamic load magnitude, is plotted against the cycles to failure (N), i.e. load cycles, on a logarithmic scale. The latter means that a small decrease of the stress magnitude leads to a considerable increase of the cycles to failure. This improves eventually the reliability.

Finally, taking into account that the dynamic load magnitude of the drive train output is emitted to the electro-mechanical conversion and electrical subsystem (cp. Figure 6.3) it becomes clear that the electrical power train components are exposed to higher load magnitudes in the direct drive and thus demonstrate a lower reliability than in a geared drive.

This coincides with the reliability analyses provided by [7], i.e. the failure frequencies of generators and converters are greater in direct drive than in geared wind turbines.

6.5 Discussion

Now, after determining the wind turbine drive train transfer functions and calculating them exemplary for a direct drive and geared wind turbine, some issues still remain for discussion.

In this chapter fundamental shaft and gear dimensions like radii, lengths and widths are used to determine the transfer functions. As these dimensions are often available in assembly plans, in addition to system designers, system owners and service providers can also execute the transfer function calculation. This means that the proposed methods have a diverse field of application, i.e. they can be used at early concept and design stages, but also for maintenance and reliability considerations.

Further, the system (drive train) transfer function is determined by its configuration, active damping and high gear mesh stiffness. So if system owners and service providers categorize different systems based on these aspects and on the calculated transfer function, they will be able to estimate the failure probability of these system. Then, the failure probability indicates which system tends to have a lower reliability and thus, requires more (future) maintenance activities.

Moreover, the transfer function can be used to identify instable dynamic system responses leading to an increase of dynamic loads and failures. If system owners or service providers identify instable system behavior, they can assess critical system components which suffer the most from dynamic loads. Knowing these components can be used to improve maintenance planning and activities and eventually, the system availability.

In addition, active (viscous) damping is essential in dynamically loaded systems. However, it is also important to use it effectively. This means that the active damping characteristic must be considered together with the system inertia and stiffness, so that an optimal damping ratio is achieved. An effective use of the damping is indicated by the damping ratio as well as by the transfer function. As the effective use of active damping influences both the dynamic load magnitude and dynamic system behavior, it also serves as indicator for the maintenance intensity and reliability of a system. In other words, the detection of poorly used active damping indicates system owners or service providers that their system will require higher maintenance activities.

Finally, in the case of a (geared) drive train the gear mesh stiffness also affects the transfer function. A higher gear mesh stiffness reduces the transfer function, i.e. the dynamic load magnitude, and hence, is beneficial for reducing maintenance activities (costs) and increasing system reliability. However, a higher gear mesh stiffness is often related to higher investment costs of the drive train because single or even double helical gears are required. This demonstrates that a system owner can use the insights from the transfer function to find the optimal costs of owner ship, i.e. a proper balance between investment and maintenance costs.

6.6 Conclusion

In the present chapter equations and models have been proposed to quantify the dynamic load absorption, i.e. the transfer function, of the wind turbine drive train and its effect on the wind turbine reliability. The reliability is determined based on the load-strength interference. The following specific conclusions can be drawn:

- The computationally efficient transfer function calculation, only requiring basic dimensions which are readily available in assembly plans, is the main novelty of the proposed analytical method.
- Due to its flexibility and accessibility the proposed method can be applied by a wide range of stakeholders, like system designers at early concept and design stages, but also system owners and service providers for maintenance and reliability assessments and improvements.
- It is demonstrated that the system (drive train) transfer function, i.e. the dynamic load absorption, is determined by its configuration, active damping and gear mesh stiffness. Especially, the system configuration is essential for a robust performance of the dynamic load absorption.
- The geared drive demonstrates a 2 - 10 times lower transfer function magnitude, i.e. higher dynamic load absorption, than the direct drive. This means that the geared drive provides a significantly higher absorption of the dynamic wind turbine rotor loads, as caused by unsteady, asymmetric wind flow, than the direct drive.
- The geared drive provides a stable dynamic behavior while the direct drive is prone to instable, i.e. oscillating, dynamic behavior. This means that the electro-mechanical conversion and electrical power train subsystem in the direct drive is exposed to higher dynamic loads, and thus yields a lower reliability than the geared drive.
- Considering the damping ratio, it is shown that the geared drive uses the active damping characteristics of the wind turbine rotor more effectively than the direct drive, as it normally has a longer main shaft and thus a lower main shaft stiffness. This leads to a higher drive train damping and eventually to higher dynamic load absorption (and reliability).

References

[1] J. Ribrant, “Reliability performance and maintenance - A survey of failures in wind power systems,” 2006.

[2] J. Ribrant and L. M. Bertling, “Survey of Failures in Wind Power Systems With Focus on Swedish Wind Power Plants During 1997-2005,” *IEEE Trans. Energy Convers.*, vol. 22, no. 1, pp. 167–173, 2007.

[3] Noordzee Wind CV, “Operations Report 2008,” 2009.

[4] Noordzee Wind CV, “Operations Report 2009,” 2010.

[5] M. Wilkinson *et al.*, “Methodology and results of the reliawind reliability field study,” 2010.

[6] Tavner, *Offshore Wind Turbines: Reliability, availability and maintenance*. 2013.

[7] F. Spinato, P. J. Tavner, G. J. W. van Bussel, and E. Koutoulakos, “Reliability of wind turbine subassemblies,” *IET Renew. Power Gener.*, vol. 3, no. 4, p. 387, 2009.

[8] J. Carroll, A. Mcdonald, and D. Mcmillan, “Reliability comparison of wind turbines with DFIG and PMG drive trains,” *Energy Conversion, IEEE Trans.*, vol. 30, pp. 663–670, 2015.

[9] C. Peeters *et al.*, “Drivetrain reliability improvements from long-term field data processed in the cloud,” *J. Phys. Conf. Ser.*, vol. 1222, no. 1, 2019.

[10] E. Artigao, S. Martín-Martínez, A. Honrubia-Escribano, and E. Gómez-Lázaro, “Wind turbine reliability: A comprehensive review towards effective condition monitoring development,” *Appl. Energy*, vol. 228, no. May, pp. 1569–1583, 2018.

[11] W. Musial, S. Butterfield, and B. Mcniff, “Improving wind turbine gearbox reliability,” *Eur. Wind Energy Conf. Exhib. 2007, EWEC 2007*, vol. 3, pp. 1770–1779, 2007.

[12] H. Li, H. Cho, H. Sugiyama, K. Choi, and N. Gaul, “Reliability-based design optimization of wind turbine drivetrain with integrated multibody gear dynamics simulation considering wind load uncertainty,” *Struct. Multidiscip. Optim.*, 2017.

[13] A. Beržonskis and J. D. Sørensen, “Reliability Analysis of Fatigue Fracture of Wind Turbine Drivetrain Components,” *Energy Procedia*, vol. 94, pp. 146–154, 2016.

[14] F. Wang, J. Chen, B. Xu, and K. A. Stelson, “Improving the reliability and energy production of large wind turbine with a digital hydrostatic drivetrain,” *Appl. Energy*, vol. 251, no. December 2018, p. 113309, 2019.

[15] R. Bergua, J. Jove, and E. Javier, “Pure torque drivetrain design: A proven solution for increasing the wind turbine reliability,” *Brazil Wind. 2014 Conf. Exhib.*, no. August 2014, p. 15, 2014.

[16] M. Whittle, J. Trevelyan, W. Shin, and P. Tavner, “Improving wind turbine drivetrain bearing reliability through pre-misalignment,” *Wind Energy*, vol. 17, no. 8, pp. 1217–1230, 2014.

[17] M. Silverman and A. Kleyner, “What is design for reliability and what is not?,” *Proc. - Annu. Reliab. Maintainab. Symp.*, no. November, 2012.

[18] Z. Matić and V. Sruk, “The Physics-of-Failure approach in reliability engineering,” *Proc. Int. Conf. Inf. Technol. Interfaces, ITI*, no. May, pp. 745–750, 2008.

[19] S. Kotz, Y. Lumelskii, and M. Pensky, *The Stress-strength Model and Its Generalizations: Theory and Applications*. World Scientific, 2003.

[20] D. P. Rommel, D. Di Maio, and T. Tinga, “Wind Turbine Power Train Reliability from a Physics Based Design Perspective,” *submitted-2020*.

[21] D. P. Rommel, D. Di Maio, and T. Tinga, “Calculating wind turbine component loads

for improved life prediction," *Renew. Energy*, vol. 146, 2020.
[22] N. Mohan, T. M. Undeland, and W. P. Robbins, *Power electronics: converters, applications, and design*. Wiley, 1995.
[23] H. D. Giesecke, "Steam turbine-generator torsional response due to interaction with the electrical grid," *IEEE Power and Energy Society General Meeting*. 2012.
[24] C. Liu, D. Jiang, and J. Chen, "Coupled torsional vibration and fatigue damage of turbine generator due to grid disturbance," *J. Eng. Gas Turbines Power*, vol. 136, no. 6, 2014.
[25] D. P. Rommel, D. Di Maio, and T. Tinga, "Stabilization of the Renewable Energy Grid by Wind Turbine Generators," *submitted-2019*.
[26] D. Thorby, *Structural Dynamics and Vibration in Practice: An Engineering Handbook*. Elsevier Science, 2008.
[27] T. P. Pavlic, "Review of Circuits as LTI Systems," 2009.
[28] W. D. Mark, "Transfer Function Method for Gear System Dynamics Applied To Conventional and Minimum Excitation Gearing Designs.," *NASA Contract. Reports*, 1982.
[29] F. Küçükay, *Dynamik der Zahnradgetriebe: Modelle, Verfahren, Verhalten*. Springer, 1987.
[30] H. W. Müller, *Die Umlaufgetriebe: Berechnung, Anwendung, Auslegung*, no. v. 27-30. Springer-Verlag, 1971.
[31] H. Mevada and D. Patel, "Experimental Determination of Structural Damping of Different Materials," *Procedia Eng.*, vol. 144, pp. 110–115, 2016.
[32] K. H. Grote and E. K. Antonsson, *Springer Handbook of Mechanical Engineering*, no. v. 10. Springer, 2009.
[33] G. Müller and B. Ponick, *Grundlagen elektrischer Maschinen*. Wiley, 2012.
[34] T. Fuglseth, "Modelling a 2.5 MW direct driven wind turbine with permanent magnet generator," *... Electr. Power Eng. Nor. Univ. ...*, no. 7491, 2005.

A6.7 Appendices

A6.7.1 Direct drive transfer function

Equations to calculate the transfer function of the direct drive *(DD)* wind turbine:

wind turbine rotor:

$$D_0 = \left(\frac{16}{\pi}\frac{P}{\omega_{LSS}\,\tau}\right)^{\frac{1}{3}} \quad \text{(A6.1)}$$

$$c_{t,0} = \frac{\pi}{32}\frac{G}{l_{LSS}}D_0^4 \quad \text{(A6.2)}$$

$$J_0 = 9\cdot 10^6 kgm^2 + \frac{\pi}{64}\rho_{st}D_0^4 l_{LSS} \quad \text{(A6.3)}[3]$$

$$A_0 = \left(1 + j\omega\frac{d_{t,0}}{c_{t,0}} - \omega^2\frac{J_0}{c_{t,0}}\right) \quad \text{(A6.4)}$$

generator:

$$c_{t,5} = \frac{T}{\varphi_{load}} = \frac{P}{\omega_{LSS}\,\varphi_{load}} \quad \text{(A6.5)}$$

$$J_5 = \frac{1}{8}m_5 D_5^2 + \frac{\pi}{64}\rho_{st}D_0^4 l_{LSS} \quad \text{(A6.6)}$$

$$A_1 = \left(1 + \frac{c_{t,0}}{c_{t,5}}\left(1 - \frac{1}{A_0}\right) - \omega^2\frac{J_5}{c_{t,5}}\right) \quad \text{(A6.7)}$$

A6.7.1 Geared drive transfer function

Equations to calculate the transfer function of the geared (*GB*) wind turbine:

It is with the pitch diameter gear width ratio $D_{p,p} / b = 1$ and the torque T proportional to the power three of the shaft (approx. pinion pitch) diameter $D_{p,p}$, i.e. $T = \pi/16\ \tau\ D_{p,p}^3$.

wind turbine rotor:

$$D_0 = \left(\frac{16}{\pi}\frac{P}{\omega_{LSS}\,\tau}\right)^{\frac{1}{3}} \quad \text{(A6.8)}$$

$$c_{t,0} = \frac{\pi}{32}\frac{G}{l_{LSS}}D_0^4 \quad \text{(A6.9)}$$

$$J_0 = 9\cdot 10^6 kgm^2 + \frac{\pi}{64}\rho_{st}D_0^4 l_{LSS} \quad \text{(A6.10)}$$

$$A_0 = \left(1 + j\omega\frac{d_{t,0}}{c_{t,0}} - \omega^2\frac{J_0}{c_{t,0}}\right) \quad \text{(A6.11)}$$

stage 1 = planetary gear stage with $k_{pl} = 4$ planets, $D_{s,p} / b = 1$ and stationary gear ratio $i_{0,1}$ as well as fixed ring gear:

$$i_1 = \frac{1}{(1 - i_{0,1})} \quad \text{(A6.12)}$$

[3] Inertia of a three blade wind turbine rotor for a power of 2.5MW [34] plus half inertia of the main shaft

$$i_{s,1} = \frac{D_{s,1}}{D_{pl,1}} = \frac{-2}{1+i_{0,1}} \tag{A6.13}$$

$$D_{s,1} = D_0 i_1^{\frac{1}{3}} \tag{A6.14}$$

$$D_{pl,1} = D_0 \frac{1}{i_{s,1}} i_1^{\frac{1}{3}} \tag{A6.15}$$

$$D_{rg,1} = D_0(-i_{0,1}) i_1^{\frac{1}{3}} \tag{A6.16}$$

$$c_{t,1,1} = c_{1,1}\left(r_{pl,1} + r_{s,1}\right)^2 = \frac{\pi}{32} G D_{s,1}\left(D_{pl,1} + D_{s,1}\right)^2 c'_{n,mesh} = \\ = \frac{\pi}{32} G D_0^3 i_1 \left(\frac{1}{i_{s,1}^2} + 1\right) c'_{n,mesh} \tag{A6.17}$$

$$c_{t,1,2} = c_{1,2}\left(r_{pl,1} + r_{s,1}\right)^2 = \frac{\pi}{32} G \frac{D_{pl,1}^2}{D_{s,1}}\left(D_{pl,1} + D_{s,1}\right)^2 c'_{n,mesh} = \\ = \frac{\pi}{32} G D_0^3 \frac{i_1}{i_{s,1}^2}\left(\frac{1}{i_{s,1}^2} + 1\right) c'_{n,mesh} \tag{A6.18}$$

$$J_1 \approx \frac{\pi}{32}\rho_{st} D_0^5 \left(k_{pl}(i_1)^{\frac{5}{3}} \frac{1}{i_{s,1}^2}\left(\frac{1}{i_{s,1}^2} + 2\left(1 + \frac{1}{i_{s,1}}\right)^2\right) + \frac{1}{2}\frac{l_{LSS}}{D_0}\right) \tag{A6.19}$$ [4]

$$J_1\, \ddot{\varphi}_1 = c_{t,0}(\varphi_0 - \varphi_1) + 4k_{pl} c_{t,1,1} i_1 (\varphi_2 i_1 - \varphi_1) + 4k_{pl} c_{t,1,2} \varphi_1 i_1 i_{0,1} \tag{A6.20}$$

$$A_1 = \left(i_1 - \frac{c_{t,1,2}}{c_{t,1,1}} i_1 i_{0,1} + \frac{c_{t,0}}{4k_{pl} c_{t,1,1}}\left(1 - \frac{1}{A_0}\right) - \omega^2 \frac{J_1}{4k_{pl} c_{t,1,1}}\right) \tag{A6.21}$$

stage 2 = wheel pinion stage with ratio i_2 (and shaft inertia correction factor k_S)[5]*:*

$$D_2 = D_0 \left(\frac{i_1}{i_2^2}\right)^{\frac{1}{3}} \tag{A6.22}$$

$$c_{t,2} = \frac{\pi}{32} G D_0^3 \frac{i_1}{i_2} c'_{n,mesh} \tag{A6.23}$$

$$J_2 = \frac{\pi}{32}\rho_{st} D_0^5 i_1^{\frac{5}{3}} \left(1 + k_S + \left(\frac{1}{i_2}\right)^{\frac{7}{3}}\right) \tag{A6.24}$$

$$A_2 = \left(1 + 4k_{pl} i_1^2 \frac{c_{t,1,1}}{c_{t,2}}\left(1 - \frac{i_1}{A_1}\right) - \omega^2 \frac{J_2}{c_{t,2}}\right) \tag{A6.25}$$

stage 3 = wheel pinion stage with ratio i_3:

$$D_3 = D_0 \left(\frac{i_1 i_2}{i_3^2}\right)^{\frac{1}{3}} \tag{A6.26}$$

$$c_{t,3} = \frac{\pi}{32} G D_0^3 \frac{i_1 i_2}{i_3} c'_{n,mesh} \tag{A6.27}$$

$$J_3 = \frac{\pi}{32}\rho_{st} D_0^5 (i_1 i_2)^{\frac{5}{3}} \left(1 + k_S + \left(\frac{1}{i_3}\right)^{\frac{7}{3}}\right) \tag{A6.28}$$

[4] Note that for simplifications the relative rotation between planet carrier and planet gears is not considered in the inertia calculation, i.e. it is assumed that the planet gears are fixed to the planet carrier. Then, the inertia is evaluated with the Steiner's theorem.

[5] The correction factor k_S considers the shaft inertia in addition to the wheel and pinion inertia.

$$A_3 = \left(1 + i_2^2 \frac{c_{t,2}}{c_{t,3}}\left(1 - \frac{1}{A_2}\right) - \omega^2 \frac{J_3}{c_{t,3}}\right) \quad \text{(A6.29)}$$

high speed shaft:

$$D_4 = D_0(i_1\, i_2\, i_3)^{\frac{1}{3}} \quad \text{(A6.30)}$$

$$c_{t,4} = \frac{\pi}{32}\frac{G}{l_{HSS}} D_0^4 (i_1\, i_2\, i_3)^{\frac{4}{3}} \quad \text{(A6.31)}$$

$$J_4 = \frac{\pi}{32}\rho_{st} D_0^5 (i_1\, i_2\, i_3)^{\frac{5}{3}}\left(1 + \frac{l_{HSS}}{2\, D_0}\left(\frac{1}{i_1\, i_2\, i_3}\right)^{\frac{1}{3}}\right) \quad \text{(A6.32)}$$

$$A_4 = \left(1 + i_3^2 \frac{c_{t,3}}{c_{t,4}}\left(1 - \frac{1}{A_3}\right) + j\omega \frac{d_{t,4}}{c_{t,4}} - \omega^2 \frac{J_4}{c_{t4}}\right) \quad \text{(A6.33)}$$

generator:

$$c_{t,5} = \frac{T}{\varphi_{load}} = \frac{i_1\, i_2\, i_3\, P}{\omega_{LSS}\, \varphi_{load}} \quad \text{(A6.34)}$$

$$J_5 = \frac{1}{8} m_5 D_5^2 + \frac{\pi}{64}\rho_{st} D_0^5 (i_1\, i_2\, i_3)^{\frac{5}{3}} l_{HSS} \quad \text{(A6.35)}$$

$$A_5 = \left(1 + \frac{c_{t,4}}{c_{t,5}}\left(1 - \frac{1}{A_4}\right) - \omega^2 \frac{J_5}{c_{t,5}}\right) \quad \text{(A6.36)}$$

CHAPTER 7

Stabilization of the Renewable Energy Grid by Wind Turbine Generators

ABSTRACT

Renewable energies like wind and solar destabilize the electrical grid because grid infrastructures, dominated nowadays by generators, become dominated by electrical power converters (EPCs) in the future. This is due to the design of today's wind turbine (WT) power trains and photovoltaics which have a number of fundamental drawbacks. Firstly, EPCs of power supply and short term energy storage operate the electrical grid at a fixed reference frequency whereas an imbalance between power supply and demand is not any longer causing a grid frequency fluctuation. Secondly, the reaction time to re-stabilize the grid is extended because EPCs do not back up and release energy by a self-controlled mechanism. Thirdly, EPCs cannot withstand critical grid operating conditions like short circuits and shut down when such conditions occur. Therefore, for guaranteeing a stable grid, this chapter demonstrates that WT generators need to be connected directly to the electrical grid. However, this requires a variable speed transmission because of the variable WT rotor speed. It is shown that hydrodynamic power transmission systems fit best for multi megawatt power trains with speed variability. Finally, a power train concept is proposed that has an efficiency and speed variability very similar to today's WT power trains.

This chapter is based on: Rommel, D. P., Di Maio, D., Tinga, T. (n.d.). Stabilization of the Renewable Energy Grid by Wind Turbine Generators. submitted.

7.1 Introduction

The installed base of power plants based on renewable energies like wind and solar is continuously growing in order to substitute conventional power plants based on carbon, natural gas, nuclear energy, etc. in the near future. Consequently, the amount of conventional power plants connected to the electrical grid will decrease and the amount of renewable power plants will increase. However, an increasing population of renewable power plants like wind turbines and solar panels (photovoltaic) will reduce the stability of the electrical grid. This grid instability is caused, on the one hand, by the reduction of the spinning reserves [1] and, on the other hand, by the increase of harmonic distortion due to the non-linear switches [2] of electrical power converters[6] in wind turbines and photovoltaics [3][4]. Spinning reserves are used for short term energy storages in the grid and are provided by the inertia of the generator and rotating machinery connected to it [1]. Conventional power plants have an high amount of spinning reserves and thus, keep the electrical grid stable. In contrary, renewable power plants, which are connected to the grid by an electrical power converter, do not have spinning reserves to stabilize the grid and, in addition, emit a notable amount of harmonic distortion into the grid [5]. Therefore, research nowadays focuses on the grid integration and power quality issues of wind and solar energy systems [6]. To compensate the lack of spinning reserves short term grid energy storages like flywheels, supercapacitors and batteries are considered in the grid [1][7]. However, these systems are again connected to the grid by power converters. Considering that wind turbines and photovoltaics will dominate the renewable energy production, most power plants and short term energy storages will be connected to the future renewable energy grid by a power converter. Therefore, the performance of power converters determines the stability of renewable energy grids. Current research focuses on improving the performance and controllability of electrical power converters [8]. Models are developed to predict harmonics in the grid [9], to describe the harmonic interaction of grid connected converters [10] or the harmonic distortion emitted by photovoltaics. Power converter control systems are improved to reduce harmonic distortion [11] or grid control techniques are enhanced to ensure renewable grid stability [12]. However, it is not clear yet whether these efforts will be sufficient to operate renewable energy grids as stable as conventional energy grids.

Therefore, in the present chapter essential requirements for grid stability are derived. It is, then, analysed, whether the electrical power converter and grid connected (synchronous) generator comply with these requirements. Further, it is shown that a grid connected generator is needed to stabilize the grid. However, to connect the generator of a wind turbine to the grid a mechanical power converter is necessary because of the variable wind turbine rotor speed. So it is also evaluated which technology of variable speed transmissions fits best in the power train of multi megawatt wind turbines. Finally, a concept of a mechanical power converter is proposed which seeks to have a total efficiency and speed variability similar to today's concepts of wind turbine power trains but with a higher weight specific power.

[6] Note: in this chapter electrical power converters also include electrical power inverters used for DC-AC links

7.2 The principle of balancing power in the grid

In the electrical power grid, power generation (supply) and consumption (demand) must be in equilibrium because the power grid itself does not have the ability to store energy. To maintain the equilibrium between supply and demand, the supply is adjusted to the demand. As the power adjustment of the supply (provided by a power source) is determined by the control system and reaction time of the power source, a delay time t_{delay} occurs after a drop or jump of the demand, until supply and demand are again in equilibrium. Figure 7.1 shows schematically the (apparent) power supply (S_{in}) and demand (S_{out}) in the grid over time.

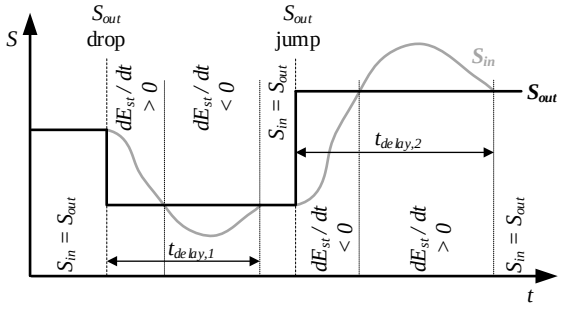

Figure 7.1 Imbalance of (apparent) power due to power drop and jump and associated delay time

To compensate the power imbalance during the delay time an energy storage (E_{st}) is needed which backs up energy, if $S_{in} > S_{out}$, i.e. $dE_{st} / dt > 0$ and releases energy, if $S_{in} < S_{out}$, i.e. $dE_{st} / dt < 0$ (cp. Figure 7.1). So the power balance in the electrical grid can be expressed by the following equation, with the (apparent) power S:

$$S_{out} = S_{in} - \frac{dE_{st}}{dt} \tag{7.1}$$

From Eq. 7.1 it can be seen that the energy storage backs up and releases (apparent) power depending on the power imbalance of supply and demand. Further, to guarantee the power balance the energy storage must contain sufficient energy to be able to back up or release energy any time.

Moreover, the power balance in the electrical grid is not only influenced by the power difference between supply and demand. Firstly, grid harmonics (harmonic distortion) caused by electrical power converters (used for connecting power supply [5] and energy storage to renewable energy grids) generate power fluctuations. These power fluctuations create a power imbalance and thus, affect the grid stability. As short term energy storages are used for grid stabilization, they also must be able to compensate the power imbalance due to harmonic distortion. However, grid harmonics occur suddenly and randomly in the grid and can vary in magnitude, frequency and phase. This means that the power fluctuations due to grid harmonics can neither be influenced nor compensated by any energy storage controller. Consequently, such an energy storage must, on the one hand, back up and release energy automatically (self-controlled) and, on the other hand, respond immediately. The latter means that is should ideally respond within the periodic time T_h given by the frequency of grid harmonics $f_h = 1/T_h$ (e.g.: $T_5 = 1/250Hz = 4ms$). So the higher the frequency of grid harmonics is, the faster the grid stabilizing energy storages must react to power fluctuations. If the power

imbalance due to grid harmonics is not compensated by a short term energy storage, then these must be handled by the components in and connected to the grid. These components normally dissipate the power fluctuations, i.e. the operating temperature and associated loads of these components are increased and thus, their life time is reduced.

Secondly, the power imbalance in the grid can also be caused either by bridging grid and load impedances (short circuits) or by varying load impedances (voltage flickers). A reduction of grid and load impedances due to short circuits leads (according to Ohm's law) to high currents and thus, to a sudden additional power demand for a short time period (milliseconds up to few seconds). Consequently, an energy storage used for grid stabilization must be able to operate under short circuit conditions because, in the worst case, the short circuit occurs at the connection between energy storage and electrical grid. On the other hand, sudden variations of load impedances lead to voltages jumps or drops. Hence, the voltage does not remain constant within the grid. So an energy storage used for grid stabilization must also be able to operate under unstable grid voltage conditions. Again, as also the bridging and variation of grid and load impedances occur randomly, grid stabilizing energy storages must back up and release energy based on a self-controlled mechanism because a control mechanism will not be able to react fast enough to short circuits and flickers.

Finally, based on these considerations, some essential requirements can be defined which must be fulfilled by energy storages used for grid stabilization. Such a storage must be able to:

- back up and release (apparent) power
- back up and release energy by a self-controlled mechanism
- back up and release energy fast, ideally, within a few milliseconds
- maintain a sufficiently high energy level in the storage
- operate under short circuit conditions
- withstand grid voltage fluctuations

In the following section these requirements are used to analyse the performance of different types of grid energy storages. It is important to note that the ability of backing up and releasing power respectively stabilizing the grid is not determined by the energy storage itself rather by the grid – energy storage connection. The grid – energy storage connection specifies how the energy storage reacts to the electrical grid behaviour. Therefore, it is sufficient to consider this connection in order to evaluate the grid performance of energy storages.

7.3 Grid – energy storage connections

In general, the types of electrical grid – energy storage connections can be split in two categories: generators, typically used to connect mechanical energy storages, and electrical power converters for electrical energy storages. Therefore, in this section it is analysed and discussed how these two energy storage connections fulfil the above defined requirements for grid stabilizing energy storages.

7.3.1 Grid connected synchronous generator

The function of a generator is the conversion of mechanical rotating energy into electrical energy (in the form of alternating current: AC). This means that mechanical power given by the product of torque T and angular shaft speed ω_s is converted into electrical power given by the product of current $i(t)$ and voltage $v(t)$. Further, the generator and rotating machinery connected to it, like gas, steam, Pelton, Kaplan or wind turbines, contain rotating masses. A rotating mass with the inertia J and speed ω_s is equivalent to a certain amount of kinetic energy, i.e. energy E_{st} is stored in rotating masses.

$$E_{st} = \frac{1}{2} J \omega_s^2 \tag{7.2}$$

Consequently, a generator does not only provide power but also has the ability to operate as an energy storage. Therefore, a grid connected generator is power supply (power source) and energy storage at the same time. Then, the grid power balance can be written as follows[7]:

$$[T(t) - J\dot{\omega}_s(t)] * \omega_s(t) \leftrightarrow v(t) * i(t) \tag{7.3}$$

This means that the electrical grid uses a mechanical energy storage to compensate any power imbalance between supply and demand. The product of inertia J and change of angular speed $d\omega_s / dt$ is equivalent to an additional torque (cp. Eq. 7.3). So power is backed up, if the rotating masses are accelerated, i.e. $dE_{st} / dt > 0$ respectively $d\omega_s / dt > 0$ and power is released, if the rotating masses are decelerated, i.e. $dE_{st} / dt < 0$ respectively $d\omega_s / dt < 0$. Thus, a power imbalance between grid power supply and demand is indicated by an increasing or decreasing angular shaft speed ω_s.

Further, the angular shaft speed ω_s and grid frequency f_{grid} are directly coupled by the number of pole pairs p of the generator, i.e. angular shaft speed and grid frequency change simultaneously.

$$\omega_s = \frac{\omega_{grid}}{p} = \frac{2\pi}{p} f_{grid} \tag{7.4}$$

Hence, the power balance of the electrical grid is related to the grid frequency. The power balance between supply and demand, again, is influenced by the power supply (cp. also Figure 7.2). Therefore, by adjusting the power supply such that the grid frequency is maintained around a given frequency (set point), which is normally 50Hz or 60Hz, it is guaranteed that both the grid operates in a stable manner and the (mechanical) energy storage remains balanced. This also means that the energy of the rotating masses oscillates around the energy set point defined by the inertia J of the rotating masses and the nominal shaft speed ω_s.

In addition, it is important to note that a generator backs up and releases energy automatically, i.e. a generator reacts to power imbalance by changing its shaft speed (and thus grid frequency) without any controller. Thus, a generator includes a self-controlled grid

[7] Note that in Eq. 7.3 an equal sign does not apply because the left side is mechanical (active) power while the right side electrical (apparent) power. Synchronous generators convert mechanical into electrical (active) power and provide reactive power to the grid depending on phase (load) angle and excitation [26].

energy storage. Further, due to the self-controlled mechanism the generator rotor can, to a certain extent, follow the power fluctuations caused by grid harmonics and thus, can compensate them. Only when the generator rotor cannot follow these power fluctuations anymore, then they are converted into thermal energy which, again, increases the thermal and mechanical loads in the generator.

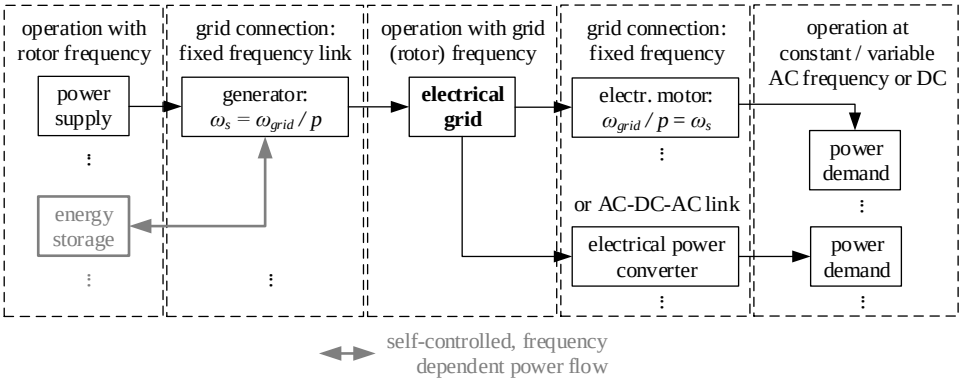

Figure 7.2 Electrical energy grid using generators as grid connection of power supply and energy storage

Finally, according to the above defined requirements a grid energy storage must also be able to withstand voltage fluctuations and to provide sufficient power during grid short circuits. Voltage fluctuations mean that that the terminal voltage of the generator is not constant anymore because of changing load impedances. In the worst case, the terminal voltage drops to zero which is equivalent to a short circuit. Therefore, it can be argued that if a generator can continue to operate under short circuit conditions, it can also withstand voltage fluctuations. According to the design standard IEC 60034-1 the coils of generators are dimensioned for short circuit currents. This means that a generator is designed to continue operation under short circuit condition.

Therefore, it can be concluded that generators used as grid stabilizing energy storages are able to provide (apparent) power to the grid despite of voltage fluctuations and short circuits in the grid. By controlling the grid frequency the mechanical energy storage of the generator maintains a balanced energy level. In addition, a generator has the capacity to back up and release power by a self-controlled mechanism and thus within a short time period. This means that all six requirements from section 7.2 are met.

7.3.2 Grid connected electrical power converter

After considering the grid connected (synchronous) generator as grid – energy storage connection in the previous subsection, the grid connected electrical power converter is now analysed. The function of the electrical power converter is the conversion of the power of an alternating current (AC) to a direct current (DC) and back to an AC. Thereby, the frequency of the electrical (AC) power is changed from f_1 to f_2. Further, it is important to note that the electrical power converter itself is a pure grid – energy storage connection, i.e. the electrical power converter cannot store energy. DC-links of power converters realized for example by

a capacitor bank are used for reactive power compensation. The electrical power conversion can be expressed as follows (neglecting all losses during conversion):

$$[v(t) * i(t)]_{AC,f_1} = V_{DC} * I_{DC} = [v(t) * i(t)]_{AC,f_2} \quad (7.5)$$

Using this type of grid connections has a number of implications. First, the equation of electrical power conversion (Eq. 7.5) applies for both power supply and energy storage in today's renewable energy grids (cp. Figure 7.3). This means that the grid frequency is not determined by the power supply and energy storage rather by the grid connection, i.e. by the control algorithm and reference frequency of gate drivers of power switches like Insulated Gate Bipolar Transistors (IGBTs) used to create AC-DC-AC links. Consequently, the power generation is decoupled from the grid by the electrical power converter (AC-DC-AC link) because their frequencies are not directly interconnected anymore. If the grid frequency is then set to a reference frequency (set point), it will be quasi constant for any grid operating condition even in case of a power imbalance in the grid. Therefore, if the population of electrical power converters dominates the grid infrastructure, a power imbalance of the grid cannot be identified anymore from a change of the grid frequency (cp. also Figure 7.3), as it is the case in traditional generator-dominated grids.

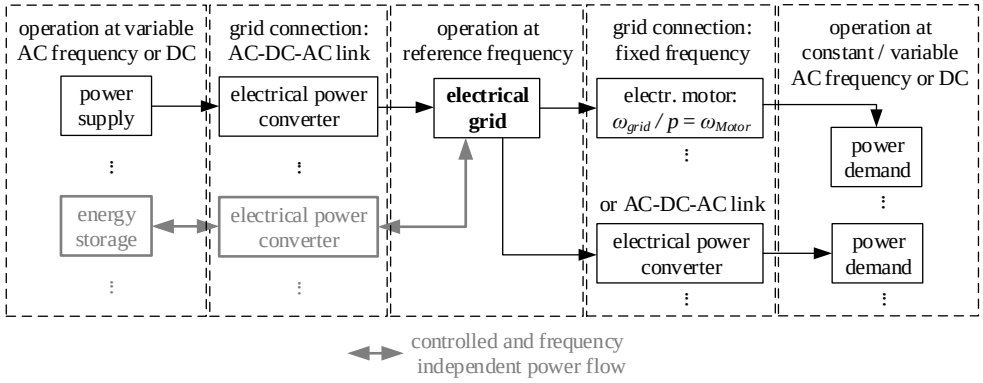

Figure 7.3 Electrical energy grid using electrical power converter as grid connection of power supply and energy storage

Second, because of decoupling the energy storage (cp. Eq. 7.5) with an AC-DC-AC link from the grid, any of these energy storages operates as an independent unit at the grid. An independent grid unit, however, requires its own control system and algorithms to interact with the grid, i.e. in the case of an energy storage, to back up and release power. This means that any energy storage which is connected to the electrical grid by an electrical power converter can only back up and release power as fast as its control system can identify and react to the power imbalance in the grid. Thus, grid harmonics, whose occurrence increases with the population of electrical power converters in the grid infrastructure, are not absorbed by the energy storage itself, rather by other components connected to the grid. For these components the grid harmonics are thus additional loads. Further, the control system of the energy storage defines and maintains the balanced energy level. Therefore, the energy storage control system does not only have to detect a power imbalance in the grid but also has to

guarantee that the energy storage goes back to the balanced energy level after backing up or releasing power to the grid.

Third, according to the defined requirements a grid energy storage must also be able to withstand voltage fluctuations and to provide sufficient power during grid short circuits. This means that the power switches (like IGBTs) must withstand voltage drops and short circuit currents. Voltage drops over power switches lead to current rises. However, power switches are not designed to operate under high current or even short circuit current conditions because the semiconductor material of the power switches is not dimensioned for these conditions.

In conclusion, an electrical power converter can back up and release energy from a grid stabilizing energy storage. However, the process of backing up and releasing energy follows a control mechanism inherent to its design, namely using controlled power switches. The control mechanism also includes the maintenance of a balanced energy level in the storage as well as the control of the grid frequency. Because of this control mechanism electrical power converters cannot react within a few milliseconds to power imbalances in the grid. Further, as the grid frequency is continuously adjusted to the reference frequency by the control mechanism, the power imbalance in the grid cannot be detected anymore from grid frequency fluctuations. Finally, power switches (like IGBTs) used in electrical power converters are not designed for high grid voltage fluctuations and short circuit currents. Therefore, electrical power converters will shut down, if these conditions occur in the grid.

7.4 Concept of wind turbine power train

In the previous chapter the performance of a generator and electrical power converter as grid – energy storage connection was analysed. It was shown that grid connected (synchronous) generators and their connected rotating machineries (inertia) are able to stabilize the electrical grid while grid connected electrical power converters are not. This means for the renewable energy grid that all in the grid available generators should be connected directly to the electrical grid to contribute to and ensure a stable grid operation. Photovoltaics do not use and need generators for energy production and power conversion, but wind turbines do. Consequently, wind turbines with grid connected generators can play an essential role in the future for stabilizing renewable energy grids. However, this would require a reconsideration of wind turbine power train concepts and designs, because todays wind turbines are almost exclusively connected to the grid by an electrical power converter (cp. Figure 7.4). To operate the generator at the grid a mechanical power converter is needed (cp. Figure 7.4), because the variable rotor speed of the wind turbine and gearbox must be adjusted to a constant shaft speed of the generator. This leads to the question which principle of variable speed transmission fits best to the requirements of wind turbine power trains?

A significant, economical requirement for wind turbine designs is the reduction of weight because the weight of the different power train components, like gearbox, generator, etc. influence the nacelle weight and thus, the tower construction. So components used in the wind turbine power train should have high values of the power-weight or power-volume ratio. Consequently, the mechanical power converter used in a wind turbine should be based on a principle of variable speed transmission that provides high power scaling factors. This means that scaling up the power train to higher power should lead to only a moderate increase of the weight or volume. For evaluating a principle with high power scaling factors, three common approaches of variable speed transmission are compared, namely continuous variable

transmission (CVT with pully), hydrostatic and hydrodynamic power transmission (see Appendix A7.7.1 for further details). It is shown that from the perspective of power scaling the hydrodynamic power transmission is the most suitable for multi-megawatt power trains because i) the transmitted power can be significantly scaled up by only small component increases and ii) the number of parts of the hydrodynamic transmission hardly increases when scaling up the transmitted power. However, power train components of multi-megawatt wind turbines do not only require high values of power-weight or power-volume ratios, but also must guarantee an adequate performance. So using the principle of hydrodynamic power transmission in a mechanical power converter should also provide a high converter efficiency and, in the case of the wind turbine, at the same time be able to accommodate a large speed variability. Furthermore, due to safety reasons the mechanical power converter should enable a controlled and fast shut down of the power train during normal stop and, especially, during emergency stops.

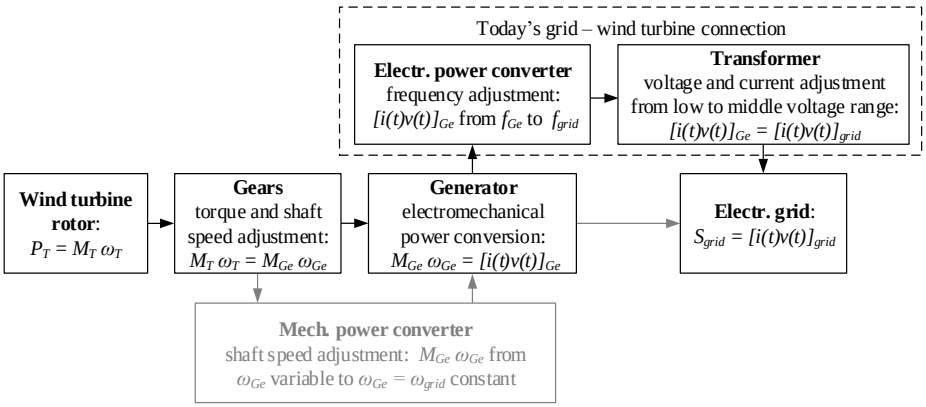

Figure 7.4 Wind turbine power train concept including different power conversions (lossless)

In today's multi megawatt industrial applications highly efficient, variable speed transmissions based on the principle of hydrodynamic power transmission are realized by a hydrodynamic torque converter in combination with a rotating planetary gear [13] [14] (cp. also Appendix A7.7.2). Such power transmissions achieve a speed variability of 65-100% [13] of the input speed with an total efficiency of over 95% [14]. In comparison, an electrical power converter has also an efficiency of approx. 95% [15]. This means that the efficiency of variable speed transmissions based on hydrodynamics is within the same efficiency range as today's electrical power converter. However, the speed variation of 65-100% is not sufficient for wind turbines. For example, assuming a cut-in rotor speed of three rotations per minute and a nominal rotor speed of twelve rotations per minute a speed variability of approx. 25-100% of the nominal speed is needed. From this consideration, it can be seen that the assembly of a hydrodynamic torque converter combined with a rotating planetary gear cannot be installed straight away between the gearbox and generator of typical wind turbine power trains.

In addition, a controlled and fast shutdown of the wind turbine power train is crucial for the safety of the entire wind turbine, especially, in case of unexpected events in the power train or electrical grid. However, the wind turbine rotor cannot be stopped within seconds due to i) the huge rotor inertia and ii) slow blade pitching needed to avoid excessive dynamic loads.

Consequently, the generator continues to provide energy to the electrical grid during any shutdown because of the mechanical connection between wind turbine rotor and generator. This can be critical for emergency stops triggered by electrical grid events. To solve this problem a brake (power sink) is needed so that the generator can be disconnected from the grid and the rotating masses can be slowly decelerated (controlled shutdown). Further, for disconnecting the generator from the grid as fast as possible or for braking the wind turbine rotor at rated speed, the power sink has, ideally, the capacity to absorb the rated power, which is in the multi megawatt range. This means that the power sink in the wind turbine power train should also use the principle of hydrodynamic power transmission because of its high power scaling factors (cp. Appendix A7.7.1). Consequently, a hydrodynamic brake (cp. also [16]) should be installed between gearbox and generator. The application of the hydrodynamic brake in the wind turbine power train is beyond the scope of this chapter and thus, is not further considered here.

From these considerations, it can be concluded that designing a mechanical power converter for wind turbine power trains based on hydrodynamic power transmission (torque converter and brake) is not only promising from a power scaling point of view but also from an efficiency and safety point of view. As the speed variability (65-100%) of a hydrodynamic torque converter combined with a rotating planetary gear is not sufficient for a wind turbine, it will now be shown that a power transmission system based on hydrodynamics and with a speed variability of 25-100% is feasible with some design and construction effort. To do so, an alternative concept of the wind turbine power train is proposed. It is schematically shown in Figure 7.5 and contains the following elements:

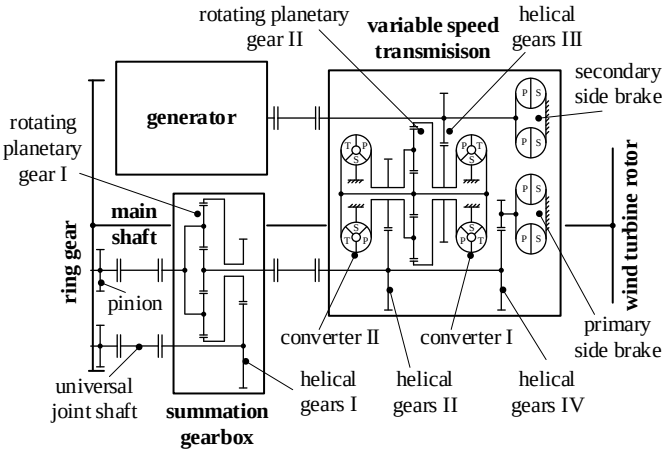

Figure 7.5 Proposed wind turbine power train based on hydrodynamic power transmission

- *Ring gear + pinions:*
  A ring gear with external teeth is used as first gear step because it provides high transmission ratios and is commonly used in industrial low speed application like mills. The ring gear can be designed with pitch diameters up to 16 meters [17]. Pitch diameters around 3 to 5 meters are probably adequate for wind turbines in order to limit the weight and inertia of the ring gear itself. The ring gear is installed at the opposite side of the wind

turbine rotor (cp. Figure 7.5) to use it as counterweight on the main shaft and to increase the main bearing distance to almost the length of the nacelle. This will lead to a reduction of the main bearing loads (cp. Appendix A7.7.3). Further, at the ring gear the total transmitted power is split to pinions. The power splitting is necessary because, on the one hand, the power capacity of the pinion is limited [17] and on the other hand, the dimensions of the low speed side components like low speed shafts, universal joint shafts, steady bearings and pinions can be designed smaller because of reducing the transmitted torque.

- *Summation gearbox:*
  The power transmitted by (two) pinions is combined into one shaft by a rotating planetary gear. For using the rotating planetary gear also as step-up gear unit, i.e. for speed increase, the two pinions are connected to the ring gear and planetary carrier of the rotating planetary gear. Additional helical gears (cp. helical gears I in Figure 7.5) are installed to adjust the ring gear speed such that the pinions transmit the same power. Furthermore, the additional helical gears change the rotation direction of the ring gear (in comparison to the rotation direction of the pinions). This is necessary to add the power of the planetary carrier and ring gear to the sun gear.

- *Variable speed transmission:*
  The power curves of the wind turbine, hydrodynamic torque converter and hydrodynamic brake are equivalent, i.e. their power increases with the power three of the shaft speed (cp. Appendix A7.7.1). This characteristic provides the opportunity to connect the pump wheels of the hydrodynamic torque converter (cp. Figure 7.5 - converter II) and brake (cp. primary side brake in Figure 7.5) directly to the wind turbine rotor (by a fixed gear ratio). Further, two converters are utilized, i.e. one converter operates in the low speed range and the other in the high speed range (cp. Figure 7.6). The usage of two converters does not only provide a higher variable speed range but also increases the total efficiency of the variable speed transmission because both converters operate at their optimal operating point (cp. also [18]). Moreover, helical gears (II and III in Figure 7.5) are used, again, to adjust the converter speed and transmission output speed, respectively. The helical gears II and III provide also the advantage that the summation gearbox and generator can be installed in parallel whereby a compacter, i.e. shorter, wind turbine power train assembly is obtained. In addition, hydrodynamic brakes are installed to slow down wind turbine rotor and generator while switching the speed of the dual speed generator and to realize the speed switching within a few seconds. This means that hydrodynamic brakes are needed on both primary and secondary side of the converters because the hydrodynamic torque converters cannot provide braking of the generator rotor. The hydrodynamic brake on the primary side is the main brake (cp. primary side brake in Figure 7.5) and slows down the wind turbine rotor during the change of generator speed at 50% rated wind rotor speed (cp. Figure 7.6) as well as during normal and emergency shut downs. The helical gears IV increases the speed of the hydrodynamic brake (on the primary side) and thus also the braking power (cp. Appendix A7.7.1). The hydrodynamic brake on the secondary side is mainly used to decelerate the generator rotor while switching its operating speed from generator speed II to I (cp. Figure 7.6). During shut downs, the secondary side brake can provide additional braking power. Besides, the variable speed transmission (shown in Figure 7.5) provides a speed variability of approx.

50-100% rated speed with an efficiency of over 94.5% assuming a stationary gear ratio $i_0 = -3$ of the rotating planetary gear II, an average efficiency of converter I and II of 86% based on [14] and an efficiency of the rotating planetary gear efficiency of 99% [19]. The speed variability can further be increased for shaft speeds higher than rated speed (cp. Figure 7.6), i.e. converter II continues operation, if the converters and rotating planetary gear are designed for overspeed conditions.

- *Generator:*
  A high voltage, dual speed generator is installed and directly connected to the electrical grid. Due to the high voltage a power transformer in the nacelle of the wind turbine is not needed. The dual speed or pole-changing operation increases the total speed variability of the power train assembly (shown in Figure 7.5) to approx. 25-100% (cp. also Figure 7.6).

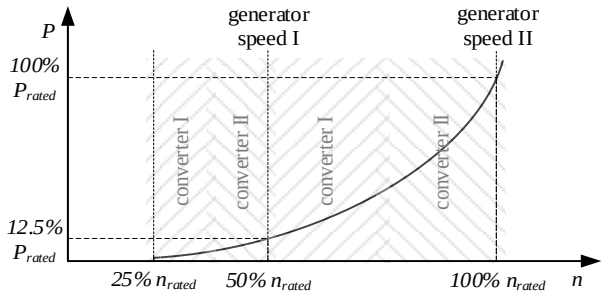

Figure 7.6 Operation of converter I and II in the power shaft speed curve of wind turbine rotor

Table 7.1 Comparison of total power train efficiency

proposed power train (after Figure 7.5)	**efficiency η**	**traditional power train (direct drive generator)**	**efficiency η**
ring gear + pinion [22]	99%	direct drive generator [23]	94%
summation gearbox I (1 planetary gear with 100% power and 1 helical gear with 50% power)	98.5%		
hydrodynamic torque converter I + II & rotating planetary gear	>94.5%	electrical power converter [15] [23]	95%
Helical gears II + III	98%		
high voltage (dual speed) generator (estimated)	97%	electrical power transformer from low to high voltage (estimated)	98%
total power train efficiency	87-88%	total power train efficiency	87.5%

In addition to the high speed variability, the proposed power train assembly (after Figure 7.5) must provide a high efficiency and low component weights. Table 7.1 shows a comparison of the efficiency η of the proposed power train after Figure 7.5 and today's power train with a direct drive generator. The efficiency of helical and planetary gear steps are estimated to have an efficiency of 99% [20] [19]. It can be seen that the proposed power train is within the same efficiency range as a typical power train with a direct drive generator.

Then, in Table 7.2 the weight of the proposed power train is estimated for a maximum power of 8MW to be 70 tons (without nacelle and wind turbine rotor). The weight estimations are a first guess whereas the weight of the different power train components may differ after a first pre-design. Nevertheless, by comparing, the weight of a 4.5 MW direct drive permanent magnet synchronous generator (220 tons [21]) with the roughly estimated total weight of the 8MW power train after Figure 7.5, it becomes clear that the usage of a mechanical power converter based on hydrodynamic power transmission in multi megawatt power trains provides a higher power-weight ratio than current wind turbine designs.

Table 7.2 Weight estimation of proposed power train (without nacelle)

power train components	**estimation**	**weight**
main shaft and ring gear (rated power 8MW) + two pinion (each 4MW) with speed ratio 1:8	• ring gear (diameter 4m) and pinion (diameter 50cm) approximated as a disc with a thickness of approx. 50cm, • main shaft approximated as a cylinder with a diameter of 50cm and a length of approx. 10m • steel density of 7.8 tons/m³	8 tons
summation gearbox I (rated output power 8MW)	• total input torque (both shafts) equivalent to a current 2MW wind turbine gearbox (due to ring gear – pinion ratio 1:8) • similar configuration as current gearboxes in wind turbines which have one planetary gear and two helical gear sets • weight estimation by a 2MW gearbox (approx. 15 tons [19]) • but, weight increase of planetary gear due to torque summation of two input shafts (ring gear and planetary carrier)	20 tons
hydrodynamic torque converters + rotating planetary gear (rated power 8MW)	• weight of one hydrodynamic torque converter combined with planetary gear plus one helical gear step given as 10.2 tons for a power of 6MW [13] • weight scaling with power 1/3, i.e. shaft scaling factor (cp. Appendix A7.7.1) and thus 10.2 tons ➔ approx.12 tons • variable speed transmission: two hydrodynamic torque converters, two helical gear steps, one planetary gear, hydrodynamic brakes	24 tons
generator (rated power 8MW)	• generator torque increases with the power two of its diameter and with the power one of its length [24] • scaling the weight of a 3MW generator (8.5 tons) [25] equally as the generator diameter	14 tons
further components like steady bearings, universal joint shafts, etc.	• roughly estimated	4 tons
all power train components		70 tons

7.5 Discussion

Nowadays, smart grids and their control systems aim to stabilize renewable energy grids [1]. This chapter has shown that these control systems face two main problems: i) identification of instable grid conditions (power imbalance) and ii) reaction time to compensate these conditions and to re-stabilize the grid. Firstly, due to the usage of electrical power converters power imbalance in renewable energy grids cannot be detected anymore from the grid frequency. But since the variation of grid and load impedances, grid harmonics or short circuits make that current and voltage vary independently of the power imbalance, these can also not be used for detection. Secondly, some reaction time is needed until the

energy storage starts to back up or release power. A self-controlled mechanism reduces this reaction time to a minimum and guarantees, therefore, a robust and stable grid operation. From these two consideration, it has been concluded that for a stable operation of a renewable energy grid, the electrical grid infrastructure should be dominated by generators. This can only be realized, if wind turbine generators are directly connected to the electrical grid because i) wind and solar (photovoltaics) power will be the dominant renewable energies in future and ii) solar power (photovoltaics) does not have a mechanical rotating system and generator.

To solve this problem, a new wind turbine power train concept has been proposed. In addition to the technical details, as discussed in section 7.4, the reliability and economical aspects will be considered here. The realization of a variable speed transmission requires a planetary and helical gear set (cp. Figure 7.5). As current gearboxes in wind turbines tend to fail quite often, variable speed transmissions with several planetary and helical gear sets might do so, too. But, it must clarified here that the loads on current wind turbine gearboxes and the loads on the summation gearboxes shown in Figure 7.5 differ significantly. Current wind turbine gearboxes are directly coupled to the wind turbine rotor by the main shaft. So any aerodynamic imbalance of the wind turbine rotor introduces a direct load into the gearbox and its different gear stages (assembly of gear, shaft and bearings). Further, loads and constraining forces, are also introduced to the gearbox and main shaft due to the undetermined shaft assembly of two main bearings and rubber bushes. In contrary, the proposed summation gearbox and variable speed transmission (Figure 7.5) are disconnected from the wind turbine rotor. Thus, the loads of these units are mainly determined by torque and speed fluctuations (torsional vibrations). It is a matter of robust and stiff gear and shaft design to withstand these fluctuations. In addition, torsional vibrations are, at least partly, damped by the hydrodynamic torque converter which is also an active damping element in the mechanical rotating system. In the power train after Figure 7.5 the wind turbine rotor is directly connected to the ring gear by the main shaft. So the loads due to aerodynamic imbalance will affect the ring gear. But these loads, i.e. forces and displacements, are reduced by a long main shaft and long main bearing distance. From these considerations, it is clear that the proposed power train cannot be compared with the type of failures of current wind turbines, but promises to improve the power train reliability of multi megawatt wind turbines.

Finally, a wind turbine power train design with a grid connected generator does not only contribute to the stabilization of the electrical grid but also is more economical than a design with an electrical power converter. A power train with a grid connected generator does not require any adjustments of the present grid infrastructure because the grid power source and grid stabilizing energy storage connection (generator) remain the same. So for the grid it is irrelevant, whether the power source and energy storage is powered by wind, natural gas, carbon, etc. However, a power train with an electrical power converter requires grid infrastructure adjustments because the power source (generator) is decoupled from the grid whereas the generator cannot be used anymore as a grid stabilizing energy storages. This means that, for example, additional grid stabilizing energy storages must be placed in the grid infrastructure. In other words, a wind turbine power train with a grid connected electrical power converter is based on the philosophy of adjusting the grid infrastructure to the chosen power train concept and design. A wind turbine power train with a grid connected generator follows the philosophy of adjusting the power train concept and design to the grid infrastructure and its requirements. From this point of view, it can be seen that the total investment of the wind turbine power train with a grid connected generator is less because it

is limited to the investment of the power train and does not require further expensive investments in the electrical grid infrastructure.

7.6 Conclusion

In this chapter essential requirements are derived for grid stabilizing energy storages and applied to two different types of electrical grid – energy storage connections, namely: i) grid connected electrical power converters and ii) grid connected generators. It is shown that the generator complies with the requirements for grid stabilization, but the electrical power converter does not. This means that a grid infrastructure dominated by electrical power converters cannot ensure stable operation. Furthermore, it is discussed that the design and performance of electrical power converters have a negative influence on the grid stability. Consequently, current renewable energy grids will not operate in a stable manner because wind turbines, photovoltaics and energy storages like flywheels, batteries, supercapacitors, etc. use electrical power converters as grid connection. It is therefore reasoned that for a stable operation the infrastructure of the renewable energy grid should be dominated by grid connected generators. This is realized by changing the concept and design of the wind turbine power train in such a way that the generator is directly connected to the grid, i.e. a mechanical power converter is needed to adjust the variable wind turbine rotor speed to the required constant generator speed. It is shown that the hydrodynamic power transmission is the most adequate principle for speed variation of multi megawatt power trains because it provides the highest power-weight and power-volume ratio in comparison to other principles of speed variation. Finally, based on the principle of hydrodynamic power transmission a wind turbine power train concept is proposed which does not only have an total efficiency and high speed variability like current wind turbines power trains but also provides improvements of the power train reliability.

References

[1] J. Pramod, *Energy Storage in Grids with High Penetration of Variable Generation*. Asian Development Bank, 2017.

[2] N. Mohan, T. M. Undeland, and W. P. Robbins, *Power electronics: converters, applications, and design*. Wiley, 1995.

[3] T. E. C. De Oliveira, P. M. S. Carvalho, P. F. Ribeiro, and B. D. Bonatto, "PV hosting capacity dependence on harmonic voltage distortion in low-voltage grids: Model validation with experimental data," *Energies*, vol. 11, no. 2, 2018.

[4] Y. Du, D. D. C. Lu, G. James, and D. J. Cornforth, "Modeling and analysis of current harmonic distortion from grid connected PV inverters under different operating conditions," *Sol. Energy*, vol. 94, no. August, pp. 182–194, 2013.

[5] F. Santjer, G. J. Geredes, P. Christiansen, and D. Milborrow, "Wind Turbine Grid Connection and Interaction." Deutsches Windenergie-Institut GmbH Germany, Tech-wise A/S Denmark, DM Energy United Kingdom, 2001.

[6] V. Kumar, A. S. Pandey, and S. K. Sinha, "Grid integration and power quality issues of wind and solar energy system: A review," *Int. Conf. Emerg. Trends Electr. Electron. Sustain. Energy Syst. ICETEESES 2016*, vol. 2011, pp. 71–80, 2016.

[7] S. Kazokoglu, "Short Term Energy Storage on Grid," vol. 24, pp. 21–24, 2016.

[8] A. Anuchin, V. Kulmanov, and Y. Belyakov, "Simulation of power converter control system with compensation of harmonic distortion in output voltage waveform," *2015 Int. Sib. Conf. Control Commun. SIBCON 2015 - Proc.*, no. August, 2015.

[9] P. M. Ivry, O. A. Oke, D. W. P. Thomas, and M. Sumner, "Predicting Harmonic Distortion of Multiple Converters in a Power System," *J. Electr. Comput. Eng.*, vol. 2017, pp. 1–9, 2017.

[10] J. Kwon, X. Wang, F. Blaabjerg, C. L. Bak, V. S. Sularea, and C. Busca, "Harmonic Interaction Analysis in a Grid-Connected Converter Using Harmonic State-Space (HSS) Modeling," *IEEE Trans. Power Electron.*, vol. 32, no. 9, pp. 6823–6835, 2017.

[11] M. Adnan, M. Tariq, Z. Zhou, and H. V. Poor, "Load flow balancing and transient stability analysis in renewable integrated power grids," *Int. J. Electr. Power Energy Syst.*, vol. 104, no. May 2018, pp. 744–771, 2019.

[12] M. Mehrasa, E. Pouresmaeil, A. Sepehr, B. Pournazarian, M. Marzband, and J. P. S. Catalão, "Control technique for the operation of grid-tied converters with high penetration of renewable energy resources," *Electr. Power Syst. Res.*, vol. 166, no. April 2018, pp. 18–28, 2019.

[13] Voith, "The New Vorecon NX," 2017. [Online]. Available: http://www.gaselectricpartnership.com/L Voith Vorecon NX.pdf. [Accessed: 04-Feb-2019].

[14] L. Pengfei and W. Wang, "Principle, Structure and Application of Advanced Hydrodynamic Converted Variable Speed Planetary Gear (Vorecon and WinDrive) for industrial drive and wind power transmission," *Int. Conf. Fluid Power Mechatronics*, pp. 839–843, 2011.

[15] A. Stabile, A. J. M. Cardoso, and C. Boccaletti, "Efficiency analysis of power converters for urban wind turbine applications," in *2010 IEEE International Conference on Sustainable Energy Technologies, ICSET 2010*, 2010.

[16] E. Kickbusch, *Föttinger-Kupplungen und Föttinger-Getriebe: Konstruktion und*

Berechnung. Springer Berlin Heidelberg, 1963.
[17] SEW-Eurodrive, “Complete Drive Systems with Industrial Gear Units,” 2014. [Online]. Available: https://download.sew-eurodrive.com/download/pdf/21222193.pdf. [Accessed: 04-Feb-2019].
[18] Voith, “Efficient Control of Pumps and Compressors. Vorecon Variable Speed Planetary Gear,” 2015. [Online]. Available: https://voith.com/ita-en/214_e_cr168_en_vorecon-variable-speed-planetary-gear.pdf. [Accessed: 04-Feb-2019].
[19] J. Ukonsaari and N. Bennstedt, “Wind Turbine Gearboxes - Maintenance Effect on Present and Future Gearboxes for Wind Turbines,” 2016.
[20] Voith, “Increase Performance for Turbo Gears - BHS AeroMaXX,” 2016. [Online]. Available: https://d2euiryrvxi8z1.cloudfront.net/asset/445934742530/39a4abc88fcb7a7cb0d7e814613efc7d. [Accessed: 04-Feb-2019].
[21] D. Bang, H. Polinder, G. Shrestha, and J. A. Ferreira, “Review of generator systems for direct-drive wind turbines,” *Eur. Wind Energy Conf. Exhib.*, pp. 1–11, 2008.
[22] J. Brown, “Ring gear drives huge grinding mill,” 2000. [Online]. Available: https://www.machinedesign.com/mechanical-drives/ring-gear-drives-huge-grinding-mill. [Accessed: 04-Feb-2019].
[23] G. Bywaters *et al.*, *Northern Power NW 1500 Direct-Drive Generator*. National Renewable Energy Laboratory, 2007.
[24] G. Müller and B. Ponick, *Grundlagen elektrischer Maschinen*. Wiley, 2012.
[25] Vestas, *General Specification - V90 3.0MW*. 2004.
[26] A. Kremser, *Elektrische Maschinen und Antriebe: Grundlagen, Motoren und Anwendungen*. Vieweg+Teubner Verlag, 2013.

A7.7 Appendices

A7.7.1 Power scaling of variable speed transmissions

In Table 7.A1, three common principles of variable speed transmission are considered, namely: Continuous Variable Transmission (with pully), hydrostatic and hydrodynamic power transmissions. Further, the electrical power converter is included to compare it with these principles.

Note that mechanical transmission systems need shafts to transmit mechanical power from the transmission input to the transmission output. Therefore, the power scaling factor of shafts should also be considered when scaling up the power of the transmission system. Shafts are scaled by the power three of their diameter assuming a constant torsional stress and shaft speed.

$$P = T * \omega = \frac{2*\tau*I_p}{D} * \omega = \frac{\pi}{16} * \tau * \omega * D^3 \quad (7.A1)$$

with: P power, T torque, ω shaft speed, D shaft diameter, I_p polar momentum of inertia, τ torsional stress

Table 7.A1 Principles of speed and frequency variable power transmission (continuous variable and hydrostatic power transmission)

	continuous variable transmission (CVT)	**hydrostatic power transmission**
schematic diagram	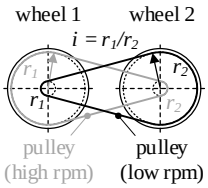	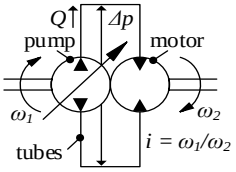
principle	• coned wheel • pulley operation at different wheel diameters	• pump: conversion of mechanical power to hydrostatic power • motor: conversion of hydrostatic power back to mechanical power • operation of pump and motor at different (variable) speeds
power equation	*mechanical power:* $P = r * F * \omega$ *pulley force:* $F = \sigma * A$ *pulley tension:* $\sigma = const.$ *pulley cross section:* $A = b * t$	*fluid power:* $P = \Delta p * Q \sim D^2$ *pressure:* $\Delta p = const.$ *Discharge:* $Q = A * c \sim D^2$
nomenclature	P power r wheel radius ω shaft speed F force σ tension A pulley cross section b pulley width t pulley thickness	P power Δp pressure difference Q discharge A tube cross section D tube diameter c fluid velocity
limitations	• radius: size and weight of wheels • shaft speed: friction between wheel and pulley (slip) • tension: pulley material • width: cone angle of wheels • thickness: pulley radii	• pressure: sealings, materials of tubes, pump and motor • fluid velocity: maximum speed of (piston) pump and motor
scaling	increasing power by the number of wheels and pulleys, i.e. linear power scaling	increasing power by tube diameter and number of pistons, i.e. scaling factor of power two.

Table 7.A1 Principles of speed and frequency variable power transmission (hydrodynamic power transmission & electrical power converter)

	hydrodynamic power transmission	**electrical power converter**
schematic diagram	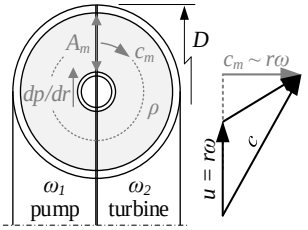	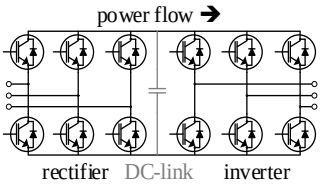
principle	• pump: conversion of mechanical power to hydrodynamic power • turbine: conversion of hydrodynamic power back to mechanical power • operation of pump and turbine at different (variable) speeds	• rectifier: conversion of electrical AC to DC power • DC-link: smoothing DC voltage, reactive power compensation • inverter: conversion of electrical DC to AC power by power switches • operation of input and output at different (variable) frequencies
power equation	*fluid power:* $P = \Delta p * Q \sim \rho\omega^3 D^5$ *pressure:* $\frac{dp}{dr} = \rho\omega_1^2 r$ $\Delta p = {}^1/_2\, \rho\omega_1^2 (r_{max}^2 - r_{min}^2)$ *Discharge:* $Q = A_m c_m \sim \omega D^3$	*electrical power:* $S = [v(t) * i(t)]_{f_1} =$ $= \mathrm{V} * \mathrm{I} = [\mathrm{v(t)} * \mathrm{i(t)}]_{f_2}$
nomenclature	P power Δp pressure difference Q discharge ω pump / turbine speed r pump / turbine radius D pump / turbine diameter ρ fluid density c fluid velocity c_m meridian fluid velocity A_m flow cross section u circumferential speed	S (apparent) power $v(t)$ AC voltage $i(t)$ AC current V DC voltage I DC current f frequency
limitations	• pump / turbine speed: centrifugal forces on rotating parts	• voltage: design of power switches like IGBTs, semiconductor materials • current: design of power switches like IGBTs, semiconductor materials
scaling	increasing power by pump and turbine diameter, i.e. scaling factor of power five	increasing power by the number of power switches, i.e. linear scaling factor (only valid for multi megawatt applications)

In conclusion, from the perspective of power scaling the hydrodynamic power transmission is the most suitable for multi-megawatt power trains because i) the transmitted power is significantly scaled up by only small component increases (factor power three and five) and ii) the number of parts of the hydrodynamic transmission hardly increases despite of scaling up the transmitted power.

A7.7.2 Hydrodynamic torque converter

Variable speed transmissions based on the principle of hydrodynamic power transmission are realized by a hydrodynamic torque converter in combination with a rotating planetary gear [13][14]. The high efficiency and speed variability is obtained by splitting the transmitted power at the hydrodynamic torque converter and by summing up the power at the rotating planetary gear [14] (cp. Figure 7.A1). Thereby, the power is split such that via the main shaft and rotating planetary gear the majority of the power is transmitted and that via the hydrodynamic torque converter the minority of the power. Further, the speed variation is obtained by varying the turbine speed of the hydrodynamic torque converter, i.e. by adjustable guide vans in the stator [14] or by adjustable pump blades [13] which modify the fluid (oil) flow in the hydrodynamic torque converter (cp. also Figure 7.A1). As the turbine is mechanically connected to the sun gear [13], a change of the turbine speed means automatically a change of the sun gear respectively ring gear of the rotating planetary gear (cp. also Figure 7.A2).

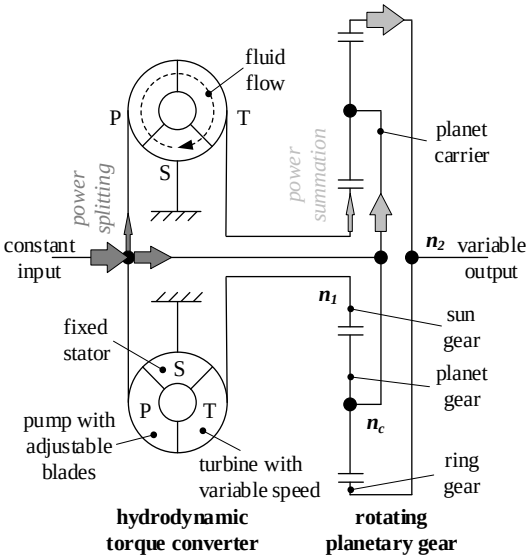

Figure 7.A1 Hydrodynamic torque converter combined with a rotating planetary gear

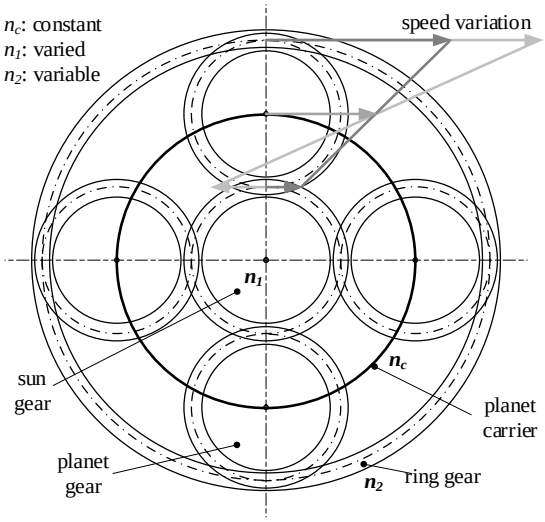

Figure 7.A2 Speed variation of rotating planetary gear (superimposition principle)

A7.7.3 Reduced bearing load

If the aerodynamic rotor loads are neglected in the hub centre of the wind turbine rotor, then a first estimation of the main bearing loads is given by the masses of wind turbine rotor, main shaft and ring gear. With the sum of all forces and moments, the main bearing forces are defined as follows (cp. also Figure 7.A3):

$$L_{B1} = g\left[m_{rotor}\left(1+\frac{l_H}{l_B}\right) + m_{shaft}\left(1-\frac{l_S}{l_B}\right) - m_{gear}\frac{l_G}{l_B}\right] \quad (7.A2)$$

$$L_{B2} = g\left[m_{shaft}\frac{l_S}{l_B} + m_{gear}\left(1+\frac{l_G}{l_B}\right) - m_{rotor}\frac{l_H}{l_B}\right] \quad (7.A3)$$

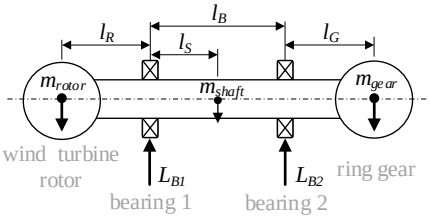

Figure 7.A3 Main shaft assembly

CHAPTER 8

Discussion

Despite the discussions in the previous chapters, several higher level scientific and practical aspects have not been considered yet. Therefore, these aspects are discussed in the following sections. As in the whole thesis, the design, maintenance and reliability perspectives will be considered again.

8.1 Scientific aspects

In this work several models and methods have been proposed, all following the underlying reliability and maintenance requirements of modern wind power turbines. In this section, the selection of the approach, the generalization to other application fields and the limitations of the approach will be discussed.

Selection of the approach

In this thesis load-based simulation models and methods were developed and presented. While such models and methods can be realized in many different ways, this research work investigates the development and use of analytical equations derived from ready available information. The first reasons for that choice is that analytical equations allow calculations which are computationally much less demanding than numerical methods like finite element (FE), computational fluid dynamics (CFD) or multi-body dynamic analyses.

Although predictions for the remaining useful life can be calculated with relatively large time intervals, e.g. every week, the load calculations can be performed continuously or in shorter time intervals. For example, to calculate the load profiles for one rotation of a wind turbine rotor (cp. chapter 2) spinning with ten rotations per minute, i.e. one entire rotation per six seconds, calculation (execution) rates less than one second are needed. The same applies for the reaction load calculations of the flexible connecting coupling due to misalignment between gearbox and generator shafts during operation (cp. chapter 3). This means that an accurate load profile evaluation (over one shaft rotation) requires the execution of the models within milliseconds. Since many of these loads are repetitive, they don't need to be analyzed real-time. However, to be able to analyze load variations over longer (representative) periods of time (e.g. a year), deriving the loads from a certain moment in time should also not take much more time than the moment itself.

Moreover, the values (data) of system design parameters might be easy to obtain from assembly plans and are time-invariant in the calculations. However, the values of the operational and environmental system parameters vary continuously and thus require measurements at adequately chosen sampling rates. Those sampling rates are determined by the measured parameters. For example, measuring the misalignment of the gearbox and generator shaft during operation requires sampling rates of a few milliseconds. Other measurements like temperatures may allow greater sampling rates up to a few seconds or even minutes. The shortest sampling rate of these measurements determines the model acquisition time, i.e. the model calculation (execution) rate.

In addition, if the sampling rates of these measurements are reduced to large time intervals, information will be lost, i.e. the values of the measured parameters are not properly detected anymore. This does not mean that the calculations cannot be executed. However, it leads to a lower prediction accuracy because the values used for the calculations deviate from the actual ones. The usage of average values has a comparable effect, i.e. peak values are neglected. Therefore, the incorporation of actual operational and environmental conditions in the prediction models requires a fast calculation, i.e. ideally quasi real time, so that the acquired time series of the measurements and the load profile calculations almost coincide and a much better accuracy can be guaranteed.

The second reason to focus on analytical equations is that, once they are established, they are easy to update according to deviations from nominal design information and applications. This means that a generic set of equations, as proposed in the previous chapters of this thesis, can easily be adapted to a specific application (e.g. wind turbine), size and operational

environment. This typically only requires changing some of the parameter values. In comparison, the numerical methods, finite element based, can be more accurate but also less flexible and computational intensive because of geometry, mesh and boundary conditions requirements.

This flexible formulation and low computational demand make the analytical equations particularly useful for sensitivity analyses, as a full range of configurations, load cases and operational conditions can be easily compared by just varying some parameters. This means that, by using the analytical equations during system concept stages and in design processes, the dominant parameters determining the system life time can be specified. In maintenance the analytical equations can quickly identify critical operating and environmental conditions which might stress weak system components. The analytical equations also offer reliability, i.e. failure probability, estimations based on the load-strength interference, fundamental design parameters and critical operating and environmental conditions. In other words, the quick-fix model adaptability can be used for reliability analysis across several and different systems. These insights are highly beneficial for a system owner or a service provider in order to define and adjust the maintenance intervals and activities of their systems, without the need to perform complex and computationally demanding analyses

Generalizing the approach

As mentioned before, the use of analytical equations allows generic formulations of the component models, i.e. the scaling to one of the most relevant geometrical parameter or several of them. This makes it easy to adapt the proposed models to other applications than the power trains in wind turbines that have been discussed in this thesis. The framework can be transported across different application in (heavy) industrial and automotive applications by plugging in the new value of the geometry. Industrial applications are, for example, crushers, shredders, mills and others. Automotive applications are electrically driven cars, trucks and other vehicles which are currently under development. These applications use the same components like gearboxes and electrical machines (generators). They only differ in size and power range. Therefore, the proposed models and methods have a broad range of applications. Such a flexibility and transportability cannot be achieved by FE models.

This broad applicability is, in addition to the use of analytical equations, also related to the approach chosen in this thesis and presented in the introduction (chapter 1), where a system is considered from the perspective of power transmission and conversion, i.e. power train and power chain. Part of this approach is also that the power train is applied to different applications like the wind turbine rotor. Consequently, the presented models of the wind turbine rotor demonstrate some of the benefits of modeling any power train application. This means that models describing (industrial) applications like wind turbine rotor, (ship) propellers or belt conveyors provide insight about which design parameters, operational and environmental conditions can be crucial for the life time of the considered power train, and thus how maintenance and reliability might be affected. Therefore, it is not only important to model the power train itself, but also consider the specific application. Otherwise, crucial design, maintenance and reliability aspects remain undiscovered or even misunderstood. The methods proposed in this thesis allow this integral analysis of the power train components with its environment.

Further, the proposed load-based prediction methods clearly demonstrate a direct interconnection between design, maintenance and reliability. This interconnection is created by the system loads, which are (i) defined based on expectations during the system design, (ii) are applied for the system maintenance prediction and (iii) determine the system

reliability. Consequently, a profound understanding of the system loads, i.e. knowing the critical design parameters, operational and environmental conditions, is essential for any (mechanical and electrical) system. As discussed above, analytical equations are advantageous for that. This means that an effort in developing analytical models and methods is beneficial for any system because it provides an extensive system understanding for designers, owners and service providers.

Limitations

However, the usage of analytical models and methods also has some drawbacks. Although analytical equations are accurate in principle, their application to a real system requires assumptions and simplifications to reduce the degree of complexity. This leads to calculation errors which can be quantified by comparing the results of the analytical-based calculations with either actual measurements or more complex (numerical) calculations like multibody analyses. The latter is, for example, done for the power analysis of standing jumps (of human beings) in [1] and in the study of a V6 engine piston in [2]. In both cases the calculation error between the analytical and the multibody dynamic approaches proved to be less than 10%. This means that analytical models and methods are capable of providing a moderate to good accuracy, despite system assumptions and simplifications. However, in system designs a calculation error of 5-10% might not be sufficiently accurate. Hence, the proposed analytical models and methods could be used for the system pre-design demonstrating the weakest link under certain global loads. Then, in the second design stage it could be focused on the calculation accuracy by executing a more complex multibody dynamics based calculation used for system fine tuning and verification. However, this two-stage approach cannot be applied by system owners and service providers, because they do not have access to the detailed system design information required for the execution of the more complex multibody dynamics based calculation. Nevertheless, they can still execute the load-based prediction models and methods to obtain various scenarios, e.g. a best and a worst case scenario. They can then consider to take a more conservative decision based on a scenario close to or even equal to the worst case. This would then compensate for the calculation error in their maintenance and reliability predictions.

Further, reducing the degree of complexity implies that the actual system is approximated, for example by an equivalent single degree of freedom system. This means that the required (system) assumptions and simplifications yield a model that only consider the main effects and dominant parameters. It also means that the analytical and load-based prediction models and methods provide insight in the determining system conditions and behaviors. However, neglecting minor effects and system influences or information can lead to less conservative predictions or less detailed insights. Less conservative calculations are caused, for example, by the one-dimensional (1D) spring stiffness approximation of the metal disc pack as applied in chapter 3. In such a case the user of the analytical models and methods must consider the less conservative calculations in the results. To account for this inaccuracy, they could implement a correction, which can be quantified in system design by a more complex calculation or in maintenance by measurements, for instance, of the actual disc pack stiffness (cp. chapter 3). Another example of less detailed insights are the transfer functions determining the dynamic system behavior (response) in chapter 6. Due to the assumptions and simplifications, the calculated transfer function does not demonstrate the actual dynamic behavior of every system element. Especially in transmission systems, the dynamic behavior of the individual system elements like shafts, gears or teeth can influence the system predictions. This means that the users of the analytical models and methods must be aware

that the gained insights are rather a trend or rule of thumb and that a more complex multibody dynamics based calculation is necessary to fully understand the system (behavior).

Another limitation of this work is that the proposed models and methods do not yet cover the entire power train, i.e. load-based prediction models and methods are still missing for electrical machines and electrical power (frequency) converters. These models will be necessary to fully predict the maintenance and reliability of the entire (wind turbine) power train including the dynamic interaction between all power train components. Developing these models is not fundamentally different from the development of the models presented in this thesis, but mainly a matter of time. Following the approach from chapters 2-7, combined with the right amount of system and domain knowledge in principle allows the development of the missing models. In chapter 4, the power transformer modeling and temperature hot spot calculation already demonstrate the expansion of the approach to electrical power train components.

A further missing part in this work is the application of the proposed models and methods to a real system. This would require the models to be executed with inputs and parameters obtained from actual measurements on the real system, and the comparison of their results with actual failure statistics. In the present work, the models have been verified with results from literature. This proves that trends in the results are valid, and relative analyses (i.e. comparing two configurations or conditions) can be performed. But to fully validate the model, also for absolute predictions, the comparison with real data is required. In the absence of measurements from real wind turbines, future research may also combine the load-based prediction with statistics-based models and methods including failure statistics. This will be advantageous, if the conversion of the actual, i.e. measured, system loads into a particular life time or remaining useful life cannot be realized straightforwardly. Then, the insights of the load-based prediction models and methods are used to assess the failure probability and thus, to improve the accuracy of the results calculated by the statistics-based models and methods. This so-called hybrid approach is partly applied and shown in chapters 5 and 6.

8.2 Practical aspects

From the load-based prediction models and methods presented in this thesis, as well as their application to the wind turbine power train, a few essential aspects can be deduced which are useful for the engineering, i.e. design, maintenance or simulation, of any system. These aspects can be considered as some important practical contributions of the present work, in addition to the scientific contributions (previous section) and the specific (wind turbine related) insights that already have been presented in the separate chapters.

Integral approach and system knowledge

Due to the interconnection of design, maintenance and reliability by the system loads, any profound attempt to reduce the maintenance intensity, or to increase the reliability, starts with the system design. It is important to note that these improvements are related to the system as a whole. Improving or substituting one component (subsystem) will not lead to a significant enhancement of the system maintenance intensity and reliability, because subsystems are interconnected and thus affect each other. This means, for example, that removing one subsystem does not necessarily solve the problems; rather, it shifts them from one point to another of the power train assembly. In the case of the wind turbine power train, this can be observed by comparing the failure rates of a direct and geared drive. Removing

the gearbox shifts the high failure rates to the electrical components, like the generator and electrical power converter.

Another important aspect is the consideration of the specific application of the power train system (i.e. in a (on-shore or off-shore) wind turbine, propulsion system, etc.), which largely determines the system loads, behaviors, dimensions and configurations. Consequently, the system design and functional requirements to achieve a high reliability and low maintenance effort differ for every application. This means that a deep understanding of the system application is needed, for which the proposed detailed analytical application models are very suitable. It is highly discouraged the simple copy-paste from one system to another, if the global loads are not evaluated at the outset. The modelling framework is robust as far as the system loads are identified at the early stage as the main driver of failure in system components. This means that system designs are application-specific considering their needs and effects on the functional and structural system performance. Note that some systems also interconnect the application to a superordinate system. This is, for example, the case for the wind turbine power train, which connects the wind turbine rotor to the electrical grid. In such a case, the system design has to satisfy the needs, and to cope with the effects, of both application (wind turbine) and superordinate system (electrical grid).

Load reduction, monitoring and root causes

Furthermore, in system designs it is often assumed that the maintenance intensity reduction and reliability increase can only be achieved by a system strength increase, i.e. by oversizing the system. However, as it demonstrated in this thesis, a more effective way of improving the reliability is the approach of load reduction, i.e. decreasing load magnitude and avoiding load superposition. Consequently, system configurations, behaviors and dimensions should be chosen such that the system loads are minimized and are not superimposed, respectively. As the latter can be obtained by applying the proposed models and methods, the processes and system design decisions that lead to the aimed load reduction are accessible for the different system stakeholders. This means that the benefits of particular system designs become transparent. In other words, system designers can demonstrate to system owners and service providers that their design decisions, which in some cases might require additional investment costs, will benefit them during system operation. For example, in a geared drive the torsional vibrations might be shifted away and at much higher frequencies than in a direct drive. This means that the load filtering which the geared drive applies to the input load justifies additional investment costs. Then, the lower system maintenance costs, higher reliability and hence, higher system availability will reduce the total cost of ownership or total life cycle costs.

It is also important to realize that measurements of actual operational and environmental system conditions are needed for the application of load-based prediction models and methods for maintenance planning. But since the models and methods have their specific input parameters, i.e. determine the required measurements, an effective and cost efficient measurement strategy can be realized: models and methods exactly indicate what sensors and measurements they need, and simultaneously demonstrate the added value of installing these sensors (and the associated investment costs). This means that the number of measurements can be restricted to only those that are absolutely necessary, which is called a bottom-up approach. The alternative (and commonly applied) top-down measurement strategy is the installation of an extensive number of (more or less randomly selected) sensors and measurements to generate as much data as possible. This huge amount of data is often "randomly" interconnected by algorithms to detect unusual system behavior. The main

drawback of such a data-driven approach is that it does not underpin the root cause of an unexpected system response. The analytical and load-based prediction models and methods provide a big advantage here, as critical system conditions, i.e. abnormal system loads (stresses), can be identified rather easily. As these abnormal loads normally lead to failures, the load root causes also indicate the failure root causes. Therefore, the load-based prediction models and methods also provide insight into system failures and their root causes.

In addition, the critical system conditions, abnormal loads and thus potential system failures and their root causes determine which of the system components and parts are critical. These insights are highly beneficial for all system stakeholders, i.e. system designer, owner and service provider. A designer can use them for improving the system design and an owner or service provider for enhancing maintenance planning and execution. This means that the load-based prediction models and methods provide maintenance and reliability improvements in new system designs by recommending system modifications, while in installed systems they lead to improvements by identifying and predicting critical component failures. It also means that the proposed analytical models and methods support the system stakeholders in finding the best solution. Depending on their interests the best solution is characterized, for example, by a high reliability and low maintenance intensity. As the analytical models and methods also identify system solutions with higher investments but lower maintenance costs, they provide already during the system design an estimation of the system reliability and maintenance intensity and thus an approximation of the total costs of ownership. These additional insights are beneficial for system owners while selecting a particular system solution.

Knowledge management

Finally, the usage and application of the analytical and load-based models and methods are normally straightforward. A few input parameters are needed to solve the set of analytical equations which are behind the models and methods. The analytical equations are often expressed in a simple form and thus are easy to understand. This means that the knowledge provided by the analytical models and methods is accessible for all the system stakeholders. It also means that analytical models and methods are a source of fundamental knowledge, i.e. they are an important part of knowledge management and knowledge generation in the organizations to which the system stakeholders belong. Consequently, analytical models and methods are essential for the development of both (engineering) systems and people and organizations. In other words, the analytical-based framework acts as precursors of more detailed, refined and expensive analyses which can be strategically planned based on the insights gained from the early simulations. Therefore, stimulating the development and implementation of analytical models and methods is highly beneficial for the product (system) and people's professional and personal skills development, resulting eventually into a growing organization and business.

However, the development of the set of equations, i.e. the models and methods, is challenging. The description of the actual system (behavior) by adequate analytical equations requires a profound engineering comprehension. Further, the latter should be combined with creativity to find proper system assumptions and simplifications. Another important element is the persistency to develop and derive the analytical equations by hand, i.e. using pen and paper. There is no computer program that can develop the complex system of analytical equations and can include assumptions or simplifications, if necessary. Therefore, the development of analytical and load-based prediction models and methods requires a skilled engineering expertise. The models proposed in this thesis do contain that knowledge and

understanding, but can now be used and applied by a large group of less-experienced engineers.

References

[1] G. Palmieri, M. Callegari, and S. Fioretti, "Analytical and multibody modeling for the power analysis of standing jumps," *Comput. Methods Biomech. Biomed. Engin.*, vol. 18, no. 14, pp. 1564–1573, 2015.

[2] M. Cavalli, G. Lavacchielli, R. Tonelli, G. Nicoletto, and E. Riva, "Comparison of analytical and multibody dynamic approaches in the study of a V6 engine piston," *Proc. Inst. Mech. Eng. Part K J. Multi-body Dyn.*, vol. 231, p. 146441931770598, 2017.

CHAPTER 9

Conclusions and Recommendations

In this thesis, load-based prediction models and methods were developed for the system design, maintenance and reliability of the wind turbine power train. However, loads are a generic concept and any system is exposed to them. This means that load-based prediction models and methods can be developed for and applied to any system. Therefore, the following conclusions and recommendations can be drawn.

9.1 Conclusions

The different considerations and discussions in this thesis lead to the subsequent scientific and practical conclusions:

9.1.1 Scientific conclusions

- Analytical and load-based prediction models and methods are time efficient, and once established, easy to adapt and execute, which clearly distinguishes them from commonly used numerical methods like FEM and CFD. They can conveniently be applied for system design, maintenance and reliability because they demonstrate fundamental design parameters and critical operating and environmental conditions. They can be used by system designers, owners and service providers.
- The application of analytical models and methods to real systems requires system assumptions and simplifications, which may lead to calculation errors up to 10%. However, for application in the pre-design stages of system design this is no problem, as mainly comparative studies are performed. In maintenance and reliability analyses, the errors can be compensated by performing a more conservative calculation, i.e. system owners or service providers may tend to choose prediction results obtained from scenarios close to or even equal to the worst case.
- The load-based prediction models and methods proposed in this thesis have a broad field of application. Power trains in wind, heavy industrial or automotive applications use the same components like gearboxes or electrical machines, which only differ in size and power range.
- An analytical and load-based application model provides insight in which design parameters, operational and environmental conditions are crucial for the system (power train) life time. Therefore, the modelling of the application is as important as the system itself. Otherwise, crucial design, maintenance and reliability aspects remain undiscovered or even misunderstood.
- The analytical and load-based prediction methods demonstrate a direct interconnection between design, maintenance and reliability given by the system loads. This means that a profound understanding of the system loads is essential for any system development, design and operation. It also means that the effort in developing analytical and load-based models and methods is beneficial for any system because it provides an extensive system understanding for all system stakeholders.

9.1.2 Practical conclusions

- Due to the interconnection of design, maintenance and reliability by the system loads, any profound attempt to reduce the maintenance intensity or to increase the reliability starts with the system design as a whole. Improving or substituting one component (subsystem) will not lead to a significant enhancement of the system maintenance intensity and reliability.
- The system needs and design to achieve a high reliability and low maintenance differ for every application. This means that a deep understanding of the system application is needed. It also means that a “copy-paste” design approach or a system performance

comparison is risky and even questionable, because crucial needs or aspects from the application are not considered, misunderstood or even neglected.

- The approach of load reduction, i.e. decreasing the load magnitude and avoiding load superposition, is an effective way of improving maintenance and reliability. This means that system configurations, behaviors and dimensions should be chosen such that the system loads are minimized and are not superimposed, respectively. Applying the proposed models and methods can make the benefits of particular system designs transparent, for example, a high system reliability or a low maintenance intensity.
- The analytical and load-based models and methods indicate both the need for and the benefit of certain sensors and measurements for their application in maintenance planning and execution. This yields an effective and cost efficient measurement strategy because the number of sensors and measurements can be restricted to the minimum necessary.
- Critical system conditions, i.e. abnormal system loads (stresses), can be identified by analytical and load-based models and methods. In addition to that, they provide insight into system failures and their root causes, because abnormal system loads normally lead to failures. These insights are highly beneficial for all system stakeholders and offer improvements in system design, maintenance and reliability.
- Analytical and load-based models and methods support system stakeholders in finding the best system solution characterized, for example, by a high reliability and low maintenance intensity. They also identify system solutions with higher investments but lower maintenance costs and thus, provide an estimation of the total costs of ownership during system design.

9.2 Recommendations

In addition to the conclusions, the following scientific and practical recommendations can be drawn from this thesis:

9.2.1 Scientific recommendations

- The models and methods developed in this thesis do not cover the entire power train i.e. load-based prediction models and methods for electrical machines and electrical power (frequency) converters are still missing. These models will be necessary to fully predict the maintenance and reliability of the entire (wind turbine) power train including the dynamic interaction between all power train components. It is therefore recommended to develop these missing models, where the approach followed in this thesis for the other components can be used as guideline. The expansion of the approach to electrical power train components is already demonstrated for electrical power transformers in thesis.
- The models and methods proposed in this thesis are not applied yet to an actual system. This means that their execution with actual measurements and the comparison of their results with actual failure statistics are still needed to fully validate them, also for absolute predictions.
- It would be interesting to connect the load-based prediction with statistics-based models and methods including failure statistics. Such a hybrid approach will combine the

advantages of both approaches, i.e. the high accuracy of the (specific) load-based prediction models and methods and the lower demand for system details of the (generic) statistics-based models and methods.

9.2.2 Practical recommendations

- A significant reduction of the system maintenance intensity and increase of the reliability can be achieved only by a system (re)designs because system design, maintenance and reliability are interconnected. This means for already installed systems that owners and service providers should focus on the optimization of maintenance planning and activities, i.e. they should accept that a certain amount of maintenance needs to be done for this specific design. Lowering the system maintenance intensity and increasing the reliability can only be realized by a system retrofit, i.e. system redesign. The interconnection of system design, maintenance and reliability also means that a high maintenance intensity and low reliability indicate a poor system design. So to save high maintenance expenses, i.e. costs on the long term, the decision of a system retrofit (redesign) might be preponed although this leads to high costs on the short term.
- System designers, owners and service providers will only be able to identify and understand the power train system needs, if they have a profound understanding of the application, i.e. the components driving or driven by the power train. This means that the development of a (simplified) application model (e.g. the wind turbine rotor model in Chapter 2, or a ship propeller model) is crucial for these stakeholders because it will provide them important insights in the power train system design, maintenance and reliability.
- The analytical and load-based models and methods specify the needed sensors and measurements. This means that before installing any sensors and executing any measurements, it is beneficial to develop prediction models and methods for both the application and the power train system. Otherwise, system stakeholders run the risk of spending (expensive) resources without complying with their expectations. In other words, the installed sensors and measurements might then not provide the expected application or system performance.
- Failure root causes are mostly directly related to the loads. This means that early or unexpected system failures indicate overload conditions. While these overloads are typically attributed to operational or environmental conditions, they might also be caused by improper component integration and neglecting the associated interface loads (cp. Chapter 3 on flexible connecting couplings). System stakeholders should be aware of this potential load source when investigating failure root causes.
- Solving the analytical equations behind the load-based models and methods is a straightforward process. A few input parameters are needed and the equations are expressed in simple forms, i.e. they are easy to understand and to apply. This means that the knowledge provided by the analytical models and methods is accessible for all system stakeholders. It also means the analytical models and methods are a source of fundamental knowledge, i.e. they are an important part of knowledge management and knowledge generation in organizations and thus are essential for the development of both (engineering) systems and people and organizations. Therefore, it is recommended that managers stimulate the development of analytical models and methods to enhance the growth of organization and business

Acknowledgments

In accomplishment of my PhD I have had the great opportunity to contribute to the Wind turbine Maintenance and Operation decisions Support (WiMOS) project. It was funded and supported by TKI Wind op Zee, IX Wind and Joulz Energy Solutions and executed in collaboration with the University of Twente.

I would like to thank Tiedo (University of Twente), Erik (IX Wind) and Kerem (Joulz Energy Solutions) for initiating and contributing to this PhD project. Without them, this research would not have been possible.

I would like to thank my supervisor Tiedo and co-supervisor Dario for their continuous support and feedback. Special thanks to Tiedo for the freedom to develop myself further in the field of my interests.

I would like to thank my colleagues from the Dynamic Based Maintenance Group as well as Debbie for their support.

Un agradecimiento cordial para Diana e Sarah. Ese proyecto (de vida) no hubiera sido posible sin su ánimo y apoyo incondicional.

Ein herzliches Dankeschön auch an meine Eltern, die den Grundstein für diese Arbeit vor vielen Jahren gelegt haben.

ISBN 978-90-365-5008-6